ADVANCED REACTOR SAFETY RESEARCH
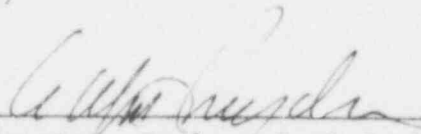## QUARTERLY REPORT
OCTOBER-DECEMBER 1979

Advanced Reactor Research Department
Sandia National Laboratories
Albuquerque, NM 87185

APPROVED: _____

Manager, Advanced Reactor Research

_____

Director, Nuclear Fuel Cycle Programs

8011058526

FOREWORD

Sandia Laboratories' Advanced Reactor Safety Research Program, initiated in FY 1975, is a comprehensive research activity conducted on behalf of the U.S. Nuclear Regulatory Commission (NRC) and is part of NRC's confirmatory research effort to assure that the necessary safety data and theoretical understanding exist to license and regulate the Liquid Metal Fast Breeder Reactor (LMFBR) or other advanced converters, breeders, or advanced light water reactors which may be commercialized in the United States. The program includes a broad range of experiments to simulate accidental transient conditions to provide the required data base to understand the controlling accident sequences and to serve as a basis for verification of the complex computer simulation models and codes used in accident analysis and licensing reviews. Such a program must include the development of analytical models, verified by experiment, which can be used to predict reactor performance under a broad variety of abnormal conditions. Major program elements include studies of the coolability and containment of rubblized cores to assure containment integrity. This work along with that of other U.S. and international researchers should provide the technology base on which licensing decisions can be made with confidence that the safety of the public is assured.

The early thrust of Sandia's program was designed to provide data associated with the hypothetical core disruptive accident, with emphasis on prompt burst (~1-ms period) energetics and the behavior of postaccident core debris. The scope of the program was expanded in FYs 1976 and 1977 to encompass other energetics and inherent retention concerns such as large-scale sodium containment and structural integrity; aerosol source studies; transition phase energetics; fuel failure and motion; probabilistic accident delineation; and studies to quantify elevated temperature failure modes of critical component materials. A portion of the early effort in the program was directed toward obtaining data to support the licensing review of the Clinch River Breeder Reactor (CRBR) and the Fast Flux Test Facility (FFTF). Recently the emphasis has shifted toward applying advanced reactor safety technology to LWR Class 9 accident concerns which have been of considerable interest following the accident at TMI-2. For FY 1980, the program is organized in the following subtasks, progress on which is reported herein.

Task 1   Energetics

      Subtask 1.1   Prompt Burst Energetics

      Subtask 1.2   Irradiated Fuels Response

Task 2   Fuel Dynamics

      Subtask 2.1   Transition Phase

      Subtask 2.2   Initial and Extended Fuel Motion

      Subtask 2.3   Fuel Motion Detection

Task 3   Core Debris Behavior - Inherent Retention

      Subtask 3.1   Molten Core Containment

      Subtask 3.2   PAHR Debris Bed

      Subtask 3   PAHR Molten Pool

      Subtask .4   Fragmentation

      Subtask 3.5   Sodium Containment and Structural Integrity

Task 4   Aerosol Source Normalization

Task 5   Containment Analysis

Task 6   Elevated Temperature Design Assessment

Task 7   LMFBR Accident Delineation

Task 8   Test and Facility Technology

CONTENTS

ILLUSTRATIONS

ILLUSTRATIONS (cont)

ILLUSTRATIONS (cont)

TABLES

EXECUTIVE SUMMARY

Introduction

Sandia Laboratories, Albuquerque, New Mexico is conducting the Advanced Reactor Safety Research Program on behalf of the U.S. Nuclear Regulatory Commission (NRC). The overall objective of the program is to provide NRC a comprehensive data base essential to (1) defining key safety issues, (2) understanding the controlling accident sequences, (3) verifying the complex computer models used in accident analysis and licensing reviews, and (4) assuring the public that advanced power reactor systems will not be licensed and placed in commercial service in the United States without appropriate consideration being given to their effects on health and safety.

The NRC program is carefully planned to complement the larger DOE program, but at the same time to satisfy the NRC obligation of independent confirmatory research.

Together with other programs, the Sandia effort is directed at assuring the soundness of the technology base upon which licensing decisions are made, and includes experiments and model and code development.

Sandia has been tasked to investigate eight major areas of interest which are intimately related to overall NRC needs. These are

1. Energetics

2. Fuel Dynamics

3. Core Debris Behavior - Inherent Retention

4. Aerosol Source Normalization

5. Containment Analysis

6. Elevated Temperature Design Assessment

7. LMFBR Accident Delineation

8. Test and Facility Technology

These major tasks are subdivided as necessary into subtasks to facilitate the organization of work and the interaction of subtask results into a body of coherent information which supports the requirements of the NRC.

EXECUTIVE SUMMARY

1. Energetics

1.1 Prompt Burst Energetics

Prompt Burst Energetics (PBE) experiments provide information on the energetic response of various reactor fuel-clad-coolant systems to superprompt critical conditions. This program is directed at characterizing the phenomena which result in pressure generation and the conversion of thermal energy to work, and at understanding the reactivity effects arising from rapid coolant voiding and initial fuel motion. These experiments examine integral effects of fuel-clad-coolant interactions (FCI), fission gas release and fuel and fission product vapor pressures during superprompt critical core disruptive accidents and determine the potential for damage to the primary containment. The rate of coolant voiding in a positive reactivity void-coefficient system determines the reactivity insertion rate and hence the magnitude of the transient under accident conditions. The experimental work is closely interfaced with analytical efforts to develop models which uniquely describe the observed phenomena for incorporation into predictive accident analysis as well as to provide data to verify existing accident analysis codes. These experiments also provide information about the thermodynamic states and spatial distribution of fuel, clad, and coolant following a superprompt excursion. These data serve as initial conditions for postaccident heat removal (PAHR) and molten core containment analysis.

In tests performed to date, single fuel pins have been pulse fission heated in the Annular Core Research Reactor (ACRR) (or its predecessor the ACPR) to temperatures resulting in fuel vaporization. The pins, which have been surrounded by helium or sodium, are contained in a rigid pressure vessel which is instrumented with thermocouples and pressure transducers and which is fitted with a movable piston at its upper end. Estimates of the conversion of thermal energy to work result from comparisons of the kinetic energy of the piston to the fission energy input to the fuel. Pressure, temperature, and piston displacement histories are determined for a variety of fuel-coolant systems and initial conditions. A series of experiments with fresh uranium dioxide fuel and sodium coolant and a series with fresh uranium carbide fuel in sodium have been completed. Additional oxide experiments are now being performed. Future pin experiments will examine fission product effects in preirradiated fuel.

EXECUTIVE SUMMARY

The scope of the PBE work is being enlarged to include separate effects experiments to examine FCI phenomena between oxide fuel and sodium. The first area to be addressed in these studies is to determine if the oxide/sodium system is capable of supporting large scale, propagating, escalating interactions and if so to characterize the controlling phenomena. Conceptually, the experiments would examine the response of a mixture of relatively large droplets of molten fuel in a sodium volume to externally applied pressure transients.

Work during this quarter included detailed analysis of the series of fresh uranium carbide/sodium PBE experiments (PBE-SG1, -SG2, and -SG3) and preparation of a topical report describing that series.

A detailed comparison of the observed pressure histories and piston displacement histories demonstrated total consistency for PBE-SG1 and -SG3. However, for PBE-SG2, a significant difference was found between the measured pressure history and that observed in piston motion, suggesting a considerably greater impulse than piston displacement indicated. Using a gas shock tube, preliminary evaluation of the response of the Kaman pressure transducers to step changes in pressure indicates a transient "overshoot" from the transducer lasting 0.1 to 0.5 ms with amplitude 2 to 5 times the applied pressure. Qualitatively, these effects would explain the observed discrepancy in PBE-SG2. The actual pressure transient in that experiment appears to have had a much faster rise time than in other experiments. Work has been initiated to derive response functions for sibling transducers and then to attempt to unfold the measured pressure histories for PBE-SG2. The actual amplitudes of the pressures in PBE-SG2 appear, at this point, to have been less than indicated by the pressure transducers. This result, however, does not alter the previously stated conclusions that the pressure transients were the results of significant fuel coolant interactions (FCI).

Heat transfer analyses were performed for the carbide experiments to determine temperature states and fuel vapor pressure during the experiments. This work modeled the intact pin geometry. The analysis showed that temperature profiles peaked near the fuel surface at failure for all three experiments. For that portion of the experiment prior to clad failure, the results of the analysis when compared with temperature measurements validate the model of the gap conductance between

the solid fuel and the clad as used in this work and in the EXPAND pin-failure code. The model of intact pin geometry tends to overpredict fuel vapor pressure especially at later times. Essentially no fuel vapor pressure was predicted for PBE-SG1 and -SG3 and values consistent with the initial pressure observed at failure were predicted for PBE-SG2.

Modeling of plausible hydrodynamic pressure sources for the pressure transient that was observed following piston stoppage in PBE-SG2 fails to describe the observed pressurization. The only remaining explanation is an FCI triggered by the low amplitude, short duration pressure transients that are predicted by the modeling.

SIMMER-II analysis of PBE-5S has continued with the three-fold objective of: (a) investigating the applicability at SIMMER to these complex experiments, (b) providing insight into the separate pressure-generation and pressure-quenching mechanism, and (c) providing information for model development and verification. Current work involves comparison of experiment data and SIMMER results for PBE-5S and an assessment of possible fuel-vapor-quenching mechanisms.

1.2 Irradiated Fuels Response

The Sandia Laboratories Irradiated Fuels Response program is aimed at determining the response of fresh and irradiated reactor fuels to both prompt burst (disassembly timescale) and loss-of-flow (LOF) heating conditions. On prompt burst timescales, the pressure source from both fuel vapor and fission gases as well as the accelerations produced by these pressure sources are of central importance. Thus the program in this area centers on determination of the effective equation-of-state (EEOS) of both fresh and irradiated fuels, the dynamics of pressurization (rate effects) and the ability of this pressure to disperse fuel. On LOF timescales, the mode of initial fuel disruption and its timescale for both fresh and irradiated fuels are of crucial importance.

1.2.1 LOF-Timescale Fuel Disruption

A topical report on the first series of fuel disruption experiments, FD1, was published and distributed in this reporting period. The report addresses the motivation, conduct, some of the results, and analysis of the test series. Preliminary results

were given in a previous quarterly report. The results and analysis will be presented in a separate report.

The obtaining of approval from Washington for shipment of some of the FD1 fuel to KfK, Karlsruhe, West Germany has progressed. This fuel, which KfK will analyze microscopically on a cooperative venture with Sandia, is the fuel which swelled but did not otherwise disrupt. The main interests concern Cs content and migration, Pu, U, and O_2 distribution, and stoichiometry as functions of power transient and fuel radius. The fuel probably will be shipped next quarter.

An extensive report has been written on fuel fragmentation by fission gases during rapid heating transients. It presents criteria for the advance of cracks between fission gas bubbles in LMFBR irradiated fuel under transient power conditions. Calculations performed with the latest version of the transient intragranular gas release and swelling code (TIGRS) for a number of hypothetical transients tend to indicate that heating at 100 K/ms produces fuel dispersal in the solid state, while rates of the order of 1 K/ms do not. These results agree with the results of four of the FD1 series tests. Furthermore, the rates and amounts of swelling observed also can be predicted by TIGRS.

The latest series of LOF-timescale fuel-disruption experiments, FD2, has continued. In the previous quarter three fresh fuel tests were conducted. These yielded sufficient data, together with calibration tests performed earlier, to proceed to the preirradiated-fuels set of experiments in FD2. Thus the first test, FD2.4, of this set was carried out. Preliminary examination shows the fuel dispersed very rapidly, significantly earlier than fresh fuel for identical power history; and the clad and fuel ruptured into large pieces rather than melting as in the case of fresh fuel. This preirradiated fuel probably was contaminated with atmospheric gases. Six more tests remain in this series and these will use uncontaminated fuel, extracted from pins sectioned in the Sandia ultraclean, shielded glovebox.

Neutronic and thermal heat-transfer calculations for fresh and irradiated fuel are continuing using the power pulse actually employed, with gap conductivity as a parameter.

Finally, for FD2, LASL and Sandia have agreed to have LASL perform the requisite spectrometric analysis of the gas sampled from that which effuses from the preirradiated fuel during each test. In fact, the first two samples have been sent to LASL.

A discussion on the high-ramp-rate (HRR) series of fuel disruption experiments has led to a tentative matrix of 10 tests. These experiments, currently being planned for FY 1980, will investigate the relative efficacies of fission gas and fuel vapor as dispersants during fuel disassembly in prompt-burst power ramps. This series of experiments is a collaborative program between the UKAEA (SRD) and the USNRC (Sandia).

2. Fuel Dynamics

2.1 Transition Phase

Following the loss of initial geometry in a core disruptive accident, and assuming that neither early shutdown nor rapid hydrodynamic disassembly takes place, the accident enters the transition phase. The progression of the transition phase toward possible second recriticalities may strongly influence the severity of the accident and it is, therefore, important to understand in detail the phenomena associated with this accident stage. Sandia work is currently directed toward the mechanics of fuel blockage formation since this defines conditions leading to recriticality.

The formation of fuel blockages by freezing is an important aspect of the transition phase since this phenomenon controls fuel penetration through the upper core structure and hence the amount of negative reactivity available for accident termination. Heat transfer between flowing molten fuel and ablating steel walls which ultimately controls fuel penetration distance is affected by transpiration as molten steel moves away from the solid wall and is ablated into the bulk flow.

Design of in-core fuel-freezing experiments using prototypic reactor materials is in progress. To study the fuel freezing process, parameters such as driving pressure, fuel temperature and steel temperature will be varied over wide ranges in a controlled fashion. These experiments significantly extend the range of fuel temperature

and the degree of control of experiment parameters, in comparison with previous work.

Preliminary apparatus design is almost complete, and certain critical components have been ordered for testing. Detailed neutronic design and heat-transfer calculations are in progress.

2.2   Initial and Extended Fuel Motion (IEFM)

The purpose of the IEFM Program is to investigate various phenomena associated with fast reactor initiating accidents such as a loss of coolant flow (LOF) and transient overpower (TOP) without SCRAM. In these hypothetical accidents, dispersive fuel motion is a major source of negative reactivity insertion. However, depending upon failure location, failure mode and final fuel relocation, positive reactivity effects are also possible. Therefore, it is important to identify and model phenomena such as fuel motion inside the clad prior to failure, axial fuel-failure location, mode of cladding failure, fuel disruption modes, rate of dispersal, fuel plateout, and extended fuel motion into the blanket (potential for blockage). Data to support model development and verification of these phenomena are severely limited. Irradiated fuel experiments are currently being planned that will use the newly developed coded aperture fuel motion detection system currently being installed in the ACRR. Investigators hope that, due to the considerably improved resolution of this diagnostic device, direct observations of these phenomena will be possible. These tests in the ACRR will require operating modes allowing preheats at nominal power followed by ramp, square wave or pulse power profiles. The required hardware to provide these modes is being constructed. This capability is expected to be available in early FY 1980. An additional facility needed for these experiments is a flowing sodium loop. Design of a prototype loop for single fresh fuel pin tests is currently underway. A program (Phase 2) involving many tests is proposed as a follow-up to the prototype loop program. Work on the Phase 2 program has been initiated and includes definition of the hot cell and fuel handling requirements.

These experiments are complementary to those currently being performed in the CABRI reactor in France. Consequently, cooperative efforts are underway through the ACRR/CABRI exchange agreement to provide a continuing interchange of expected data and analysis results.

EXECUTIVE SUMMARY

Phase 1 IEFM tests have been re-evaluated to clearly delineate the demonstration portion from the experiments which will focus on specific safety issues. Also a preliminary test definition has been written for the first IEFM test (L/D-1). The rationale, general approach, and fundamental test requirements have been established and preliminary design and diagnostic requirements have been defined.

The design effort has begun for the out-of-pile flowing sodium loop. This loop will aid in the prediction of the actual thermal-hydraulic conditions to be obtained with the in-pile loop, provide a test bed for instrumentation, and help uncover potential design problems.

Sandia investigators reviewed the instrumentation and control requirements for the loop, identified required instrumentation and signal-processing electronics, and conducted a literature search.

A work order was placed with Plant Engineering for hot cell modifications to handle the in-pile loop.

One Sandia staff member went to the French Nuclear Research Center, Cadarache, to discuss the CABRI calorimeter project. An export license for shipping the Sandia detectors to France was applied for. Also, Sandia fabricated five fission thermocouple detectors and five gamma thermocouples for calibration in the SPR-III.

2.3   Fuel Motion Detection

The feasibility of in-core fuel motion detection is being investigated at Sandia because many facilities which can be used for NRC fast reactor safety tests do not have instrumentation slots. Also, in those reactors which do have slots, self-shielding may preclude the use of high-resolution techniques for large-scale tests. Consequently, 7-, 19-, and 37-pin experiments are being conducted in the SPR-III to test both detectors and unfolding methods. Following the completion of these experiments, fuel motion detection will be performed in the ACRR as part of prototypic accident situations generated during PBE experiments.

The 7-pin gross fuel motion experiments planned for early October were postponed at the request of SPR-III operating personnel. The experiments are now expected to be performed in January 1980.

Detectors for both the French CABRI calorimeter experiments and Sandia fuel motion experiments in the ACRR were fabricated during this time. The main effort has addressed the tailoring of detector sensitivities so that the detectors will be more sensitive to fuel motion and less sensitive to background.

3. Core Debris Behavior - Inherent Retention

3.1 Molten Core Containment

If, following a major reactor accident the core debris is not permanently coolable, the debris will penetrate the reactor vessel, and come into contact with structural and containment materials. The interaction of the melt with these materials causes (1) pressurization of the containment structure, (2) release of the radioactive aerosols production, and (3) erosion, possibly to melt-through of the containment.

The attack of high temperature, reactor core materials on containment materials is the focus of this task.

Two sustained molten steel/concrete interaction tests were run this quarter. The results of these tests will be used to assess the operating effectiveness of computer models of melt/concrete interactions. Each of the two tests involved the deposition of about 200 kg of stainless steel into crucibles made of the so-called Clinch River limestone concrete. Induction coils embedded in the concrete were used to sustain the melts at high temperatures for 60 and 87 minutes, respectively.

Some descriptions of the test procedure are presented in this report. Detailed results of the test will be reported once the computer model predictions have been made. High quality data on the melt temperature, concrete temperatures, and concrete erosion rates were obtained. Once the solidified melt has been extracted and weighed, data on the extent of melt oxidation will be available.

A sustained test of molten steel interacting with high alumina cement was also run during this report period. The test procedure was similar to that used for the code comparison tests. Induction coils embedded in the high alumina cement were used to maintain and raise the melt temperature once the melt had been teemed into the crucible. The melt was sustained for over two hours. Significant erosion of the cement did not occur until the melt temperature was above 1973 K (1700°C).

Installation of the large-melt facility achieved approximately 90% completion. In January, the facility will be ready for shakedown experiments to be performed during the remainder of that quarter.

Sandia staff members are preparing a crucible-tapping experiment in which an aluminum container will simulate the crucible and lead will simulate the UO_2.

The oxide crucible was completed and shipped to Sandia. The crucible contains 211.8 kg of oxide charge.

3.2 PAHR Debris Bed

Requirements for the safe shutdown of an LMFBR have led to many studies of Post Accident Heat Removal (PAHR) from disrupted-core geometries. Studies of in-vessel and ex-vessel PAHR have been motivated largely by the significant reduction in radiological hazard potential which results from retention of fuel and coolant within the primary or secondary containments.

Following a core disruptive accident, molten core materials may exit the core region and contact sodium where solid fuel debris will be formed and collected on horizontal surfaces within the vessel. This debris is still capable of generating significant power through the decay of fission products. Should insufficient cooling be afforded by natural processes, the debris could remelt and threaten the vessel. The purpose of this task is to determine the natural cooling of such debris.

Four major first-of-a-kind in-pile experiments have been performed so far at Sandia and have provided significant (and unexpected) data for modeling the behavior of debris beds.

EXECUTIVE SUMMARY

In late September 1979, debris bed experiment D-4 was performed. Preliminary results indicate that for large sodium subcooling (460 K) the incipient dryout heat flux was 367 kW/m^2 while for the lower sodium subcooling case (190 K) it was 1971 kW/m^2. Thus the degree of sodium subcooling strongly influenced the specific bed power required to reach incipient dryout. The preliminary results indicate a factor of 5 between the two cases. The mechanism responsible for the increased coolability of the low-subcooled bed was not delineated, but observed channeling and belching were assumed to have played an important role.

Postdryout behavior was observed for both cases of subcooling. The ultrasonic thermometers (UTs) used in the D-4 experiment provided first-of-a-kind measurements of the length of the two-phase and conductive zones within the bed. For the large subcooled case, the two-phase length was 4.5 cm and the conductive length was 3.8 cm. For the small subcooling case, most of the bed experienced two-phase conditions. For both cases the two-phase regions did not appear to grow in length during postdryout transients. Although two-phase and conductive behavior were observed by the UT, dryout conditions were not observed due to the large spatial resolution of the UT and the relatively smaller dryout zone.

The objectives and preparations for the D-5 and D-6 experiments are proceeding. The D-5 experiment will investigate high temperature characteristics of debris beds and will evaluate crucible designs for future high temperature experiments. The D-6 experiment is currently scheduled to be conducted in September 1980. D-6 differs from other D-series experiments in that a stratified bed will be used to determine the characteristics of a bed in which particle size is a function of depth. D-6 will duplicate D-2 as closely as possible so that a comparison of data can be made.

A new dryout model for non-subcooled beds based on the concept of flooding was developed. In previously presented viscous dryout models, the dryout heat flux depends on the square of the particle diameter whereas in the flooding model it depends on the square root of the diameter. The flooding model predicts significantly lower dryout heat fluxes than viscous models predict for beds with mean particle diameters greater than about 1 mm. The flooding model was compared to experimental data for inductively heated water-steel and water-lead beds. These comparisons yielded better correlation than did viscous models.

EXECUTIVE SUMMARY

A one-dimensional viscous dryout model was extended to include effects of capillary forces (which constitute a major portion of the pressure gradient term). The model predicts the liquid fraction of sodium as a function of elevation within the bed, an incipient dryout dependent on length, and postdryout behavior. Part of the model developed is a discussion of the possibility of capillary forces augmenting downward heat removal in bottom-cooled beds by inducing downward boiling.

A third model addresses very deep beds supported on highly permeable plates (e.g., the fuel rod ground support plate). In this configuration, the liquid driven by natural circulation is introduced directly to the bottom of the bed (rather than being drawn through the bed as in previous models). The resulting equations indicate very similar dryout heat fluxes as for very deep beds without liquid reentry at the bed bottom. The effects of capillary force were not considered in this model.

3.3   PAHR Molten Pool

In the assessment of postaccident heat removal (PAHR) possibilities, the case must be considered in which the debris formed by the hypothesized accident cannot be cooled and progresses to a molten state. Understanding the behavior of such pools is important in determining if a pool of given characteristics will be retained within engineered barriers and if not, what retention times are afforded by these barriers to permit reduction of decay heat levels.

The in-core molten pool experiments are aimed at investigating the short and long term behavior of internally heated pools of reactor materials. The studies will determine the exact nature of the progression to a molten state, the thermal and kinetic behavior of the pool, and the interaction of the pool with retention materials. Concurrent with the in-core program, high-temperature furnace experiments are conducted to provide the capability of performing extensive studies in support of the in-core experiment results. One important task in this program is the determination of the patterns of thermal energy flow. The greater the downward heat flux, the more the structure supporting the pool is attacked. Therefore, the first goal of the molten pool program has been to develop a versatile experiment in which heat flux and structural ablation can be studied using real materials under typical temperature and heating conditions.

EXECUTIVE SUMMARY

Three in-core experiments were conducted in the first molten pool series prior to the shutdown of the ACPR for upgrading. In the first "fuel-only" experiment, MP-1, the ultrasonic thermometry indicated fuel temperatures and axial temperature gradients similar to pretest calculations. In the second "fuel-only" experiment, MP-2, the on-line ultrasonic thermometry and posttest x-radiography indicated that a significant amount of fuel had melted. In MP-3S, a 220-g stainless steel sample was melted by 628 g of overlying fission-heated UO_2 which reached 2673 K (2400°C) during the experiment. Thus, the initial series of in-core experiments confirmed the operational capabilities of the experiment-package design, and demonstrated that fission-heating of enriched UO_2 to the desired temperatures could be achieved. Ultrasonic thermometry developed for this program has been shown to be a valuable diagnostic of temperatures and temperature gradients up to the UO_2 melting point.

The second series of in-pile molten pool experiments was initiated this quarter with the conduct of MP-4 in the ACRR. The goal of this experiment was to examine the effect of internal heating on the attack of magnesium oxide brick by overlying solid UO_2 particulate. During the experiment, ultrasonic thermometry was used to measure temperatures and temperature gradients. Preliminary observations indicate that the overlying UO_2 particulate reached a maximum temperature near 3000 K. The UO_2/ MgO interface reached maximum temperatures near 2400 K and the UO_2 interacted with the MgO brick for approximately 20 minutes. Postexperiment x-radiographs of the capsule showed no visible signs of fuel melting and very little indication of fuel compaction. During the experiment, there was evidence of gas generation which appears to have been, at least in part, noncondensable. Identification of the source and nature of this gas, in addition to analysis of UO_2/ MgO interactions in the test sample, is awaiting disassembly of the experiment capsule. This disassembly is awaiting completion of the Sandia Hot Cell Facility.

Data obtained from a series of high temperature furnace tests for the diffusion of UO_2 into MgO bricks were correlated to a high confidence level with a temperature and time dependent expression. Additional furnace tests are now underway to investigate the interaction of UO_2/ ZrO_2 and UO_2/ La systems with MgO.

Preparations for conducting the fifth in-pile experiment (UO_2/ steel) were initiated this quarter. The development of an improved ultrasonic thermometer and

associated data acquisition system is receiving high priority attention and is expected to be completed in time for this fifth experiment.

3.4   Fragmentation

Most severe accident scenarios for advanced sodium-cooled reactor systems involve the production of significant amounts of molten fuel and steel. The ultimate dispersal of this molten material often depends on either bulk freezing of the melt or the establishment of coolable particulate beds. Scenarios which differentiate between the dispersal modes involve questions of the fragmentation of substantial quantities of melt when contacted with coolant. Previous investigations yielding quantitative information involve very small quantities of fuel melt, leaving unanswered the question as to whether or not large quantities would yield different particulate size distribution due to vapor blanketing of the bulk stream. A knowledge of particle size distributions is crucial to the resolution of post-accident coolability of cores which have been reduced to rubble.

Following whole-core accidents in which all, or most, of the sodium remains in the reactor vessel, molten/vaporized core materials and sodium will come in contact, resulting in sudden freezing and fragmentation of the core debris, which may then settle on various surfaces within the vessel. If recriticalities do not occur, this fragmentation and onset of settling roughly denotes the beginning of the post-accident sequence.

During this quarter, a procedure was developed for characterizing the debris bed. Core samples of the debris bed, obtained by driving thin-walled tubing into the bed, were x-rayed along two diameters 90° apart, with a beam perpendicular to the core axis. A gamma-ray attenuation technique was used to determine the average density profile of the bed with the gamma-ray beam in the same directions as the x-ray photographs. The core samples were then cut into disks 0.25 to 0.5 in. thick. These disks were then x-ray-photographed along the axis to get a more detailed local display of the bed structure.

The photographic activity was followed by removal of sodium from the samples and the determination of weight fractions and bed density for the purpose of calculating

the local void fraction. Also, the fragments were seived to obtain local particle size distribution. Investigators found that larger and heavier particles tended to be closer to the bottom of the bed accompanied by a noticeable graduation toward smaller, lighter particles with an increase in the distance from the bottom of the bed. The median particle size was 300 μm.

A reverse experiment was performed in which 23 kg of sodium at 791 K were released into 20 kg of UO_2 melt. The subsequent interaction was very vigorous. The resulting bed particles were highly stratified and some particles in the bed appear to have a greater diameter than that of the sample tube (1 in.).

3.5   Sodium Containment and Structural Integrity

In the event of vessel or pipe rupture, large quantities of liquid sodium at temperatures in excess of 873 K would come into contact with concrete or other containment materials. This task is aimed at identifying and quantifying the dominant phenomena involved in the erosion and possible breach of containment.

Any loop-type LMFBR system must accommodate the interaction of hot sodium with cell liners and, given either a failed liner or a CDA, the interaction of hot sodium with concrete. The data base available for safety assessments involving these interactions is extremely limited, especially for the concrete and failed-liner interactions.

Six physical separate effects experiments were conducted on sodium-concrete interaction, one with magnetite concrete and five with basalt concrete. These tests investigated the effects of initial sodium-pool temperature, sodium-pool depth, concrete-surface-water content and sodium hydroxide additions to the sodium pool.

EXECUTIVE SUMMARY

Chemical separate effects experiments have concentrated on the reaction rate between molten sodium hydroxide and silica and upon the products formed. These studies are aimed at refining the chemical model of molten-sodium attack on basalt concretes.

Large-scale sodium-concrete interaction Test 16 was conducted. The test involved a bare basalt-concrete crucible. Two-hundred thirty-five kilograms (235 kg) of sodium at 873 K were dumped into the cavity of this crucible resulting in a pool depth of 27 cm. Except for the pool depth, the test was similar to Test 11. In that test, a 13.5-cm-deep sodium pool had required about 60 minutes to initiate significant concrete penetration. Doubling the sodium pool depth (Test 16) to 27 cm should enable investigators to determine the rates governing the initial reaction phase. Unfortunately, a sodium fire in the test chamber burned through the test instrumentation cables at about 15 minutes and all further information was lost.

4. Aerosol Source Normalization

During an energetic hypothetical core disruptive accident, fuel vapor may be produced which subsequently condenses to form small very particulated debris (molten or solid) which can be transported to the upper vessel regions and through breaks which may have occurred in the vessel. The possibility of transporting this material depends strongly on its initial character.

Aerosol produced from in-pile (ACRR) experiments is being characterized to determine the physical properties of fuel particles resulting from the vaporization and melt breakup of fuel pins subjected to simulated overpower excursions. The characteristics of these particles are being compared with those produced by out-of-pile experiments at ORNL which are part of the NRC sponsored aerosol transport program. Subsequent in-pile studies will examine the interaction of particles with the supporting structure and with sodium.

In a recent series of experiments at ORNL, fuel debris was sampled and fuel temperatures measured by methods previously demonstrated in Sandia's ACPR.

EXECUTIVE SUMMARY

Previous quarterlies have described the temperature response of an exposed fuel pellet in a stack of fuel pellets when the stack was resistively heated to vapor. Calibrated photographic film was used to measure the temperatures of the fuel surface and of the bottom of a hole drilled to the pellet centerline. Several tests established the accuracy of the temperature measurements.

Sandia has continued to cooperate with ORNL in a joint program of aerosol studies in which the results of out-of-pile and in-pile aerosol experiments are being compared and analyzed. The purpose of these studies is to determine the validity of each type of test to portray the behavior of aerosols in actual reactor-accident situations. This joint effort is expected to continue.

Most of this quarter was devoted to microscopic examination of fuel debris collected in the sampling wheel on out-of-pile Test CDV76. This run most closely matched the in-pile sampling experiment in total energy. Disassembly of certain sampling wheel channels preceded study in a scanning electron microscope (SEM) and a transmission electron microscope.

SEM photographs are making possible particle count as a function of size and location in the channel, the determination of particle size and velocity distributions, and the establishment of the nature of collected particles. A particle count is being taken as a function of particle size and position in the channel. Data obtained from this work showed particles ranging from 0.2 to about 200 μm. The largest particles were about an order of magnitude larger than the largest collected in the in-pile experiment and appeared as sintered UO_2 which had not melted during heating. The source of these particles is unknown so far. Most of the smaller particles were either sphere-like, or left a splattered trail on impact, indicating, in both cases, a prior state of melt. Significantly, fewer smaller particles were collected in this experiment than in the in-pile experiment.

A plan for at least six more out-of-pile experiments has been proposed to NRC by ORNL to complete the comparison study of source aerosols. ORNL has asked Sandia to assist. In these out-of-pile experiments, test parameters will be varied to assure rigor and completeness in the execution of the program.

EXECUTIVE SUMMARY

5. Containment Analysis

This task is directed toward developing a total containment systems code (CONTAIN) which will be a basic computational tool for the analysis of a variety of possible postaccident sequences, generally beginning with primary containment failure and proceeding to the definition of the radiological release from the secondary containment failure. Core-melt accidents, energetic disassemblies, reactor vessel rupture, and large scale sodium spills are addressed. Existing containment models are being adapted where feasible and new models are being supported by containment-related experiment programs, some of which are described in previous sections. Major phenomenological factors are

      a. postaccident heat removal

      b. debris bed behavior

      c. vessel failure

      d. concrete-sodium interactions

      e. concrete-melt interactions

      f. melt-sodium interactions

      g. liner response

      h. sodium pool/spray burning

      i. chemical reactions products and kinetics

      j. gas flow, pressurization, and venting characteristics

      k. heat transfer (pool/wall/atmosphere)

      l. fission product chemistry and inventory

      m. aerosol transport behavior

The CONTAIN code development continued. The code framework is now complete and in a preliminary form suitable for running test problems. The cavity debris pool model, SINTER, is also operational with preliminary material interaction models. The atmosphere phenomenology routines are operational. A series of test problems was run to checkout CONTAIN and to identify areas requiring future improvement. Several areas were indeed identified; modifications were initiated this quarter.

EXECUTIVE SUMMARY

6. Elevated Temperature Design Assessment

The primary objectives of the elevated-temperature design assessment studies are (a) to develop correlative NDE techniques that can be used to monitor progressive creep, fatigue, and combined creep-fatigue damage in materials used in advanced reactor primary- and secondary-loop components; (b) to evaluate analytical methods (and correlate with experimental data) for creep buckling of advanced-reactor components operating at elevated temperatures; and (c) to design, fabricate, and operate a multiaxial creep-fatigue facility for the purpose of evaluation of creep-fatigue damage rules.

6.1 Uniaxial Creep-Fatigue Behavior

6.1.1 Creep Testing

No creep testing was performed during the current reporting period.

6.1.2 Creep-Fatigue Testing

Three low cycle fatigue tests of 316 stainless steel were initiated for sequential, surface Doppler-broadening positron annihilation (PA) measurements. Surface PA readings are being taken at five cyclic intervals to determine the response of this technique as it represents lineshape parameter versus fatigue cycles. Two intervals have been measured for each specimen.

6.1.3 Nondestructive Examination

Setup was completed on an apparatus to make Doppler-broadening PA measurements on the surfaces of gauge sections of fatigue test specimens. This setup allows sequential measurements to be made on a single sample with increments of mechanical deformation (monotonic or fatigue cycling).

6.1.4 Microstructural Analysis

Transmission electron microscopy has been completed on nine samples of 316 stainless steel exposed to several mechanical histories at 866 K (593°C). These include thermal aging only for 8000 hr, creep at 200 MPa for 3221 hr, and seven creep-fatigue tests lasting as long as 1230 hr. Observations from this microscopy are being

32

organized for comparison with previously published results. A report will be issued.

6.1.5 Multiaxial Test Facility

Additional tests were conducted on tubular specimens for the multiaxial facility to check on the uniformity of strain distribution. Two types of specimens with radius (r) to thickness (t) ratios of 5.23 and 9.54 were tested. The thin-walled design (r/t = 9.54) appears suitable for tests at low strain limits because it produces a more uniform strain distribution throughout its thickness than does the thicker-walled design (r/t = 5.23).

6.2 Creep-Fatigue Damage Analysis

Analysis of the thin-walled specimen for the multiaxial test facility was initiated. Two loading cases were examined: (1) monotonic axial compression of the specimen at 294 K (70°F), (2) cyclic loading of the specimen at 866 K (1100°F). Preliminary results indicate that for uniaxial compressive loading, no significant buckling of the specimen occurs up to an axial strain 0.05 mm/mm. For cyclic loading, the largest predicted cyclic strain range occurs outside the gauge section. This indicates the specimen will fail outside the gauge section. However, there is some uncertainty in this conclusion and further investigations are needed to clarify this point.

6.3 Structural Analysis

The effort to prepare a report on the piping elbow analysis continued in this quarter.

6.4 Structural Evaluation

Technical review of the Westinghouse Clinch River Breeder Reactor Plant Piping Document (WARD report CRBRP-ARD-0185) was continued in this reporting period. A technical report assessing the merit of this report will be prepared.

EXECUTIVE SUMMARY

7. LMFBR Accident Delineation

The principal objective of this program is to determine the applicability of event tree methodology to all phases of LMFBR accidents. The results of the study are intended to (1) provide a demonstrated methodology for developing accident sequence diagrams for an LMFBR, (2) identify and systematize the key phenomena and phenomenological or system uncertainties in the accident sequences, and (3) illustrate the methodology by determining the dominant accident sequences.

Over the past year, Sandia Laboratories initiated the LMFBR Accident Delineation Study to examine the applicability of logic techniques, such as event and fault tree methods in the overall safety assessment of advanced reactor power systems. The purpose of this study is to (1) delineate the significant accident sequences in candidate advanced reactors (2) develop the methodologies necessary to estimate the relative importance of both specific accident sequences and key phenomena within these sequences, and (3) utilize this perspective on important accident sequences to ultimately help to focus research resources on the most crucial reactor safety issues. This is a broad based program which combines logical and analytic methodologies in an attempt to present a state-of-the-art view of important accident features. Early phases of this study have utilized CRBRP as an illustrative facility. Future efforts will be directed toward proposed candidate LMFBR designs when design information becomes available.

Work continued during this period in all areas of the LMFBR Accident Delineation Study. Efforts in the Accident Initiation and Engineered Safety Systems Response areas concentrated on improving the delineation of protected accidents and completing the fault trees for Detection, SCRAM, and SHRS failure in the CRBRP.

In the Accident Phenomena area, this quarter's work was concentrated on local fault propagation (LFP) accidents. The generic LFP accident event tree, developed during the preceding quarter, was applied to the various specific LFP initiators discussed in the CRBRP preliminary safety analysis report (PSAR). Qualitative relative probability judgments were assigned and this format was used to summarize the PSAR results, offer critical comment on these results where appropriate, and

consider some possible safety improvements that might be provided by additional instrumentation for local fault detection. In general, convincing arguments exist for a slight probability that a fault will either initiate at a scale involving large numbers of pins (a considerable fraction of a subassembly), or propagate to this scale without detection and shutdown after initiating at the single-pin scale. Nonetheless, it would still be desirable to determine whether, if such an event does unexpectedly occur, further propagation to whole-core involvement is still highly unlikely.

During this reporting period, some efforts were also devoted to continuing the delineation of protected accidents.

A reorganization of the primary envelope and containment response event tree into a large number of smaller and less complex trees has been completed. Each tree now applies to one of three regimes: In-Vessel PAHR, Reactor Cavity Response, and Upper Containment Response. A complete accident sequence can be traced by placing these three sections in series, with minor exceptions.

Preparation of the Accident Initiation and ESS Response sections for the LMFBR Accident Delineation Study, Phase I Final Report began during this period.

8. Test and Facility Technology

8.1 ACRR Fuel-Motion Detection System

The fuel-motion detection (FMD) system for the ACRR has been developed to monitor the movement of fuel in simulated core disruptive accidents. This system successfully recorded the movement of fuel from a single pin disrupted within the ACRR in July of 1979. The July 1979 experiment also demonstrated that changes could be made to significantly improve the signal-to-noise ratio in the reconstructed images. The upgrade effort has concentrated on five major areas: (a) scintillator development, (b) radiation transport calculations, (c) modifications to the main shield, (d) scene-beam studies, and (e) image-reconstruction development. The experiments and radiation studies have indicated that additional shielding around the scintillator detectors and the image intensifiers, especially the incorporation of a thermal neutron shield everywhere just inside the last lead shield layer, will significantly reduce the background from shield penetration. Calculations of scintillator response indicate that

alternative scintillators may be less sensitive to low energy gamma rays and thermal neutrons, but the superiority of x-ray film over the scintillators that have been investigated has not yet been explained. Tests of these alterations will be conducted in March.

The analysis of the data from the fuel motion experiment has continued during the quarter. Included in this quarterly report are a sequence of curves for radiation intensity vs position along the pin and as a fraction of time during the ACRR pulse. These curves show what appears to be a break near midplane, buildup of fuel at this location, and then slumping toward the bottom of the pressure vessel. More quantitative information is expected to accrue from additional analysis.

8.2   ACRR Status

A request to modify the Technical Specifications for the ACRR was submitted in September 1979 for the purpose of updating all the calculated performance values with measured values. The requested changes include increasing the reactivity worth of the transient rod bank from $3.20 to $4.25, providing a reactivity insertion of $3.50 instead of $2.95 for a maximum single pulse, and increasing pulse energy release from 450 MJ to 500 MJ. No significant changes were requested in the safety limit and the limiting safety system settings on fuel temperature. All the changes were approved by the DOE Albuquerque Operations Office in December 1979.

An additional control system has been designed to permit a programmed withdrawal of the transient rod bank, and the transient rod drive motors have been replaced permitting rod drive speeds up to 23 cm/s. Two systems for programming the rods were fabricated: one a hardwired system and one based on a microprocessor capable of being programmed using an HP minicomputer.

Modifications were made to the ACRR itself to permit easier handling of experiment hardware as apparatus is placed i' and removed from the reactor.

ADVANCED REACTOR SAFETY RESEARCH PROGRAM
QUARTERLY REPORT
OCTOBER - DECEMBER 1979

1. ENERGETICS

1.1   Prompt Burst Energetics (K. O. Reil, 4423; M. F. Young, 4425;
J. T. Hitchcock, 4424)

1.1.1 Introduction

Prompt Burst Energetics (PBE) experiments provide information on the energetic response of various reactor fuel-clad-coolant systems to superprompt critical conditions. This program is directed at characterizing the phenomena which result in pressure generation and the conversion of thermal energy to work, and at understanding the reactivity effects arising from rapid coolant voiding and initial fuel motion. These experiments examine integral effects of fuel-clad-coolant interactions (FCI), fission gas release, and fuel and fission product vapor pressures during superprompt critical core disruptive accidents and determine the potential for damage to the primary containment. The rate of coolant voiding in a positive reactivity void-coefficient system determines the reactivity insertion rate and hence the magnitude of the transient under accident conditions. The experimental work is closely interfaced with analytical efforts to develop models which uniquely describe the observed phenomena for incorporation into predictive accident analysis codes. These experiments also provide information about the thermodynamic states and spatial distribution of fuel, clad, and coolant following a superprompt excursion. These data serve as initial conditions for postaccident heat removal (PAHR) and molten core containment analysis.

In tests performed to date, single fuel pins have been pulse fission heated in the Annular Core Research Reactor (ACRR) (or its predecessor, the ACPR) to temperatures resulting in fuel vaporization. The pins, which have been surrounded by helium or sodium, are contained in a rigid pressure vessel which is instrumented with thermocouples and pressure transducers and which is fitted with a movable piston

at its upper end. Estimates of the conversion of thermal energy to work result from comparisons of the kinetic energy of the piston to the fission energy input to the fuel. Pressure, temperature, and piston displacement histories are determined for a variety of fuel-coolant systems and initial conditions. A series of experiments with fresh uranium dioxide fuel and sodium coolant and a series with fresh uranium-carbide fuel in sodium have been completed. Additional oxide experiments are now being performed. Future pin experiments will examine fission product effects in preirradiated fuel.

The scope of the PBE work is being enlarged to include separate effects experiments to examine FCI phenomena between oxide fuel and sodium. The first area to be addressed in these studies is to determine if the oxide/sodium system is capable of supporting large scale, propagating, escalating interactions and if so to characterize the controlling phenomena. Conceptually, the experiments would examine the response of a mixture of relatively large droplets of molten fuel in a sodium volume to externally applied pressure transients.

During this quarter, detailed analysis of the fresh uranium carbide/sodium series of PBE experiments was completed and a topical report describing the results of that series was assembled. The report, entitled Prompt Burst Energetics Experiments: Fresh Uranium Carbide Sodium Series, will be published next quarter. Portions of the analysis are described below. These include comparisons of the pressure measurements with observed piston motion, heat transfer modeling of the three carbide-fueled experiments, and examination of pressure sources arising from piston deceleration.

SIMMER-II analysis of PBE-5S has continued with the threefold objective of (a) investigating the applicability of SIMMER to these complex experiments, (b) providing insight into the separate pressure-generation and pressure-quenching mechanism, and (c) providing information for model development and verification. Current work involves comparison of experiment data and SIMMER results for PBE-5S and an assessment of possible fuel-vapor-quenching mechanisms.

1.1.2 Analysis of the PBE Carbide/Sodium Series

During this quarter, a detailed analysis of the results of fresh uranium carbide fueled PBE experiments (PBE-SG1, PBE-SG2, and PBE-SG3) was completed. Several parts of that work are described below.

1.1.2.1 Comparison of Pressure Data With Piston Response -- In order to evaluate the consistency of the pressure and piston diagnostics and to estimate the amount of energy not reflected in piston motion because of its limited travel, a detailed comparison was made of the impulse represented by the top pressure history and the measured piston velocity.

The piston displacement and top and bottom pressure histories from PBE-SG1, PBE-SG2, and PBE-SG3 are shown in Figures 1.1-1, 1.1-2, and 1.1-3, respectively.

The piston velocity was derived by differentiating the piston displacement history using a quadratic fit-smoothing procedure. A piston velocity was estimated from the measured pressure histories as follows:

$$V_P(t) = \frac{A}{m} \int_0^t \left[P(\tau) - P_B(\tau) \right] d\tau$$

where

      A = the face area of the piston

      m = the piston mass

      $P(\tau)$ = the measured pressure history

      $P_E(\tau)$ = ঞ়e pressure behind the piston

The pressure behind the piston arises from the argon cover gas in the capsule and ranges from an initial value of ~0.2 MPa to ~0.35 MPa as the piston compresses the cover gas.
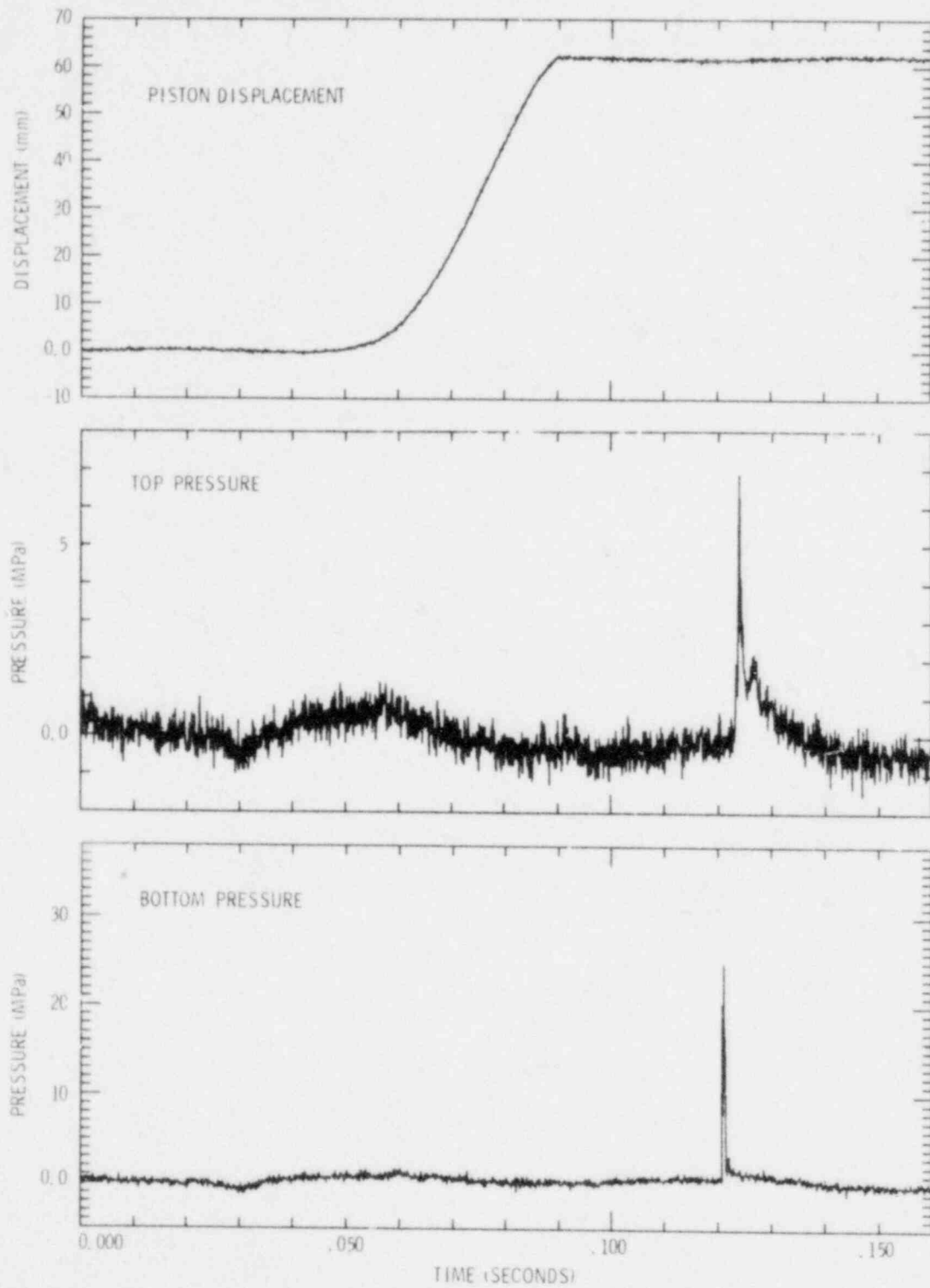
Figure 1.1-1 PBE-SG1 Pressure and Piston Displacement Histories
(time of peak of reactor power = 30.61 ms)
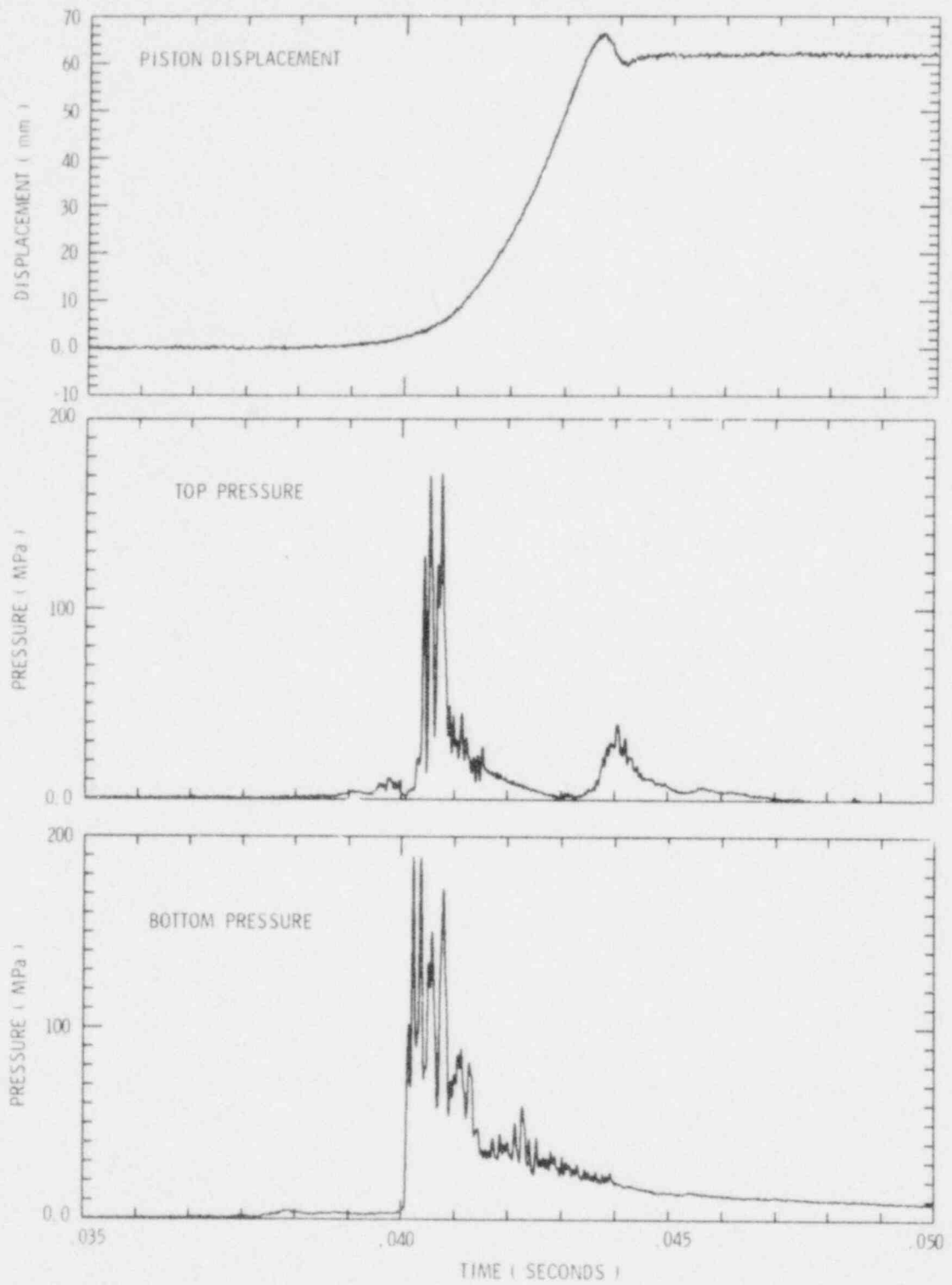
Figure 1.1-2   PBE-SG2 Pressure and Piston Displacement Histories
(time of peak of reactor power = 31.37 ms)

41
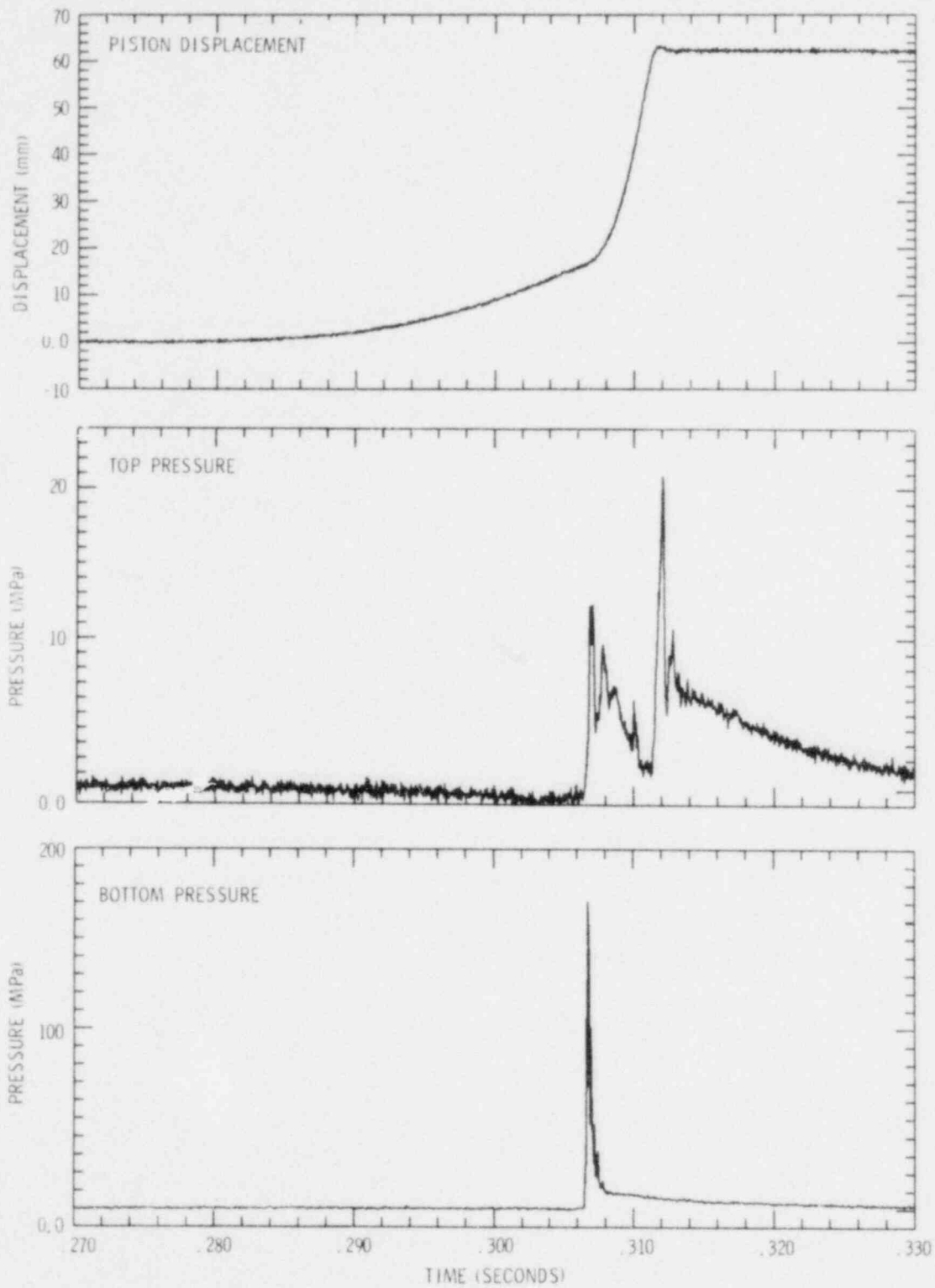
Figure 1.1-3 PBE-SG3 Pressure and Piston Displacement Histories
(time of peak of reactor power = 270.85 ms)

As Figures 1.1-1, 1.1-2, and 1.1-3 show, the top pressure histories contain some negative going artifacts which result from the transient heating of the face of of the transducer as hot sodium and fuel debris move past it when the piston is displaced. This noise signal is time dependent and is controlled by heat transfer to and through the pressure transducer. For this analysis, a constant pressure bias was removed so as to match the initial piston velocity. The validity of that correction decreases with increasing time but appears to be adequate over the time interval during which the piston was moving.

The use of velocity histories for these comparisons was chosen because of the difficulty in computing valid second derivatives of the piston displacement history and the difficulties in eliminating the thermal biases in the pressure data to produce valid second integrals of pressure. Thus, velocity yielded an acceptable compromise.

Figure 1.1-4 shows the piston velocity and velocities derived from the two pressure transducer histories for PBE-SG3. The difference in velocities derived from the two transducers appears to be a constant multiple (1.16) apparently arising from a sensitivity shift in the transducers or gain shifts in the data acquisition system. Substantial agreement between the piston and pressure data is observed over much of the history. Note that even the same detailed structure appears in both. The lack of agreement prior to piston stoppage is a result of uncorrected thermal effects in the transducers. From this comparison, the piston and pressure diagnostics in PBE-SG3 are concluded to be totally consistent.

Figure 1.1-1 clearly shows that the noise content of the top pressure histories for PBE-SG1 masks the detailed pressure information during the piston motion. However, if the mean value of the measured signal is assumed to be the true pressure and if the back pressure measured out-of-pile is used, the comparison of velocities derived from the piston and pressure diagnostics agree to within 20% over the duration of piston motion for PBE-SG1.

Figure 1.1-5 displays the comparison of measured and derived piston velocity for PBE-SG2. While agreement does exist during early piston motion (up to ~40.3 ms), over most of the piston travel the agreement is very poor. Comparison of Figures 1.1-5 and 1.1-2 reveals that the departure of the two velocity histories begins coincident with the high amplitude pressure transient. Several possibilities are suggested to explain the discrepancies.

43

Figure 1.1-4   Comparison of Measured Piston Velocity With Impulse
Derived From Top Pressure History in PBE-SG3
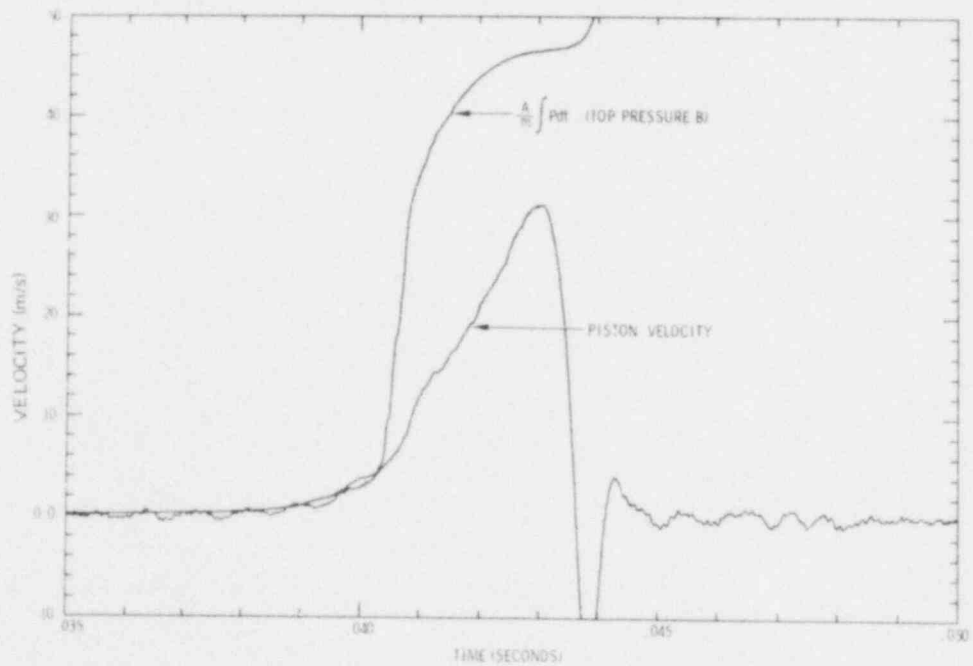
Figure 1.1-5   Comparison of Measured Piston Velocity With Impulse
Derived From Top Pressure History for PBE-SG2

The first possibility is a substantial retarding force acting on the piston. This force could arise from abnormal friction or drag between the piston and the walls of the piston-housing portion of the pressure vessel or between the armature of the linear motion transducer and the body of that device. Such behavior has not been noted in any other PBE experiments but will be investigated during the detailed postmortem examination of this experiment. A second possibility is that the pressure transducer signal is not an accurate representation of the pressure. The amplitude and frequency content of the pressure histories measured for PBE-SG2 are greater than in other experiments. Recall that two transducers were destroyed in the experiment. The sensitivity of the transducers at extreme pressures was investigated previously.[1-1] From that work, which involved static calibrations, the transducer response to high pressures was concluded to be essentially linear if no permanent deformation of the sensing diaphragm occurred. As the histories in Figures 1.1-2 show, no permanent-zero shift was noted for the transducers that survived in the experiment.

Another source of error may be the response of the transducers to high frequency pressure transients. Evaluation of the way the Kaman transducers respond to step changes in pressure is in progress using a gas shock tube. Preliminary results indicate a transient "overshoot" from the transducer lasting 0.1 to 0.5 ms with amplitude 2 to 5 times the applied pressure. Qualitatively, these effects would explain the discrepancy noted between the observed PBE-SG2 pressure and piston response displayed in Figure 1.1-5. Work has been initiated to derive response functions for sibling transducers and then to attempt to unfold the measured pressure histories for PBE-SG2.

At this point, the actual amplitudes of the pressures in PBE-SG2 appeared to have been less than indicated by the pressure transducers. This result, however, does not alter the previously stated conclusion that the pressure transients were the results of significant fuel coolant interactions.

As in previous experiments, the pistons in all three experiments in this series stopped while the channels were still pressurized. This is illustrated in Figures 1.1-6, 1.1-7, and 1.1-8 which show for the three experiments, extended comparisons of piston velocity and velocity derived from the pressure histories. For all of the histories that are based on pressure the roll-over results from the previously noted thermal effects

in the pressure transducers. Clearly, when the piston stops, the boundary condition on the system changes; thus, the derived velocity based on pressures is not the same as would be observed for a piston. However, the trends are valid. Thus, the measured thermal-to-mechanical energy-conversion ratios (see Section 4.5 below) which extend to ~0.2% for PBE-SG2 clearly underestimate the work potential of these systems. The values would extend into the percent range if the system expansion were not limited by the finite travel of the piston.
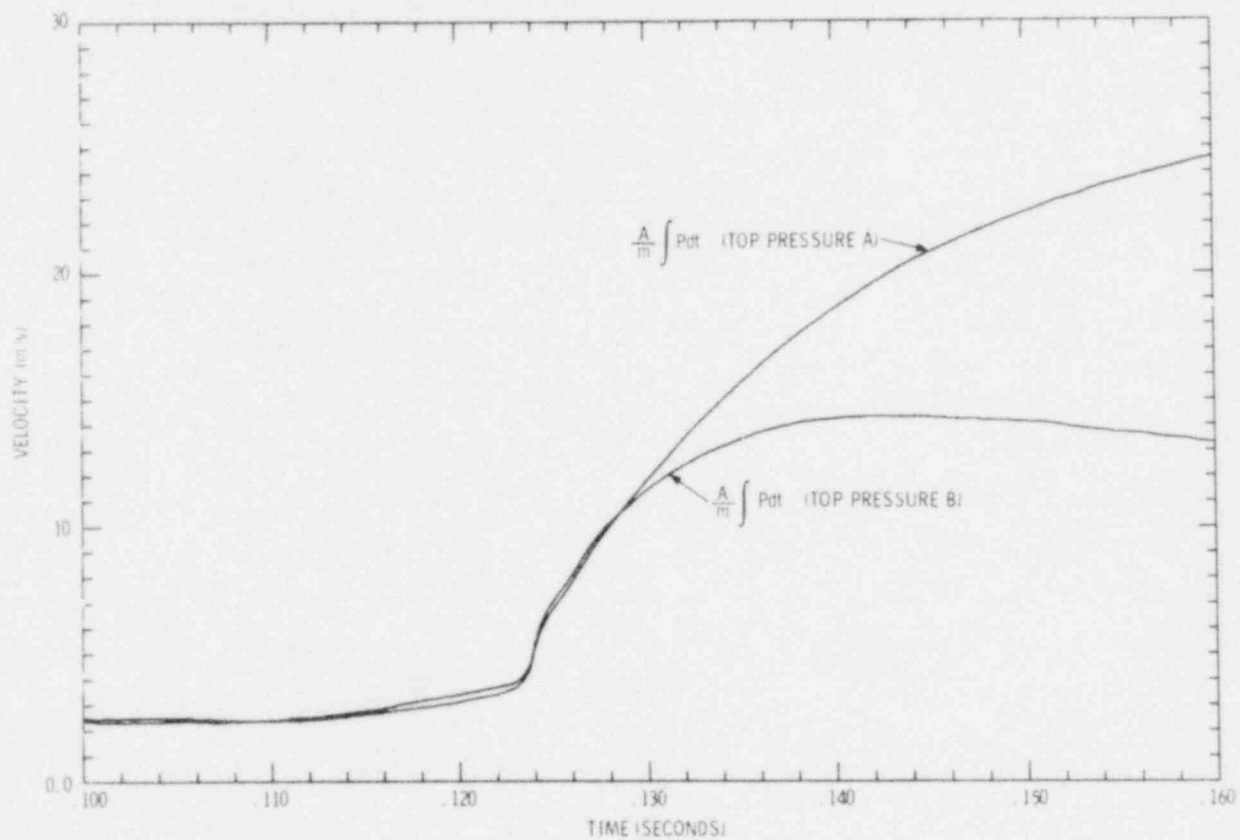
Figure 1.1-6 Impulse Represented by Top Pressure Histories in
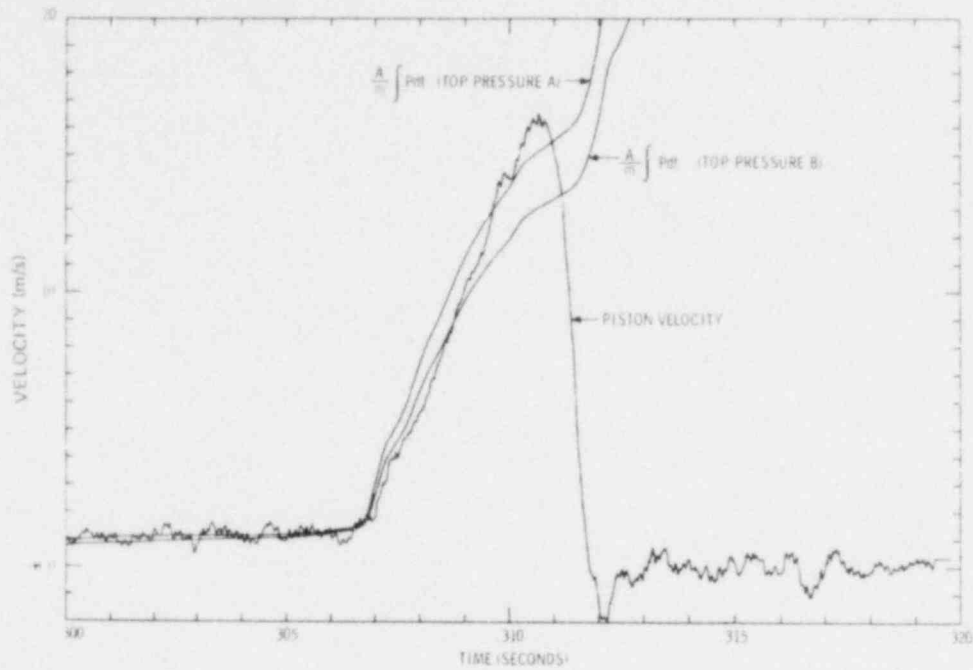PBE-SG1
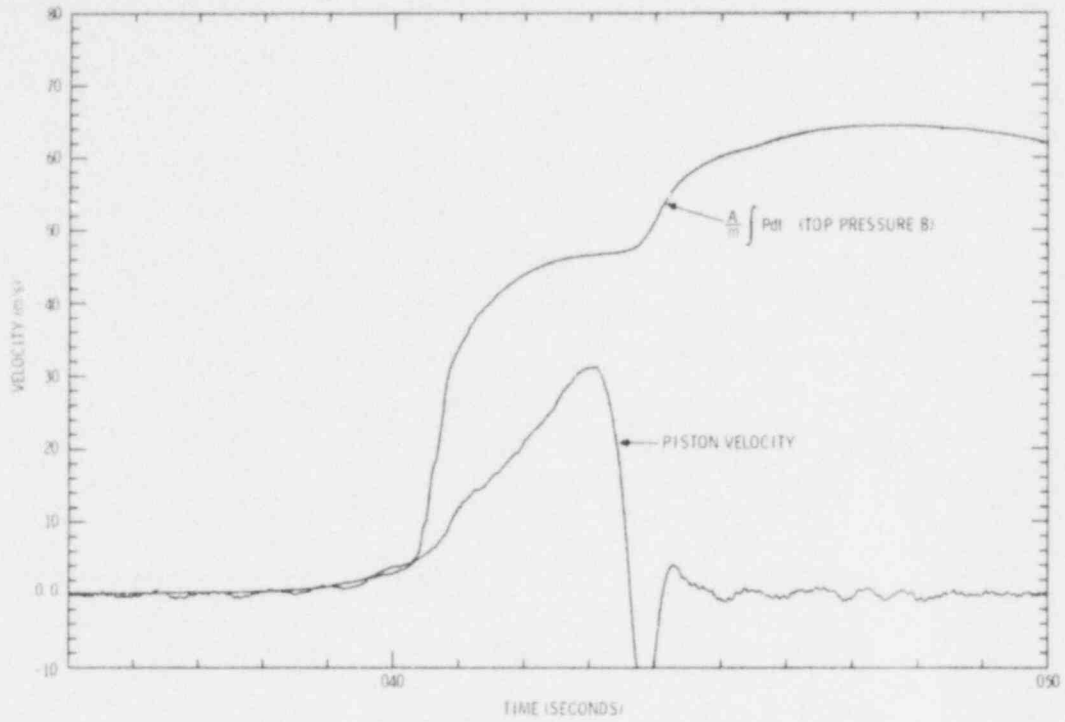
Figure 1.1-7   Extended Comparison of Measured Piston Velocity With
Impulse Derived From Top Pressure History in PBE-SG2
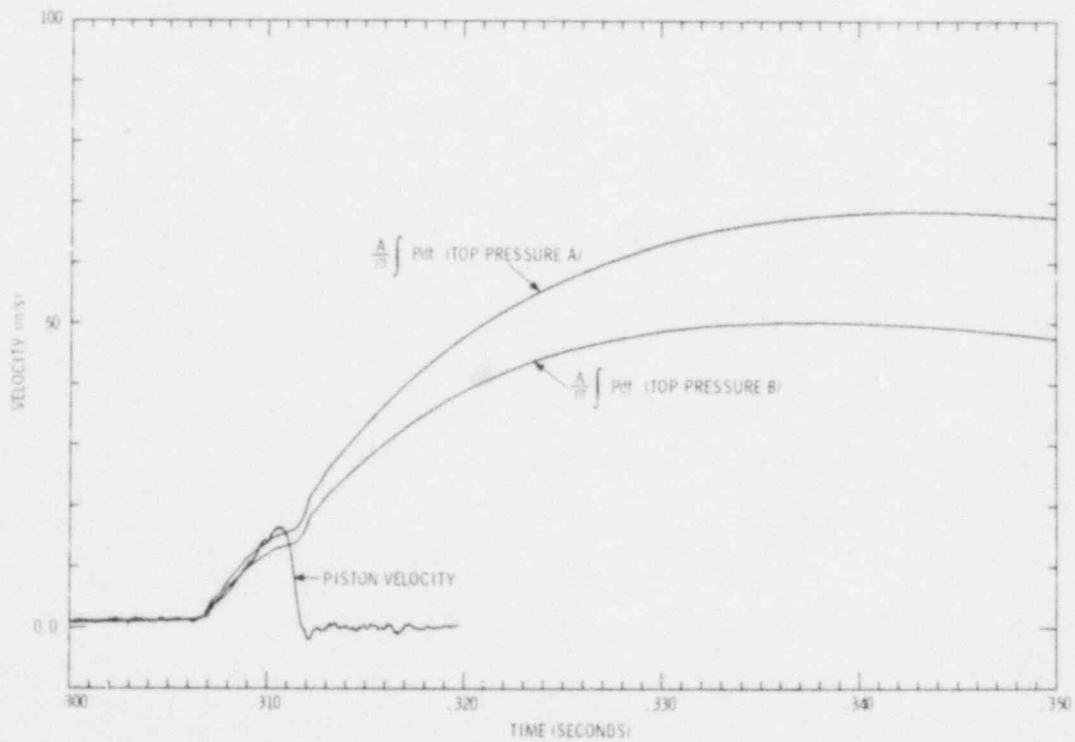
Figure 1.1-8   Extended Comparison of Measured Piston Velocity With
Impulse Derived From Top Pressure Histories for PBE-SG3

1.1.2.2 <u>Heat Transfer Calculations</u> -- Heat transfer for the carbide/sodium experiments PBE-SG1, -SG2, and -SG3, was calculated with a two-dimensional finite difference heat transfer code, TAC2D.[1-2] The calculations were done for a one-dimensional cross section of the pin and channel in cylindrical geometry, ignoring axial conduction. The heat transfer model is shown in Figure 1.1-9 along with the number of finite difference nodes in each section. The model includes the fuel, gap, clad, sodium channel, molybdenum wall, Inconel vessel, and beryllium heat sink. Temperature dependent properties were used for the UC fuel, gas gap, the stainless steel 316 cladding, and the sodium. Cladding and sodium properties are from the Argonne Blue Book.[1-3] Molybdenum, Inconel 718, and beryllium properties are from References 1-4 and 1-5. The actual pin power histories were used as input to the calculations.[1-6]
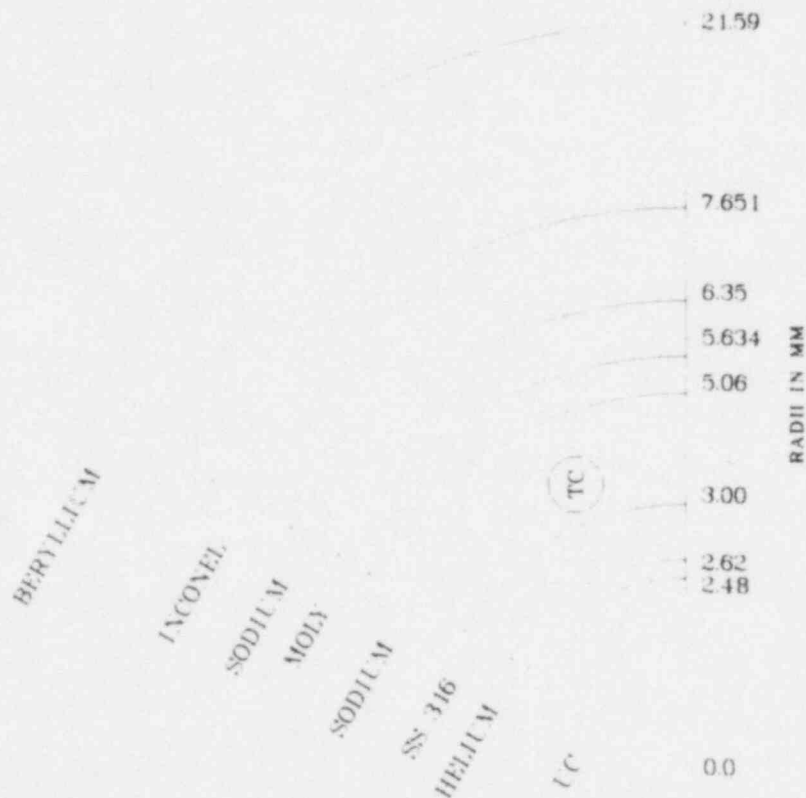
Figure 1.1-9   Heat Transfer Model of PBE
Experiments (TC is thermocouple
position)

Calculations were performed for the three experiments at the axial hot spot and at the thermocouple locations. Graphs presented later show the fuel time history at the axial peak for several radial locations, temperature vs radius at times close

to the time of pin failure for the axial peak location, and time histories for the sodium at the thermocouple locations.

The time histories for the sodium channel at the top, middle, and bottom thermocouple locations were calculated by correcting the energy input with the axial energy deposition shape. The relative power factors are shown in Table 1-I.

Table 1-I

Relative Power Factors at Thermocouple Locations

Thermocouple	Location[1] (mm)	Relative Power Factor[2]
top	322.	.697
middle	157.	.998
bottom	4.	.774

[1] Measured from bottom of enriched fuel column
[2] Relative to axial maximum

The following figures give the fuel temperature history and radial temperature distributions for the pin and channel around pin failure time. Figures 1.1-10 and 1.1-11 are for PBE-SG1, Figures 1.1-12 through 1.1-15 for PBE-SG2, and Figures 1.1-16 through 1.1-19 for PBE-SG3. The fuel temperature profile is clearly inverted at time of failure for all three experiments with a maximum temperature difference of 1490 K for PBE-SG2. The peak fuel temperatures were: for SG1, 4590 K occurring at 37 ms; for SG2, 6680 K at 38 ms; and for SG3, 4760 K at 285 ms. In PBE-SG2 and -SG3, the peak fuel temperatures occurred after failure. At the time of failure the homogeneous nucleation criterion was satisfied for all three cases, taking 2250 K as the homogeneous nucleation temperature (90% of the critical point). The sodium was well below boiling (1100 K) at failure in all cases. Table 1-II summarizes parameters of interest at the time of pin failure, such as peak and average fuel and sodium temperatures, fuel vapor pressure, fuel-sodium interface temperature, and fuel and sodium temperature differences.
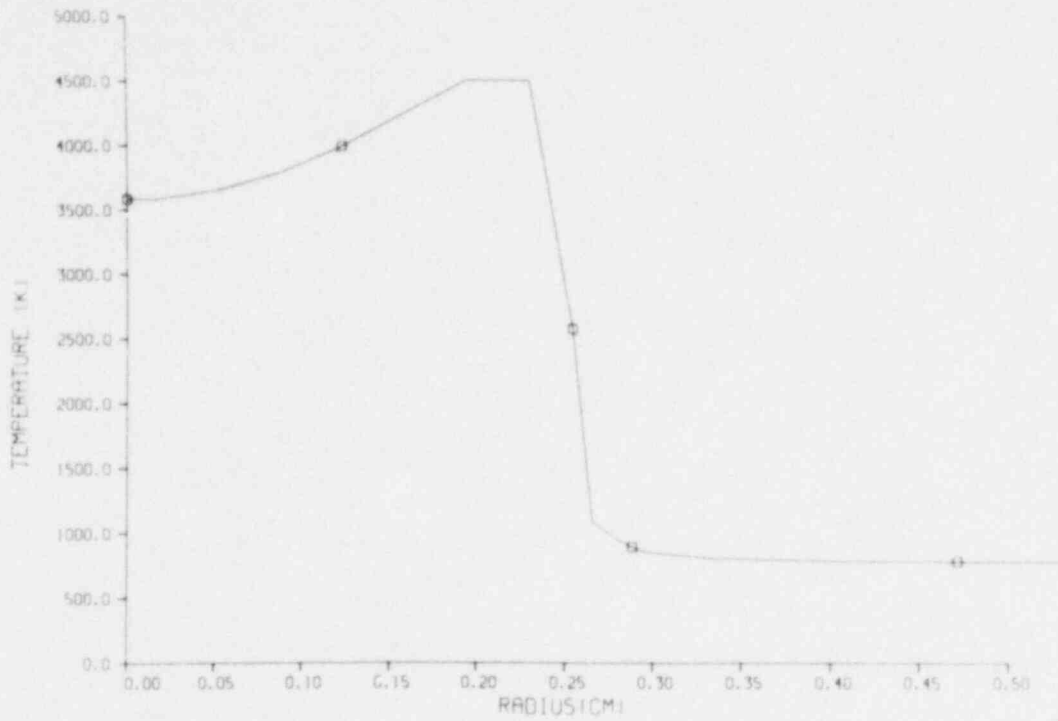
Figure 1.1-10   Calculated Radial Temperature Profile for
PBE-SG1 at 42 ms (failure time)
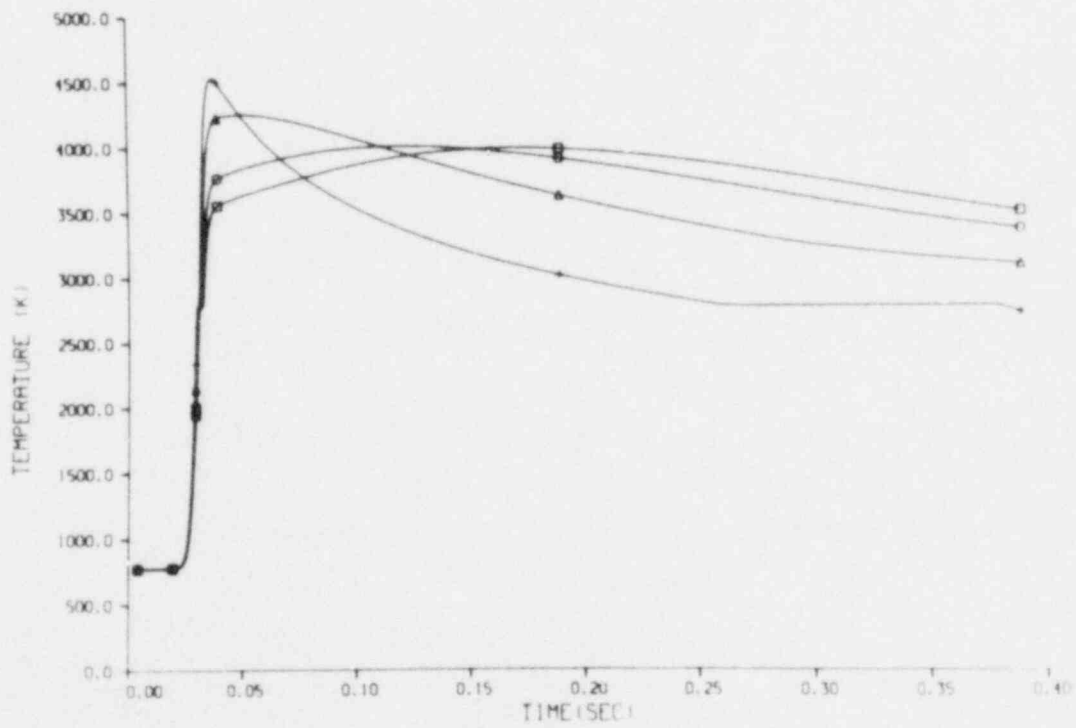
Figure 1.1-11   Fuel Temperature vs Time for PBE-SG1
at Four Radii
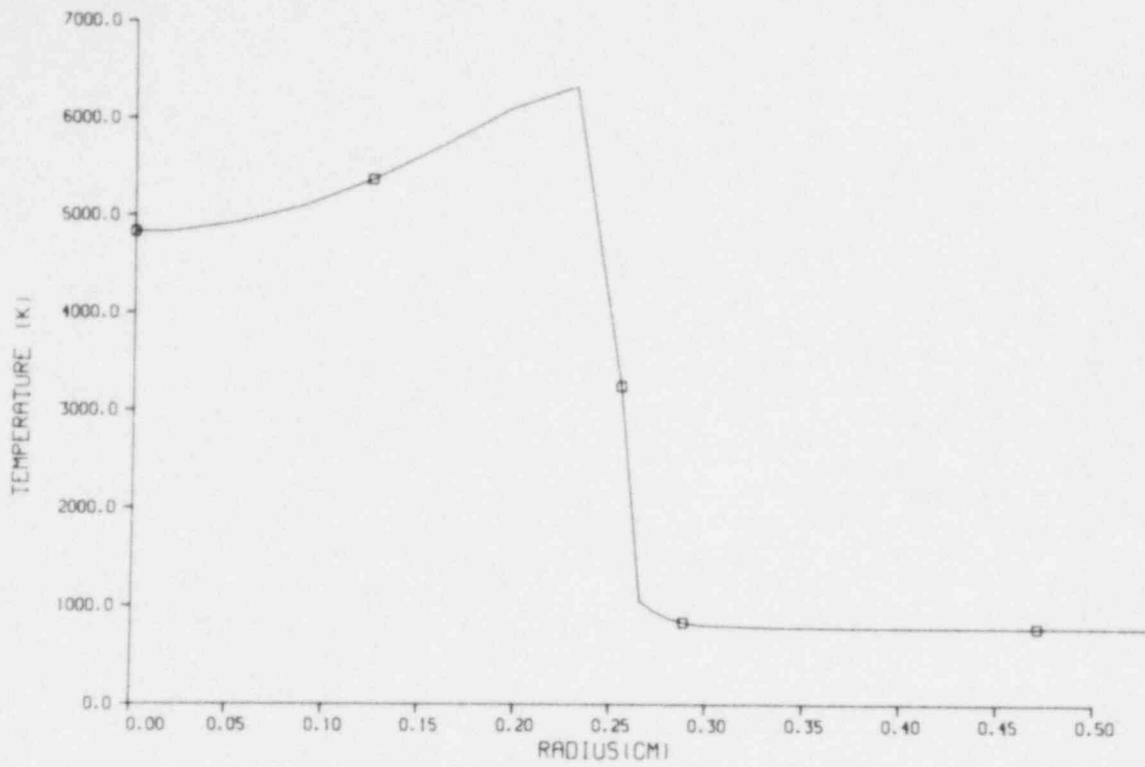
Figure 1.1-12   Radial Temperature Profile for PBE-SG2 at 35 ms
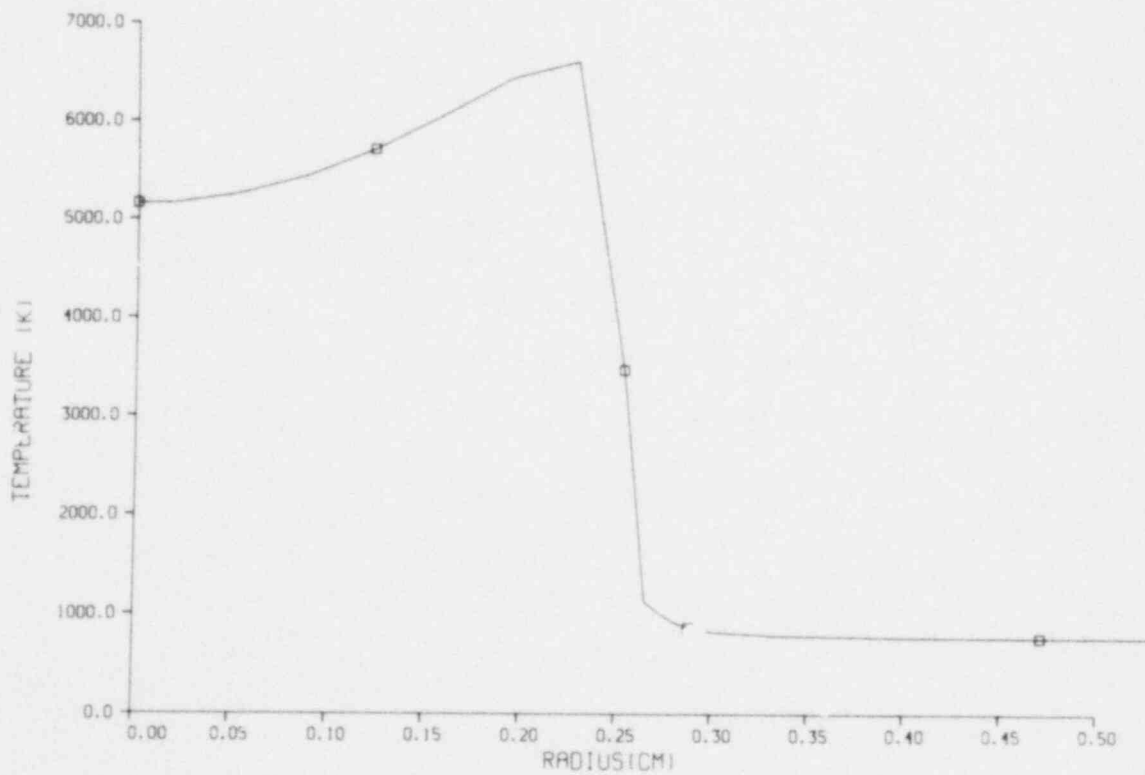
Figure 1.1-13   Radial Temperature Profile for PBE-SG2 at 37 ms
(failure time)

51
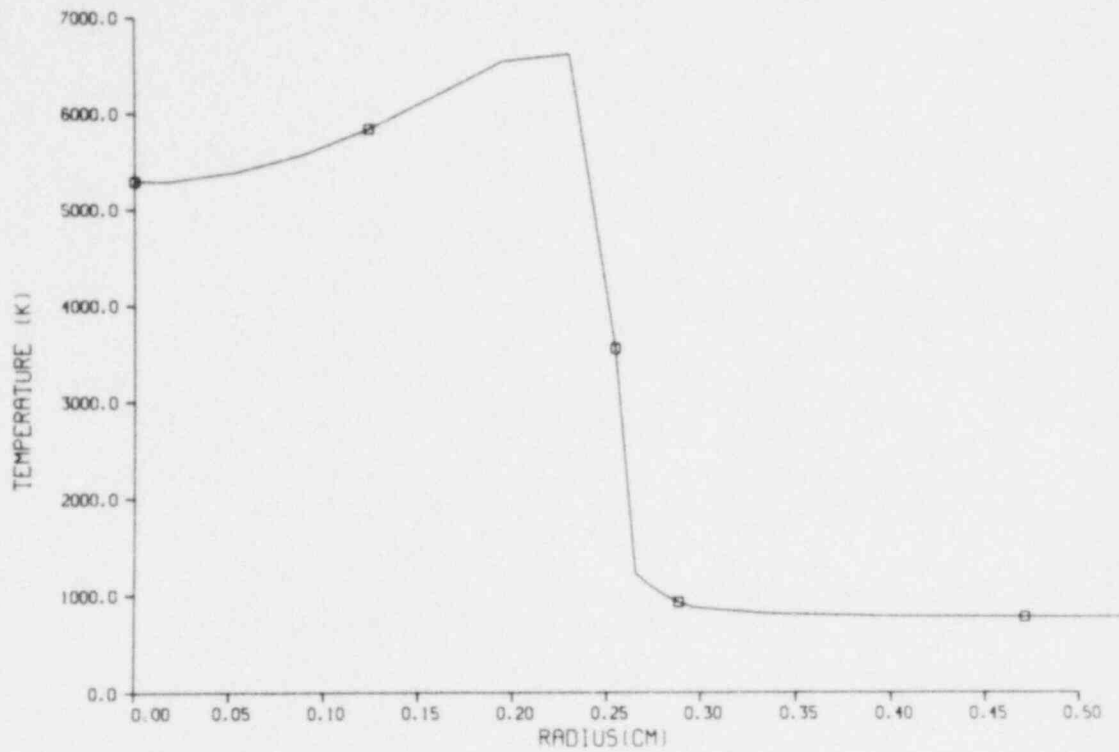
Figure 1.1-14   Radial Temperature Profile for PBE-SG2 at 40 ms
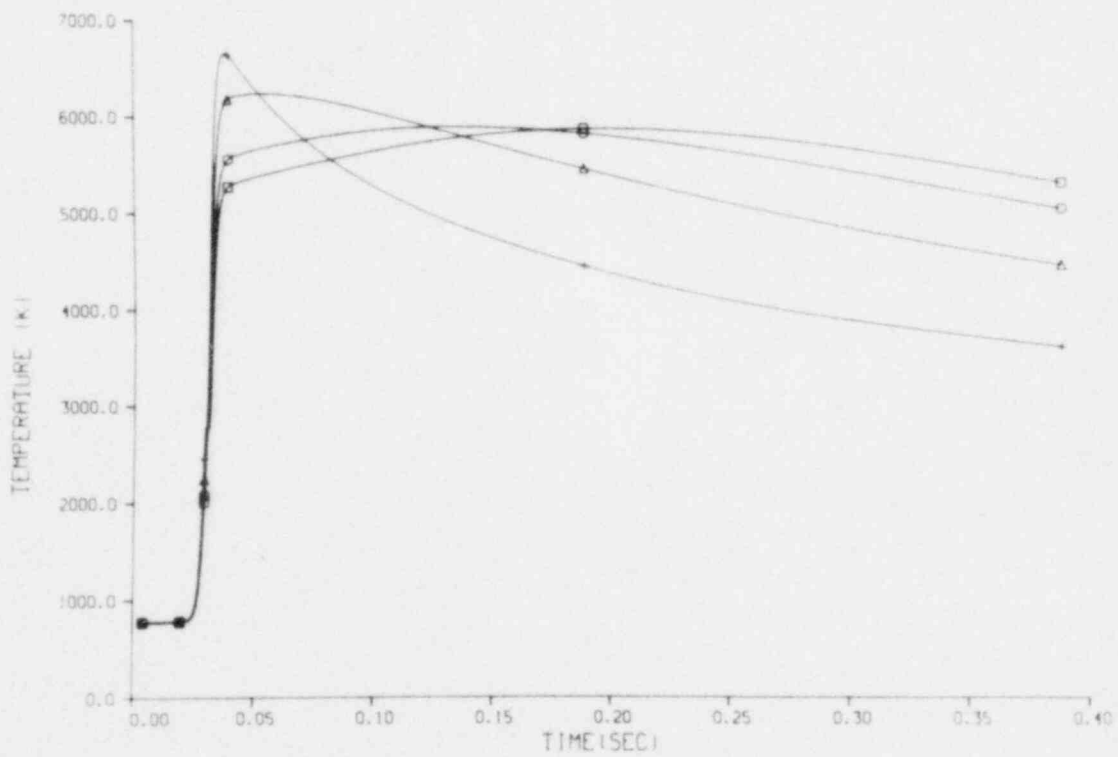
Figure 1.1-15   Fuel Temperature vs Time for PBE-SG2 at Four
Radii

52
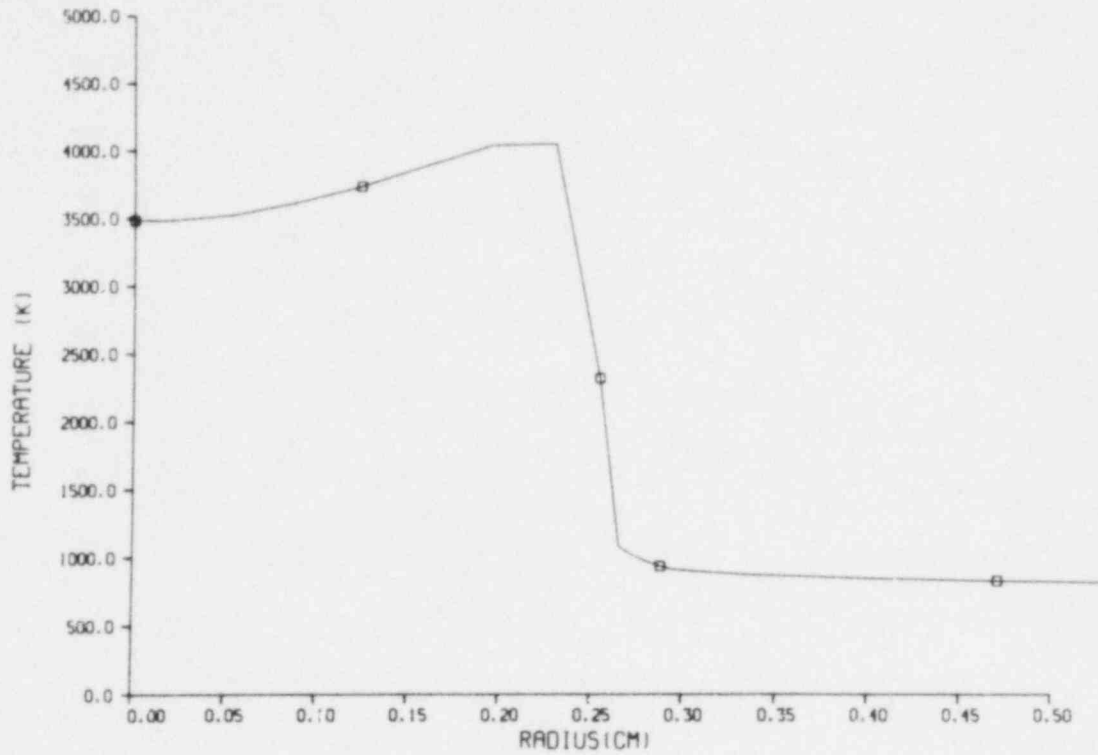
Figure 1.1-16   Radial Temperature Profile for PBE-SG3 at 275 ms
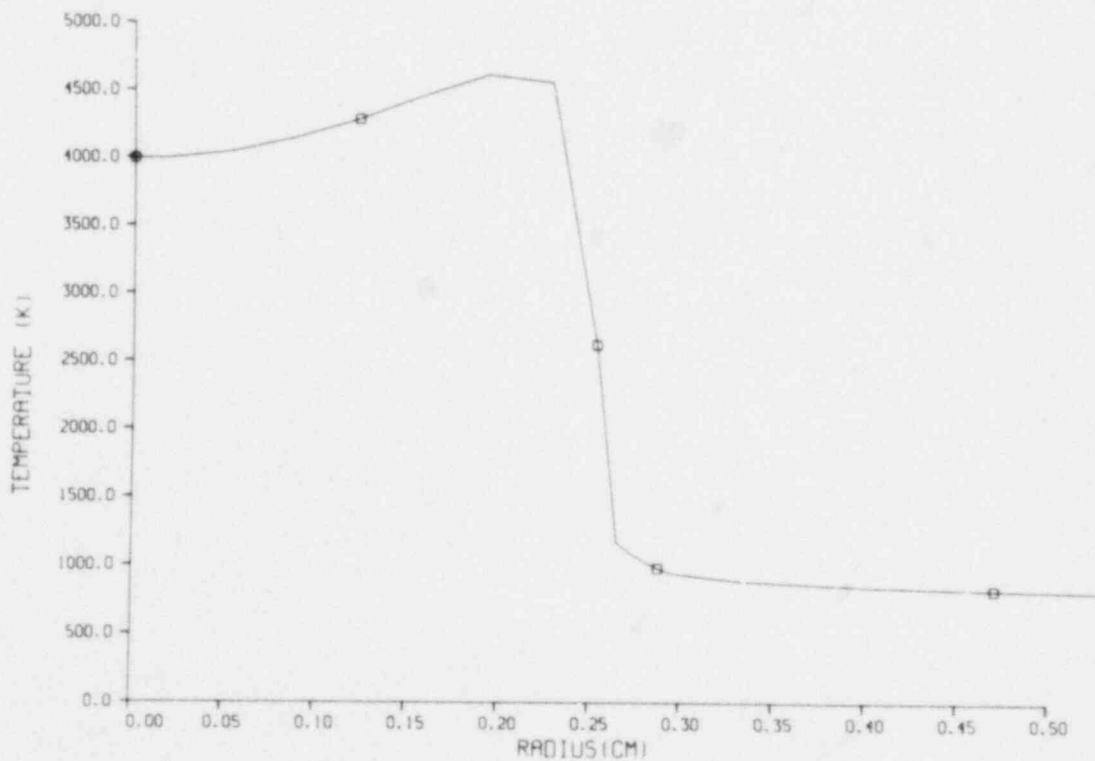
Figure 1.1-17   Radial Temperature Profile for PBE-SG3 at 280 ms
(failure time)

53
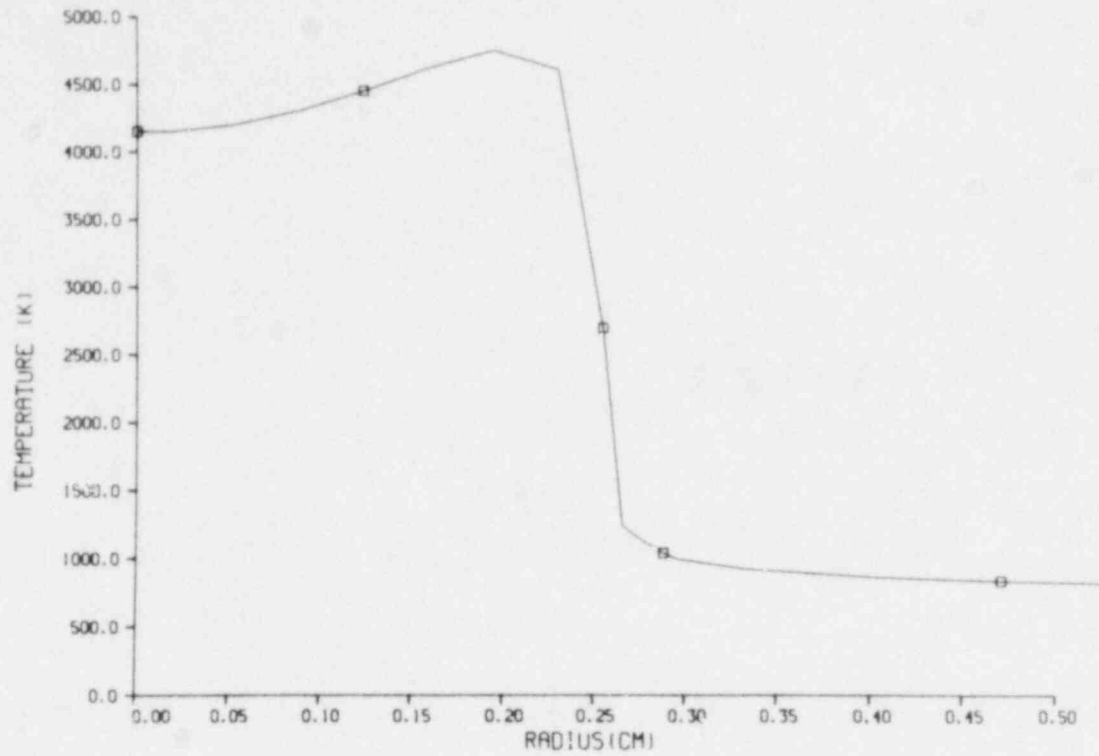
Figure 1.1-18 Radial Temperature Profile for PBE-SG3 at 285 ms
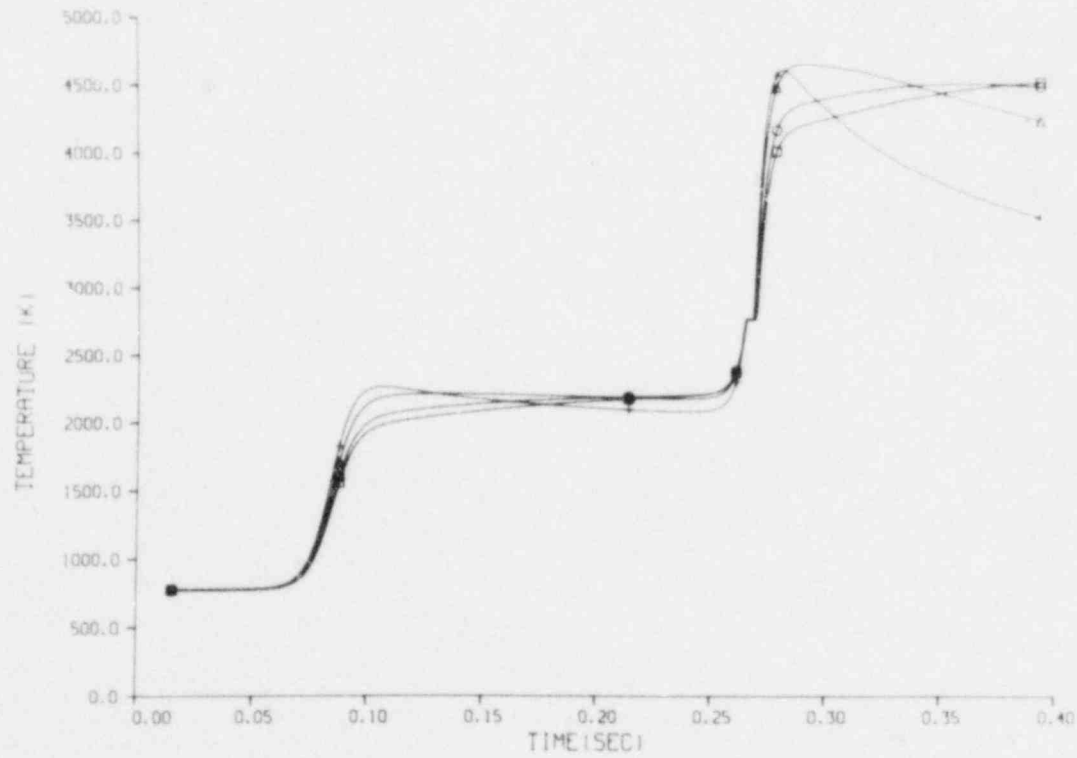
Figure 1.1-19 Fuel Temperatures vs Time for PBE-SG3 at Four
Radii

54

Table 1-II

Calculated Parameters at Pin Failure Time

Experiment	SG1	SG2	SG3
Failure Time (ms)	42.5	37.2	279
Peak Fuel Temperature (K)	4500	6650	4630
Average Fuel Temperature (K)	4240	6140	4440
Peak Sodium Temperature (K)	800	790	8..
Average Sodium Temperature (K)	780	780	840
Fuel Temperature Difference (K) (max to min)	920	1490	630
Sodium Temperature Difference (K) (max to min)	27	17	64
Fuel Vapor Pressure (MPa)	0.06	12.4	0.10
Fuel-Sodium Interface Temperature (K)[*]	2290	3100	2440

---

[*] Calculated on the basis of average fuel and sodium temperatures using properties from Reference 1-3.

Figures 1.1-20 through 1.1-22 compare the calculated sodium temperatures to the top, middle, and bottom thermocouple data for the three experiments. The thermocouples occupy a position between the inner radius of the molybdenum liner and the cladding; thus the two innermost sodium finite-difference nodes bracket the thermocouple location and are most directly comparable to the experimental data. Calculated temperatures are not valid past pin failure time due to the change in geometry.

PBE-SG1 and -SG2 data are hard to compare with the calculations because of the short time between pulse heating and pin failure. In PBE-SG1, the inner sodium node temperature rises more quickly than the thermocouple data. PBE-SG3, with a long heating time, shows an excellent match between calculated and measured temperatures up to failure.
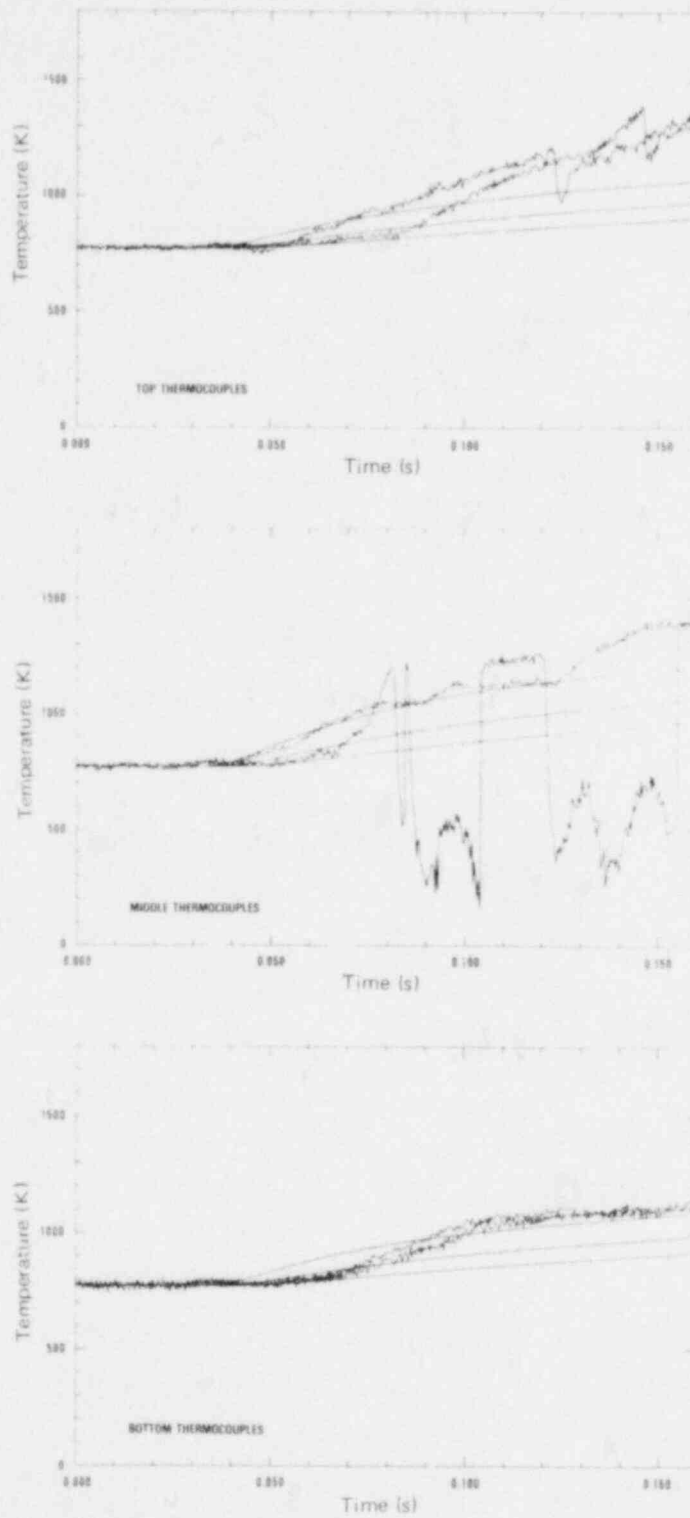
Figure I.1-20   Comparison of the Three Calculated
Sodium Node Temperatures With
Thermocouple Data for PBE-SG1
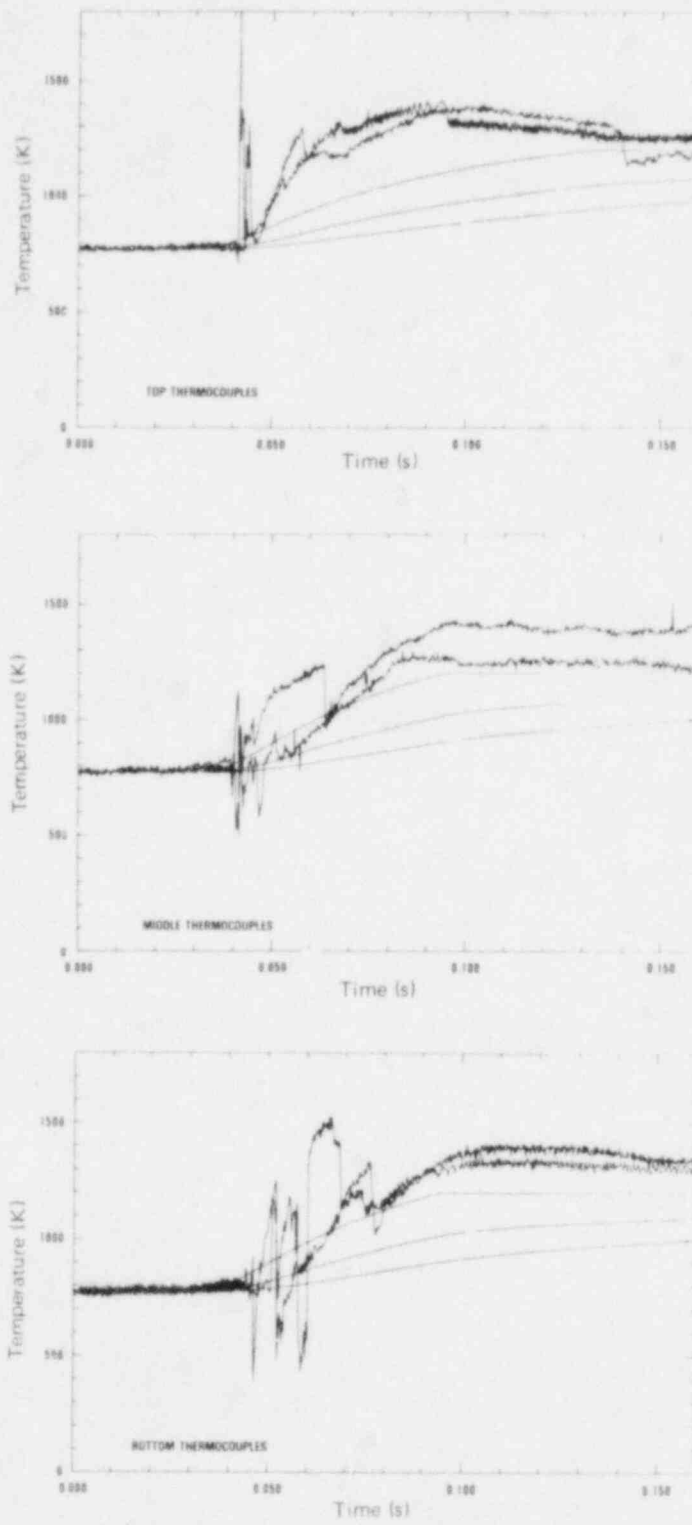
Figure 1.1-21 Comparison of the Three Calculated
Sodium Node Temperatures With
Thermocouple Data for PBE-SG2
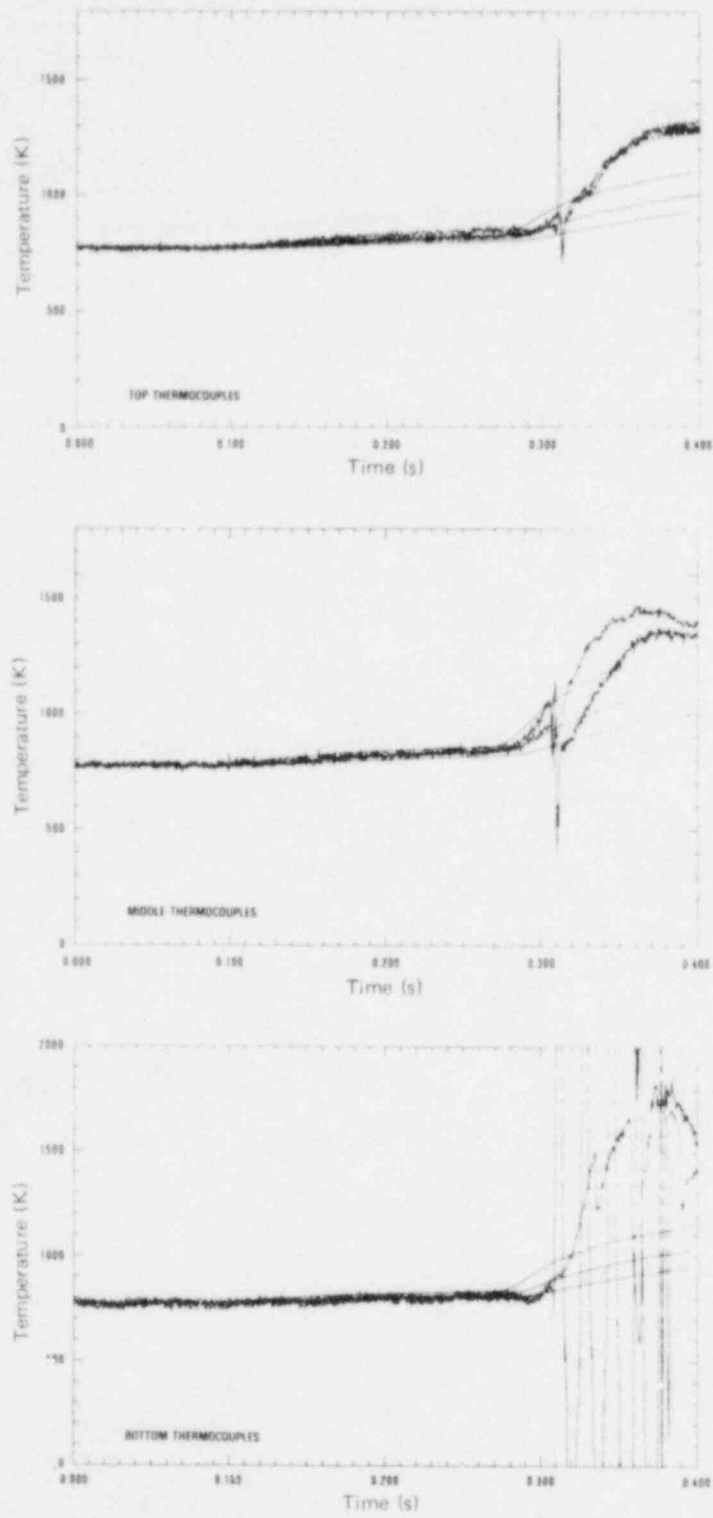
Figure 1.1-22   Comparison of the Three Calculated
Sodium Node Temperatures With
Thermocouple Data for PBE-SG3

This confirms that the solid-fuel to clad gap model is accurate; the trends after fuel melting give some support to the molten fuel-clad gap conductance chosen, although this is inconclusive due to the short time between fuel melting and clad failure. Calculated sodium temperatures actually track the thermocouple data for several milliseconds past pin failure; this might be expected for the bottom and possibly the top thermocouples, but is probably fortuitous for the midpoint thermocouples near the pin failure location.

In the data, the large oscillations seen in one of the PBE-SG1 middle, PBE-SG3 bottom, and PBE-SG2 bottom thermocouples are the result of the thermocouple junctions opening and closing due to the presence of hot fuel near the junction or the leads which are routed up the capsule behind the molybdenum liner.

1.1.2.3 Piston Deceleration -- A secondary peak, seen on the PBE-SG2 and -SG3 top pressure transducers occurred coincident with piston deceleration. In SG2, the pressure rise began as the piston stopped; the pulse is 50 MPa high and roughly 0.6 ms wide (FWHM). Explanations suggested are (1) a reflection of the 21 MPa pressure in the voided region of the channel (seen on the lower transducer) or (2) an FCI triggered by piston deceleration.

Simple buildup of the void pressure when the expansion of the void volume stops is ruled out by the absence of a corresponding pulse on the lower transducer. Analysis with HONDO, [1-7] a transient finite-deformation code, has shown that a 3-MPa pressure pulse of 0.3 ms duration (FWHM) is generated by piston deceleration as shown in Figure 1.1-23. (A detailed description of this work is given in Reference 1-8). According to work by Patel and Theofanous, [1-9] this is of the correct magnitude to trigger hydrodynamic breakup, leading to an FCI. Further analysis with HONDO using a 20-MPa pressure applied to the sodium column resulted in 40 to 50 MPa pressure pulses in the sodium due to acoustic ringing (see Figure 1.1-24); however, these were only 0.23 ms FWHM, much shorter than the observed pulse, with a period of 0.4 ms. Although high frequency oscillations of this type are seen superimposed on the experimental data, the main pulse envelope itself does not ring, suggesting that the main pulse results from two-phase pressurization.
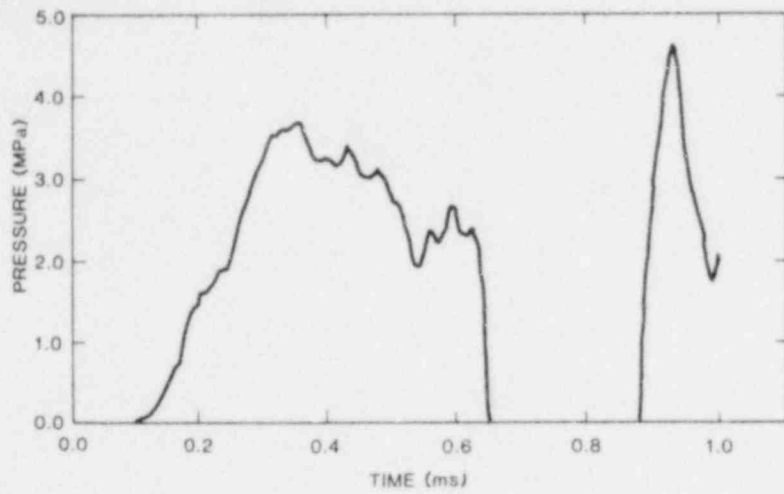
Figure 1.1-23   HONDO Pressure History in Sodium Slug
as Result of Piston Deceleration
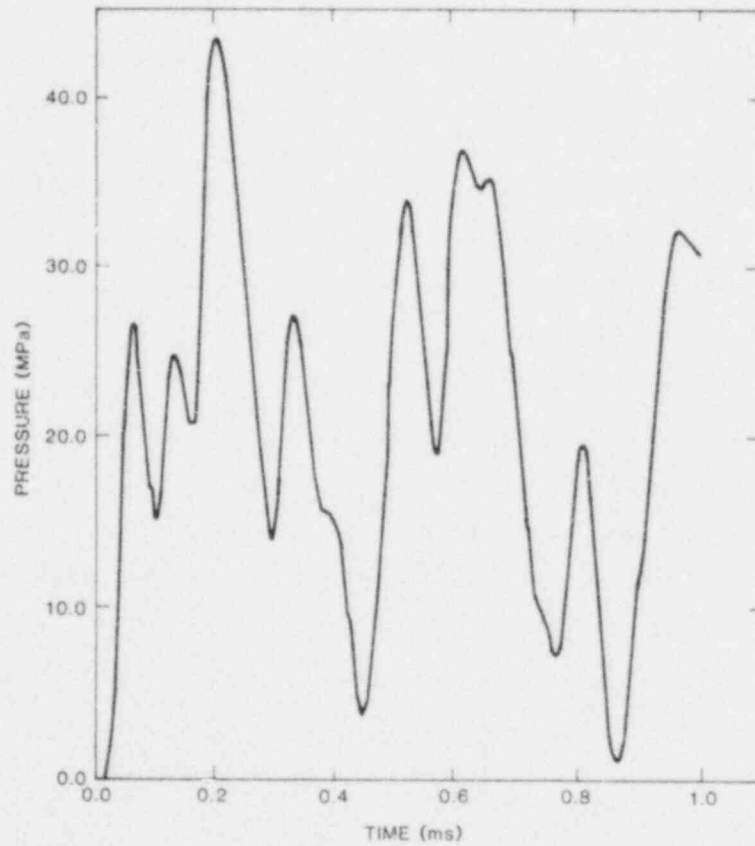
Figure 1.1-24   HONDO Pressure History in Sodium Slug
on Piston Impact (20 MPa Applied)

1.1.3 SIMMER-II Analysis of the PBE-5S Experiment

Work with SIMMER-II[1-10] has continued to be directed toward PBE-5S.[1-11]
The objective of this PBE analysis program is threefold: (a) to investigate the ap-
plicability of SIMMER to these complex experiments, (b) to provide insight into the
separate pressure-generation and pressure-quenching mechanisms, and (c) to pro-
vide information for model development and verification.

The PBE-5S experiment consisted of failing a single uranium oxide pin im-
mersed in sodium using a maximum pulse in the ACPR. The peak radially averaged
energy deposition was about 2350 J/g. The principal experimental diagnostic con-
sisted of pressure traces measured at the top and bottom of the test channel. The ac-
curacy of a calculation is evaluated by comparing calculated and measured pressure
histories at these locations. Earlier work has demonstrated the utility of SIMMER-II
in analyzing the PBE experiments.[1-12, 1-13] However, in the calculations of PBE-5S,
SIMMER did not accurately predict the rapid decay in the pressure train. Investigators
considered that the inaccurate prediction might have been caused by geometric model-
ing approximations. In the current work, extensive improvements have been made in
the modeling of this experiment in an attempt to improve the calculation of pressure-
quenching mechanisms.

As in the previous work, SIMMER was started at pin failure. Initial conditions
were obtained with the EXPAND[1-14] pin-failure code with the energy deposition normal-
ized to give approximately the correct magnitude on the initial pressure peak. The fuel
equation-of-state was based on measurements by Reil[1-15] which used dosimetry tech-
niques consistent with the PBE experiments. In the current calculations, Sandia investi-
gators have set the level of energy normalization about 15% larger than the best esti-
mate of the actual deposition. This is done in order to obtain an initial pressure of
20 MPa in the pin at failure. The 20-MPa vapor pressure corresponds to a peak fuel
temperature of 4670 K. If the SIMMER EOS correlations were based on ANL
Blue Book[1-3] data for UO_2, the energy-deposition normalization would have to be signi-
ficantly increased.

In the current SIMMER work, geometric modeling improvements included
changes both within the fuel pin and in the coolant channel. Within the pin, the num-
ber of radial mesh intervals was increased from 2 to 3 and fuel temperatures were
entered for point locations within the experiment rather than for zones to more

accurately describe the extent and location of the hottest fuel which drives the experiment. A solid fuel crust on the inner clad was modeled as predicted by EXPAND. Finally, the liquid/structure heat transfer was enhanced in order to investigate its effect on the pressure-source quenching. Outside of the pin the molybdenum liner was more accurately represented by modeling it as a thin tube surrounded on the outside by stagnant sodium. A parametric investigation was also made of the break size. A schematic of this model is shown in Figure 1.1-25.
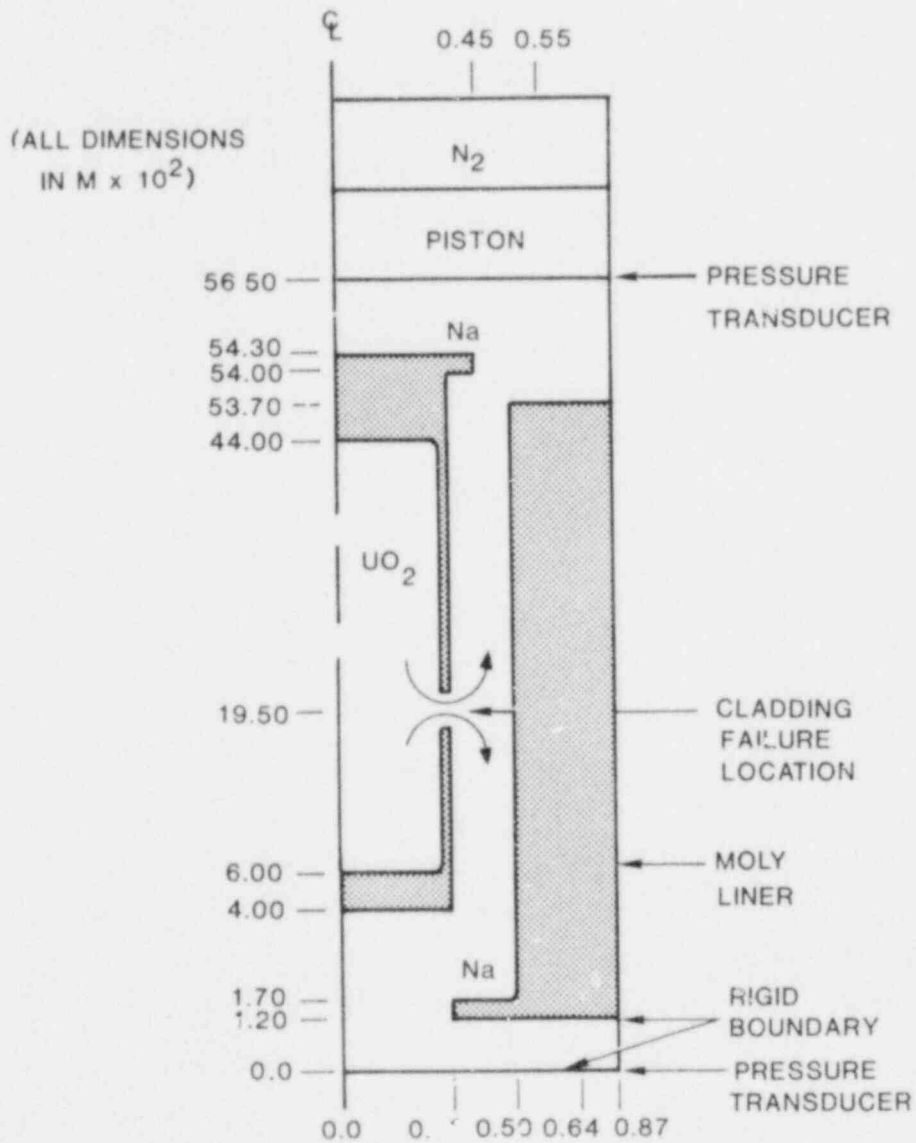
Figure 1.1-25   SIMMER Model of PBE-5S

Pressure traces calculated for two of the cases, one with a 1-cm break and one with a 5-cm break, are shown in Figures 1.1-26 and 1.1-27 along with the measured results. The measured pressure at the top of the pressure canister goes negative at about 3 ms past pin failure. This is due to thermal effects on the transducer face as hot material streams up the channel with piston motion. The shape of the curve is considered to be correct but a thermal drift begins at some unknown time and effects the normalization. Assuming the top and bottom transducers equilibrate after 10 ms, the maximum correction is about 3 MPa. Comparing the calculated pressure traces with the measurements, investigators observed that at the top transducer location the envelope of the pressure calculated for a 5-cm break seems to behave generally as in the experiment. There is a large initial peak followed by a smaller peak (more sustained in the calculation than in the measurement) which dies away to about 5 MPa in a few milliseconds. The pressure at this location is obviously greatly affected by the movement of the piston. At the bottom transducer, the calculation does not agree at all with the observed behavior. After a high initial peak, the pressure oscillates about 20 MPa with no decay. With no relief from a piston, the pressure at the bottom of the capsule is dominated by the pressure in the interaction zone which is calculated by SIMMER to remain near 20 MPa. In the calculation with a 1-cm break, the initial pressure peak is lower but the general behavior is the same.

Inside of the pin and in the interaction zone outside of the break, SIMMER does not predict any decay of the pressure. At the beginning of the calculation, the fuel temperature is peaked both radially and axially resulting in a much larger vapor pressure than would be observed with equilibration. Mixing is enhanced by the break, but as the temperature begins to equilibrate, additional nuclear heating from the tail of the pulse maintains approximately the same peak temperature and peak fuel vapor pressure. In addition, fuel in the channel heats a significant amount of sodium to very high temperatures. (Liquid sodium has a temperature over 2000 K and a volume fraction over 50% in many of the interaction-zone nodes.) Thus, even if the fuel vapor source dissipated, the pressure would be sustained by sodium vapor.

63
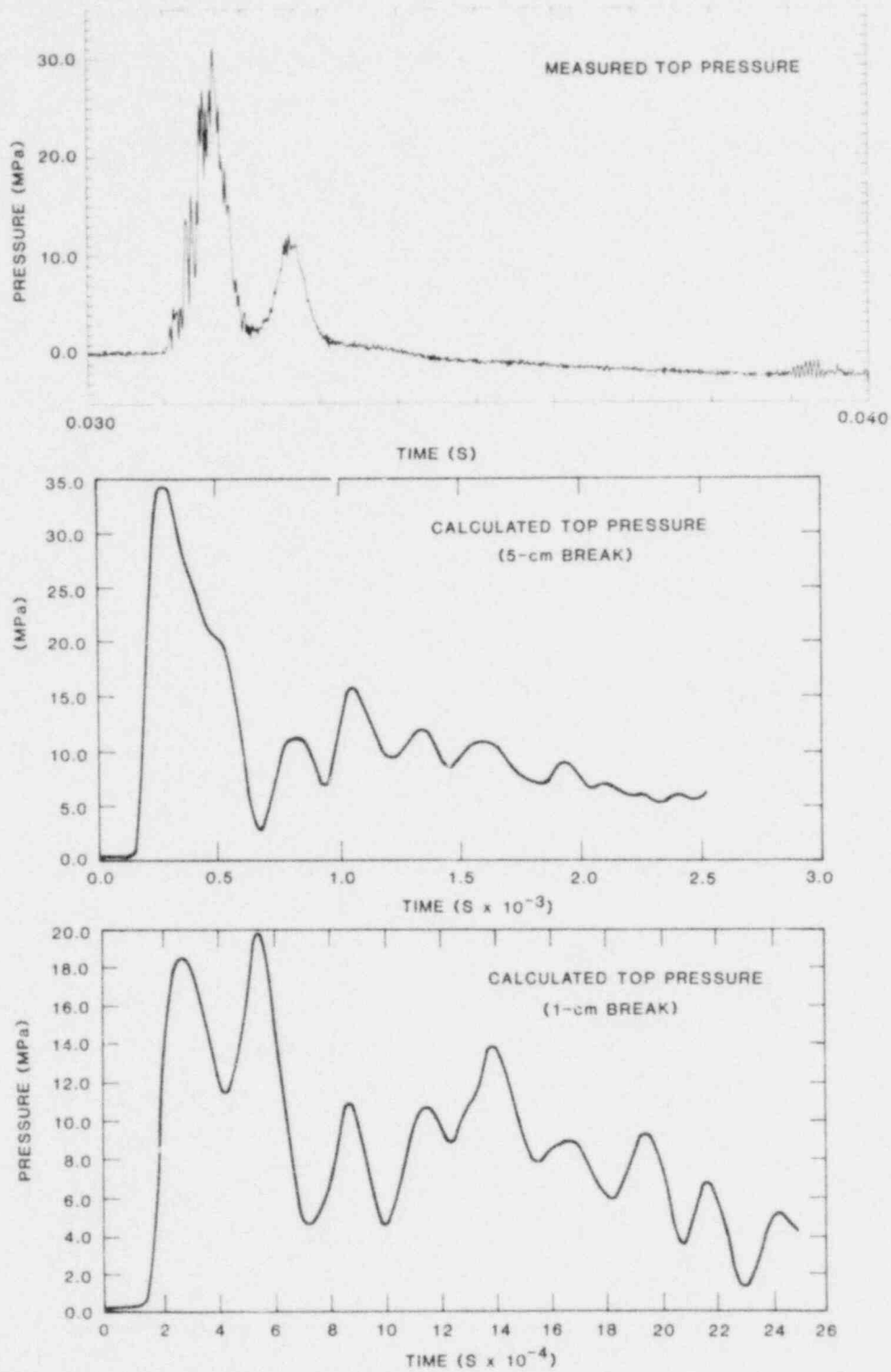
Figure 1. 1-26   Data at the Location of the Top Pressure
Transducer in PBE-5S
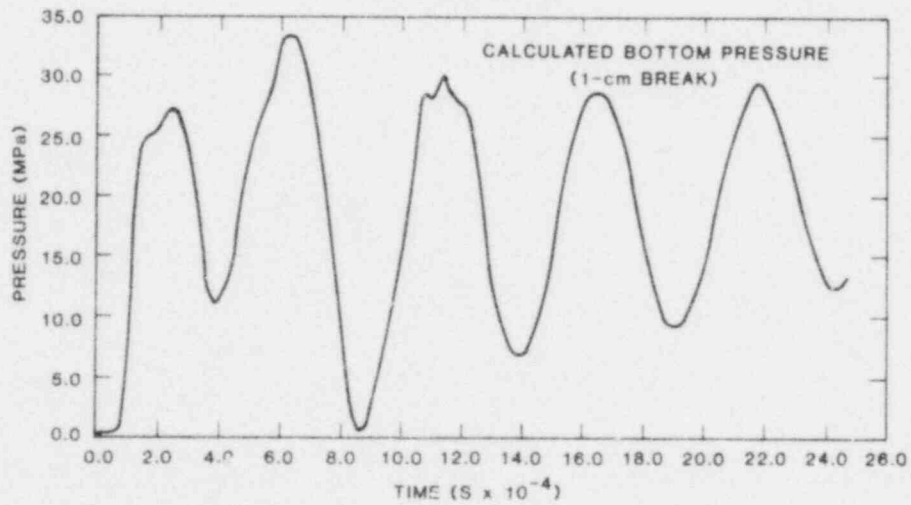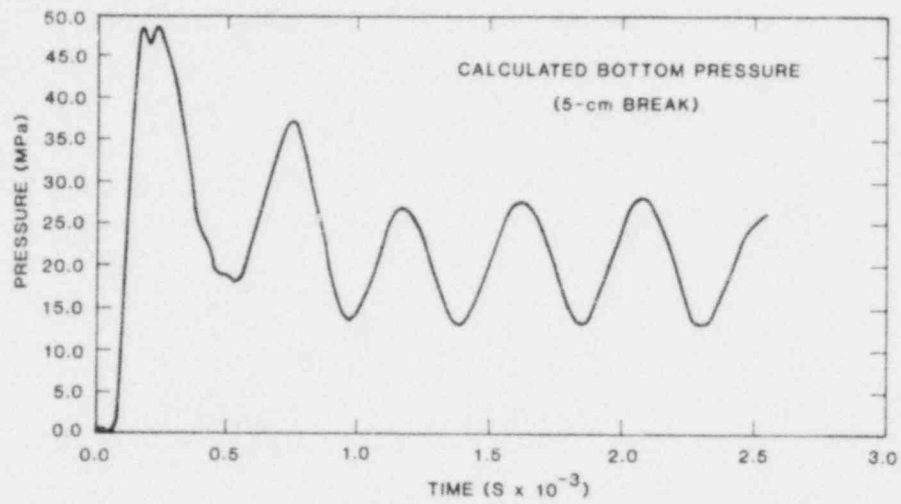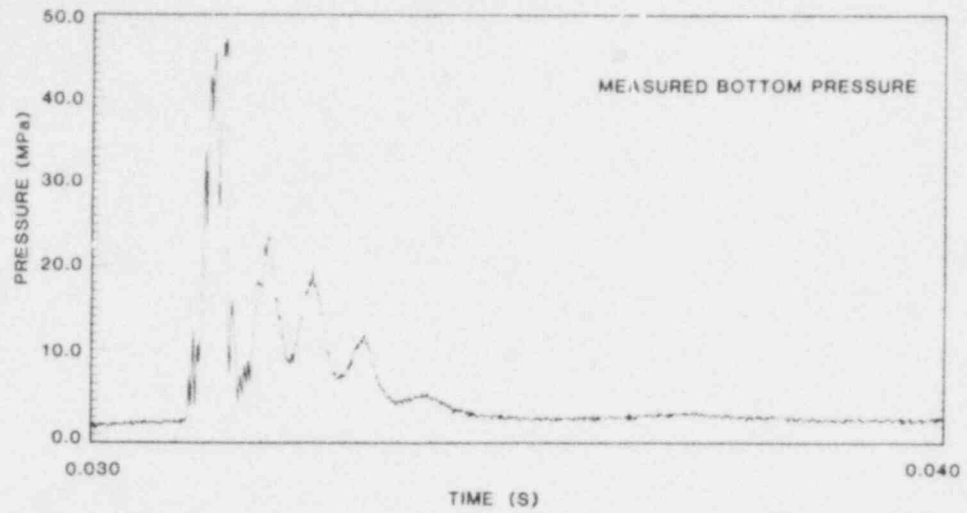
Figure 1.1-27   Data at the Location of the Bottom Pressure
Transducer in PBE-5S

The character of the measured pressure traces seems to indicate fuel vapor as the driving pressure. The dilemma with this explanation is that if the peak fuel temperature at failure corresponds to half of the observed initial pressure peak (assuming acoustic effects will double it), the equilibration temperature yields too high a pressure at late times. There are two suggested explanations. First, there may be a much more peaked temperature distribution than predicted by EXPAND, which then disperses rapidly by internal mixing. Second, unmodeled rate effects may exist in the fuel equation-of-state resulting in a high transient vapor pressure. Both of these hypotheses would also require substantially less heat transfer to the sodium than predicted by SIMMER. This is reasonable as SIMMER does not model the formation of vapor films in its liquid/liquid heat transfer model. Such films surely exist and impede the sodium heating. Also, there is no model to evaluate the possible generation of a vapor barrier between liquid components, which would minimize mixing and prevent significant heat transfer to the sodium. In fact, the process of homogenizing materials across a node results in mixing being predetermined by the choice of node size rather than deterministically calculated. If small axial nodes are chosen, the calculated mixing is minimized whereas large nodes enhance mixing.

The difficulty in analyzing the PBE experiments is the lack of adequate experimental diagnostics. These are very integral experiments in the sense that there are no measurements of the details of disassembly. There are no data on the pressures inside of the pin, the extent of the clad break, mixing, fuel motion, or the interacting masses. Without additional diagnostics it is difficult to use these experiments, to evaluate the SIMMER models.

Additional work is planned which will investigate several of the areas of uncertainty. First, mixing and temperature equilibration within the pin can be analytically evaluated. Second, fresh UO_2 equation-of-state experiments, scheduled for late 1980, will provide information on rate effects. Finally, improved diagnostics on future PBE experiments, provided by the Coded Aperture Imaging System (CAIS) for fuel motion detection and in-core fuel motion monitors will provide additional data for interpreting these experiments.

1.1.4 Status

A topical report entitled <u>Prompt Burst Energetics Experiments: Fresh Uranium Carbide/Sodium Series</u> has been completed and is being reviewed for publication. A complete summary of experiment data from PBE-13S will be assembled as soon as the transition to the new Data Acquisition and Display System is complete.

Examination of the fast transient response of the Kaman Pressure Transducers is continuing. The next step in that work is to derive transient response functions for a sibling transducer of those used in PBE-SG2 and then to attempt reconstruction of the actual pressure history by unfolding the measured pressure histories.

Work has been initiated to develop a nuclear heated wall for single pin PBE experiments. The conceptual design includes concentric molybdenum tubes with vibrapacked UO_2 between them. The objective is to design a channel boundary which has a temperature response similar to cladding. This work is coupled to efforts directed at defining reactor operating conditions, pin enrichment, and moderator characteristics which will yield optimal fuel temperature distributions for future pin experiments.

An assessment is underway of the feasibility of conducting the Coarse Predispersed Mixture FCI experiments in the ACRR with particular concern for the heat transfer from fuel particles to sodium during the relatively long heating time (15 to 20 ms) associated with a maximum ACRR transient. Conceptual experiment designs are being pursued.

Work is underway to examine fuel mixing within a fuel pin during a PBE experiment as a mechanism for the observed rapid decay of the fuel vapor pressure source in these experiments. The SIMMER-II code will be utilized for this modeling work.

1.2   Irradiated Fuels Response (G. L. Cano, 4423; W. J. Camp, 4425;
       D. H. Worledge, 4424; W. R. Trebilcock, 4424)

1.2.1 Introduction

The Sandia Laboratories Irradiated Fuels Response Program is aimed at de-
termining the response of fresh and irradiated reactor fuels to both prompt burst
(disassembly timescale) and loss-of-flow (LOF) heating conditions. On prompt burst
timescales, the pressure source from both fuel vapor and fission gases as well as
the accelerations produced by these pressure sources are of central importance.
Thus, the program in this area centers on determination of the effective equation-of-
state (EEOS) of both fresh and irradiated fuels, the dynamics of pressurization (rate
effects) and the ability of this pressure to disperse fuel.

On LOF timescales, the mode of initial fuel disruption and its timescale for
both fresh and irradiated fuels are of crucial importance. Various mechanisms for
disruption have been proposed: liquid fuel slumping, rapid solid/liquid state swelling,
solid-state breakup, and liquid/gas froth formation. Of these, the last two are dis-
persive and would tend to reduce reactivity, while the first two are not dispersive and
thus would not diminish reactivity. Indeed, they could have deleterious effects on the
accident progression. Thus, it is important to determine the disruption mechanisms
operating under various LOF heating conditions. To assist in accomplishing this de-
termination, the FD1 series of fuel disruption experiments has been performed, and
the FD2 series, with significant improvements over FD1, has been initiated. The
first series involved multipulse heating of single fresh and irradiated fuel pellets,
individually, in the ACPR. Film records of fuel behavior were obtained for all 12
experiments. Significant results from this series included the observation of rapid
swelling as a disruption mechanism.

Currently, the experimental program centers on the FD2 series in which
larger fuel sections (three pellets) are being irradiated in the ACRR with heating
conditions much more typical of LOF conditions than those which were obtainable in
the ACPR. Additional improvements include filming of both sides of the pellet stack,
gas sampling, dynamic clad thermometry for the fresh fuel, the contamination-free
fuel handling facilities for sectioning the preirradiated fuel. Four tests have been
conducted in this series; three used fresh UO_2 fuel, and one used preirradiated,
mixed-oxide fuel.

Analytical work in the EEOS and LOF/FD programs involves neutronic and thermohydrodynamic analysis of the experiments directly. In the case of the EEOS program, this work is coupled to EOS theories and rate theories to unfold the equilibrium and dynamic pressure sources. In the case of LOF/FD experiments, this work is coupled directly to the FISGAS code. FISGAS is intended to calculate fuel mechanics including swelling, cracking, frothing, and gas release. In its current form FISGAS concentrates on the dynamics of gas release and fuel swelling. A new module, TIGRS, which also includes cracking, has been developed recently and will be incorporated into FISGAS-II.

1.2.2 LOF-Timescale Fuel Disruption Phenomenology

1.2.2.1 FD1 Experiments and Analysis -- An extensive report[1-16] on the first series of fuel disruption experiments, FD1, has been published and distributed. It details the motivation, conduct, results, and analysis of the FD1 series. The light optical micrography, done at LASL on some of the FD1 fuel, is not included in this report. This phase of the experiments and the results will be presented in a separate report.

The cooperative project between Kernforschungszentrum, Karlsruhe, West Germany (KfK) and Sandia on a detailed microscopic analysis of selected FD1 fuel has progressed. Preliminary approval for shipment of the fuel was received; and it now appears the material will be sent in the next quarter. The fuel to be examined includes that used in three FD1 tests and a sibling pellet, and is fuel which swelled extensively but did not otherwise disrupt. KfK will perform electron microprobe analysis in an attempt to determine particularly the Cs content and migration, Pu, U, and O_2 distribution, and stoichiometry. In addition, KfK will perform scanning electron microscopy to study fission-gas-bubble morphology and finally total gas analysis by dissolving the fuel and spectrometrically determining the constituents. The elemental constituency, stoichiometry, and bubble morphology will be determined as functions of radius and power transient.

An extensive paper was written this quarter detailing calculations on fuel disruption; it includes the latest improvements in the model, TIGRS, such as crack growth and propagation as a function of heating rate and amount. The paper develops criteria for the advance of cracks between fission gas bubbles which can lead to fuel fragmentation or swelling during and depending on the power transient. The criteria involve

stress states, differential and total energy conditions, and mass transfer at the crack.

Bubble-dynamics calculations treat both intergranular and intragranular bubbles to examine pressure conditions prevailing in fuel during slow, fast, and very fast heating rates. Internal bubble pressure, which is developed during heating transients that produce rapid bubble coalescence leaving the new bubble in mechanical disequilibrium, can significantly modify the differential, localized energy state. This modification can lead to crack generation and propagation. However, at high temperature ($\gtrsim 2100$ K), mass transfer by surface diffusion of matrix atoms along the internal surfaces of cracks can arrest crack growth.

The adopted value of brittle fracture stress for this fuel at temperatures below 2300 K is $\sim 1.5 \times 10^8$ N/m^2, while that at higher temperatures is $\sim 5 \times 10^7$ N/m^2. The yield mechanism in these cases is through release of grain boundary adhesion. The corresponding intragranular yield values are approximately five times larger. Thus, within the modeling framework, intragranular bubble sizes and densities are not found to be high enough to allow an interconnected network of intragranular cracks to develop before the proper criteria for fuel dispersal are achieved on grain boundaries for heating rates ≥ 100 K/ms. For rates on the order of 1 K/ms, cracks heal and thus fragmentation is avoided. However, at these low-heating rates, if the fuel temperature gets within 100 to 200 K of the fuel liquidus temperature, the fuel loses its material strength and the bubbles proceed to equilibrium. This mechanism produces swelling to varying degrees depending on the fuel pretreatment and power-transient history.

A limited calculational effort was carried out with about 20 calculations using a variety of transients for one "gassy fuel" node. All the transients were started from 1500 K and averaged over the following timescales:

a. dwell times from 0.5 s to 20 s at temperatures from 1500 K to 2100 K, followed by heating ramps to 3000 K at rates varying from 1 K/ms to 300 K/ms;

b. continuous linear heating ramps to 3000 K at rates from 0.1 K/ms to 300 K/ms.

Figure 1.2-1 shows in oversimplified format the general trend of the results for intergranular bubbles only.
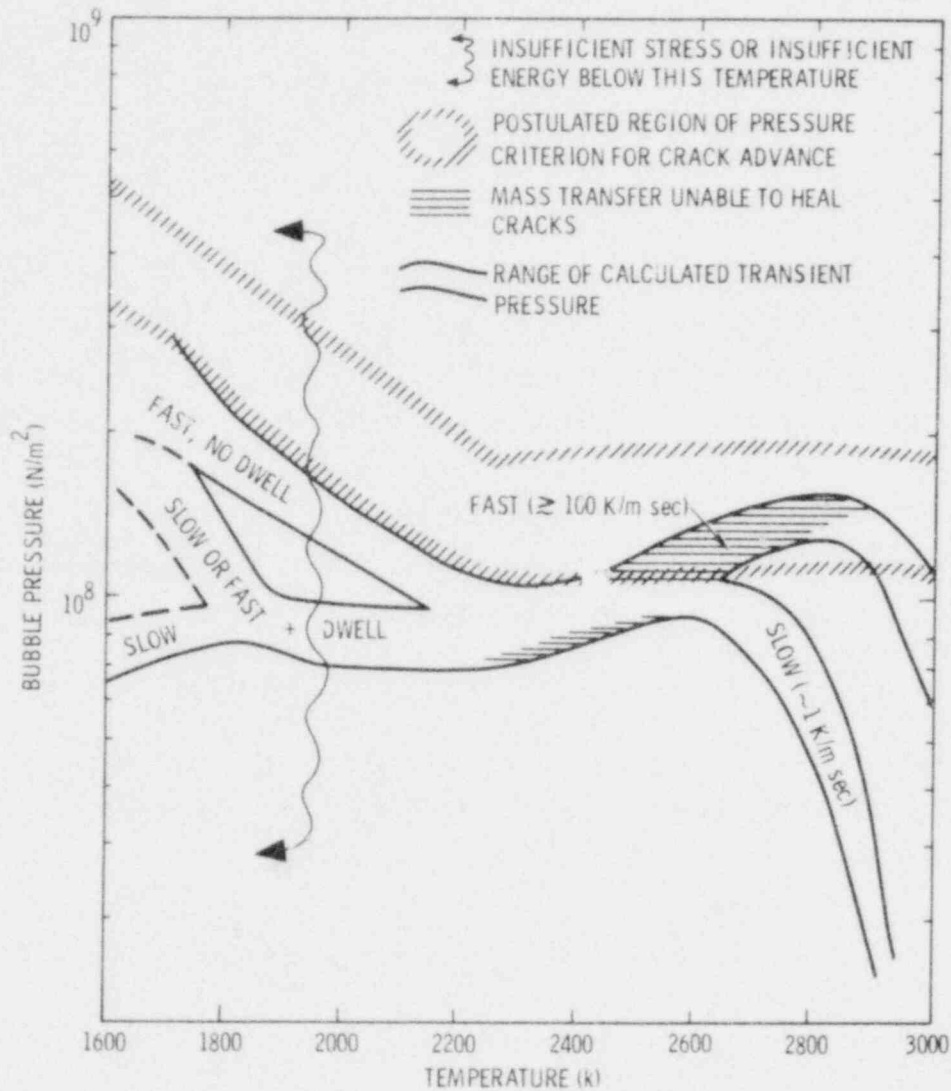
Figure 1.2-1   General Trend of Calculated Bubble Pressure
for Range of Transients

Near the start of all the transients at temperatures below ~ 2000 K, high pressures are developed early in small bubbles (radius ~ a few nm). These pressures result mainly from coalescence within the grains. The overall pressures are high, but the criterion for crack advance in this range of bubble sizes is probably higher than 10^8 N/m^2 because of small crack openings. At such low temperatures the stress criterion may be associated with the brittle fracture stress. At this stage in the

71

transients the bubbles just do not possess enough energy to propagate cracks to their neighbors.

Depending on the initial bubble size used, pressures at the start can vary appreciably, although after a few tenths of a second these effects dissipate with pressures around 8×10^7 N/m^2. Heating through this low temperature region on a millisecond timescale leads to higher pressures (factor of 2 or 3) but these too fall to about 10^8 N/m^2 by 2400 K. Thus grain boundary separation appears unlikely below 2000 K.

Above 2300 K the pressures rise until creep causes a reversal of slope below the melting point. The slower transients are much more susceptible than the fast ones to creep relaxation, and pressures barely reach 10^8 N/m^2. The faster transients rise to the postulated pressure criterion rather easily before creep intervenes within 100 K of the melting point.

Mass transfer at the cracks is thermally dominated and is generally able to heal cracks dynamically above ~2300 K for slow transients but not for the millisecond scale transients.

The consequence of these trends, although generalized, is that heating at rates of the order of 100 K/ms above 2300 K seems most likely to lead to fine-scale fuel disruption for a wide range of conditions earlier in the transient. Heating at slow rates over a few seconds seems unlikely to achieve the same behavior. This is in accordance with the limited experimental evidence that exists, namely, FD1.3 and 1.6.

The bubble pressures depend on many features of the dynamics; however, some confidence in the calculated values is derived from the observation that the gross high-temperature swelling observed late in the FD1.4, 1.7, and 1.8 experiments is approximately reproduced by this model. The model does not give an appreciable contribution to the swelling from grain face bubbles since the amount of gas needed to saturate the available grain boundary area is small. The maximum swelling expected from this contribution is ~10%. The contribution from edge porosity is not calculated.

Note that the present work is concerned only with the loss of internal structural stability that crack propagation implies. This is a necessary condition for fine scale

dispersion but not necessarily a sufficient one. For FD1.6 the calculations were performed for the extreme axial end of the fuel column, in a system that required only 2 bars gauge pressure to allow fuel to escape from its confining end restraint. This is a low constraint condition that would not be met in a reactor environment until clad failure or meltoff. In real reactor accidents, perhaps the clad does not melt and the restraint is different (probably larger) than for FD1.6. Under these constraint conditions, pin disassembly can occur very differently. Thus, these crack growth criteria need to be investigated more extensively. A later series of experiments will address this issue.

1.2.2.2 **FD2 Experiments, Calculations, and Analysis** -- The latest series of LOF-timescale fuel disruption experiments, FD2, has continued. In the previous quarter, three fresh fuel experiments were conducted. These, together with calibration tests done earlier, yielded sufficient data on power coupling factors, peak-to-minimum energy generation profiles and fuel response, to allow proceeding to the preirradiated fuel set of FD2 experiments. Thus, the first of these mixed oxide, pre-irradiated fuel tests, FD2.4, was carried out. This test utilized fuel which, with high probability, was contaminated by atmospheric gases, in particular by N_2, H_2O, CO, and CO_2. This fuel was extracted from its parent pin, PNL 10-12, in June 1977 and has been in the same environment (N_2 with ~ 300 ppm impurities) since then. Thus, one of the principal goals in this test was to record the response of the fuel to a simulated LOF transient for future comparison to the response of fuel yet to be cut and loaded in the Sandia ultraclean-environment shielded glovebox. The glovebox facility is currently being developed.

The response of the FD2.4 fuel to the transient rod withdrawal (TRW) power sequence was recorded, as in previous tests, by high speed cinematography. Analysis of the film record showed that fuel disruption occurred very differently from fresh fuel subjected to identical power-transient conditions. The FD2.4 clad and fuel ruptured and disassembled in large pieces in contrast to the clad meltoff and fuel melting and squirting in the fresh fuel case. Also, the disruption occurred significantly earlier (0.75 s before clad melt and 1.25 s before squirting of fresh fuel), and more rapidly. The clad and fuel chunks varied in size up to about 3 mm. The early disassembly did not allow enough time for sufficient energy to transfer to the clad for it to melt. Unfortunately, the clad-temperature history was not obtained. The maximum surface temperatures determined for one of the fuel chunks was ~ 2500 K. The surface

temperature at disassembly was ~2300 K. Thus, disassembly occurred at lower-than-expected surface temperature. Further analysis is required.

Execution of the remaining six experiments in this series is awaiting completion and approval of the shielded glovebox in which to section the fuel pins in the high purity environment and to extract the segments for use in these tests. The matrix of remaining experiments addresses fuel response ranging from controlled swelling to total disassembly and dispersal.

Neutronic and thermal heat-transfer calculations for both fresh and irradiated fuel using the power pulse actually applied, and gap conductivity as parameters have continued. A comparison of data and calculations agree within ~5% in terms of clad meltoff time, fuel melt time, and fuel surface temperature for fresh fuel. However, to achieve this agreement the energy coupling factor between reactor output and energy generation in the test fuel had to be reduced by 20% from that given by TWOTRAN calculation. Thus, this difference remains to be reconciled. In the case of FD2.4, at time of disruption neither the clad nor the fuel had gone through its respective heat of fusion (as evidenced by the absence of fuel or clad "balling") and the fuel surface temperature was determined by radiometry to be ~2300 K. Calculations without a 20% reduction in power factor from TWOTRAN indicate the clad and some of the fuel were at their respective melt temperature, and the fuel surface temperature was ~275 K hotter than measured. Additional calculations will now be performed using the reduced power factor and will also examine the sensitivity of these results to gap conductivity.

Finally in FD2, a contract has been let to LASL for performance of the requisite spectrometric analysis of the gas sampled during each of the irradiated fuel tests. In FD1, during the course of the power transient, gases were observed effusing from the fuel. Also, contaminant gases are known to infiltrate into the fuel during cutting and handling. Therefore, determining what these gases are is important, whether fission and/or contaminant, as is determining their relative amounts. Thus, two gas sampling bottles are included in each of the irradiated fuel tests. The two used in FD2.4 are already at LASL.

A new series of high ramp rate (HRR) fuel disruption experiments has been described in previous quarterlies. This series is now planned for the last half of FY 1980. A tentative matrix of 10 tests was generated based on discussions between UKAEA and Sandia staff. These experiments will consist of eight tests using a pellet stack as in FD2, and two using powdered fuel. The eight will consist of four contaminated-fuel tests, two uncontaminated-fuel tests, and two fresh fuel tests. The final two tests will utilize uncontaminated, pulverized fuel. These powdered-fuel experiments are for direct comparison of companion tests in the EEOS series. The UKAEA will partially-fund these 10 tests in a collaborative effort with the USNRC.

Preliminary neutronic and heat transfer calculations have commenced for these tests. An ACRR double pulse, as in FD1.6, will be used, with the first pulse serving to pretreat the fuel and the second pulse taking the fuel to dispersal with heating rates in the vicinity of 100 K/ms.

References for Section 1

1-1   Advanced Reactor Safety Research Quarterly Report, January-March 1978 SAND78-1421, NUREG/CR-0335 (Albuquerque, NM: Sandia Laboratories, Advanced Reactor Research Department, January 1979).

1-2   T. F. Petersen, TAC2D - A General Purpose Two Dimensional Heat Transfer Computer Code - Users Manual, GA-8868, Gulf General Atomics, 1969.

1-3   Properties for LMFBR Safety Analysis, ANL-CEN-RSD-76-1 (Argonne, IL: Argonne National Laboratory, 1976)

1-4   Aerospace Structural Metals Handbook, 2, AFML-TR-68-115, Mechanical Properties Data Center, Belfour Stulen, Inc, 1976.

1-5   Y. S. Touloukian, Ed, Thermophysical Properties of High Temperature Solid Materials, Vols 1 and 4, Macmillan, 1967.

1-6   K. O. Reil, M. F. Young, H. Jacobs, and H. Plitz, Prompt Burst Energetics Experiments: Fresh Uranium Carbide/Sodium Series, SAND   , NUREG/CR-   (Albuquerque, NM: Sandia Laboratories, to be published).

1-7   S. W. Key and Z. E. Beisinger, HONDO-II - A Finite Element Computer Program for the Large Deformation Dynamic Response of Axisymmetric Solids, SAND78-0422 (Albuquerque, NM: Sandia Laboratories, 1978).

1-8   Advanced Reactor Safety Research Quarterly Report, April-June 1978, SAND78-2001, NUREG/CR-0469, p 26 (Albuquerque, NM: Sandia Laboratories, Advanced Reactor Safety Department, 1978).

1-9   P. D. Patel and T. G. Theofanus, "Fragmentation Requirements for Detonating Vapor Explosions," Trans Am Nuc Soc, 28, 451, 1978.

1-10 L. L. Smith, "SIMMER-II: A Computer Program for LMFBR Disrupted Core Analysis," LA-7515-M (Los Alamos, NM: Los Alamos Scientific Laboratory, October 1978).

1-11 K. O. Reil, M. F. Young, and T. R. Schmidt, Prompt Burst Energetics Experiments: Fresh Oxide/Sodium Series, SAND78-1561 (Albuquerque, NM: Sandia Laboratories, August 1978).

1-12 Advanced Reactor Safety Research Quarterly Report, April-June 1979, SAND79-1597 (Albuquerque, NM: Sandia Laboratories, November 1979).

1-13 J. L. Tompkins, J. T. Hitchcock, and M. F. Young, Prompt Burst Energetics (PBE) Experiment Analysis Using the SIMMER-II Computer Code, Proceedings of the International Meeting on Fast Reactor Technology, Vol 2, p 1001, Seattle, WA, August 1979.

1-14 . F. Young, EXPAND, A Pin Failure Analysis Model for Fresh Fuel Pins, to be published (Albuquerque, NM: Sandia National Laboratories).

1-15 K. O. Reil and A. W. Cronenberg, "Effective Equation-of-State Measurements of Uranium Dioxide," Trans Am Nucl Soc, 27, 576, 1977.

1-16 G. L. Cano, R. W. Ostensen, and M. F. Young, Visual Investigation of Reactor Fuels Response to Simulated LOF Heating Conditions, First Series, SAND79-0940, NUREG/CR-0914 (Albuquerque, NM: Sandia Laboratories, October 1979).

2. FUEL DYNAMICS

2.1 Transition Phase (D. A. McArthur, 4423; R. W. Ostensen, 4425)

2.1.1 Introduction

Following the loss of initial geometry in a core disruptive accident, and assuming that neither early shutdown nor rapid hydrodynamic disassembly takes place, the accident enters the transition phase. At this point, one or more subassemblies have melted down and radial propagation takes place as subassembly hexcans are melted through. The progression of the transition phase may strongly affect the severity of the accident, and it is, therefore, important to understand the phenomena associated with this accident stage in detail. In particular, several key questions need to be answered. First, in the early stages of the accident is the fuel dispersive, that is, how far can the molten core material and fission gas mixture move axially before it freezes? Secondly, if blockages form and the core is bottled up, what is its configuration--does it remain boiled up, or does the pool collapse followed by the occurrence of a recriticality? Answers to these questions depend upon resolving the uncertainties in transition phase phenomenology. Work at Sandia is directed toward the mechanics of fuel blockage formation and boiling pool behavior. Both analytic and experimental studies are included in this effort.

2.1.2 Description of In-Core Fuel Freezing Experiments

During this quarter, detailed planning was begun for a series of in-core fuel freezing experiments, several of which are to be conducted in the ACRR during the current fiscal year. Because of the importance of fuel freezing to transition-phase phenomena, and because the initial conditions of the molten fuel and the steel structure are uncertain, Sandia is initiating phenomenological experiments covering a broad range of parameters and combinations of parameters.

A schematic drawing of the apparatus to be used appears in Figure 2.1-1. A simple cylindrical steel freezing-tube geometry is planned for the initial experiment series, with the initial temperature of the tube being varied over the range from

673 K to 1273 K. An ACRR pulse (typically ~ 10 ms wide) will be used to melt and preheat the UO_2 to an arbitrary initial temperature, thus permitting independent variation of fuel temperature over a range from 3273 K to 4273 K, and also avoiding the use of thermite, which contains gas and molten Mo in addition to UO_2. The uncertainty in fuel temperature will be minimized by minimizing both the spatial variation in initial energy deposition and the heat transfer from the molten fuel. The molten fuel will be forced upward into the freezing tube by an arbitrary (but temporally almost constant) driving pressure between 10 and 100 atmospheres, supplied by the He gas reservoir and fast-acting valve. The driving pressure will be maintained until freezing is complete. Following the cooldown of the experiment, x-radiographs will be made of the freezing tube to determine the length of the molten-fuel penetration. Some blockages will also be sectioned and examined to determine the blockage structure.
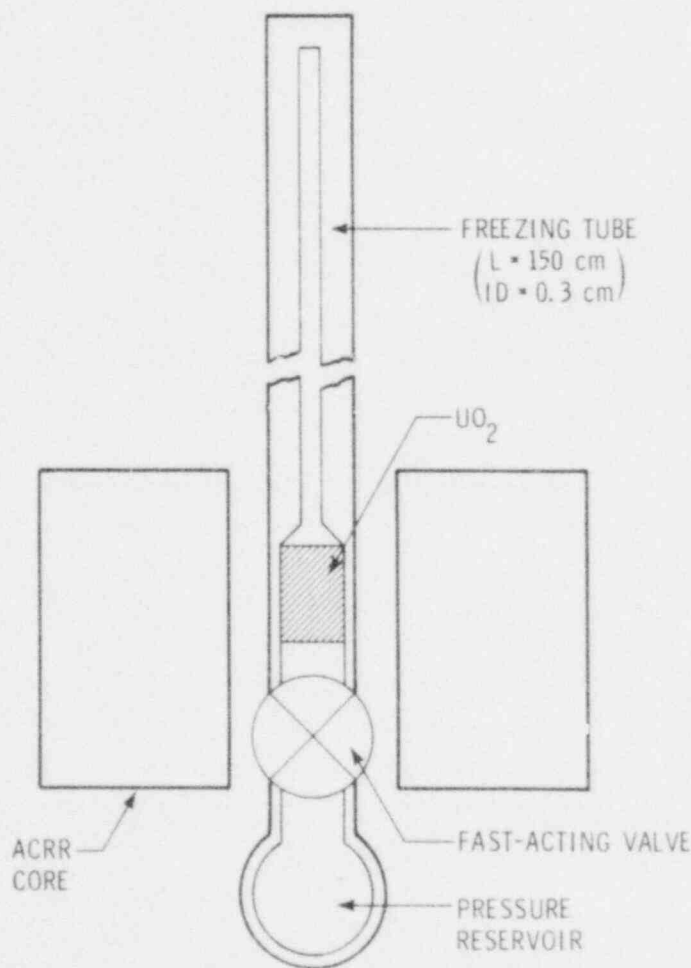
Figure 2.1-1   Schematic of Apparatus for Use
in In-Core Fuel Freezing Experiments

A future experiment series is also envisioned, in which the freezing of UO_2-steel mixtures and the effects of geometry (fuel pin structure and hydraulic diameter) on the freezing process are studied.

The purpose of these experiments is to provide a data base on fuel penetration as a function of fuel temperature, steel temperature, and driving pressure, using prototypic materials. These major parameters will be varied independently over wide ranges to ensure that all important phenomena are included. The data base resulting from the first experiment series can be used not only to judge the validity of various theoretical fuel penetration models, but also will be directly applicable to freezing and plugging in reactor accident scenarios if geometrical effects are relatively unimportant. The second experiment series is intended to investigate the importance of these geometrical effects for geometries containing a few fuel pins.

These phenomenological in-core experiments are designed to study the fuel-freezing process over ranges of driving pressure and fuel temperature which have not been explored in previous ANL or French work. By using the ACRR to pulse-melt the actual reactor material, investigators can avoid two non-prototypical aspects of the ANL thermite experiments: high void fraction of the molten material, and the presence of molten metallic Mo in the thermite simulant material. The Sandia experiments will also differ from previous ANL work in the use of a fuel driving pressure which can be independently varied and which is constant in time (rather than varying continuously as in the ANL thermite experiments).

Apart from experiments using simulant materials, the other work related to the fuel freezing problem is the French program of experiments at Grenoble using the Cocotte apparatus. As reported at the Brookhaven conference on December 5-6, 1979, this work consisted of fewer than 10 experiments conducted with induction-heated UO_2 of unknown but approximately constant initial temperature. No applied driving pressure was used, and the two-atmosphere H_2 pressure required by the induction-heating apparatus complicated attempts to measure any actual driving pressure (on at least one occasion, the normal gravity flow of the UO_2 was opposed by a transient H_2 pressure). Most of the experiments were conducted using relatively short ($L/D \leq 100$) steel freezing tubes at 293 K. These experiments were also complicated by the presence of solid pieces of UO_2 in the initial part of the flow. Because of these problems, none of the French tests to date have provided applicable data. Compared

to this French work, the Sandia experiments will use a known variable driving pressure, a more precise initial fuel temperature varied over a much wider range, and much longer freezing tubes (L/D ~450).

Other unique features of these experiments are the use of upward injection of the molten fuel into the freezing tube (rather than the more customary downward or sideward injection), and the consistent use of freezing tubes with very large ratios of length L to diameter D (L/D ~450) so that freezing is measured even under conditions of large fuel penetration.

2.1.3   Progress in Experiment Design and Fabrication

Figure 2.1-2 shows a detailed preliminary layout of the experiment apparatus. Commercial components are available for most of the pressure-system components. Two possible fast-acting valves have been identified and preliminary calculations have been made of the expect pressure pulse characteristics. However, a test pressure system will be fabricated to verify pressure system operation. Orders have been placed for pressure system components. Calculations on pressure safety and heat transfer from the preheated freezing tube have been performed. A method for fabricating the long freezing tube has been worked out with the Sandia Laboratories shops. Finally, fuel temperature uniformity has been investigated preliminarily, as discussed in Section 2.1.4.

2.1.4   Fuel Temperature Uniformity

The injection of molten fuel into the test section must be done in such a way that the uncertainty in fuel temperature is significantly less than the temperature range of the test series. Otherwise, information on the sensitivity of penetration depth to temperature will not be reliable.

There are two sources of temperature uncertainty: (1) radial temperature peaking due to neutron flux depression in the fuel, (2) temperature drop due to heat transfer prior to test section entry. Flux depression can be minimized by using as low an enrichment in the fuel as is consistent with necessary energy deposition.

Figure 2.1-2   Preliminary Layout for Apparatus for Fuel Freezing Experiments

VIEW A-A

SECTION B-B

SECTION C-C

SECTION D-D

Based on calculations for the PBE test capsule, a fuel enrichment of 2.5% would yield an energy deposition of 2200 J/g, with a maximum pulse and 3/4 in. of polyethylene. This would lead to a temperature rise of 4400 K, which is more than sufficient for this program. With a fuel column diameter of 5 mm, the peak-to-average (P/A) temperature profile is 1.038. With an average fuel-temperature rise of 3000 K, this leads to a temperature peaking of 114 K at the fuel surface.

For larger fuel diameters, the temperature peaking will be higher. An approximate calculation of this effect is shown in Figure 2.1-3. Note that for a large, 10-mm diameter pellet column, the temperature peaking exceeds 300 K. Turbulent mixing of the fuel as it flows to the test section, and wall heat transfer, will sharply reduce this peaking; however, the extent of the mixing is uncertain. Therefore, pellet columns with diameters greater than about 10 mm or with high enrichments will involve additional temperature uncertainty.

Preliminary estimates indicate that mixing may reduce the peaking to less than 100 K for a 10-mm column. This is adequate if the range of test temperatures is on the order of 800 K, as planned. These energy-profile estimates are being verified by more detailed computer computation.

The temperature drop, prior to entry into the test section, is due to heat transfer to the pellet chamber wall. The leading edge of the flow is of primary interest so the temperature drop at a distance 20 cm behind the leading edge of the flow in the test section was calculated.

The most pessimistic assumption is that the urania crust on the wall flakes off, leading to a driving temperature difference for heat transfer of ~3000 K. This would lead to a temperature drop, ΔT, of

$$\Delta T = 166/D^2 ,$$

at the 20-cm point when it just enters the test section, where D is the pellet chamber diameter. This result is also plotted in Figure 2.1-3.
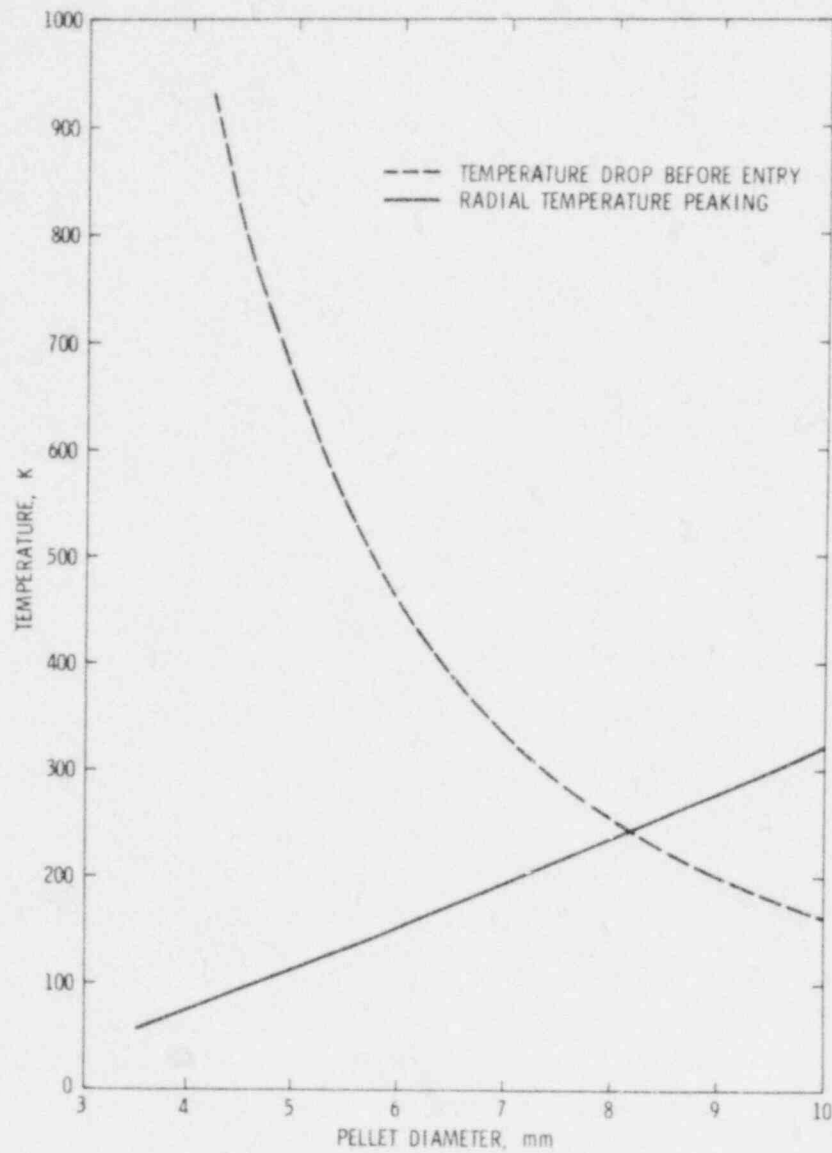
Figure 2.1-3   Plots of "Temperature Drop
Before Entry" and "Radial
Temperature Peaking"

The temperature drop for a 10-mm column is 165 K.   However, larger pellet diameters would lead to excessive temperature peaking from the flux depression. These approximate calculations employed highly pessimistic assumptions, so that the actual temperature drops are probably less significant.   More detailed calculations are underway.

2.2   Initial and Extended Fuel Motion (IEFM) (A. C. Marshall, 4423;
       J. A. Brammer, 4423; G. Randall, 4452; E. Bergeron, 4425; K. O. Reil,
       4423; W. J. Whitfield, 4453; D. J. Sasmor, 4453; W. H. Sullivan, 4426;
       S. A. Wright, 4426; W. Trebilcock, 4424; M. Aker, 4452; R. W. Ostensen,
       4425)

2.2.1 Introduction

Phenomenological investigations are being conducted in transient overpower
(TOP), loss-of-flow (LOF), and LOF-driven-TOP advanced reactor accident sequences.
To support accident analysis, detailed phenomena associated with core disruption must
be identified and modeled. These phenomena include fuel motion inside the clad prior
to failure, axial fuel failure location, mode of cladding failure, fuel disruption modes,
rate of dispersal, fuel plateout, and extended fuel motion into the blanket (potential for
blockage).

Current activities in the program are directed toward planning for preirradiated
fuel tests of up to 19 pins in the ACRR and participation in the NRC international ex-
change program on CABRI through preanalysis of A and B series tests (TOP and LOF-
driven-TOP respectively) with single-pin geometries.

Some reactor safety tests that involve larger bundle sizes and full length pins
may be required. Facilities in which to conduct these tests are, therefore, being
evaluated on a continuous basis. Work on LOF and TOP accidents has been done in
the DOE program at TREAT and will continue in the TREAT Upgrade. The Sandia
program will be coordinated with the DOE program in order to take the maximum ad-
vantage of the available data.

The tests being planned for the ACRR will require an in-pile flowing sodium
system, high power operating modes in the reactor, preirradiated fuel, hot-fuel
handling facilities, and a high resolution fuel-motion-diagnostics system. The fuel
motion diagnostic system has been completed and installed in the ACRR tank. The
capability of the ACRR to operate in high power modes has been established. Work
on the design and development of a flowing-sodium system is continuing.

2.2.2 Test Definition

A preliminary document has been written to provide a test definition for the first test planned for the IEFM program. Phase I IEFM tests have been re-evaluated to clearly separate the demonstration tests from the experiments which will attempt to resolve safety issues. The Phase I IEFM tests are now divided into two parts, A and B.

Part A: Demonstration Tests-Fresh Fuel

1. L/D-1 -- This test will be used to determine the timing of the sodium boiling/voiding du.. ng a flow-coastdown in the flow velocity. With this information, the timing of the power ramp for the next test will be determined. L/D-1 will also provide general experience with the sodium loop under actual test conditions prior to the use of preirradiated fuel.

2. L/D-2 -- This test will simulate a LOF-driven-TOP accident. It will duplicate a preirradiated fuel test which will be performed in Part B of Phase I.

Part B: Issue Oriented Experiments

1. IEFM/PBE -- This fresh fuel test will investigate the FCI issue for a PBE under flowing sodium conditions.

2. IEFM/LT-1 -- This test will investigate the fuel-failure location for preirradiated fuel under LOF-driven-TOP conditions.

In the following paragraphs, the rationale, general approach, and fundamental test requirements for the first Phase I test (L/D-1) will be discussed. Detailed test requirements have been established but are not part of this report.

2.2.2.1 Rationale -- An accident has been hypothesized for an LMFBR in which the sodium coolant flow has been interrupted due to a pump outage with a failure to SCRAM. This loss-of-flow (LOF) accident causes the fuel pins to overheat from loss of forced coolant flow. The pins in the high power regions of the core will overheat first. The sodium coolant in these regions also will exceed normal allowable operating temperatures resulting in boiling followed by complete or partial voiding of

the coolant channel. Following voiding, the cladding in these regions will melt and the fuel pin will disrupt. Although this phase of the accident is important in itself, and will be investigated later in the IEFM program, the accident may lead to another phase which can cause potentially more serious consequences. The voiding of the sodium from the coolant channel and other effects, such as the slumping of fuel and loss of cladding, can result in the addition of significant positive reactivity. This reactivity addition increases the core power and can cause a rapid temperature rise in the moderate power regions leading to fuel pin failure in these regions. This phase of the accident is called a Loss-of-Flow driven Transient-Overpower (LOF-d-TOP). Depending on the axial location of the pin failure (and other effects not discussed here) the failure may or may not result in a much larger positive reactivity addition. This large additional reactivity insertion can bring about an energetic failure in the low power regions with significant work potential.

The location of the fuel failure during a LOF-d-TOP accident is an important issue. Since the possibility of this type of accident occurring in "fresh fuel" is very small and since there are basic phenomenological differences between fresh and pre-irradiated fuel, during this accident, one of the ultimate goals of the Phase I IEFM program is to determine the failure location during a LOF-d-TOP in preirradiated fuel (IEFM/LT-1). Because of the additional complications arising from the use of mixed oxide preirradiated fuel, experience will be gained with fresh fuel tests before attempting experiments with preirradiated fuel; consequently, a fresh fuel LOF-d-TOP test will be performed during Part A of Phase 1 (L/D-2).

Depending on the dynamics of the accident the LOF-d-TOP failure can occur in a voided or unvoided region. A test will be performed to clearly determine the time-to-boiling before a LOF-d-TOP test can be performed, even for fresh fuel (L/D-1). These results will be compared with calculational predictions for this test. Obviously, two tests are required for Part A of Phase I. These two tests are:

L/D-1 -- A flow coast down at approximately constant power (no ramp) to determine the time to boiling/voiding of sodium, using fresh fuel.

L/D-2 -- A flow coast down with a power ramp (LOF-d-TOP) prior to sodium boiling, using fresh fuel.

2.2.2.2 <u>General Approach to L/D-1</u> -- A PFR-type fresh fuel pin will be used in the flowing sodium loop. Resistance heaters will maintain correct sodium temperatures. Sodium flow will be initiated by a solenoid valve in the high pressure gas line to the sodium supply tank. When the flow conditions are obtained, the ACRE power transient will be initiated. The power transient will simulate nominal operating power, in the PFR-type LMFBR fuel pin. Concurrent with the power transient, a flow coast down will be initiated. After a period of time, the sodium in the test channel will boil and the test pin will disrupt. Pressure, flow, and temperature instrumentation will determine the time to sodium boiling. The choice of flow conditions, pin type, etc, is determined by requirements for later LOF-d-TOP tests. Except for a power excursion during the flow coast down, this test must match the LOF-d-TOP test conditions to assure that the timing for the boiling event will be the same for both tests.

2.2.2.3 <u>Test and Design Requirements</u> -- The fundamental test requirements for L/D-1 are

     a. Fuel pin reasonably prototypic of CRBR design,

     b. Prototypic time-dependent temperature profiles in the pin and sodium.

     c. Prototypic sodium pressure in the test section,

     d. Diagnostics to determine the timing of sodium boiling and voiding.

Although Phase I tests use CRBR as an illustrative design, later tests will ultimately be directed at future fuel pin designs as they evolve in the U.S. program.

The L/D-1 test requirements imply that several loop design requirements must be determined. These are

     a. Fuel pin design

     b. Mass flow rate

     c. Flow area

     d. Test train design

     e. Tubing inertial length

     f. Maximum pressure requirements for tubing and sodium supply
        and receiver tanks

     g. Maximum temperature for tubing and sodium supply and receiver
        tanks

h. Supply pressure

i. Hydraulic diameters

j. Reactor power history

k. Axial power profile in pin

l. Sodium purity

m. Maximum pressure for gas supply

n. Sodium supply volume

o. Maximum containment pressure

p. Handling fixture

q. Trace heaters

r. Containment temperatures

s. Meltdown ring

t. Valve regulator and controller

u. Pin mount

v. Lead shield

w. Piping thermal stress

x. Sodium fill system

Beside the fundamental diagnostic requirement for this test, that of measuring the time to sodium boiling, there are a number of additional diagnostic requirements. These are necessary to operate the loop, test the functioning of other instrumentation, provide information of secondary importance, and provide experience for later experiments. The diagnostic requirements are determined for the following instrumentation:

a. Gas supply pressure transducers

b. Sodium supply and receiver tanks pressure transducers

c. Sodium pressure transducer for test section

d. Primary containment pressure transducer

e. Sodium flowmeters for test section

f. Thermocouples for test section

g. Thermocouples for sodium supply and receiver tanks

h. Thermocouples for external sodium system

i. Environmental thermocouples

j. Gas supply thermocouples

k. Sodium level detectors

l. Sodium void detectors

m. In-core fuel motion detectors

n. Acoustic detectors

o. Coded aperture imaging system

p. Loop control system

The actual design and diagnostic requirements will be reported in topical IEFM reports.

2.2.3 Out-of-Pile Sodium Loop Design

A preliminary design effort has begun for the out-of-pile loop. As presently conceived the out-of-pile loop will resemble the in-pile loop; i.e., the physical dimensions will be approximately the same. The out-of-pile loop will aid in the prediction of the actual thermal-hydraulic conditions that will be obtained with the in-pile loop. The out-of-pile loop will also provide a test bed for instrumentation. In addition, some manufacturing and design problems that apply to the in-pile loop may be uncovered in the out-of-pile loop design. Clearly, timely completion and testing of the out-of-pile loop will aid in the design of the in-pile loop.

The out-of-pile loop will not have the same constraints as the in-pile loop, since no nuclear fuel testing will be done with this loop. Consequently, the materials requirements, tolerances, and other rigid requirements needed for the in-pile loop will not be required for the out-of-pile loop.

A flexible design is appropriate for the out-of-pile loop to examine various component designs and instrumentation. Although a convenient "bread board" arrangement will probably be used, the design should permit the insertion of the out-of-pile loop components into a simulated containment and a simulated experiment loading tube to determine the heat losses through containment, and the insulation requirements.

2.2.4 Loop Control System

A loop control system will be required to operate the out-of-pile and the in-pile flowing sodium loops and to obtain data from loop instrumentation. The instrumentation and control requirements for the loop have been reviewed. The required instrumentation and signal-processing electronics have been identified and a literature search was conducted. With the possible exception of the pressure transducers, most of the required electronics are commercially available. The system controller for the out-of-pile tests will probably be an analog type. The input, output, and control parameters for this system are being defined at this time.

2.2.5 Fuel Handling Modifications

As described in the previous quarterly report, some modifications to the hot cell will be required accommodate the in-pile loop. The modifications include

a. Coring a 3-ft diameter hole in the roof between the steel containment boxes and the large hydraulic doors in Room 2A. This hole will allow movement of the sodium loop assembly between a cask and the hot cell.

b. Strengthening the roof structure to support the weight of a 25-ton cask which will contain the loop assembly with preirradiated pins when not in the ACRR or hot cell area.

A work order has been placed with Plant Engineering for these modifications.

2.2.6 CABRI Calorimeter Experiment

During November 1979, a Sandia staff member visited the French Nuclear Research Center, Cadarache, to discuss the CABRI calorimeter project. This trip was necessary to brief the new French project leader on Sandia's participation in the project and to make final preparations for the experiments. The new project leader

is Pierre Rongier who was recently assigned to this task to replace M. Schwarz. During the discussions, the goals and purposes of the calorimeter experiments were defined, the detailed characteristics of the Sandia-provided detectors were described, the methods of interfacing these detectors in the CABRI loop were specified, and a schedule for the final preparation of the loop and performing the experiments was outlined. At the conclusion of these discussions a series of action items was proposed which when carried out would aid in the successful completion of the CABRI calibration experiments.

Table 2-I gives a brief outline of the major topics covered in the discussions. These topics are described in more detail in the previous two quarterly reports.[2-1, -2] Table 2-II gives the proposed schedule and Table 2-III lists the action items to be performed by Sandia and the Commisariat Energie Atomique (CEA).

In addition to carrying out these discussions, two tasks were performed at Sandia which partially complete some of the action items mentioned in Table 2-III. First, an export license for shipping the detectors to France was applied for. No problems were foreseen in obtaining this permit in time for shipment, according to the schedule. Second, five fission thermocouple detectors and five gamma thermocouple detectors were fabricated at Sandia. These detectors will be calibrated in the SPR-III during the first week of January 1980.

Table 2-I

Topics Covered in Technical Discussions for the CABRI
Calorimeter Experiments

Goals and Purpose of CABRI Calorimeter Tests (in order of importance):

- Determine the coupling factor between various reactor
  power monitors and the test pin

- Determine the linearity of reactor power monitors under
  transient conditions

- Determine the ratio of the neutron and gamma heating in
  the test pin

- Determine time-dependent axial energy distribution in the
  test pin

Fission and Gamma Thermocouple Detectors, and Fission Chambers:

- Design of detectors

- Neutron and gamma sensitivity of detectors in CABRI

- Electrical termination of detectors for the data acquisition
  system

- Power supplies for the fission chambers

Interface of Detectors into CABRI Loop:

- Method of mounting detectors

- Detector location in CABRI loop

- Penetration of cables through the loop and seals

- Electrical connection to detectors

Table 2-II

Schedule for the CABRI Calorimeter Experiments

January 31   -   Status of the CABRI reactor will be known and the
decision of which schedule (the accelerated or de-
layed schedule) will be made.*

January 31   -   Sandia sends the detectors to France.

January 31   -   Calorimeter is delivered.

February 1   -   Begin assembling the Test Loop Stringer.

April 30   -   Complete assembly of Stringer.

May 1-30   -   Calorimeter experiment.

June 1   -   Shut down CABRI for change of loop.

---

*Depending on the state of repair for the CABRI reactor and the
hodoscope, two schedules for performing the calorimeter experi-
ments and the AJ1 tests are proposed. These schedules are
outlined in the CABRI Project Report, August-Spetember 1979.

Table 2-III

Action Items Proposed for the CABRI Calorimeter Experiments

Action 1   (Sandia) Sandia completes calibration of detectors by early January 1980

Action 2   (Sandia) Sandia sends detectors to Cadarache by January 31, 1980. (The
major obstacle to this is getting DOE permission to send fissile material.)

Action 3   (Sandia) Sandia writes a CABRI note describing the results of the detector
calibration experiment and describes the data analysis and interpretation
of the Sandia detector responses (March 30, 1980).

Action 4   (CEA) Rongier sends a rough draft of the detailed CABRI calorimeter ex-
periment plan to Wright (Sandia) (February 1980).

Action 5   (Sandia) Wright returns the experiment plan with comments and sugges-
tions. The program will be distributed at the end of March 1980.

Action 6   (CEA) Rongier and Kussmaul write a CABRI note describing data analysis
and interpretation of the CABRI calorimeter data. Specifically, how to
generalize the results from the 1.1% enriched calorimeter to the 20%
enriched test pins taking into account the new loop which will be used in
the future experiments (March 1980).

2.3 Fuel Motion Detection (S. A. Wright, 4426)

The seven-pin gross fuel motion detection experiments were planned for early October this quarter. However, due to SPR-III scheduling considerations, the experiments will be postponed until January 1980. Consequently, the majority of the effort this quarter was focused on fabricating detectors for the French CABRI calorimeter experiments, (Section 2.2). However, during this quarter efforts also continued in producing detectors to meet the fuel motion monitoring needs of Sandia experiments.

The detector fabrication and testing effort focuses mainly on building self-powered detectors which have an angular sensitivity to either fast neutrons or gamma rays. The aim of this task is to develop a detector with a lower sensitivity to background and an enhanced sensitivity to fuel motion. Considerable progress has already been achieved since a detector has been fabricated which has a near zero sensitivity to background (provided the background flux is isotropic) and a strong sensitivity to the anisotropic flux coming from the test section. For these detectors to be useful for fuel motion, the radiation-response cross section of the detector must be determined, i.e., the fast, thermal, and gamma sensitivity of the detector. Experiments will be performed next quarter to determine these sensitivities.

The detectors are fabricated using thick-film hybrid-microcircuit electronic techniques. The detectors are extremely easy to fabricate, are inexpensive, and have the potential for very high temperature operation since the fabrication procedure requires firing the detectors at 1223 K (950°C) for several hours.

Once the detectors have been shown to give output currents proportional to the induced radiation and the sensitivity of the detectors to the various types of radiation has been identified, a patent will be applied for.

References for Section 2

2-1   Advanced Reactor Safety Research Quarterly Report, April-June 1979,
      SAND79-1597, NUREG/CR-0984 (Albuquerque, NM: Sandia Laboratories,
      Advanced Reactor Research Department, November 1979).

2-2   Advanced Reactor Safety Research Quarterly Report, July-September 1979,
      SAND79-2158, NUREG/CR-1141 (Albuquerque, NM: Sandia Laboratories,
      Advanced Reactor Research Department, April 1980).

3. CORE DEBRIS BEHAVIOR - INHERENT RETENTION

3.1 <u>Molten Core Containment</u> (D. A. Powers, 4422; R. H. Marion, 4422;
W. Luth, 5541; T. Y. Chu, 1537; J. F. Muir, 4441; T. Bartel, 4441)

3.1.1 Introduction

The Molten Core Containment program is an experimental and analytical effort
to identify and quantify the safety-related processes that could occur during interaction
of core debris with nuclear-reactor containment structures. The experimental program
involves the interaction of prototypic core materials at realistic temperatures with struc-
tures representative of those found in existing and planned nuclear reactors. The program
emphasizes the generic aspects of the interactions. Results of the program are useful
in the analysis of light-water and gas-cooled reactors as well as LMFBRs during acci-
dent situations.

The initial thrust of the program was the investigation of molten core-debris
interactions with various types of concrete and steel liners. These studies established
that melt/concrete interactions are quite vigorous. The generation of gases by thermal
decomposition of the concrete is a dominant process during the interaction. The rapid
erosion of concrete and the generation of gas continues even after the core materials
have solidified. Recently, experimental efforts in this program have been redirected
toward the study of solidified debris with concrete and the study of molten core debris
with candidate materials that would be more suitable than concrete for the retention of
molten core materials. Candidate materials being examined in this program are
magnesia, firebrick high alumina cement, and borax.

Phenomenological models developed from the experimental results of this
program will be of use in the analysis of the structural integrity of reactor contain-
ments during severe accident situations. These phenomenological models will be
incorporated in the containment analysis program.

3.1.2 Code Comparison Tests

Computer codes purporting to describe the interaction of high temperature melts with concrete have begun to proliferate. Some of the computer models of melt/concrete interactions are

> CORCON (Sandia)
> WECHSL (KfK/PNS)
> INTER (Sandia)
> BETON (KWU)
> KAVERN (KWU)
> GROWS II (ANL)

These codes have been independently developed. The development has reached sufficient maturity that comparison of the various approaches to modeling the melt interaction would be profitable.

To this end, investigators at Projekt Nucleare Sicherheit of the Kernforschungszentrum at Karlsruhe, FDR and Sandia agreed that tests appropriate for code prediction be run. Two of these tests have now been conducted at Sandia using the experimental procedure developed during the COIL series tests.[3-1, 3-2] About 200 kg of molten stainless steel at 1973 ± 10 K ($1700 \pm 10^{\circ}$C) was teemed into a concrete crucible. The crucible was a cylindrical block with a coaxial cylindrical cavity 38 cm deep and 38 cm in diameter. Induction coils embedded in the concrete allowed continued heat input to the melt once it was in the concrete crucible.

Concrete used for these code comparison tests was the so-called Clinch River limestone concrete. The chemical composition of the concrete is listed in Table 3-I. The Clinch River limestone concrete was made with calcareous large and small aggregate and crushed limestone as sand. Consequently, the concrete was quite heavily laden with substances that will evolve gases when heated. Weight losses upon heating the concrete were 4.3 w/o H_2O and 35.7 w/o CO_2. The solid product of the thermal destruction of concrete is principally CaO. Since the concrete contains little silica or other species that might combine with the CaO to yield low melting liquids, the Clinch River limestone concrete is quite refractory if its high gas generation potential is neglected. The melting range of this material was estimated to be about 1723 to 1923 K (1450 to 1650°C).

Table 3-I

Chemical Composition of Concrete Used in the
Code Comparison Tests

Species	Weight %
Fe_2O_3	1.2
Cr_2O_3	0.004
MnO	0.01
TiO_2	0.12
K_2O	0.68
Na_2O	0.08
CaO	45.4
MgO	5.67
SiO_2	3.6
Al_2O_3	1.6
CO_2	35.7
H_2O	4.1

Once the melt was within the crucible cavity and induction power was supplied to the melt, an instrumentation tower was lowered over the crucible. The instrumentation tower channeled heat, gases, and aerosols produced by the interaction so that they could be quantitatively monitored.

In the first of the code comparison tests (CC-1) the melt mass was about 204 kg. In the second test (CC-2) the melt mass was about 206 kg. The melts in the two tests were sustained with inductive power for 60 and 87 minutes, respectively.

The nominal electrical power supplied to the melts in both tests was 120 kW. Losses occurred between the power supply and the melt due to stray radiation and Joule heating of the power conduits. These losses were estimated by measuring the temperature rise in the coolant from inlet to outlet. The coolant was a 50% mixture of ethylene glycol in water. Figure 3.1-1 shows heat capacity and density data for the coolant mixture as functions of temperature. Coolant flowed through the embedded coils at the rate of 284 cm^3/s.
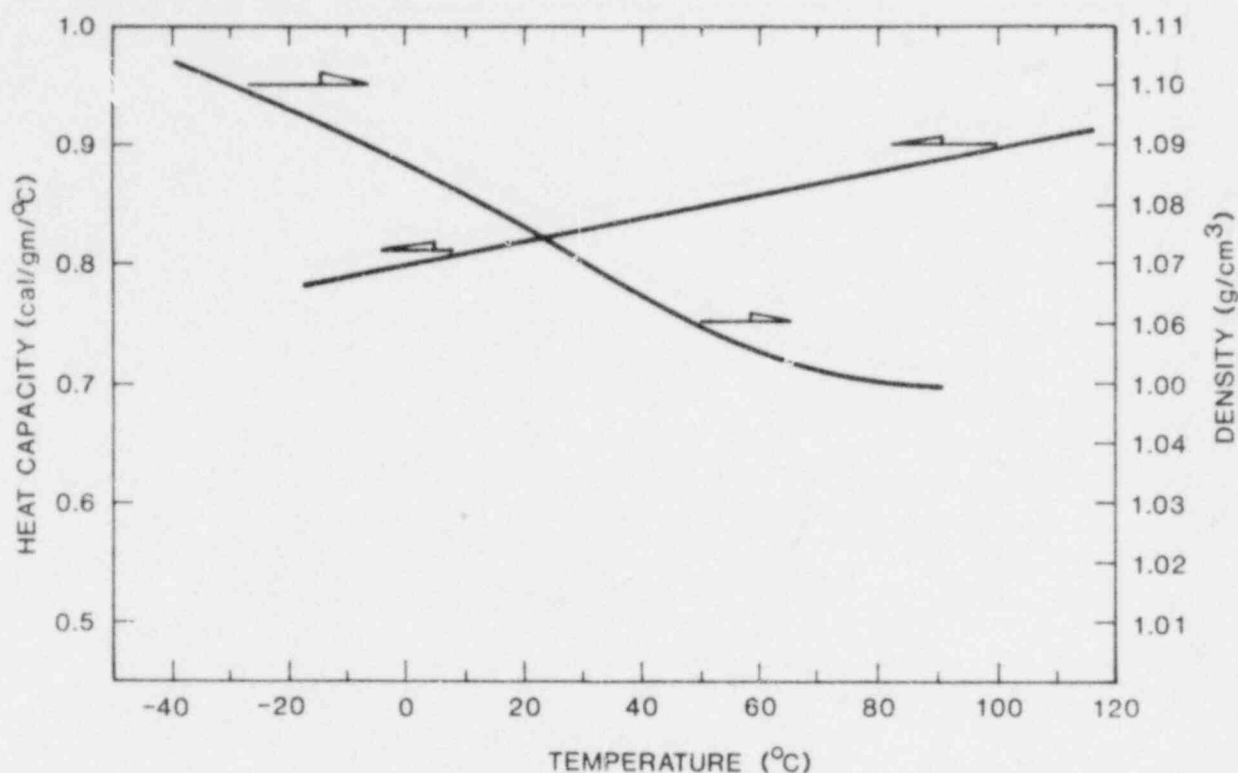
Figure 3.1-1   Heat Capacity and Density of a 50% Aqueous
Ethylene Glycol Solution

The supply of inductive power to the melt was not continuous.   Whenever it was necessary to measure the temperature of the melt with immersion thermocouples, the instrumentation tower was raised, power to the melt was shut off, and the measurements made.   The power was then restored and the instrumentation tower was brought back into place.

The net power supplied to the melt is shown in Figures 3.1-2 and 3.1-3 for Tests CC-1 and CC-2, respectively.   The sharp drops in the power input to the melts during temperature measurements are distinctly visible in these power versus time plots.   The two curves are amazingly similar, indicating the reproducibility of results from the two tests.

For both tests the input power versus time curves show distinctly higher coil efficiencies at the beginning of the tests.   Power-input efficiencies drop smoothly with time to constant values of 81 and 80 kW for CC-1 and CC-2, respectively.   These asymptotic values for the net input indicate a coil efficiency of about 67%.
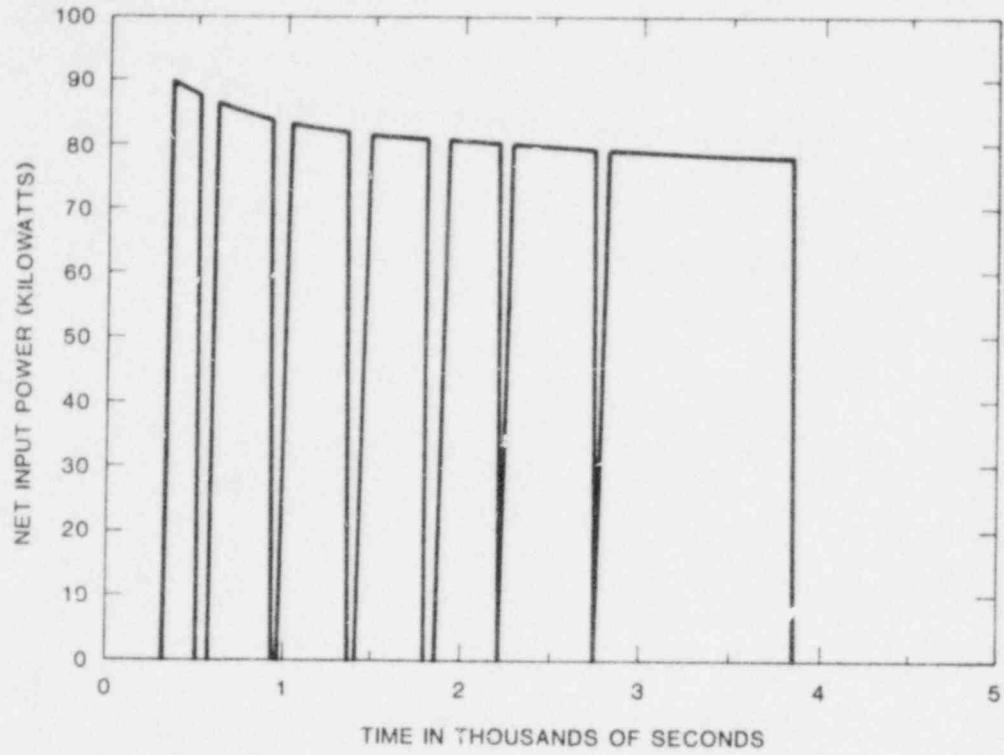
Figure 3.1-2   Net Input Power History for Test CC-1
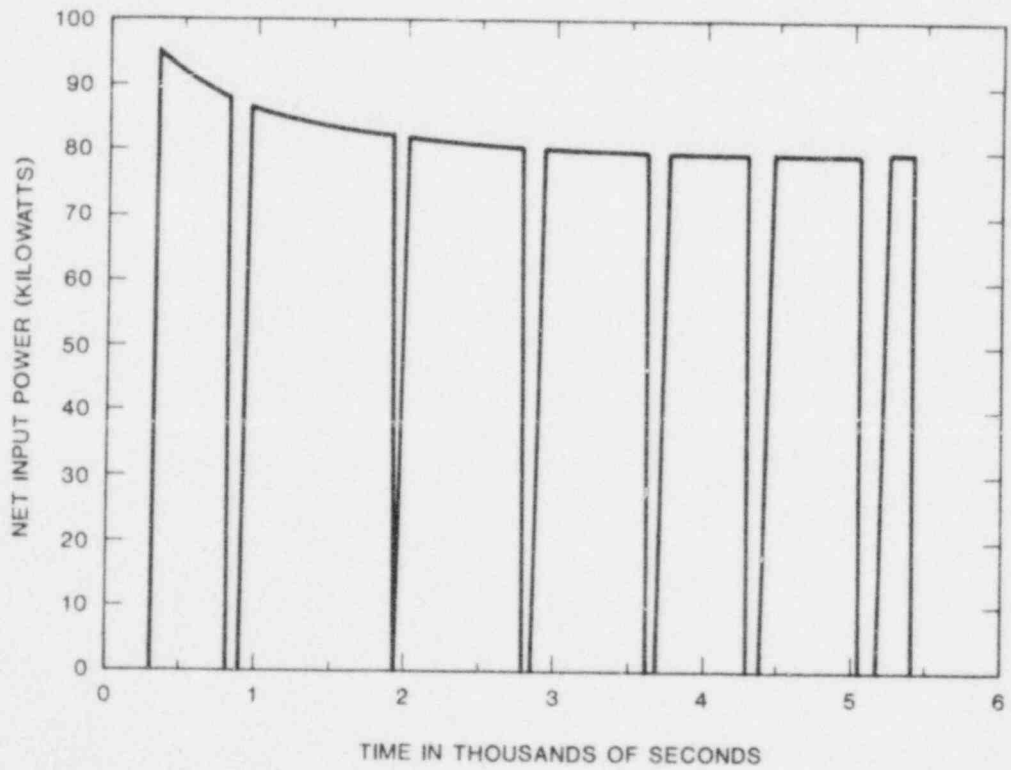
Figure 3.1-3   Net Input Power History for Test CC-2

The higher efficiency with which inductive power is supplied to the melt at early times is not fully understood. The power supplied to the melt is in reality net input power. Because the cooled induction coils are embedded in the concrete, they begin to withdraw heat conducted from the melt through the concrete. At late times in the tests, the temperature rise observed in the coolant is the result of electrical heating of the conduits and heat extracted from the concrete. The additional heat extracted from the concrete may be responsible for an apparent loss of coil efficiency with time.

None of the computer models of the melt/concrete interactions is complete. Consequently, the comparison of the effectiveness of the codes in predicting test results will be restricted to these five topics:

a. Times of crust formation over the melt

b. Temperatures within the concrete

c. Rate of concrete erosion

d. Extent of oxidation of the melt

e. Temperatures of the melt.

Whenever the melts in the code comparison were exposed for temperature measurements, they were visually examined for crust formation. No crusts were observed when the melts first came into view during these temperature measurement operations. However, as the operations progressed, some scum formation could be seen. Crusting may have been starting at the perimeters of the melt. Investigators currently do not know whether the first signs of crust formation were caused by additional heat losses from the melt when the instrumentation tower was raised or by the discontinuance of power to the melt.

More definitive data were obtained for the other elements of code comparison. To measure temperatures within the concrete, each crucible was equipped with 12 thermocouples arrayed about the sides and below the bottom of the crucible cavity. The thermocouples were located at three stations placed at points 120° apart around the cavity's periphery. Within the stations, the junctions of the thermocouples were placed at elevations of 0, 11.4, and 22.9 cm from the bottom of the crucible cavity. The thermocouple junctions were separated from the original cavity walls by 2.5, 3.8, and 5 cm. Thermocouples below the cavity bottom were positioned in two

stations. One station consisted of a 10-cm diameter ring of equally spaced thermo-couples centered on the axis of the cavity. The second station consisted of a 150° arc of equally spaced thermocouples located 13.3 cm from the axis of the cavity. On each station, the first thermocouple was located 1.3 cm from the original cavity surface. The other thermocouples were fixed at intervals of 1.3 cm from the first and each succeeding thermocouple.

The thermocouples were all stainless-steel sheathed, MgO-insulated, Type K sensors, 0.16 cm in diameter. The accuracy of their locations relative to the original cavity surfaces is estimated to have been about ± 0.2 cm. Nearly all the thermocouples functioned in the tests. Data were taken from the sensors at about 4-s intervals.

The thermocouples were also used to detect erosion of the concrete. The density of temperature sensors in the concrete allow erosion data to be presented as the propagation of isotherms. Either the 673 K (400°C) or the 1573 K (1300°C) iso-therm may be used as required by the models.

Melt-temperature data obtained with immersion thermocouples were of high quality. The data from each test showed a consistent trend with little scatter. The trends for the two tests were in surprisingly good agreement. Agreement among data obtained in the two tests was observed frequently. This suggests the duration of sus-tained melt interaction with the concrete was the only significant variable in Tests CC-1 and CC-2.

Data on the extent to which the stainless steel melt was oxidized by the gases liberated from the concrete will be obtained by weighing and chemically analyzing the solidified material. Previous examinations of this type and consideration of the thermo-dynamics of reaction suggest that chromium will be found to have preferentially oxidized during the interaction. Data to confirm this have not yet been obtained.

Apparently the two tests yielded the quality, reproducible data necessary for the code comparison tests.

In addition to the data to be used for the code comparison effort, data on a variety of other phenomena associated with the melt/concrete interaction were col-lected. These phenomena include

a. Concrete cracking

b. Moisture migration in the concrete

c. Upward heat flux from the melt

d. Gas generation rate

e. Aerosol generation rate

f. Gas composition

g. Aerosol particle size distribution and composition.

The displacement-gauge technique described previously[3-3] was used to monitor crack-
ing in the concrete. Unfortunately, not one single crack passed between the brackets
used to mount the displacement gauges. The onset of cracking was detected as a com-
pression of the concrete between the brackets. The extent of the cracking could be
determined only by posttest examinations.

Moisture migration in the concrete was detected by an experimental sensor
station consisting of a thermocouple, a stainless steel pipe extending out of the con-
crete to a pressure transducer, and a four-point electrical conductivity sensor.
Three sensor stations of this type were located below the cavity on the axis of the
crucible. Rather good data were obtained from the pressure transducers and the
thermocouples. The four-point electrical conductivity gauge yielded data that are
not readily suitable to interpretation. Recent observations indicate that decomposing
hydrates yield a thermoelectric signal.[3-4] If this effect occurs in concrete, an addi-
tional complication in interpreting the data would be present.

Gas samples were collected during the tests and yielded useful gas composi-
tions. An attempt was also made to obtain real time gas composition data by passing
sample gas through an infrared spectrometer. Persistent instability of this device
may have prevented collection of any useful information. These data are still being
examined.

The rate of gas generation was monitored by the pressure drop through the
instrumentation tower, a pitot-static device mounted in the flow path, and a turbine
flow meter. These three sensors did not give consistent results. At best they yield
a bound on the flow. During the test, gas flow was noted to increase sharply whenever

the instrumentation tower was raised. This is attributed to formation of a flue when the seal between the tower and the concrete was broken. The in-rush of air, as the evolved gases burned, also contributed to the heightened gas flow.

Upward heat flux from the melt was monitored by two gauges. One gauge was mounted with its sensing surface pointed toward the melt. This gauge would then respond to both the convective and the radiative portions of the upward heat flux. The second gauge was mounted with its surface perpendicular to the surface of the melt and could respond only to the convective contributions to the upward heat flux.

Each gauge consisted of a nickel sensor equipped with a type K thermocouple. The nickel sensors weighed about 16.35 g. The central sensor is fixed by three pointed set screws in a stainless steel guard ring. This entire assembly is mounted in a stainless steel can and packed with fibrous insulation.

The calibration curve obtained for the devices is shown in Figure 3.1-4.
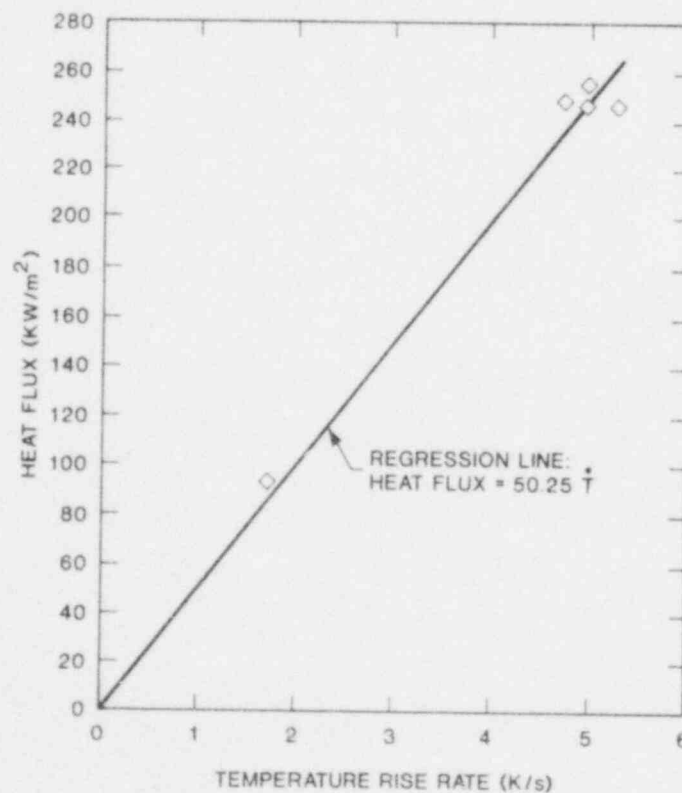
Figure 3.1-4 Upward Heat Flux Transducer
Calibration Data

Aerosols were detected by decreases in optical transmission and by the scattering of light. Both incandescent and coherent light were used. The data produced by these methods were not easily interpreted. The transmission pathways may have been too large for the aerosol concentrations encountered in the tests.

3.1.3 Test of High Alumina Cement

A test of molten steel interaction with high alumina cement was also conducted during this report period. The test repeated Test HAC-1[3-5] which was prematurely terminated due to malfunction of the power supply. The experimental procedures used in this repeat test were similar to those described for the code comparison tests. Melt interaction was sustained for over 2 hr.

Little data from the test have been examined as yet. The melt temperatures obtained with immersion thermocouples are shown in Figure 3.1-5.
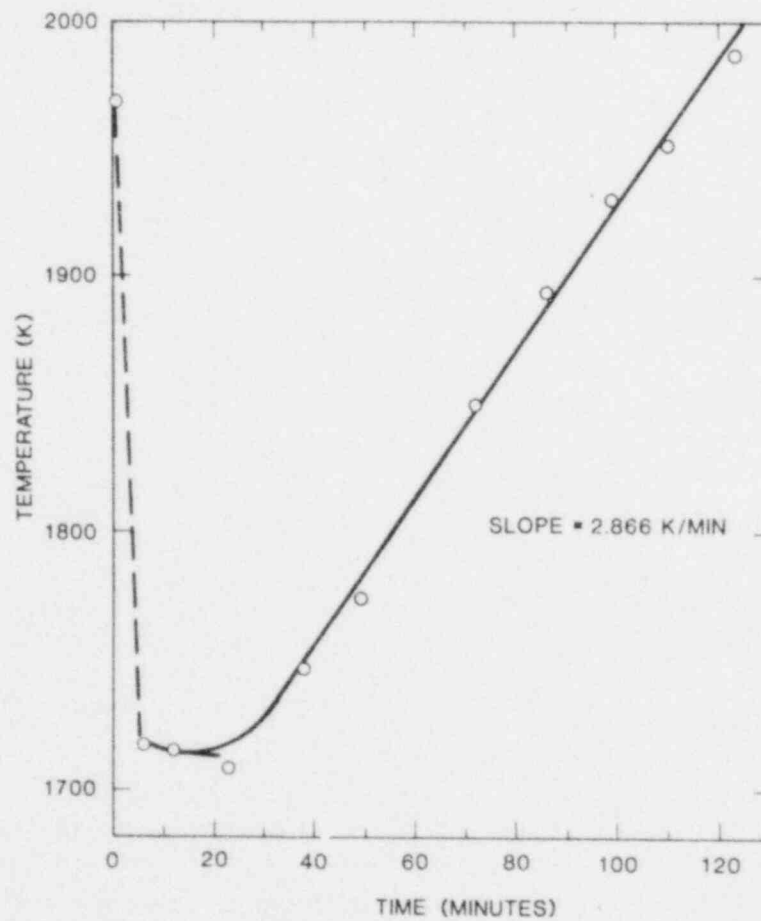
Figure 3.1-5   Melt Temperature History Test HAC-2

The heat flux gauges responded well during the early stages of the tests. There were distinct differences in the responses of the gauges oriented parallel and perpendicular to the melt. However, once the heat flux gauges reached some high temperature, losses began to balance the flux to the gauge and no further data were obtained since these devices yield useful data only by indicating changes in temperature.

Aerosols were collected with two cascade impactors. Care was taken to assure that the loading on each stage of the impactors was kept low so that accurate particle-size distributions could be obtained. Raw aerosol data from the impactors are listed in Table 3-II. Visual inspection of the aerosol suggested there was a qualitative change in the aerosol over the course of the tests.

Table 3-II

Raw Aerosol Data From Test With High Alumina Cement

Sampler Stage	Weight of Sample (g)	Description
Sampler A		
1	0.00129	tan
2	0.00259	tan
3	0.00535	tan and brown
4	0.00644	tan and brown
5	0.00794	tan with white center
6	0.01444	brown
7	0.01712	brown
Sampler B		
1	0.00163	May be contaminated with rubber from "O" rings
2	0.00121	
3	0.00064	
4	0.00070	Touch of white dust
5	0.00033	tan; some brown
6	0.00044	tan
7	0.00058	gray

3.1.4 Large Scale Melt Facility

During this reporting period, installation of the large-melt facility was essentially completed (estimated 90%). In January, the facility will be ready for shakedown experiments. The rest of the next quarter will be devoted to the shake-down tests for the furnace.

Sandia staff members are preparing an experiment on tapping the crucible using a simulant to represent the oxide. In this experiment, an aluminum container filled with lead will be heated to approximately 773 K (500°C) and will be tapped by the shotgun assembly. Aluminum at 783 K (950°F) has approximately the same strength as the Ta 10-W crucible at 3000 K and the molten lead has about the same density as UO_2. The aluminum container and the associated heaters were all fabricated during this reporting period.

The oxide crucible was completed and shipped to Sandia. The crucible contains 211.8 kg of oxide charge.

3.2　　PAHR Debris Bed (J. E. Gronager, 4421; G. W. Mitchell, 4421; R. J. Lipinski, 4425; R. W. Ostensen, 4425)

3.2.1　Introduction

The PAHR debris bed program addresses issues concerned with the formation of solid fuel debris and its collection on horizontal surfaces within the containment vessel. This debris remains capable of generating significant power through the decay of fission products. Should natural processes fail to provide sufficient cooling, the debris could remelt and threaten containment. The PAHR debris bed program seeks to determine the natural cooling of such debris. Four major first-of-a-kind in-pile experiments have been performed at Sandia and have provided significant (and unexpected) data for modeling the behavior of debris bed.

During this period, experiments and analysis of debris bed studies continued.

3.2.2　Debris Bed Experiment D-4

The D-4 experiment is the fourth in a series of experiments designed to provide quantitative information on the behavior of debris beds formed from reactor materials following a core-melt accident.

The principle objectives of the D-4 experiment were

a. To determine the incipient dryout heat flux for two levels of sodium subcooling, large subcooling (460 K) and small subcooling (190 K),

b. To investigate the possible repeatability of the dryout heat fluxes,

c. To investigate bed characteristics at heat fluxes above incipient dryout (postdryout),

d. To evaluate the performance of ultrasonic thermometry for debris bed experiments.

The apparatus package used in D-4 was similar to the D-1, D-2, and D-3 equipment. The D-4 experiment section, 1.5 m long and 0.23 m in diameter, consisted of the debris bed vessel, a helium heat exchanger, support structure, insulation, and instrumentation. The debris bed vessel, 0.5 m long, 0.102 m inside diameter, contained the debris bed of 3.65 kg fully-enriched UO_2 particulate, 2.27 kg sodium and a plenum for inert cover gas. The vessel consisted of two sections: (1) the

lower section, which contained the UO_2 debris bed with an external, high temperature insulating boundary, and (2) an upper section which was a heat exchanger, providing the cooling of the sodium plenum above the bed. The debris bed parameters are outlined in Table 3-III.

Table 3-III

Debris Bed Dryout Transients

Dryout No.	Max Bed Temp (K)	Na Temp (K)	Reactor Power (kW)	Bed Power (kW)	Heat Flux (kW/m^2)	Specific Power (MW/m^3)
1	1083	573	275	2.95 ± .23	367.3	4.45
2	1073	573	275	3.44 ± .2	427.6	5.18
3	1153	573	300	3.54 ± .17	440.8	5.34
4	1163	573	300	3.95 ± .38	490	5.94
5	1283	573	320	4.09 ± .41	508.9	6.17
6	1098	873	1170	16.07 ± .19	1997	24.2
7	1165	873	1155	15.8	1962	23.8
8	1180	873	1171	15.8	1962	23.8
9	1113	873	1110	15.38 ± .7	1911	23.2
10	1198	873	1145	15.9 ± .28	1984	24.0
11	1333	873	1172	15.6 ± .5	1938	23.5

3.2.2.1 Preliminary Results From D-4 -- The results presented here constitute a preliminary review of the D-4 data. During the performance of D-4 in September, over 60 hr of continuous operation were logged. The objectives of the experiment were satisfied and additional debris bed phenomena were identified. Each of the objectives will be separately addressed.

3.2.2.1.1 Incipient Dryout Heat Fluxes -- For the large sodium-subcooled case (460 K), the incipient dryout occurred at a heat flux of 367.3 kW/m^2. The small sodium-subcooled case (190 K) reached incipient dryout with a heat flux of 1971 kW/m^2.

3.2.2.1.2 Postdryout Bed Characteristics -- For each case of sodium subcooling, several dryout transients were observed at power levels above the incipient dryout level (postdryout). Table 3-III summarizes all the dryout transients. The

thermocouple responses during each dryout transient indicate similar debris bed behavior. The ultrasonic thermometers (UT) provided means of determining the relative lengths of the two-phase and conductive regions within the bed.[3-6] For the large subcooling case (460 K), the two-phase region was approximately 4.5 cm in length, and the conductive region approximately 3.8 cm. For the small subcooling case, most of the bed experienced two-phase conditions. The top thermocouples indicated 20 K below the bed saturation temperature, revealing a very small conduction region. For both cases the two-phase regions did not appear to grow in length during postdryout transients.

3.2.2.1.3 _UT Performance During D-4_ -- For the D-4 experiment, the UT was placed within the experiment vessel to obtain axial temperature profiles through the debris bed. The UT was a stainless steel sensor, 0.5 mm in diameter, held in a Hastalloy C sheath having a 1.5-mm outside diameter. The sensor contained ten, 1-cm long sensing regions, providing an integral temperature over each sensing region. The UT performed quite well for the first 17 hours of the experiment. After that time, a change in the echo waveform was observed. This change in waveform was suspected to have been caused by a shift in the sensor coil position. The UT axial temperature profiles were very useful in determining the length of the two-phase and conductive zones. But an actual dryout temperature transient was not observed with the UT.

3.2.2.1.4 _Additional Debris Bed Observations_ -- During the course of the experiment, several thermal transients or disturbances were identified. The thermal transients ranged in duration from very long times (order of hours) to very short times (< 10 s). The nature of the transients implies possible channeling as well as larger scale belching. Presently, the thermal transients are being characterized and the observations analyzed separately.

3.2.2.2 _Conclusions_ -- The degree of sodium subcooling strongly influences the specific bed power required to reach incipient dryout. The preliminary results indicate a factor of 5 in specific bed power between large and small sodium subcooling. The mechanisms responsible for the increased coolability of the low subcooled bed are not clear, but the observed channeling and belching behavior apparently played an important role.

The ultrasonic thermometers proved to be an important tool in the analysis of debris bed behavior, providing axial temperature profiles through the bed. From these profiles, debris bed thermal behavior can be better understood. The scarcity of observed dryout conditions, as indicated by the UT, was attributed to the UT's large spatial resolution and the relatively smaller dryout zone thicknesses.

3.2.3 Debris Bed Experiment D-5

Debris bed experiment D-5 is the first experiment in which bed behavior at extended postdryout conditions will be investigated. The principle objectives are

a. To observe bed behavior at elevated temperatures (between 1773 K and 2073 K) at which sodium subcooling will vary from 400 K to 100 K,

b. To evaluate crucible design for future high temperature experiments, and

c. To evaluate double containment concepts for D-series experiments.

The design of the D-5 vessel and support equipment has been initiated. The principle effort addressed the design of a high-temperature, insulated crucible to contain the debris bed. Severe thermal stresses are expected because of the extremely large thermal gradients applied to the crucible ($\sim$250 K/mm). Double containment for the D-5 experiment is in progress, with material compatibility experiments, out-of-pile systems tests (OPST) and stress analysis being planned for the early part of the next quarter. The data acquisition system is being evaluated in order to manage the large quantities of data expected in future experiments.

3.2.4 Debris Bed Experiment D-6

Experiment D-6 is one in a series of debris bed experiments at Sandia, intended to investigate the coolability of UO_2 debris by natural convection in sodium following an LMFBR accident. D-6 differs from previous experiments in that a stratified bed is to be used to determine the characteristics of a bed in which particle size varies as a function of depth. Except for the bed characteristics, D-6 is designed to duplicate experiment D-2 as much as possible, to allow a straightforward comparison of the data. Accordingly, D-6 will have the following characteristics:

- 4.87 kg UO_2 (100 to 1000 μm)

- 2.25 kg sodium

- 460 K subcooling at 673 K sodium bulk temperature

- 300 K subcooling at 873 K sodium bulk temperature

D-6 is currently scheduled to be conducted in September 1980.

The D-6 bed will be formed by sieving UO_2 particulate into particle size ranges and then layering these particles (larger particles at the bottom) to achieve a bed with the same overall particle size/mass distribution as Experiment D-2. To allow modeling of this type of bed, the particle size distribution as a function of depth must be determined. A series of out-of-pile experiments will be performed to accomplish this. Sand and water will be used to perform initial studies, with beds of depleted UO_2 and sodium eventually being characterized. These experiments will not only characterize the particle size distribution in the bed but will also permit the acquisition of experience in forming the bed for D-6.

The safe conduct of experiments such as the debris bed series, in which significant quantities of uranium are fissioned, is becoming increasingly important. Accordingly, new containment concepts are being investigated for D-6 and additional effort will be expended in the area of safety analysis and verification which should provide increased assurances that the experiment can be performed with minimum risk to the public as well as operational personnel.

The design of the D-6 experiment was initiated in October and is nearly complete. Detailed design drawings are underway for portions of the experiment, including most of the experiment section and a portion of the helium piping system. The design of the access section, which connects the experiment section with the helium trailer, as well as minor details of the ultrasonic thermometers, remain to be completed.

Some hardware, including piping, flanges, and valves, has been ordered. Final ordering will be completed when the design is finalized. Hardware to initiate the bed characterization efforts was ordered and has, for the most part, been received.

Neutronic analysis of the debris bed experiment was initiated in December. These analyses should provide power profiles in the bed as well as bed coupling with the ACRR.

3.2.5 Debris Bed Experiment Analysis

3.2.5.1 Flooding Dryout Model -- The dryout of a non-subcooled debris bed determined from a one-dimensional solution of bed behavior based on Darcy's law has been reported elsewhere.[3-7] In that previous case, dryout was dictated by the viscous drag in the fluid flowing through the bed particles. However, for the case of large particles, the fluid-particle drag will become less significant and the liquid-vapor counterflow involved in boiling will be limited by a flooding condition in which there is an abrupt increase in the liquid-vapor drag. The dryout criterion based on flooding may be determined as follows.[3-8]

The flooding criterion for two-phase flow in packed beds is[3-8]

$$j_l^{*\frac{1}{2}} + j_v^{*\frac{1}{2}} = 0.775 \tag{3.1}$$

where

$$j_v^* = j_v \sqrt{\frac{\rho_v}{gD\rho_l}} \tag{3.2}$$

and

$$j_l^* = j_l \big/ \sqrt{gD} \tag{3.3}$$

j_v is the upward vapor flux, j_l is the downward liquid flux, ρ is the density, g is the acceleration of gravity, and D is the flow volume per unit bed surface area.

For continuity,

$$\rho_l j_l = \rho_v j_v \ . \tag{3.4}$$

The last four equations may be combined to yield

$$j_v^c = \frac{0.601\sqrt{gD\rho_1/\rho_v}}{\left(1 + \sqrt[4]{\rho_v/\rho_1}\right)^2}$$ (3.5)

as the flooding condition. Since the vapor flux is a maximum at the top of the bed, the dryout heat flux at the top of the bed, q_d, is given by

$$q_d = \rho_v h j_v^c \quad , $$ (3.6)

where h is the heat of vaporization. This may be written as

$$q_d = \frac{0.6h\sqrt{\rho_1\rho_v gD}}{\left(1 + \sqrt[4]{\rho_v/\rho_1}\right)^2}$$ (3.7)

The value of D is unlikely to be well characterized. An approximation may be found by assuming that all of the bed particles are spherical, and have the same diameter, d. Then

$$D = \frac{\epsilon}{1 - \epsilon}\left(\frac{d}{6}\right) \quad , $$ (3.8)

where ϵ is the bed porosity. This yields

$$q_d = \frac{0.245h\sqrt{\rho_1\rho_v gd\epsilon/(1 - \epsilon)}}{\left(1 + \sqrt[4]{\rho_v/\rho_1}\right)^2}$$ (3.9)

The Kozeny equation may be used to relate the particle diameter to bed permeability. Thus,

$$d\epsilon/(1 - \epsilon) = \sqrt{180K/\epsilon}$$ (3.10)

where K is the permeability. Eqn (3.9) becomes

$$q_d = \frac{0.897\, h\, \sqrt{\rho_1}\, \overline{\rho_v g}\, \sqrt[4]{K/\epsilon}}{\left(1 + \sqrt[4]{\rho_v/\rho_1}\right)^2}$$

(3.11)

This is the basic equation for dryout by flooding.

For comparison, the dryout flux based on Darcy's law (as originally deter-mined by Hardee and Nilson[3-10]) is

$$q_d = \frac{\rho_1\, gkh}{\left(\sqrt{\nu_v} + \sqrt{\nu_1}\right)^2}$$

(3.12)

thus, the particle size at which flooding becomes dominant is

$$d_f = \frac{12.5}{g^{5/3}}\, \frac{(1-\epsilon)}{\epsilon^{5/3}} \left(\frac{\sqrt{\nu_v} + \sqrt{\nu_1}}{1 + \left(\rho_1/\rho_v\right)^{1/4}}\right)^{4/3}.$$

(3.13)

For $\epsilon = 0.43$, the critical particle diameter is 1.5 mm for sodium and 0.8 mm for water (both at one atmosphere pressure). Thus, flooding can be a dominant phenom-enon in dryout. Note that in the viscosity-dominated regime $(d < d_f)$ the dryout flux varies with the square of the particle diameter, but in the flooding-dominated regime $(d > d_f)$ the dryout flux varies with the square root of the particle diameter. Thus, the viscosity-dominated equation for dryout can grossly overestimate the dryout f   c beds with large particles. In addition, if other phenomena (e. g., capillary forc. s) increase e dryout flux over that predicted by Eqn (3.12), then the critical diameter will be even less than that predicted by Eqn (3.13).

The predictions of Eqn (3.11) may be compared with the dryout data reported by Dhir and Catton.[3-11] Since the flooding condition limits the dryout expected from viscous drag, the measured dryout flux would be expected to be less than or equal to the predicted flux. The data is plotted in Figure 3.2-1 in terms of predicted vs measured dryout flux. The acetone and methanol data (lower left group) does fall

below the predicted limit. The water data (upper right group) falls on the prediction line, suggesting that those measurements were in the flooding regime. For comparison, the Dhir-Catton model[3-11] predictions are shown in Figure 3.2-2. As can be seen, the flooding model agrees with the water data much better than the Dhir-Catton model. This is especially significant in view of the fact that the flooding model uses no free parameters, whereas the Dhir-Catton model was fitted to the data.

3.2.5.2 <u>Capillary Dryout Model</u> -- Shires and Stevens[3-12] have suggested that capillary forces are important in understanding debris bed dryout and have developed a zero-dimensional dryout model which includes this effect. Capillary forces were thus added to the one-dimensional analysis reported previously.[3-7] The conservation equations are

$$V_v = \frac{-\kappa \, \kappa_v}{\mu_v} \, \frac{\partial P_v}{\partial z} \tag{3.14}$$

$$V_l = \frac{-\kappa \, \kappa_l}{\mu_l} \left(\frac{\partial P_l}{\partial z} + \rho_l \, g \right) \tag{3.15}$$

$$S = -\frac{d}{dz} \left(\rho_l \, V_l \, h \right) \tag{3.16}$$

$$O = \frac{d}{dz} \left(\rho_l \, V_l + \rho_v \, V_v \right) \tag{3.17}$$

$$P_l - P_v = P_c \tag{3.18}$$

Where V is superficial velocity, κ is permeability, κ_v and κ_l are relative permeabilities, μ is dynamic viscosity, P is pressure, z is elevation, ρ is density, g is gravitational acceleration, S is volumetric heat source, h is latent heat of vaporization, and the subscripts l, v, and c refer to liquid, vapor, and capillary respectively. The equations may be combined to yield

$$S = \frac{d}{dz} \left(\frac{\kappa h \left(\rho_l \, g + \frac{\partial P_c}{\partial z} \right)}{\frac{\nu_l}{\kappa_l} + \frac{\nu_v}{\kappa_v}} \right) \tag{3.19}$$

where ν is the dynamic viscosity.
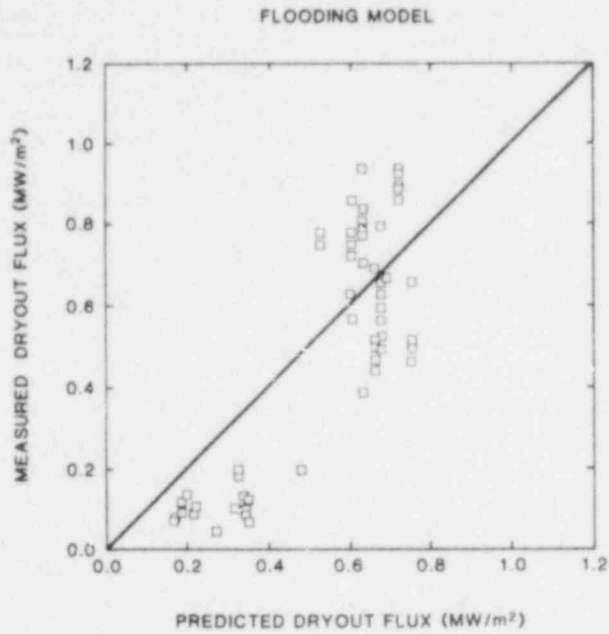
FLOODING MODEL

Figure 3.2-1   Predicted vs Measured Dryout Flux.
The flooding model is compared with
the data in Tables 3-VI of Reference 3-11.

DHIR-CATTON MODEL
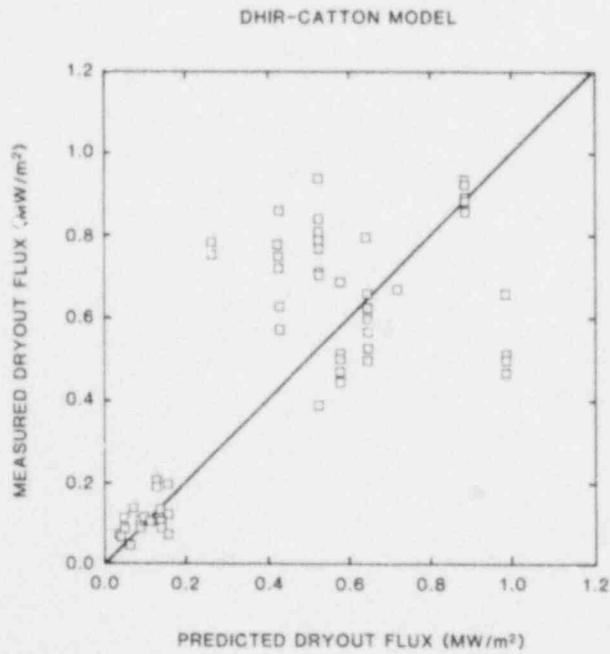
Figure 3.2-2   Predicted vs Measured Dryout Flux
Using the Reference 3-11 Model

The capillary force may be expressed as

$$P_c = \sigma \sqrt{\epsilon/K} \quad J \tag{3.20}$$

where σ is surface tension, ϵ is the volume fraction between particles, and J is the Leverett function.[3-13] The slope of the Leverett function is nearly constant leading to the assumption (for uniform permeability) that

$$\frac{\partial P_c}{\partial z} = 0.5 \sigma \sqrt{\epsilon/K} \frac{\partial \gamma}{\partial z} \tag{3.21}$$

where γ is the liquid fraction between the particles. The specific permeabilities are also functions of γ. A good empirical approximation is[3-13]

$$\kappa_v = 1 - 1.11 \gamma \tag{3.22}$$

$$\kappa_l = \gamma^3 \tag{3.23}$$

Combining Eqns (3.19), (3.21), (3.22), and (3.23) and integrating once, yields an equation for liquid fraction (r) as a function of elevation (z) for uniform permeability (k)

$$Sz = \frac{kh \left(\rho_l g + 0.5 \sigma \sqrt{\epsilon/k} \frac{d\gamma}{dz} \right)}{\frac{\mu_l}{\gamma^3} + \frac{\nu_v}{1 - 1.11 \gamma}} - q_o \tag{3.24}$$

where q_o is the heat flux at the bottom of the bed. Choosing an insulated lower boundary condition ($q_o = 0$), Eqn (3.24) may be rearranged to yield

$$\frac{d\gamma}{dz} = \frac{Sz}{\lambda_c q_v} \left(\frac{1}{\gamma^3} \frac{\nu_l}{\nu_v} + \frac{1}{1 - 1.11 \gamma} \right) - \frac{1}{\lambda_c} \tag{3.25}$$

where

$$\lambda_c = \frac{0.5 \sigma \sqrt{\epsilon/k}}{\rho_l g} \tag{3.26}$$

and

$$q_v = \frac{\rho_1 \, g \, kh}{\nu_v} \; .$$

<div align="right">(3.27)</div>

Physically, λ_c is the maximum height to which the liquid will be drawn up into the bed by capillary action, and q_v is the dryout heat flux neglecting liquid drag and capillary forces. (For beds with millimeter-sized particles, $\lambda_c \approx 0.5$ m. This implies that the formulae developed in References 3-7 and 3-10 strictly apply only to very deep beds (greater than 0.5 m)).

Equation (3.25) can be integrated numerically. As a test case, the conditions of the dryout from the D-3b experiment were used. An effective bed depth of 91 mm (corresponding to the boiling zone thickness) was used. The permeability was assumed to be 1.5×10^{-10} m^2 (as measured out-of-pile for similar beds). Thus, $\lambda_c = 0.441$ m and $q_v = 57.7$ kW/m^2. The family of curves generated by varying the power is shown in Figure 3.2-3. The assumed boundary condition was that the liquid fraction is 0.9 at the top of the bed. (This is as close to 1.0 as the liquid fraction can get using the empirical specific vapor permeability of Eqn (3.22). Physically, this probably corresponds to some trapped vapor in the bed.) Note that as the power increases, the liquid fraction at the bottom of the bed decreases until dryout is reached. Note also that solutions exist for power beyond incipient dryout. Thus, the one-dimensional capillary model predicts not only incipient dryout, but postdryout behavior as well.
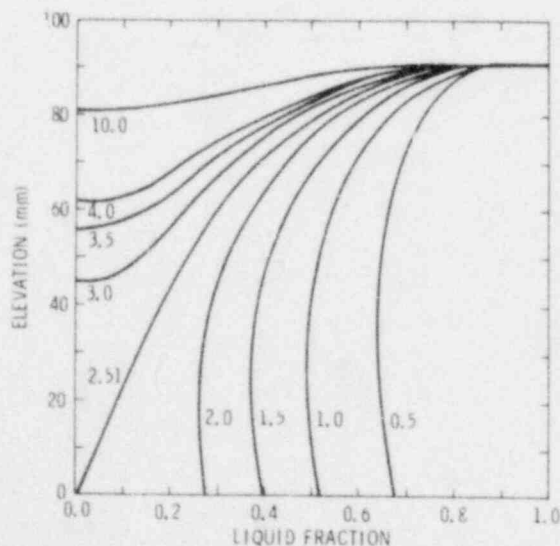

Figure 3.2-3

Liquid Fraction in a Debris Bed vs Elevation for Various Powers. (Bed height is 91 mm (D-3 boiling zone thickens at dryout). Numbers by the curves are bed power in MW/m^3.)

The incipient dryout curve is that which passes through the origin. For a fixed power, the dryout height may be found by integrating Eqn (3.25) numerically from the origin until $r = 0.9$. In doing so, an approximate solution near the origin is helpful. Thus,

$$\gamma \doteq \left(2\frac{\nu_1}{\nu_v}\frac{Sz^2}{q_v\lambda_c}\right)^{\frac{1}{4}} \quad \text{for} \quad z << \frac{q_v}{\left(1 + \sqrt{\nu_1/\nu_v}\right)^2 S} \tag{3.28}$$

The measured and predicted dryout powers for incipient dryout in the D-series experiments are shown in Table 3-IV. The effective bed height used in the predictions was the boiling zone thickness predicted by the series conduction model.[3-7] (For D-4 the boiling zone thickness used was that actually measured, and only the predisturbed dryout run was used.) The agreement is quite reasonable and indicates that the major phenomena in this regime are close to being understood.

Table 3-IV

Measured and Predicted Incipient Dryout Powers

Dryout	q_v (kW/m^2)	λ_c (m)	ν_v/ν_1	Boiling Zone Thickness (m)	Measured Dryout Power (MW/m^3)	Predicted Dryout Power (MW/m^3)
D2a	48.1	0.439	411	0.067	4.3	3.7
D3a	76.0	0.445	261	0.103	2.2	2.6
D3b	58.7	0.441	336	0.091	2.3	2.5
D4a	19.4	0.422	1037	0.045	4.6	3.3

The D-3b dryout included an additional measurement of conditions beyond dryout which indicated a dry zone thickness increase with respect to power increase[3-7] of $\Delta L_d / \Delta S = 1 \times 10^{-8}$ m^4/W. (The postdryout analysis for D-4 is not yet complete.) The one-dimension capillary model predicts $\Delta L_d / \Delta S = 4 \times 10^{-7}$ m^4/W. Uncertainty exists about whether the disagreement is inherent in the model or due to errors in the data (which was sparse and very close to incipient dryout). Future tests should contribute to resolving this issue.

An interesting consequence of recognizing capillary forces is the consideration of downward boiling. This has particular significance for bottom-cooled beds. Previous analyses had assumed that bottom-cooling effects could be modeled solely by a stagnant liquid-filled conduction layer in the lower portion of the bed. Heat removed by vaporization was assumed to be only upward since gravity-driven liquid could force the vapor only upward. However, with capillary forces, it is possible for the liquid to be drawn upward from the lower conduction zone and for the vapor to be driven downward, thus producing downward boiling. Since capillary forces dominate in most beds under consideration ($\lambda_c \approx 0.5$ m), this effect could be large. Indeed, the dryout thickness of a bottom-cooled bed would be about twice that of a bottom-insulated bed. (Previous models would predict a smaller thickness.) The equations and results of this new consideration will be presented next quarter.

3.2.5.3 <u>Bottom-Fed Debris Bed Dryout Model</u> -- In some accident scenarios the possibility exists for liquid to enter the bottom of the bed through a permeable supporting plate (e.g., the fuel rod grid support plate). The liquid would be driven by natural circulation via an open path from the top of the bed and down along the side (e.g., the core bypass channel (Figure 3.2-4)). The effect on dryout may be determined for the simplified case of very deep beds (in which capillary forces are negligible) and a linear specific permeability defined as

$$k_v = 1 - \gamma \tag{3.29}$$

$$k_1 = \gamma \tag{3.30}$$

Thus, Eqn (3.18) has $P_c = 0$ and Eqn (3.16) is integrated to

$$\rho_1 V_1 + \rho_v V_v = W \tag{3.31}$$

where W is the liquid influx at the bed bottom. The conservation equation may then be reduced to

$$Sz = \left(\frac{\nu_1}{\nu_v} \frac{hW}{\gamma} + q_v \right) \left(\frac{1}{\frac{\nu_1}{\nu_v} \frac{1}{\gamma} + \frac{1}{1-\gamma}} \right) \tag{3.32}$$
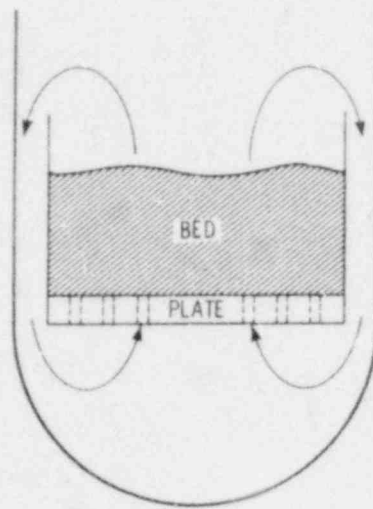
Figure 3.2-4   Debris Bed With Naturally Circulating
Flow to the Bed Bottom Through a
Permeable Plate

The liquid moves down in the upper part of the bed and up in the lower part.
The stagnation point occurs where

$$\gamma = 1 - \frac{\nu_v W}{\rho_1 g k} \tag{3.33}$$

(The elevation of this point may be found from Eqn (3.32)).

For naturally circulating systems, the incoming liquid is being driven by a
head of liquid in the adjoining downcoming channel. Thus, there is the additional
condition

$$\int_o^L P_1 \, dz = \rho_1 gL \tag{3.34}$$

where L is the total bed thickness. This reduces to

$$L - \int_o^L \frac{S_z}{q_v (1 - \gamma)} \, dz \tag{3.35}$$

123

Combining Eqns (3.32) and (3.35), and assuming constant permeability yields

$$
\mathrm{Wh} = \frac{q_v L - q_v \dfrac{\nu_v}{\nu_1} \displaystyle\int_0^L \dfrac{\gamma\, dz}{1 + (\nu_v/\nu_1 - 1)\gamma}}{\displaystyle\int_0^L \dfrac{dz}{1 + \left(\dfrac{\nu_v}{\nu_1} - 1\right)\gamma}}
\tag{3.36}
$$

Over most of the region of integration, a good approximation is

$$
\gamma \doteq 1 - Sz/q_v
\tag{3.37}
$$

Thus

$$
\mathrm{Wh} \doteq \frac{q_v}{\left(1 + \dfrac{\nu_1}{\nu_v}\right)} + \frac{SL}{\ln\left(1 - \left(1 - \dfrac{\nu_1}{\nu_v}\right)\dfrac{SL}{q_v}\right)}
\tag{3.38}
$$

To a good approximation, this in turn reduces to

$$
\mathrm{Wh} \doteq \frac{SL}{2}
\tag{3.39}
$$

An immediate consequence of this is that the stagnation point is at $^{\sim} = L/2$, suggesting that dryout would first occur at the bed midplane.

Combining Eqns (3.32) and (3.39) and solving for the dryout flux in a manner similar to that in Reference 3-7 yields

$$
q_d \doteq \frac{q_v}{\left(1 + \sqrt{\dfrac{\nu_1}{2\nu_v}}\right)^2} = \frac{\rho_1\, gkh}{\left(\sqrt{\nu_v} + \sqrt{\dfrac{\nu_1}{2}}\right)^2}
\tag{3.40}
$$

This is very similar to the dryout flux for very deep beds without liquid reentry at the bed bottom (Eqn (3.12)). In most applications, the numerical difference is negligible. Thus, apparently the permeability of the support structure does not significantly alter the dryout flux for very deep beds under natural circulation. The effect

of capillary forces on these conclusions has yet to be investigated; however, if consideration is given to the possibility of downward boiling discussed previously, the effect could be large, possibly doubling the thickness required for dryout.

3.3   PAHR Molten Pool (D. W. Varela, 4422; T. M. Kerley, 4422; D. A. Powers, 4422)

3.3.1   Introduction

Experiments and analysis addressing the interaction of UO_2 with MgO continued during this quarter. The fourth in-pile molten pool experiment (MP-4) was successfully conducted in the ACRR. For the penetration of UO_2 into MgO, the data obtained from a series of high temperature furnace experiments were correlated to a high confidence level. In addition, the fifth in-pile molten pool experiment is being prepared.

3.3.2 UO_2/MgO In-Core Experiment MP-4

The fourth in-core experiment (MP-4) was conducted in the ACRR in November 1979. The goal of this experiment was to examine the effect of internal heating on the attack of magnesium oxide brick by overlying solid UO_2 particulate. In particular, furnace experiments have shown that, at temperatures significantly lower than the UO_2/MgO dissolution temperatures, hot solid UO_2 diffuses into the MgO brick by dissolving the lower-melting-temperature grain boundary phase. The in-pile experiment, upon disassembly of the capsule and analysis of the test section, will provide the first diffusion data with internal heating. The effect of a temperature gradient (as opposed to a constant temperature field in the furnace experiments) will be of particular interest in the analysis. The temperature gradient is expected to reduce the penetration rate of UO_2 into MgO bricks.

During the experiment, temperatures and temperature gradients were measured using ultrasonic thermometers. Preliminary observations indicate that the overlying UO_2 reached a maximum temperature near 3000 K. The UO_2/MgO interface reached maximum temperature near 2400 K and the UO_2 interacted with the MgO brick for approximately 20 minutes.

During the experiment, investigators noted noncondensable gas generating unexpectedly within the inner steel vessel. The nature and amount of this gas have not yet been analyzed. The MgO may be the source but no judgments should be made now. Clearly, identification of this gas is very important and is receiving significant attention.

Reduction of the data from the experiment is in progress. Results will be reported next quarter together with the details of the experiment. The capsule will be disassembled when the hot cell facility is completed. In preparation for disassembly, the capsule was x-radiographed in Sandia's 2-MeV facility after the experiment. The radiographs showed no visible signs of fuel melting and revealed very little fuel compaction.

3.3.3 UO_2/MgO Furnace Experiments

The diffusion data obtained from a series of high temperature UO_2/MgO furnace experiments (described in Reference 3-14) were correlated with the expression

$$\frac{x^2}{t} = D_o^{eff} \exp\left(-\frac{E}{RT}\right) \tag{3.41}$$

where

$\quad\quad$ x = distance of UO_2 penetration into the brick (cm)

$\quad\quad$ t = time (s)

$\quad$ D_o^{eff} = effective diffusion coefficient (cm^2/s)

$\quad\quad$ E = activation energy for diffusion (cal/mole)

$\quad\quad$ R = gas constant

$\quad\quad$ T = absolute temperatures (K)

Figure 3.3-1 is a plot of observed values of $\ln(x^2/t)$ versus the reciprocal of the absolute temperature. The data shown in this figure for interactions at temperatures below 2500 K may be correlated with Eqn (3.41) (D^{eff} = 91000; E = 96100) to a high confidence level. Data for interactions at higher temperatures deviate from the correlation in the direction of greater penetration.

Diffusion coefficients estimated from the above data correlation are at least a factor of 10^3 greater than would be expected for bulk diffusion into MgO.[3-15] The formation of a liquid phase along the grain boundaries would account for this accelerated diffusion.
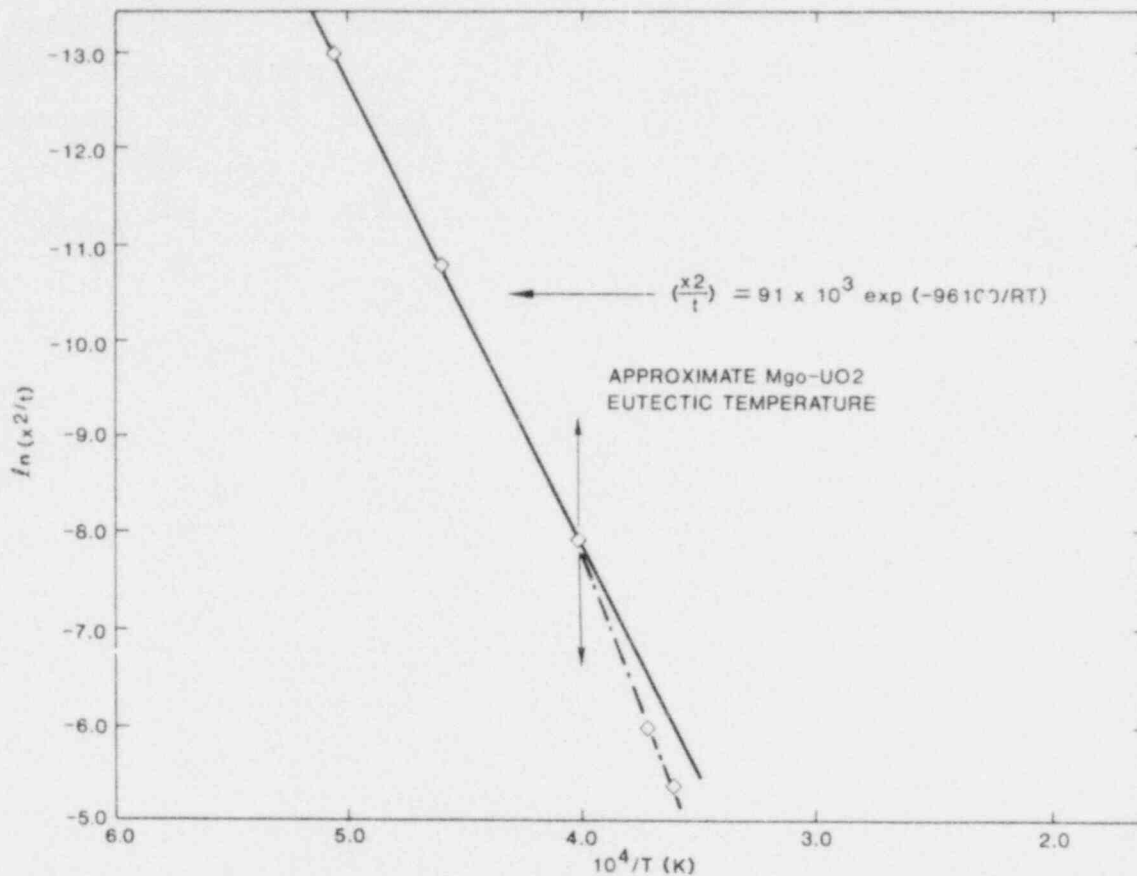
Figure 3.3-1   Correlation of UO_2 Penetration Depth
vs the Reciprocal of the Absolute
Temperature

The diffusion of UO_2 into MgO at temperatures above 2550 K is rapid and may
be the result of eutectic formation.   The temperature of the UO_2/MgO eutectic is,
however, a matter of controversy.   The eutectic temperature may depend on the
partial pressure of oxygen in equilibrium with the UO_2/MgO system.   In well-inerted
systems, the eutectic has been estimated to be about 2473 K.[3-16]   In air, the eutectic
may be lower by as much as 400 K.[3-17]

A test was conducted to examine the interaction of UO_2 (16 w/o ZrO_2) with
MgO.   The test is undergoing microscopic analysis.   Additional tests are now being
planned in which steel (and other materials such as Lanthanum) will be mixed with
UO_2 and allowed to interact with MgO as a function of time and temperature.

3.3.4 Preparations for the MP-5 In-Core Experiment

The fifth in-core experiment will investigate steel agglomeration and migration (under a temperature gradient) in a mixed UO_2/steel particulate fuel bed. Several areas of work now in progress are described below.

3.3.4.1 Ultrasonic Thermometer (UT) Development -- Work was initiated in conjunction with the Debris Bed Program to develop a housing on the primary capsule container that will fully enclose the UT and associated pulsing components. The objective is to eliminate the need for sealing of the primary containment around the sensor. Such seals cause signal reflection that interferes with the sensor signals producing large temperature measurement errors. The design of the new housing is nearly complete and fabrication will be initiated early next quarter.

3.3.4.2 Data Acquisition System -- The acquisition system for the ultrasonic thermometer and thermocouple data is being updated to accept input from a larger number of sensors. The increase in the number of diagnostic sensors has also required the fabrication of additional electronic components.

3.3.4.3 Sheath Fabrication -- Sandia has initiated a contract with Los Alamos Scientific Laboratory to fabricate ThO_2 sheaths (slip cast, closed at one end) for the UTs to be used on the UO_2/steel experiments. The previous supplier has stopped handling ThO_2 materials.

3.3.5 Activities for Next Quarter

Reduction and preliminary analysis of data from the MP-4 Molten Pool Experiment will be completed. Furnace experiments will continue for the investigation of the mutual reactions between MgO and various core materials. Preparation for the MP-5 In-Core Experiment will continue.

3.4   Fragmentation (T. Y. Chu, 1537)

3.4.1 Debris Bed Analysis

During this reporting period, considerable effort was spent on developing pro-
cedures for characterizing the debris bed. A summary of the procedures and some
of the results follows. All of the data are from test FRAG 9 which involved the re-
lease of 23 kg of sodium at 773 K (500°C) into 14 kg of iron/alumina melt.

Core samples of the debris bed were obt ned by driving thin-walled tubing into
the bed. The core samples were first x-rayed with the beam perpendicular to the axis
of the core and along two diameters (of the sample) 90° apart (Figure 3.4-1). Gamma-
ray attenuation technique was used to determine the average density profile of the bed
with the gamma-ray beam in the same directions as the x-ray photographs (Figure 3.4-2).
To further characterize the debris bed, each core was then cut into disks 0.25 to 0.5 in.
thick. X-ray photographs were then taken along the axis to obtain a more detailed local
display of the bed structure (Figure 3.4-3). The stratification of the particular size
is shown clearly here.

Following, the nondestructive characterization, the sodium in the core disks
was removed. Also, during this operation, the local (0.25 to 0.5 in.) fragment weight
fraction (WF) of the sample was obtained by weighing each core disk before and after
the removal of the sodium. From the fragment weight fraction, WF and the average
density of the bed, ρ, the local void fraction (volume fraction of sodium) of the bed
can easily be calculated from

$$\text{Void Fraction} = (1 - \text{WF}) \frac{\rho}{\rho_s}$$

where s denotes sodium. The void fraction data obtained can also be cross checked
by a separate determination of the fragment density using pychometry techniques.

Fragments from each disk were seived to obtain the local particle-size distri-
bution. With the contribution from each depth summed, the overall particle size dis-
tribution is also obtainable.

130
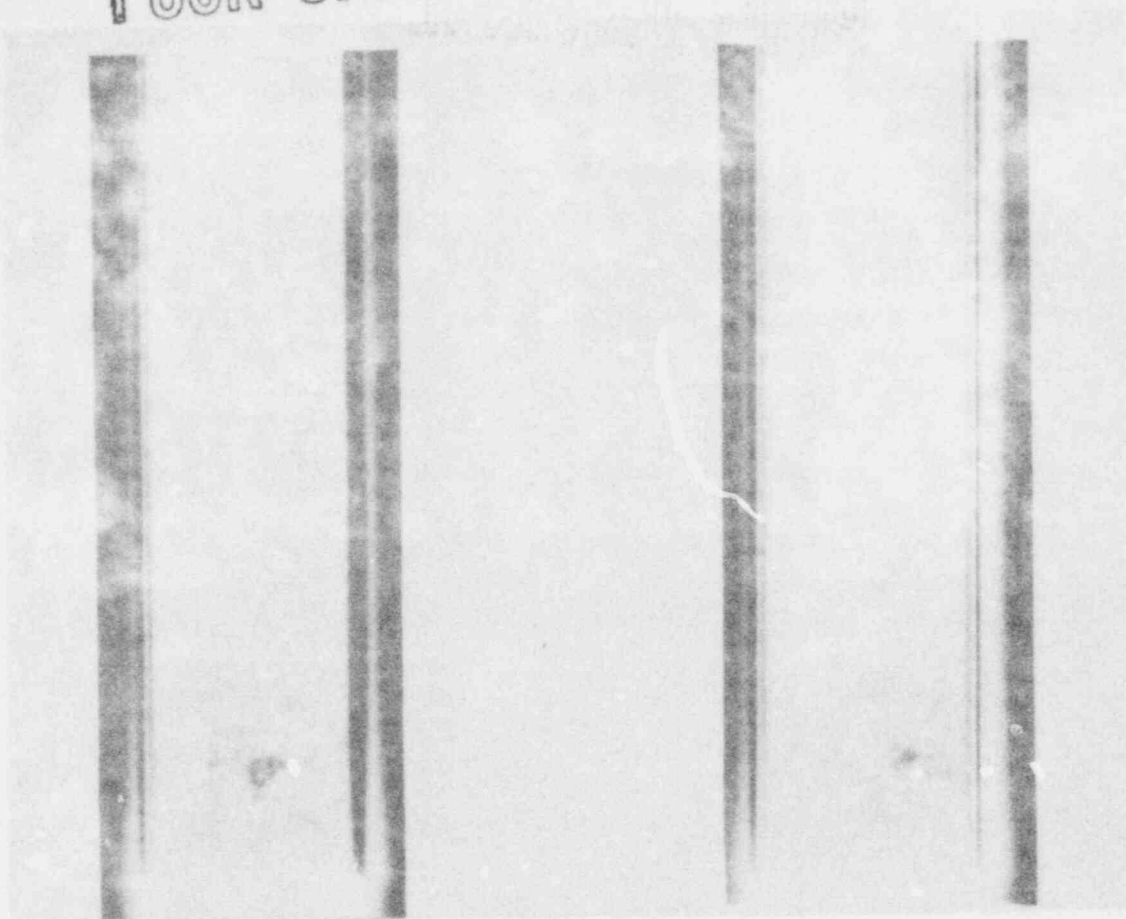
Figure 3.4-1   Core Sample X-Rayed With Beam Perpendicular to the Axis of the Core.   (X-rays taken from positions 90° apart around the periphery of the sample).
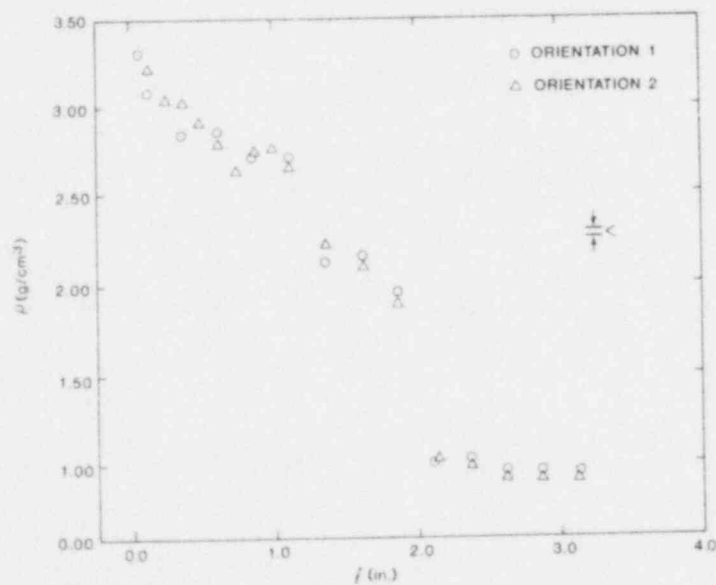
Figure 3.4-2   Density Profile of Core Sample No. 14 (1/4-in. $\phi\gamma$ beam centered ℓ inches from pipe end)

131
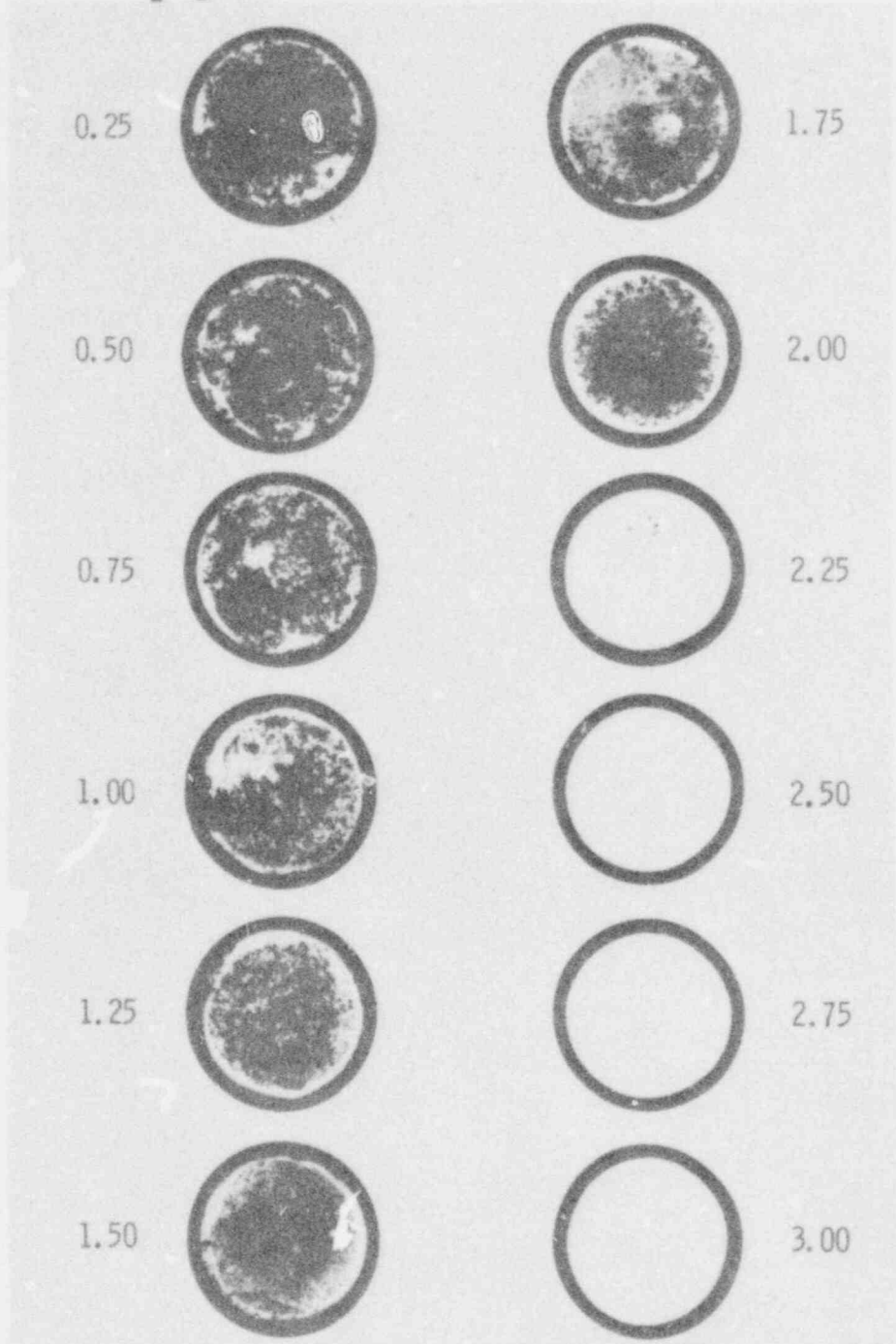
Figure 3.4-3   X-Ray Photographs Along the Axis of a Sectioned
             Core Sample (photos depict appearance of the core
             at indicated distances from the bottom in inches)

Figure 3.4-4 is a plot of a typical set of results. In the 1.5 to 2.0-in. section of the bed, 25.6% of the particles (by weight) are less than 43 μm, whereas, in the 0 to 0.5-in. section, only 0.7% of the particles are less than 43 μm. The median particle size, obtained by interpolation, for the different sections are 0 to 0.5 in., 820 μm; 0.5 to 1.0 in., 300 μm; 1.0 to 1.5 in., 110 μm; and 1.5 to 2.0 in., 70 μm. In addition, visual observations of the sieved particles indicate that there are more iron particles near the bottom of the bed and more alumina particles near the top of the bed. An overall bed distribution obtained by summing contributions from the different sections is also shown in Figure 3.4-4. The median size is 300 μm. The size distribution is found to be in the range of previous experiments. This distribution should be viewed only as an approximate indication of the bulk particle distribution since x-ray photographs taken of different core samples show that there are variations between samples.
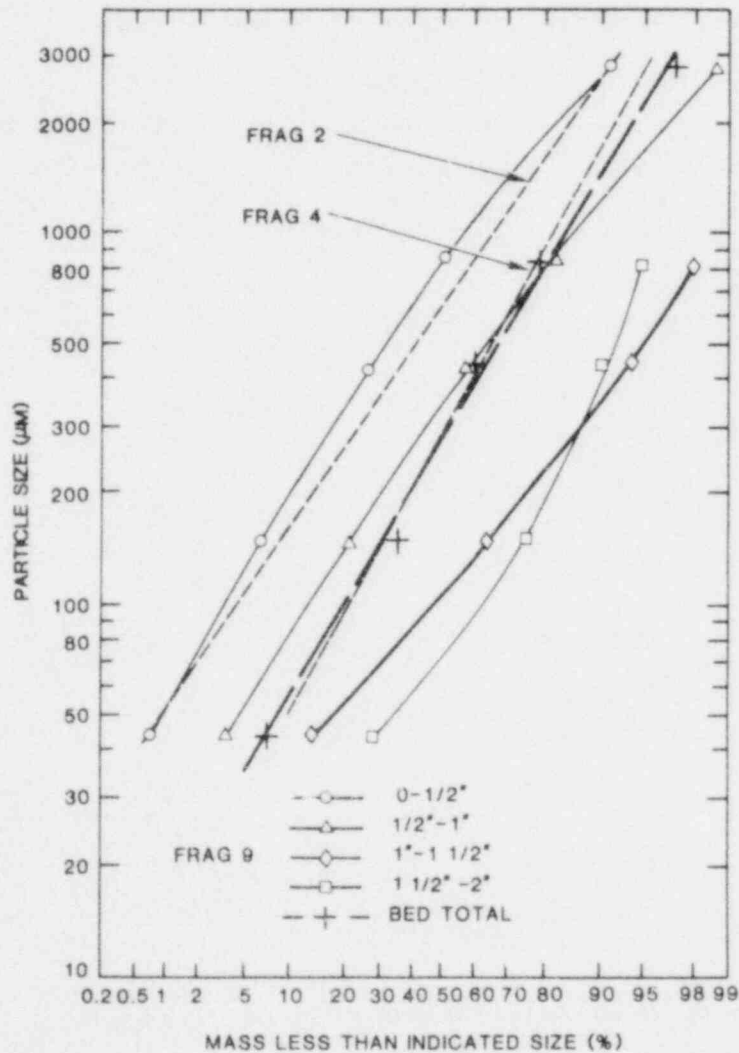

Figure 3.4-4   Particle Size Distribution as a Function
of Depth in the Debris Bed: FRAG 9,
Sample 16

3.4.2 New Experiment

A reverse experiment was performed during this reporting period. Twenty kilograms of UO_2-producing metallothermic mixture were used. The mixture was ignited in the reaction vessel and 23 kg of sodium at 791 K (508°C) were released into the melt 10 s after ignition. The interaction lasted approximately 3.6 s. The reaction was vigorous enough to cause the entire apparatus, weighing over 1000 kg, to move upward and from side to side, resulting in a net displacement of approximately 2 cm from its original position. The side to side movement could have been the result of uneven distribution of the molten steel overlaying the UO_2. Earlier observations made of the molten pool indicate that rather than a uniform layer, the molten steel tends to form a "puddle" to the side of the interaction vessel.

While making core samples, a portion of the debris bed was found to be "impenetrable," indicating that there were debris of comparable or larger size than the diameter of the core sample tube (1 in.). The actual size and spatial distribution of the longer fragments cannot be determined until all the sodium is removed from the reaction vessel. For the core sample that reached all the way to the bottom, the bed thickness was about 3.5 in. and the bed was highly stratified in particle size.

3.5   Sodium Containment and Structural Integrity (R. U. Acton, 1537;
       J. E. Smaardyk, 4422; R. L. Sallach, 5846; A. Suo-Antilla, 4425)

3.5.1 Introduction

Numerous separate effects experiments (both physical and chemical) and one large-scale sodium-concrete interaction test (Test 16) were conducted during this reporting period. The analyses of the results of experiments previously conducted are proceeding and include studies of chemical and physical characteristics and relevant properties of the materials.

3.5.2 Physical Separate Effects Test

During this reporting period, six physical separate effects tests were completed. The first test article was magnetite aggregate concrete with a heater to sustain the sodium-pool temperature. The heater setpoint of 773 K (500°C) was maintained for 2 hr. Some significant chemical interactions were evident after about 1 hr (based on pool-thermocouple data), but the reactions were not sufficient to raise the pool temperature above the heater setpoint. Posttest examination showed a small amount of reaction product on top of the frozen sodium. These products are being analyzed.

The next five test articles were made of basalt-aggregate concrete. For four of these tests, 4.5 kg of sodium were dumped at 973 K (700°C). The first test article was in the dry, "as-cured," condition. The second test article had been kept moist for about 3 weeks prior to the test. The third test article was also moist and had 0.45 kg of NaOH present in the pool. The fourth test article was similar to the third but also had a pool heater. The fifth test article had 0.91 kg of NaOH in a pan suspended in the pool, a pool heater, and 5.4 kg of sodium (dumped at 973 K).

The first two basalt test results were similar; there was no significant interaction. The third test (with the NaOH) also appeared benign, but the pool cooled only about half as rapidly as the pools in the first two tests. The fourth test (with sustained heating) was similar to the magnetic test performed earlier. Posttest examination showed a layer of NaOH and silicates about 2.5 cm thick between the frozen sodium and the concrete. The fifth test showed evidence of interactions beginning at about 2 hours after the dump. However, at 3.5 hours, the sodium began leaking through the heater feedthroughs leaving a shallow pool. This remaining sodium reacted with the concrete, producing temperatures in the pool and concrete surface of 973 K

135

$(700^{\circ}C)$. Posttest examination showed no metallic sodium remaining, a reddish-brown reaction product, and concrete erosion of about 1 cm.

3.5.3 Chemical Separate Effects Tests

The chemical separate effects tests have as their purpose a better understanding and characterization of the chemical processes which have been postulated to occur during the interaction of sodium with various concretes.

During this quarter, a series of experiments has been completed in which the reaction of molten NaOH with silica (SiO_2) was investigated. NaOH is a product of the sodium/water reaction and is the reactant which attacks the components of concrete. SiO_2 is a major component of basalt concrete.

The rate of attack of SiO_2 by NaOH was measured at temperatures up to 773 K. Extrapolation of the data into the range of 973 to 1073 K (700 to $800^{\circ}C$) yields a rate which is comparable to the rate of movement of the reaction front observed in large-scale Test 11 (0.5 mm/min). This suggests but does not prove that the controlling reaction of the front is the $NaOH/SiO_2$ reaction rather than the transport of water and/or sodium to the front.

Sodium meta-silicate (Na_2SiO_3) is a major component of the reaction products formed from the sodium/concrete reaction. However, the meta-silicate can react further with additional NaOH to form the ortho-silicate (Na_4SiO_4) as in the equation

$$2NaOH + Na_2SiO_3 \rightarrow Na_4SiO_4 + H_2O$$
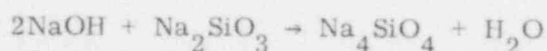
Various ratios of NaOH and SiO_2 were reacted at 773 K $(500^{\circ}C)$ to determine what the end products were. All reactions were completed in approximately 1 hour. With an excess of NaOH (over the amount of NaOH needed to form Na_2SiO_3) the ortho-silicate (Na_4SiO_4) is always formed to the extent possible. Since no Na_4SiO_4 was found (by x-ray diffraction) in the concrete reaction product, the implication is that an excessive amount of NaOH does not exist at the reaction front; i.e., it is produced by the Na/H_2O reaction as fast as it is consumed. This imposes constraints on the detailed description of the overall chemical reaction which are difficult to explain. Further work in this area is required.

3.5.4 Large-Scale Sodium-Basalt Concrete Test 16

This experiment was designed to be similar to Test 11 in which a bare basalt concrete crucible was exposed to a shallow sodium pool. In that test, erosion of the concrete did not begin until 75 minutes into the test as indicated by both pool temperature and ultrasonic erosion measurements. The delay was attributed to the time necessary for the sodium pool to saturate with sodium hydroxide (15 to 20 mole percent) from the reaction of sodium with the water thermally driven from the concrete. The sodium pool depth in Test 11 was doubled to 27 cm for Test 16. If the reaction rate is linear, then the delay time for the sodium pool to saturate with sodium hydroxide should be twice as long in Test 16. If the rate is parabolic, then the delay time for saturation should be about four times as long. Thermocouple placement is shown in Figure 3.5-1.

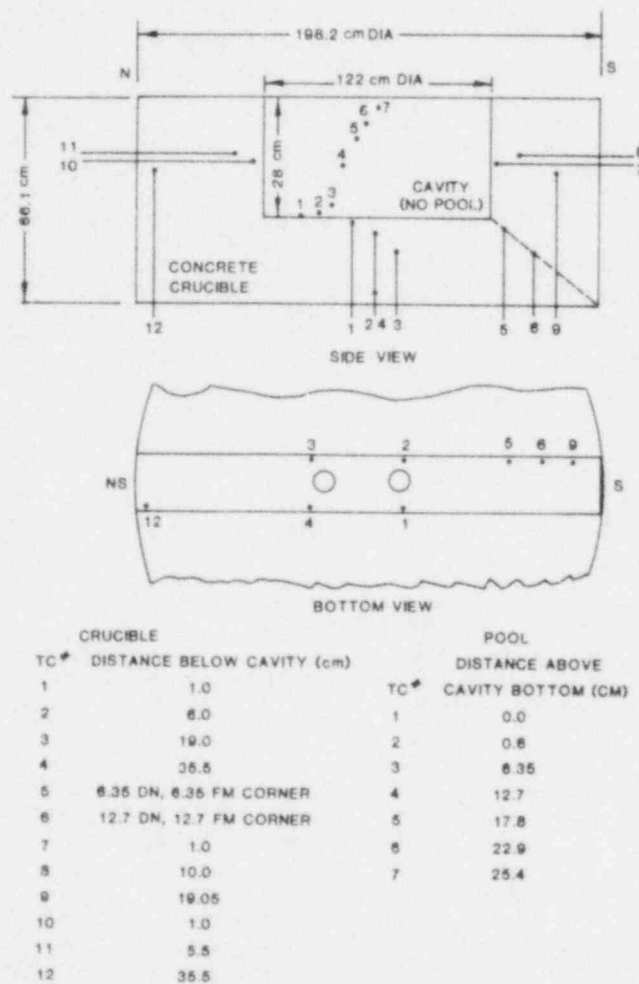| CRUCIBLE		POOL	
TC#	DISTANCE BELOW CAVITY (cm)	TC#	DISTANCE ABOVE CAVITY BOTTOM (CM)
1	1.0	1	0.0
2	6.0	2	0.6
3	19.0	3	6.35
4	36.5	4	12.7
5	6.35 DN, 6.35 FM CORNER	5	17.8
6	12.7 DN, 12.7 FM CORNER	6	22.9
7	1.0	7	25.4
8	10.0		
9	19.05		
10	1.0		
11	5.5		
12	36.5		

Figure 3.5-1 Pool and Crucible Thermocouple Locations and Orientation
(Thermocouple locations are numbered - not to scale)

A charge of 255 kg of sodium at 873 K was dumped into the bare cavity of the basalt concrete crucible. A microphone under the test chamber picked up loud popping and banging beginning within a minute of the sodium drop. Large clouds of white smoke also began coming out of the test chamber within minutes of the sodium dump. At about 16 minutes into the test, conditions inside the test chamber were such that all power, control, and instrumentation functions were lost.

3.5.4.1 <u>Posttest Analysis of Test 16</u> -- The "top hat" which fits over the crucible was buckled by heat and lost its seal with the crucible. Some 10 to 25 kg of metallic sodium were found outside of the crucible. The crucible had cracks similar to Test 11 - 0.3 cm at the outer circumference of the crucible. A small amoun. of metallic sodium came out of some of these cracks (~ 2 kg total). Five days after the test, the crucible was removed from the test chamber and the "top hat" removed from the crucible. No metallic sodium remained in the crucible cavity; about 225 kg of sodium were consumed. Reaction products filled the crucible cavity and were similar in appearance to the products found in the liner of Test 13. These products burst into flame when the "top hat" was removed.

Figures 3.5-2 through 3.5-4 show thermocouple responses. No confidence can be placed in any of the curves after about 15 minutes--the time at which the thermocouple extension cables are believed to have been burned. After chemical samples of the reaction products were taken, the crucible cavity was cleaned out and mapped for penetration. The sodium penetration into the concrete is shown for one profile in Figure 3.5-5. The average penetration was 16.5 cm on the bottom and 3.2 cm on the sidewall.

The chemical analyses of the reaction products of Test 16 are not yet available. However, this test and Test 11 were similar except for the amount of sodium and since both tests were sodium limited, the product analyses of Test 16 is expected to be similar to Test 11.

3-18

Figure 3.5-2   Pool Temperature and Crucible Bottom Temperatures, Test No. 16 (PL = pool, CR = crucible. Numbers refer to thermocouples shown in Figure 3.5-1)

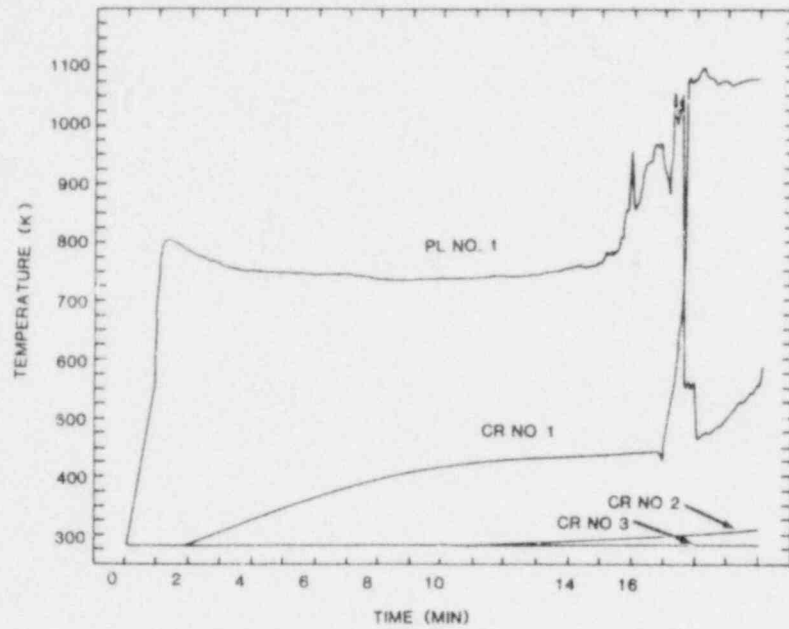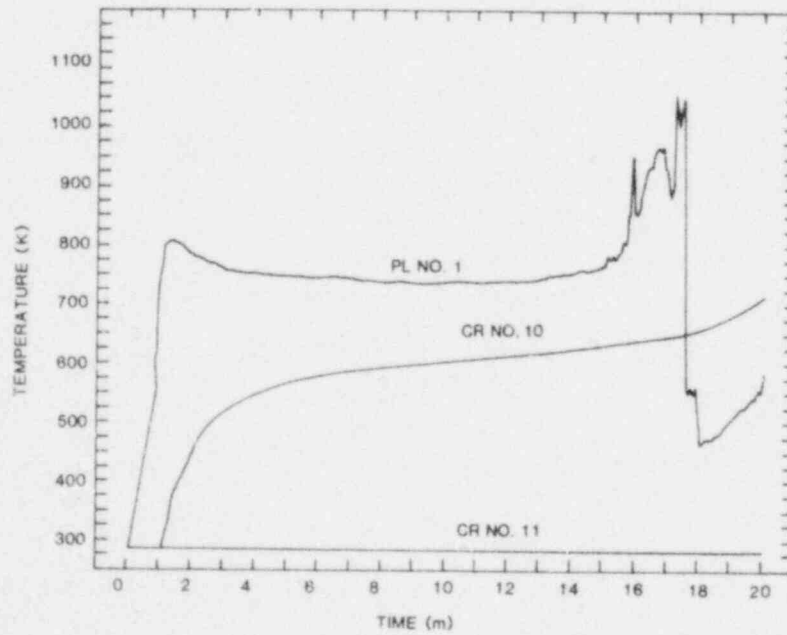Figure 3.5-3   Pool Temperature and Crucible Northside Temperatures, Test No. 16 (PL = pool, CR = crucible. Numbers refer to thermocouples shown in Figure 3.5-1)
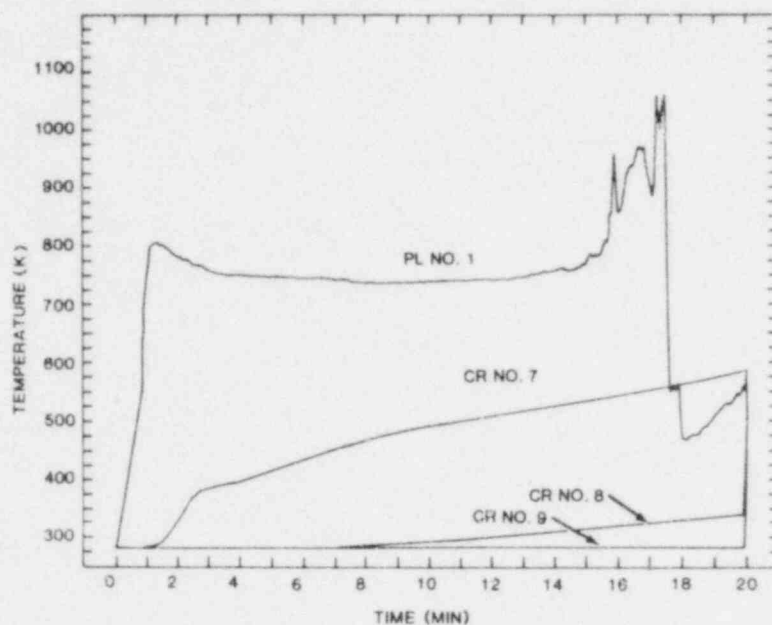
Figure 3.5-4   Pool Temperature and Crucible Southside Temperatures,
Test No. 16 (PL = pool, CR = crucible, Numbers refer
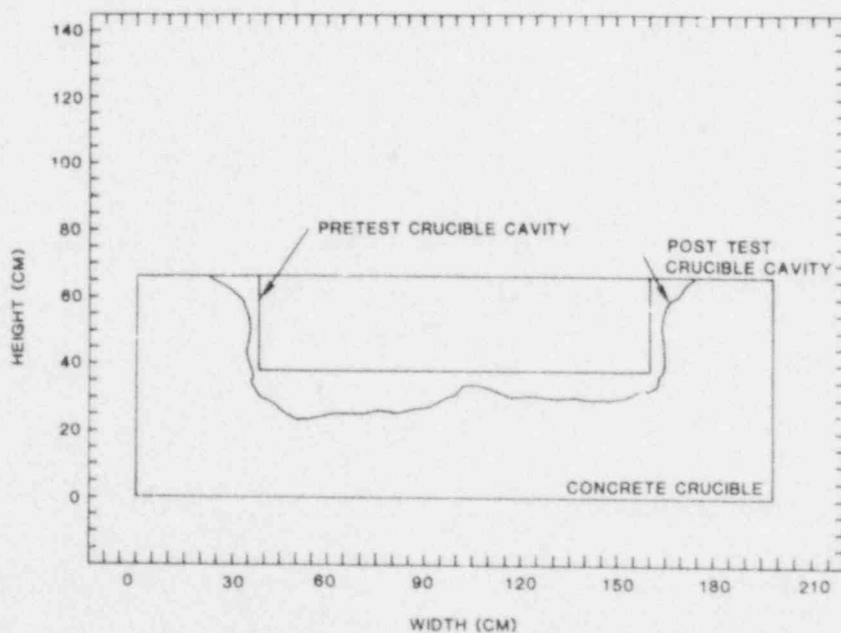to thermocouples shown in Figure 3.5-1)

Figure 3.5-5   Basalt Concrete Penetration by Molten Sodium, Test No. 16

3.5.4.2 Conclusions From Test 16 -- The original purpose of Test 16, the establishment of the rate of formation and saturation of sodium hydroxide in the sodium pool, has not been fulfilled. One basic difference existed between the crucibles of Test 11 and Test 16. The large crucibles for this test series are stored outside in the dry atmosphere of central New Mexico. After Test 11 had been conducted, investigators decided to place an open container of water in the cavity of each stored crucible, and to cover the cavities of all stored crucibles. The outer layer of concrete in the crucible cavities (the layer that reacts with sodium in the tests) would thus be kept from drying out. As is apparent from Tests 11 and 16, the amount of water available in the surface layer of concrete is clearly a prime factor in determining the time necessary for NaOH saturation of the sodium pool.

3.5.5 Heat Transfer Analysis of Test 11

Test 11[3-19] involved a bare basalt-concrete crucible cavity with a 13.2-cm deep sodium pool (128 kg). The sodium was dropped into the cavity at 873 K. Pool heaters were set to control the pool temperature at 823 K. The heaters required 50 minutes to return the pool temperature to the setpoint where control was maintained for approximately 15 minutes. At that time, chemical reaction heat raised the pool temperature above the control point (Figure 3.5-6).
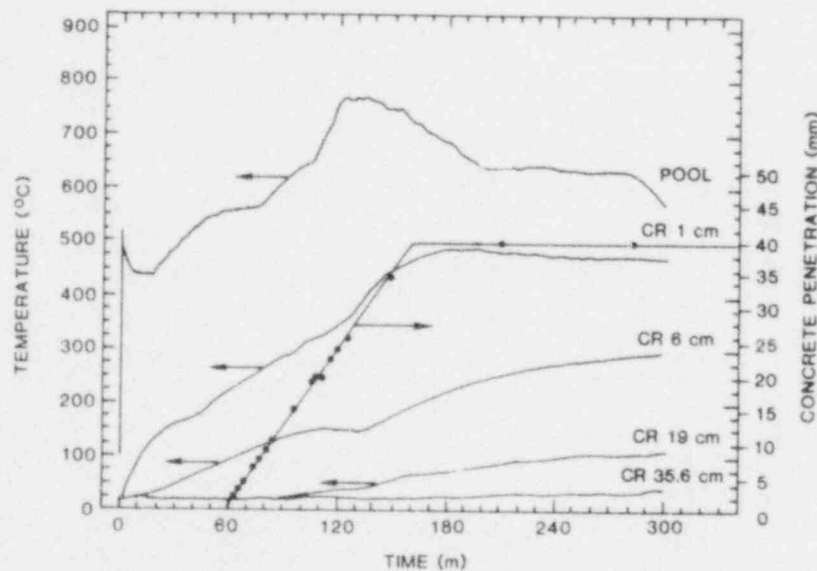
Figure 3.5-6   Penetration Data Added to Crucible Temperatures
and Pool Temperature, Test No. 11. (CR = crucible
thermocouples. Associated distances are measured
from the bottom of the crucible.)

The nonlinear inverse heat conduction code CONTA has been used to analyze the downward heat flux from the sodium pool into the concrete. The code also computes the concrete surface temperature at the interface between the crucible-cavity bottom and the sodium pool. Figures 3.5-7 and 3.5-8 show the results of this analysis. Instabilities, apparent in the curves, were caused in the code by the time step in the raw experimental data giving a Fourier number ≤ 0.05. As the sampling time during the experiment was increased beyond 4000 s, the instabilities disappear.

3.5.6 Test Summaries

Tables 3-V and 3-VI summarize the results on this project and represent large-scale and physical separate effects testing, respectively.

Figure 3.5-7 Calculated Surface Temperature, Test No. 11

Figure 3.5-8 Calculated Heat Flux, Test No. 11

Table 3-V

Summary of Large-Scale Sodium/Concrete Interaction Experiments

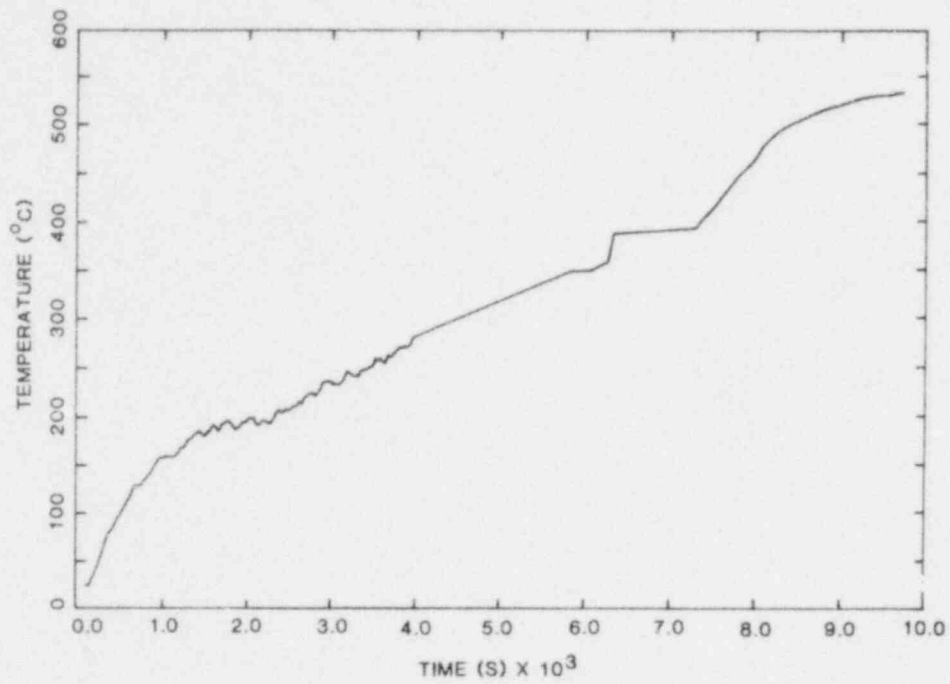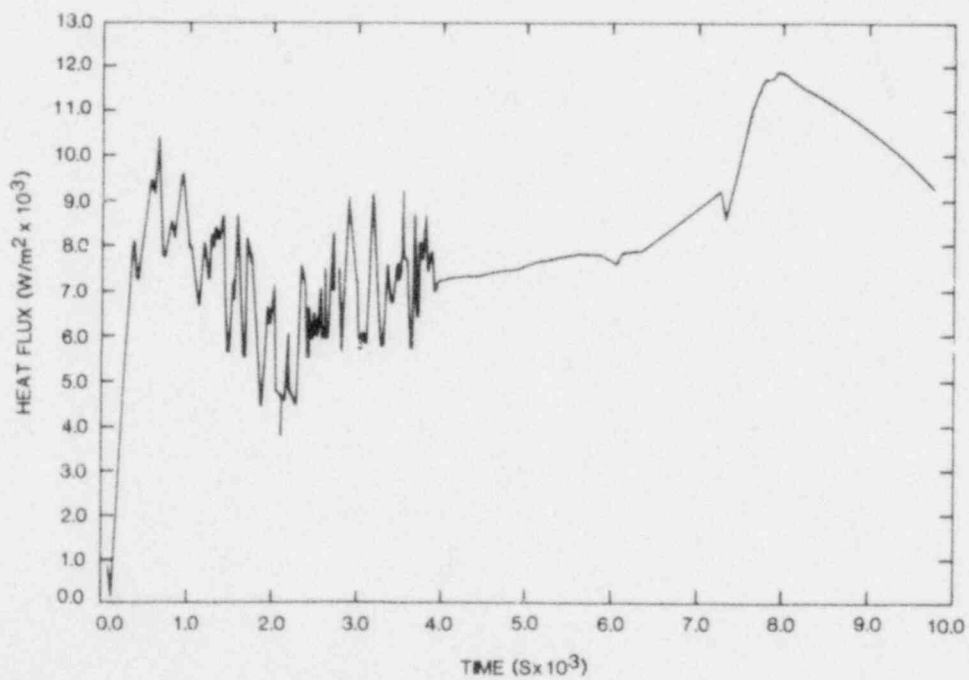| Details	Test No. 1	2	3	4	5	6	8	9	10	11	12	13	14	15	16
Crucible:	Limestone	Limestone	Limestone	Limestone	Limestone	Limestone	Limestone	Limestone	Limestone	Basalt	Basalt	Basalt	Magnetite	Magnetite	Basalt
Weight (kg)	1190	2520	3770	3780	3780	3780	4100	3900	3900	4090	3900	4000	6550	6040	4090
Cavity diam (cm)	61	122	137	91	91	91	122	91	91	122	91	76	122	83.8 square	122
Cavity Depth (cm)	17.8	17.8	27.9	50.8	50.8	50.8	28	51	51	30	51	71	28	61	28
Top Hat	No	No	No	Yes	Yes	Yes	Yes	Yes	Yes	Yes	Yes	Yes	Yes	Yes	Yes
Atmosphere	N_2	N_2	N_2	N_2	N_2	N_2	N_2	N_2	N_2	N_2	N_2	N_2	N_2	N_2	N_2
Sodium:															
Weight (kg)	21	109	186	186	186	186	127	186	182	128	68(1)	239	126	240	255
Drop Temp (°C)	420	535	560	540	540	(2)	550	600	600	600	6 0	700	640	700	600
Pool Depth (cm)	8.6	11.4	15.5	34.8	34.8	(3)	13.2	33.5	(4)	13.2	(4)	(4)	13.5	(4)	27
Pool Heater	No	No	No	No	Yes	Yes	Yes	Yes	Yes	Yes	Yes	Yes	Yes	Yes	Yes
Special Feature:	None	None	None	None	None	NaOH added	None	Cracks, Rebar, H₂O added	Steel insert	None	Insert, Firebrick	Insert, Firebrick, 1-D	None	Insert, 1 bare vertical wall and 1 vertical wall with dense firebrick	None
Results:															
Energetic Reaction	Yes	Yes	Yes	No	No	No	Partial	Yes	Yes	Yes	Yes	Yes	Yes	Only in fire-brick	Yes
Sodium Consumed	All	All	All	Little	Little	Little		Little	(5)	All	All	All	All	~175	All
Max Erosion (cm)	8.4	9.1	15.2	<1	<1	<1	1	4.5	(5)	6.4	(6)	30.5(7)	11	Only firebrick attacked	16.5 bottom 3.2 side-wall

(1) An additional 45.5 kg sodium dropped at 4 hr 22 min
(2) Sodium pool reheated from Test 5, in steps, to 700°C
(3) Sodium pool remaining from Test 5, approximately 34 cm
(4) Because a flawed steel insert was used in these tests, pool depth not informative; 0.62 cm gap between insert and concrete in Test 10; no intentional gap in Tests 12, 13, and 15 between insert and firebrick or concrete.
(5) Explosion terminated test at 25 seconds.
(6) All of sodium consumed by firebrick.
(7) All of firebrick consumed in addition to concrete penetration of 30.5 cm.

Table 3-VI

Summary of Separate Effects Sodium/Concrete Interaction Experiments

Details	Test No.												
	1	2	3	4	5	6	7	8	9	10	11	12	13
Test Article:													
Concrete	Limestone	Limestone	Limestone	Limestone	Limestone	Limestone	Magnetite	Magnetite	Basalt	Basalt	Basalt	Basalt	Basalt
Diameter (cm)	30.3	30.3	30.3	30.3	30.3	30.3	30.3	30.3	30.3	30.3	30.3	30.3	30.3
Height (cm)	30.5	30.5	30.5	30.5	30.5	30.5	30.5	30.5	30.5	30.5	30.5	30.5	30.5
Sodium:													
Weight (kg)	4.54	4.54	4.54	4.54	4.54	4.54	4.54	4.54	4.54	4.54	4.54	4.54	5.45
Drop Temp (°C)	602	650	694	750	734	731	730	701	705	713	705	700	702
Pool Depth (cm)	7.6	10.2	10.4	10.5	10.5	10.5	10.5	10.4	10.4	10.4	10.8	10.8	11.2
Pool Diam (cm)	30.3	26.7	26.7	26.7	26.7	26.7	26.7	26.7	26.7	26.7	26.7	26.7	26.7
Pool Heater Set Point (°C)								500				515	560
Special Features:	No sidewall thermal shield					Sheet metal "liner" with holes[2]				Damp surface[4]	Damp surface[4] 0.45 kg NaOH[5]	Damp surface[4] 0.45 kg NaOH[5]	Damp surface[4] 0.90 kg NaOH[6] (suspended)
Results:													
Energetic Reaction	None	None	None	None	None	None	None	Slight	None	None	Slight	Some	Yes
Sodium Consumed	None	Little	Little	Little	Little	(3)	(3)	Little	(3)	(3)	(3)	Significant[3]	All
Erosion[1]	None	50% × 5 mm	75% × 5 mm	90% × 5mm	(3)	(3)	(3)	(3)	(3)	(3)	(3)	(3)	100% × 10 mm

(1) Erosion = surface are (%) × depth (mm)
(2) 1.27 mm thick stainless steel with 5, 6-mm holes for sodium passage and separated
   from the concrete surface by about 6 mm.
(3) Posttest examination is not yet complete
(4) Concrete surface was kept damp for three weeks prior to the test.
(5) NaOH was placed in a plastic bag and set on the concrete surface prior to the test.
(6) NaOH was placed in a stainless steel pan in the sodium pool and about 50 mm
   above the concrete surface.

IMAGE EVALUATION
TEST TARGET (MT-3)

6"
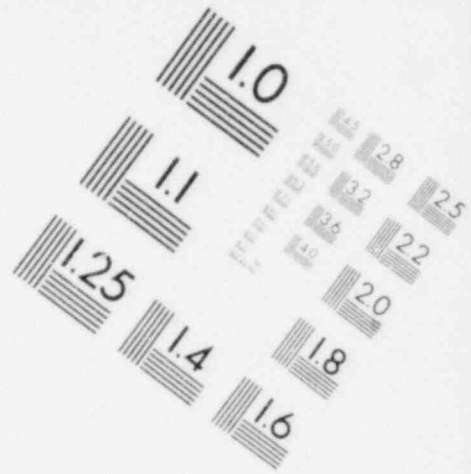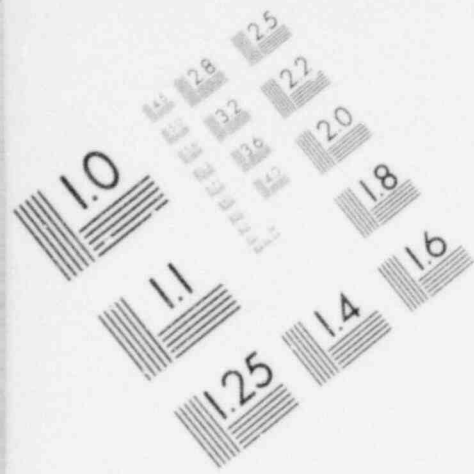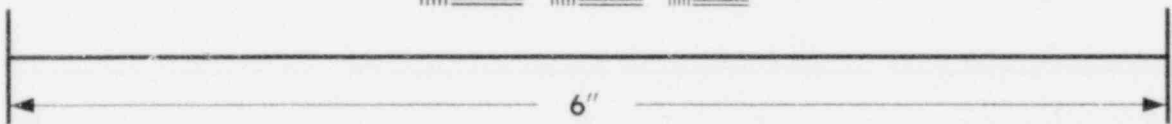
MICROCOPY RESOLUTION TEST CHART

IMAGE EVALUATION
TEST TARGET (MT-3)

6"
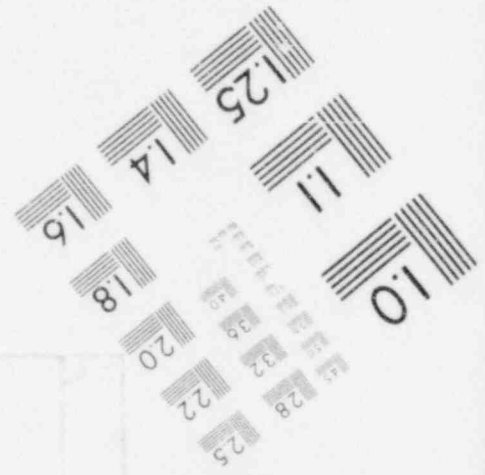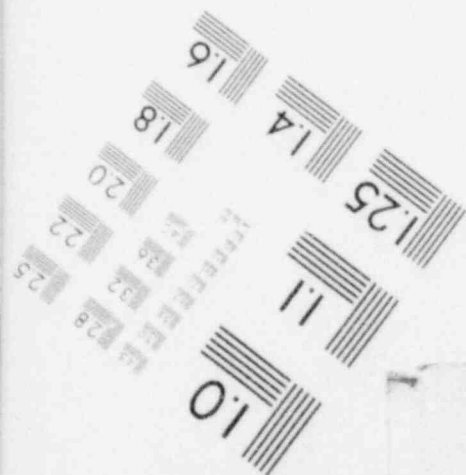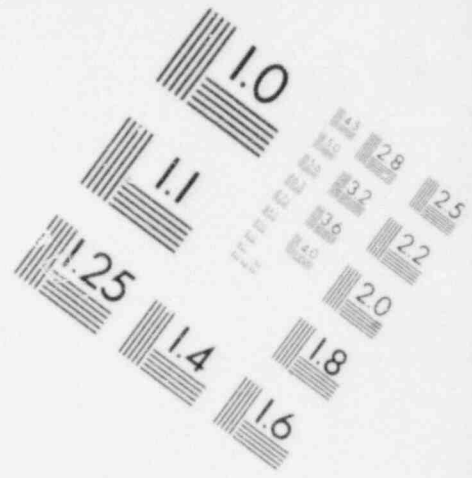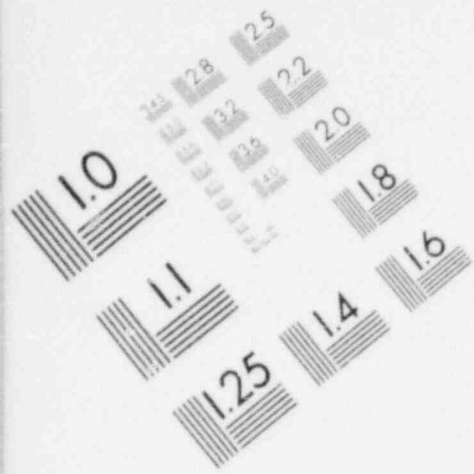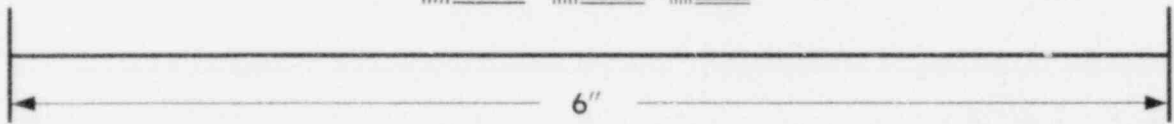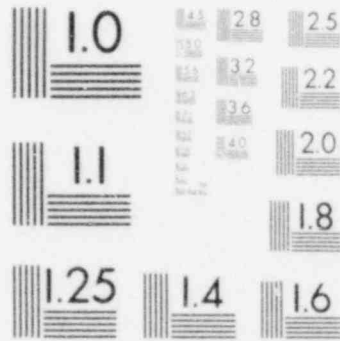
MICROCOPY RESOLUTION TEST CHART
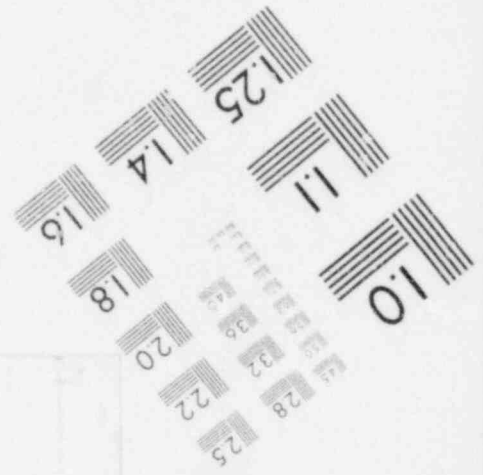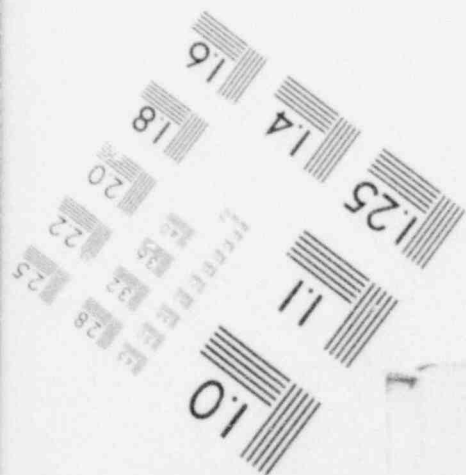
References for Section 3

3-1   D. A. Powers, Sustained Molten Steel/Concrete Interactions Tests — A Report on the Feasibility of Experimental Techniques, SAND77-1423 (Albuquerque, NM: Sandia Laboratories, June 1979).

3-2   D. A. Powers, "Sustained Molten Steel/Concrete Interactions Tests" Proceedings of the Post Accident Heat Removal Information Exchange, November 2 through 4, 1977, Argonne, IL, ANL-78-20, p 433.

3-3   D. A. Powers, D. A. Dahlgren, J. F. Muir, and W. D. Murfin, Exploratory Study of Molten Core Material/Concrete Interactions, July 1975 - March 1977, SAND77-2042 (Albuquerque, NM: Sandia Laboratories, February 1978).

3-4   W. W. Wendlandt, Thermochimica Acta 37:121 (1980).

3-5   D. A. Powers, "A Survey of Melt Interactions With Core Retention Materials," Proceedings of the Int'l Mtg on Fast Reactor Safety Technology (Seattle, WA: August 1979) Vol. I, p 379, Am Nucl Soc, LaGrange Park, IL, 1979.

3-6   J. B. Rivard, Postaccident Heat Removal: Debris-Bed Experiments D-2 and D-3, SAND78-1238 (Albuquerque, NM: Sandia Laboratories, November 1978).

3-7   R. J. Lipinski and J. B. Rivard, Proc. of Int'l Mtg on Fast Reactor Safety Technology (Seattle, WA: August 1979) p 757.

3-8   R. W. Ostensen, Memorandum of February 12, 1979, to J. B. Rivard, Sandia Laboratories, Albuquerque, NM.

3-9   G. B. Wallis, One-Dimensional Two-Phase Flow (New York, McGraw-Hill 1969).

3-10 H. C. Hardee and R. H. Nilson, Nucl Sci and Eng, 63, 119, 1977.

3-11 V. J. Dhir and I. Catton, Study of Dryout Heat Fluxes in Beds of Inductively Heated Particles, NUREG-0262, 1977.

3-12 G. L. Shires and G. F. Stevens, personal communication.

3-13 A. E. Scheidegger, The Physics of Flow Through Porous Media, U. of Toronto Press, Toronto, Canada, 1974.

3-14 Advanced Reactor Safety Research Quarterly Report, July-September 1979, SAND79-2158, NUREG/CR-1141, (Albuquerque, NM: Sandia Laboratories, April 1980).

3-15 J. Askill, Tracer Diffusion Data for Metals, Alloys, and Simple Oxides, (New York: IFI/Plenum Press, 1970).

3-16 W. A. Lambertson and M. H. Mueller, J Am Ceram Soc, 36, (20), 332, 1953.

3-17 P. P. Budnikov, S. G. Tresvyatskii, and V. I. Kushakovskii, Proc 2nd World Conference on Peaceful Uses of Atomic Energy, Vol 3 (Geneva, Switzerland, 1958).

3-18 R. U. Acton, et al, Molten Sodium Interactions With Basalt Concrete and Siliceous Firebrick, SAND79-0938 (Albuquerque, NM: Sandia Laboratories, 1979), p 25, Table 4.

3-19 See Reference 3-18, p 23.

4. AEROSOL SOURCE NORMALIZATION
(R. M. Elrick, 4422)

4.1 Introduction

During an energetic hypothetical core disruptive accident, fuel debris may be produced as vapor or formed as small very particulated debris (molten or solid) which can be transported to the upper vessel regions and through breaks which may have occurred in the vessel. The possibility of transporting this material depends strongly on its initial character.

Aerosol produced from in-pile (ACRR) experiments is being characterized to determine the physical properties of fuel particles resulting from the vaporization and melt breakup of fuel pins subjected to simulated overpower excursions.

ORNL and Sandia Laboratories have been involved in a collaborative effort to compare the characteristics of debris from UO_2 fuel resistively heated to vapor (at ORNL) with those debris characteristics from fuel heated neutronically (at Sandia). In a recent series of experiments at ORNL, fuel debris was sampled and fuel temperatures measured by methods that had previously been demonstrated in the Annular Core Pulse Reactor at Sandia.

Previous quarterlies have described the temperature response of an exposed fuel pellet in a stack of fuel pellets when the stack was resistively heated to vapor. Calibrated photographic film was used to measure the temperatures of the fuel surface and of the bottom of a hole drilled to the centerline of the pellet. These centerline and surface temperatures were described for the high preheat and capacitance discharge heating phases. Several tests established the accuracy of the temperature measurements. The thermal condition of the fuel was estimated since sampled fuel debris will be characterized in terms of the temperature state of the fuel.

Most of the effort this quarter was devoted to a microscopic examination of fuel debris collected in the sampling wheel on Test CDV76. This run most closely matched the in-pile sampling experiment in total energy. Six of the thirty sampling

wheel channels were disassembled for examination. Two to three grids were cut from the top as well as the bottom surface of each of the sampling channels for study in a scanning electron microscope; an equal number was cut for examination in a transmission electron microscope.

SEM photographs have been taken of all collection grids. From these photographs, a particle count is being taken as a function of particle size and position in the channel. From these data, distributions in particle size and velocity will be obtained. Collected particles ranged in size from 0.2 μm (the smallest particle resolvable at a magnification of 1000) to about 200 μm. These largest particles, about an order of magnitude larger than the largest collected in the in-pile experiment, appeared as sintered UO_2 which had not melted during heating. Investigators do not know if these particles came from the pellets or the UO_2 microspheres that surrounded the pellet stack. Most of the smaller particles were either sphere-like or left a splattered trail on impact indicating, in both cases, a prior state of melt. Also there were considerably fewer of these smaller particles collected in this experiment than in the in-pile experiment.

Initial examination of grids at a magnification of 100,000 in a TEM showed particle sizes down to the resolving limit of the microscope, about 2 nm. Vermiculated patterns made on the grids by unresolved particles are deposits of vapor-like UO_2.

A program plan for at least six more out-of-pile experiments has been proposed to NRC by ORNL to complete this comparison study of source aerosols. These out-of-pile runs will differ from the first series in that smaller photographic windows will be used as well as a smaller diameter radial hole in the fuel for estimating fuel centerline temperature. These changes will be less of a perturbation to the original experiment than the modifications used in the first series of experiments. ORNL has asked Sandia to assist in sampling fuel debris from at least some of the capacitance discharge tests and to photograph both capacitance discharge and preheat tests for fuel temperature measurements. A design for smaller quartz windows was agreed upon between ORNL and Sandia. Windows of two sizes were fabricated at Sandia and sent to ORNL for use in the second series of experiments to begin about the first part of March 1980.

Next quarter, analysis of fuel debris from Test CDV76 will be completed and the second series of sampling experiments at ORNL should have been conducted.

5. CONTAINMENT ANALYSIS
(P. S. Pickard, 4423;
M. Senglaub, 4424;
J. P. Odom, 4424)

5.1   Introduction

The CONTAIN code development has continued this quarter in all phases. The code framework is now complete and in a preliminary form suitable for running test problems. The cavity-debris pool model, SINTER, is also operational with preliminary material interaction models. The atmosphere phenomenology routines are operational. The current aerosol module will, however, be replaced in the next quarter to allow a more general treatment. A series of test problems for the integrated code was run for checkout purposes and to identify areas requiring improvement for future versions of CONTAIN. Several areas were identified and modifications initiated during this quarter. This report describes the current status of CONTAIN and its submodules, and a brief summary of code-checkout calculations. Modifications required before the first version of CONTAIN can be finalized and the approaches being taken in these areas are also discussed briefly.

5.2   CONTAIN Framework

The basic CONTAIN framework, as described in previous quarterly reports, is now operational. The multicell capability, which uses a "reference" cell logic for all cells, requires that data for only one cell be stored in central memory during the calculation. Data for all other cells are stored in Large Core Memory (LCM) when the information is not being used. A four-cell sample problem, with all current phenomenological models operating, can be performed on the CDC-7600 computer without overlays. This process is similar to restarting each cell at each system time step. Although this does involve some manipulation of data, the time requirement for this process is not significant in the total running time of the code. Many problems can also be run without LCM (all data in fast core) and this option has been retained in the present version.

153

All control volumes (cells) defined in a CONTAIN calculation can interact with any other control volume. This very flexible scheme allows the simulation of any arbitrary number of cells connected by vents or other flow paths, as described by effective flow areas, friction terms, and flow lengths. This scheme can also be used to simulate a dimensional network (with the appropriate definition of flow areas and lengths) if such detail is required. Fission-product aerosols and gaseous fission products flow with the atmosphere gas. This atmosphere gas is described by an ideal gas equation-of-state.

Fission product decay is carried out by cell and host material location with a linearized chain resolution technique described previously. The fission-product description is a user input and can take the form of generic fission product groups, individual nuclides, or a combination of both.

The treatment of the fission product decay and transport is attempting an approximate means of accounting for the change in chemical and physical characteristics of a fission product as it decays, if such an accounting means is desired. A fission product transport model based on tracking the materials which host the various fission products is under development.

Other atmosphere models included in the current version are sodium-spray burning, sodium-pool burning and wall heat transfer. Models based on SPRAY-3 and SOFIRE-2 are used in the sodium burning routines. These routines are operational but have not yet been compared in detail to the SPRAY-3, SOFIRE-2 codes for sodium burning experiments.

5.3 SINTER Development

In the current version of CONTAIN, the SINTER cavity-debris-pool model is operational with preliminary Na-Concrete and Phase Transition models. The drift flux formulation consists of five fields: a structure field (solid), two liquid fields, and two vapor fields. Each field can consist of an arbitrary number of components. The SINTER module has been developed to describe the way in which the mass and energy generation and transport processes of fuel debris and sodium influence structural materials and the resultant release of mass and energy to the control volume atmosphere. The SINTER framework has been applied to this problem in some

preliminary calculations using approximate models for fuel-to-sodium heat transfer.
The relatively long running-times for these prob'⸺ s, under conditions of high mass
(gas) generation, have ⸺ed to the initiation of a quasi-static version to allow shortened
running times with less transient detail. SINTER will eventually incorporate the
basic features of the USINT water-evolution-in-concrete model. This feature, and
the logic to perform mass balances on water driven from structural walls and floors,
have not yet been included in the current version. Some preliminary calculations
have been performed with CONTAIN to facilitate checkout. Figures 5.3-1 through
5.3-3 show one such calculation for the case of cell 1 pressurizing due to gas evolu-
tion and causing flow of atmosphere gas and fission products to adjacent cells. Cell 4
in these calculations represented the outside environment. Figure 5.3-1 shows the
pressure history in all cells with the flow path between cells 1 and 2 opening at an
input pressure level in cell 1. Figure 5.3-2 shows the concentration of a gaseous
fission product in all cells as a function of time and is illustrative of the quantities
calculated. Figure 5.3-3 shows a temperature map of the cavity structure, debris,
and sodium pool at the end of the calculational time.
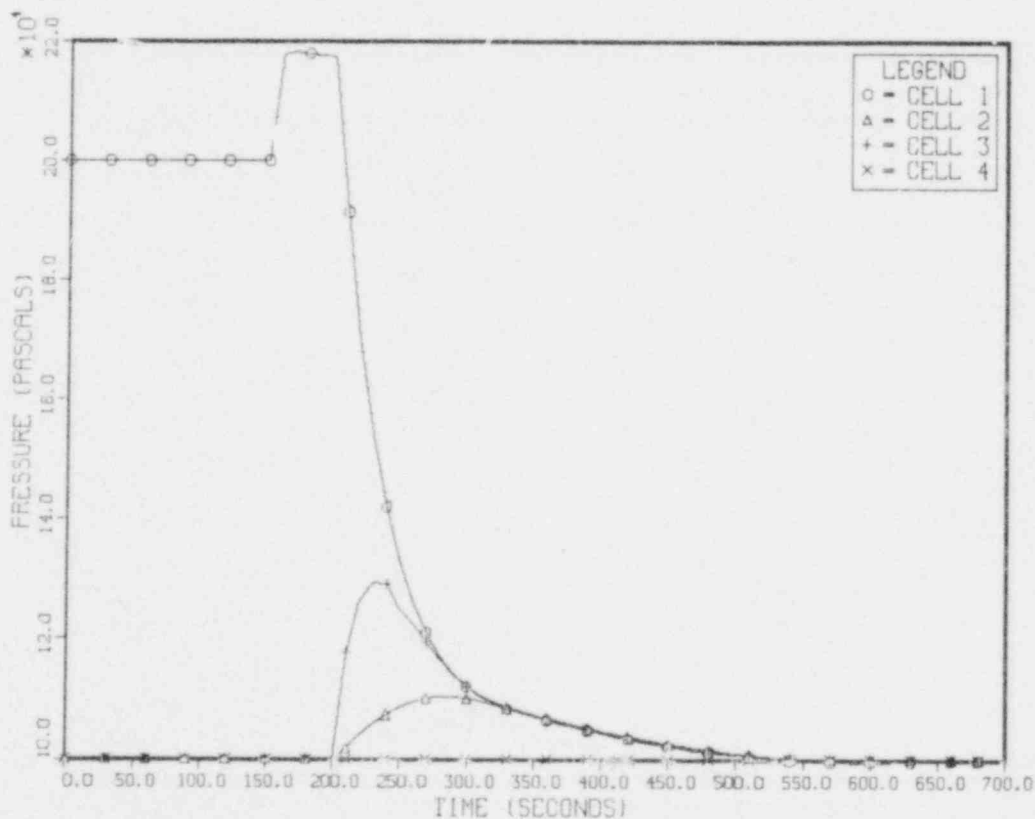
Figure 5.3-1 Pressure History in All Cells
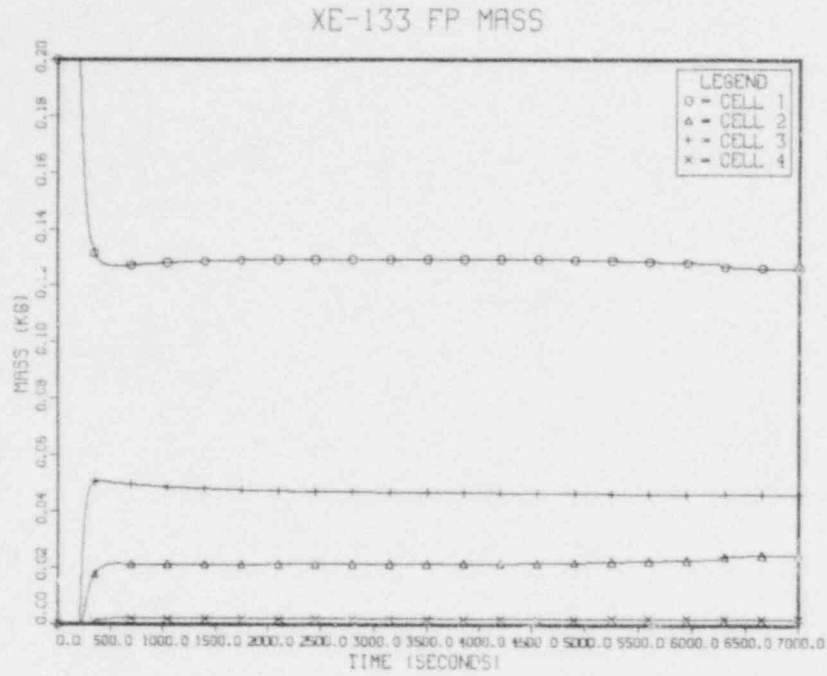
Figure 5.3-2   Concentration of a Gaseous Fission Product in
All Cells as a Function of Time

POOL TEMPERATURES AT T=   64.000
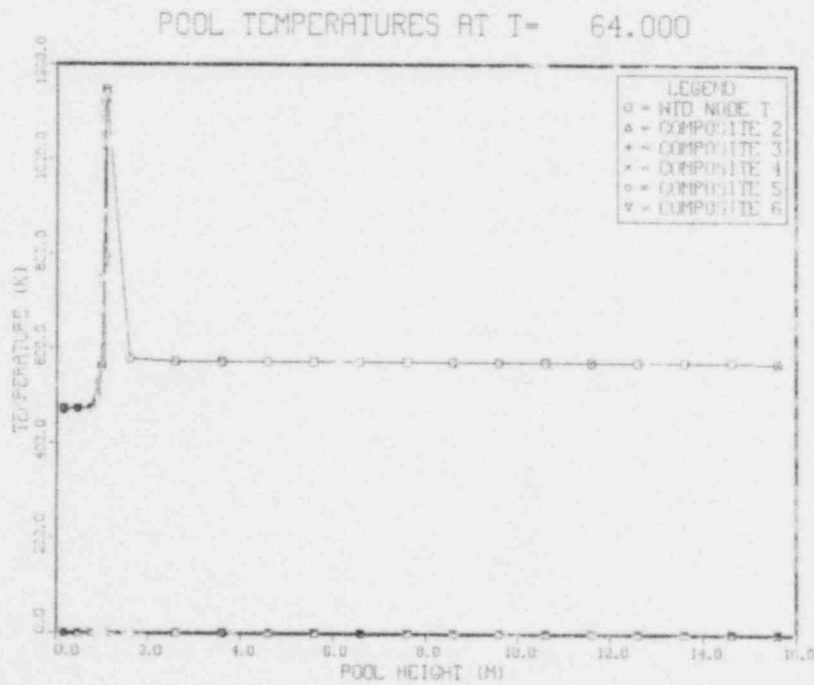
Figure 5.3-3   Temperature Map of the Cavity Structure,
Debris, and Sodium Pool at the End of the
Calculational Time

The calculations exemplify the checkout calculations underway during this period. In general, heating rates have been increased to allow shorter running times for these illustrative problems and do not reflect realistic estimates of postaccident heating rates in an LMFBR.

5.4 Code Modifications

Preliminary calculations have been used as a means of focusing on several areas of improvement that are required before a general user version of CONTAIN can be released. In the code framework, for example, the variable dimensioning scheme is being modified to include a library of array pointers to facilitate future code additions or deletions. A general library of thermophysical properties is being included to be used as a default for user-supplied properties.

A general time-step control system is being included to allow user selected time steps in selected time zones, code-selected time steps, or a combination of both. Currently, most time steps (system, cell, and physics model) are fixed at input. Input and output logic and options are being included. A post-processor plot package has been written to plot selected quantities from a CONTAIN data tape. This plot package is being modified to allow three dimensional and schematic data displays for selected data. These code-framework modifications are scheduled for completion in the second quarter of FY 1980.

A revised aerosol module has been developed during this period which will be included in the second quarter. This module will treat an arbitrary particle size distribution by a sectional (histogram) approach and allow multiple aerosol species to be included along with aerosol condensation effects. Condensation on surfaces will also be included in the atmosphere phenomenological models.

The fission product relocation scheme is currently very preliminary and is expected to be modified to account for fission product relocation effects due to decay and physical changes. This scheme will be covered in detail in the next quarterly report.

6. ELEVATED TEMPERATURE DESIGN ASSESSMENT
(E. P. Chen, 4442; D. V. Swenson, 4442;
W. A. Von Riesemann, 4442; W. B. Jones, 5835;
J. A. Van Den Avyle, 5835; S. W. Key, 5521;
D. W. Lobitz, 5521; C. M. Stone, 5521)

6.1 Uniaxial Creep-Fatigue Behavior

6.1.1 Creep Testing

No creep testing was performed during the current reporting period.

6.1.2 Creep-Fatigue Testing

Three low cycle fatigue tests of 316 stainless steel were initiated for sequential, surface Doppler-broadening positron annihilation (PA) measurements. The test conditions, listed below, are the same as those used previously for specimens which were sectioned for PA measurements.

Specimen	$\Delta\epsilon_t$ (%)	Temperature (^{O}C)
316-SLF-8	0.6	20
316-SLF-16	1.8	20
316-SLF-17	0.5	593

Surface PA readings are being taken at five cyclic intervals to determine the response of this technique as it represents lineshape parameter versus fatigue cycles. Two intervals have been measured for each specimen.

6.1.3 Non-Destructive Test Program

6.1.3.1 Ultrasonic Testing -- No ultrasonic testing was performed during this reporting period.

6.1.3.2 Positron Annihilation (PA) -- Setup was completed on an apparatus to make Doppler-broadening PA measurements on the surfaces of gauge sections of fatigue test specimens. This setup allows sequential measurements to be made on a

159

single sample with increments of mechanical deformation (monotonic or fatigue cycling). Tests were started on three samples to compare results previously generated using a technique which required specimen sectioning and thus multiple specimens to determine PA lineshape parameter versus damage (Section 6.1.2).

6.1.4 Microstructural Analysis

Transmission electron microscopy has been completed on nine samples of 316 stainless steel exposed to several mechanical histories at 866 K (593°C). These include thermal aging only for 8000 hr, creep at 200 MPa for 3221 hr, and seven creep-fatigue tests lasting as long as 1230 hr. Observations from this microscopy are being organized for comparison with previously published results and a report will be issued.

6.1.5 Multiaxial Test Facility

Additional tests were conducted on tubular specimens for the multiaxial facility to check on uniformity of strain distribution. A 316 stainless steel specimen with a radius to thickness (r/t) ratio of 5.23 was cycled at room temperature over total axial strain ranges of 1.0% and 0.5%. Measurements at several cyclic intervals showed that the gauge section remained uniform in diameter with no tendency on the part of the circular cross section to assume an oval cross section. The sample fractured near the center of the gauge length. A thinner walled specimen with an r/t ratio of 9.54 was compressed to a total axial strain of -2.0%; it showed bulging near the shoulder fillet at compressive strains above -1.0%, but strain in the center 3.8 cm of the specimen was uniform. This thin-walled design appears suitable for tests at low strain limits and has a value of r/t which produces a more uniform strain distribution throughout the thickness.

6.2 Creep-Fatigue Damage Analysis

Initial analysis of the thin walled multiaxial specimen were completed using the MARC computer code. Two loading cases were examined:

1. Monotonic axial compression of the specimen at 294 K (70°F).

2. Cyclic loading of the specimen at 866 K (1100°F).

Results of the analyses were examined for stresses and displacements; code-type creep-fatigue predictions of failure were not performed.

Figure 6.2-1 shows the axisymmetric model used in the analysis. Magnified displacements for monotonic compression loading are shown in Figure 6.2-2. Figure 6.2-3 gives displacement plots for cyclic loading and Figure 6.2-4 shows the inner surface cyclic strain range along the axis of the specimen.

a. ENTIRE SPECIMEN

b. DETAIL OF TRANSITION REGION
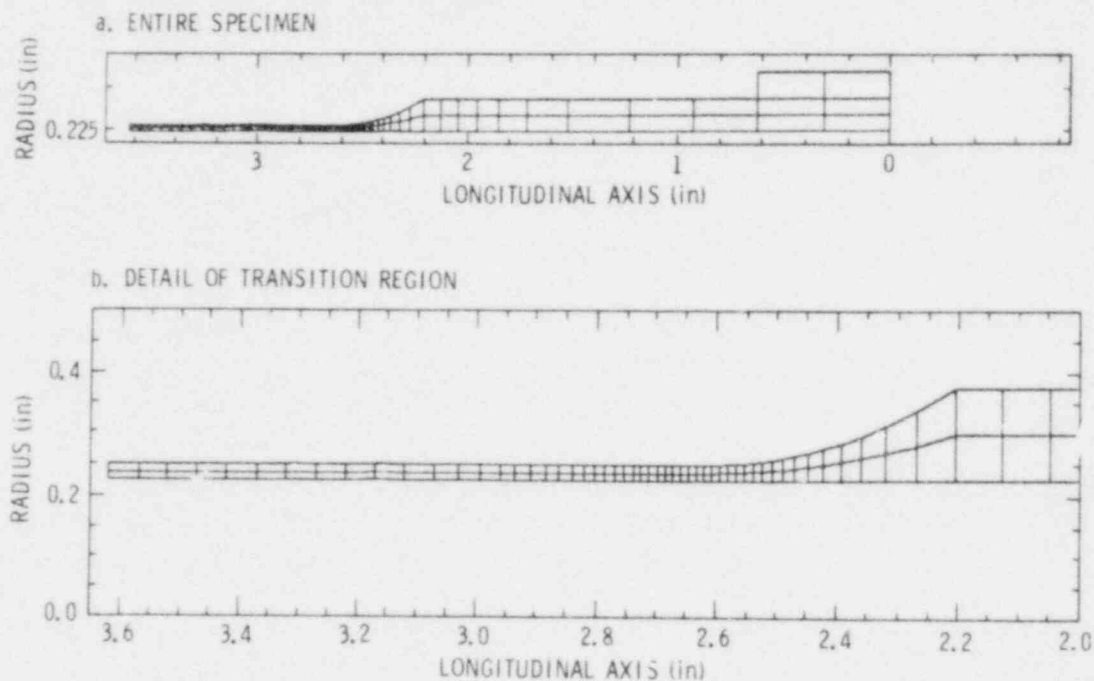
Figure 6.2-1   Multiaxial Specimen Finite Element Mesh

For uniaxial compressive loading, an examination of the load/displacement curve shows no significant buckling of the specimen up to an axial strain of 0.05 mm/mm (the end of the analysis). For cyclic loading, the largest predicted cyclic strain range occurs outside the gauge section. This indicates the specimen will fail outside the gauge section. However, there is some uncertainty in this conclusion since the peak strain range is only slightly greater than the nominal strain range in the gauge section. Also, cyclic material hardening (which was not included) could shift the location of the peak strain range. Before detailed creep-fatigue evaluations are performed, program investigators recommend that the material model be modified to include cyclic hardening. A report documenting the results is in preparation.

a. UNDEFORMED

b. AXIAL STRAIN 0.02 in/in
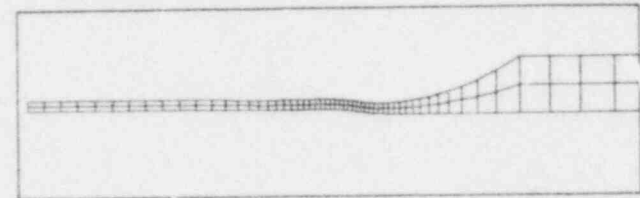
c. AXIAL STRAIN 0.05 in/in

Figure 6.2-2

Monotonic Loading Displacement Plots
(Magnification = 5)

a. COMPRESSION

b. TENSION

c. COMPRESSION
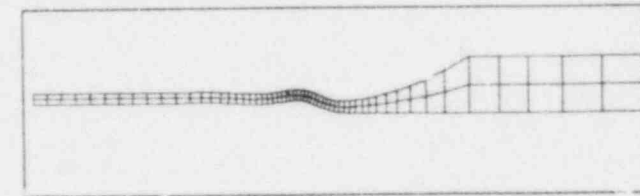
Figure 6.2-3

Cyclic Loading Displacement Plots
(Magnification = 20)
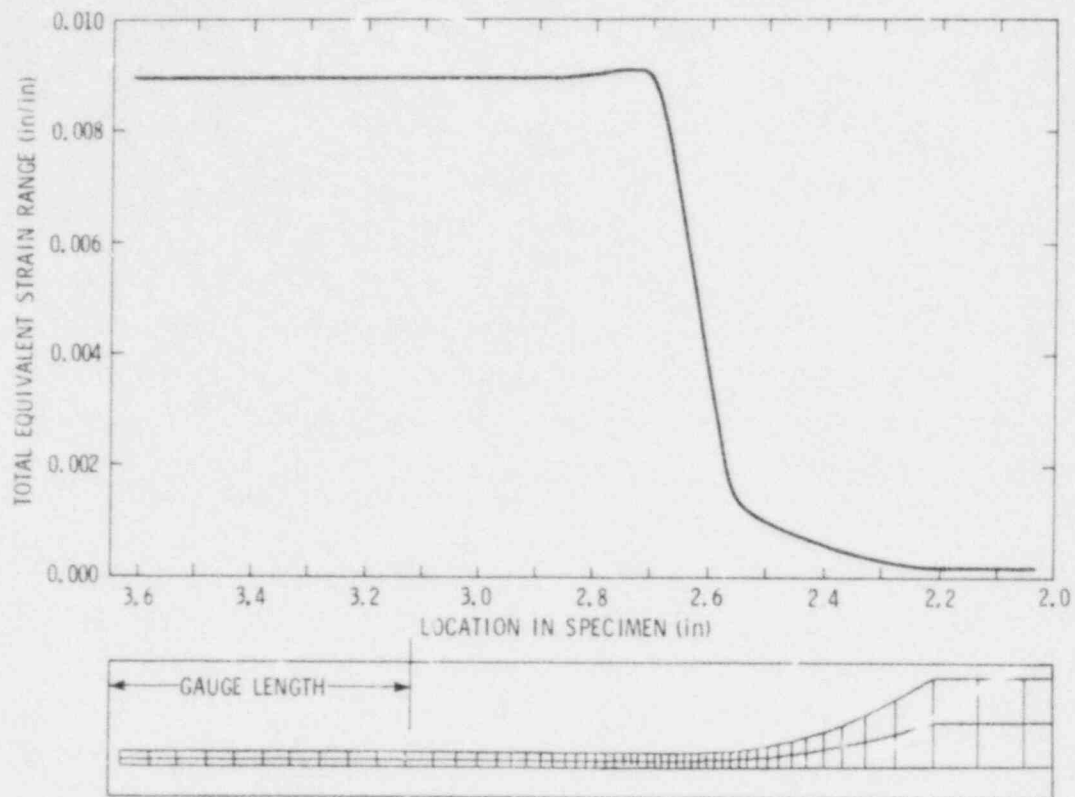
Figure 6.2-4   Cyclic Strain Range Distribution

6.3   Structural Analysis

Work on a report in the piping elbow analysis continued this quarter.

6.4   Structural Evaluati ʋ

Technical review of the Westinghouse Clinch River Breeder Reactor Plant
Piping Document (WARD report CRBRP-ARD-0185) was continued.   Considerable on-
going effort will continue to concentrate on the "leak-before-break" arguments set
forth in the report.   The initial activity will be an investigation oɪ the liʼerature to
review the efforts to date to establish this concept.   The "leak-before-break" concept
seems to have a relatively firm footing for use with brittle materials.   This apparent
acceptance is attributed to the establishment and acceptance of the K_{IC} approach for
determining critical crack lengths, and to the observation that, at least in straight
pipes, surface cracks tend to grow through the thickness without significant lengthen-
ing.

For ductile materials the vigorous establishment of this concept is much more difficult, even though intuitively crack propagation in these materials would seem to be much more inhibited than in brittle ones. The main difficulty centers around the lack of proven analytical techniques for determining such things as critical crack length, rate of fatigue-crack growth, and the morphology of the growth of surface cracks. Further complications arise through unknowns associated with creep effects (for temperatures greater than 700 K (800°F)) and complicated loadings which are present in piping elbows. In the absence of analytical tools for establishing this concept in ductile materials, an experimental approach may still be viable. However, for the complete primary and intermediate heat transports system, this task would be very time-consuming and costly.

To date the literature review has concentrated on a survey of analytical techniques that are available for the prediction of critical crack lengths in ductile materials. Techniques such as the Paris instability model, R-curve analysis, crack opening displacement method, and the J-integral are currently being studied.

7. LMFBR ACCIDENT DELINEATION

7.1 Engineered Safety Systems (J. A. Sholtis, 4424)

During this period, the basic LMFBR initiating accident event tree was modified to distinguish between protected accidents in which core disruption is inevitable and protected accidents in which core disruption may or may not ultimately occur. In this latter case, core disruption can occur if forced flow is not provided and natural circulation proves to be inadequate and/or core damage is induced by the initiator, precluding core coolability. Both of these potential core disruptive mechanisms apply to the situation where a heat-transport path to an ultimate heat sink is available after successful reactor SCRAM has occurred. This class of protected accident in which core disruption may or may not ultimately occur has been labeled "CDA Possible" in the Accident Initiation and Engineered Safety Systems (ESS) Response Area with resolution of their outcome deferred to analysis in the Accident Phenomenology Area.

To accomplish these modifications, the Shutdown Heat Removal System (SHRS) functional question at the event tree branch point was redefined and an additional branch point question was introduced to address the flow conditions existing after successful SCRAM when an adequate heat transport path to an ultimate heat sink is available. Figure 7.1-1 illustrates the CRBRP initiating-accident event tree that results from these modifications. The SHRS success branch in Figure 7.1-1 now refers to an available heat transport path to an available ultimate heat sink for the removal of decay heat. The SHRS question no longer says anything about the flow conditions available for decay heat transport nor does it address core damage which might preclude core coolability. However, the SHRS question does include other intrinsic SHRS conditions which would preclude decay heat removal such as an insufficient sodium level in the reactor vessel. This redefinition of the SHRS ensures that when the SHRS is unavailable, core disruption via melt is inevitable and is only a matter of time. Sequence C in Figure 7.1-1 represents this scenario. The initiating-accident categories illustrated for Sequence C in Figure 7.1-1 can be narrowed down to the actual category involved by considering the specific accident initiator and its potential for affecting primary boundary integrity (which governs the potential for a release) and/or core

integrity. In all cases the initiating accident categories identified at the Sequence C end point include the label "CDA Inevitable," implying that subsequent analysis in the Accident Phenomenology section will determine the timing preceding whole-core disruption by melting and the final system and plant damage that results.
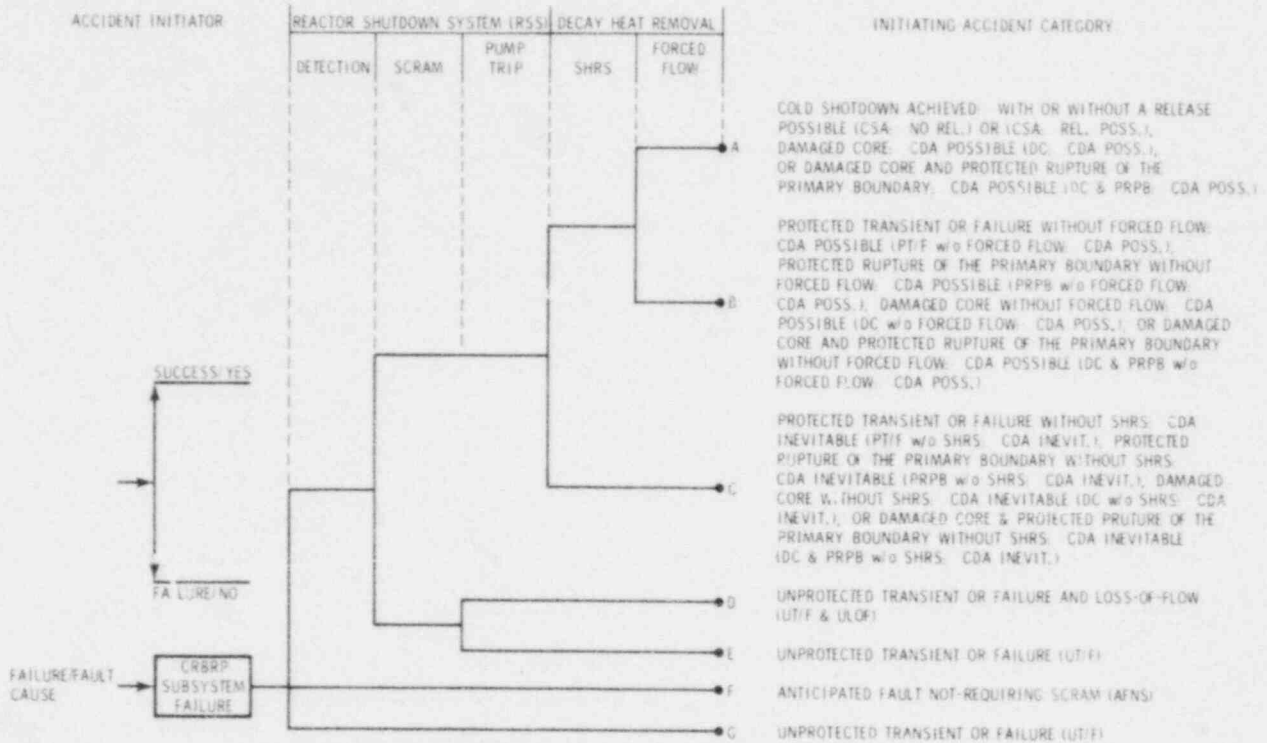
Figure 7.1-1   Modified Initiating-Accident Event Tree for a Generic Subsystem Failure in CRBRP

If the SHRS is available, the event tree in Figure 7.1-1 next determines whether natural circulation or forced flow is provided to transport decay heat to the ultimate heat sink. If forced flow is provided, cold shutdown will be achieved so long as core integrity and coolability are assured; i.e., initiator-induced core damage beyond the design basis has not occurred. ("Cold Shutdown" here means that the reactor is successfully SCRAMMED and decay heat is adequately removed over the short and long-term.) Sequence A in Figure 7.1-1 displays the possible initiating-accident categories for this basic scenario; i.e., when the SHRS is available with forced flow after successful SCRAM. The actual initiating-accident category assigned will depend on the specific accident initiator involved and its potential to affect primary boundary integrity (which governs the potential for a release) and/or core integrity

(which governs the potential for core disruption). If initiator-induced core damage is involved in Sequence A, the scenario is labeled "CDA Possible" and requires further analysis in Accident Phenomenology.

If forced flow is not provided to an available SHRS, as illustrated by Sequence B in Figure 7.1-1, then only natural circulation is available for transporting decay heat from the core to the primary sodium and from the reactor vessel to the ultimate heat sink. Since the establishment and adequacy of natural circulation in the CRBRP, even for an intact system and plant, is still an unresolved issue (not to mention the question of adequacy of natural circulation for damaged core scenarios), Sequence B scenarios are always labeled "CDA Possible." Either cold shutdown will be achieved or core disruption will occur based on subsequent analysis (in Accident Phenomenology) of the actual core/system response to operating without forced flow and either with or without initiator-induced core damage.

In all cases where "CDA Possible" is identified for an initiating-accident category resulting from Sequences A and B in Figure 7.1-1, resolution of the final outcome is deferred to analysis in Accident Phenomenology where it rightfully belongs since "CDA Possible" is only assigned when core damage is involved and/or natural circulation adequacy is in doubt; the response of the system to natural circulation and/or core damage involves phenomenological questions.

Since "CDA Possible" and "CDA Inevitable" protected accidents both require phenomenological analysis, they are both treated within a single event tree in Accident Phenomenology. This event tree includes initiation questions as well as phenomenological questions since the action of the initiator can also affect the accident progression. This protected accident event tree in Accident Phenomenology first determines whether "CDA Possible" scenarios lead to eventual core disruption or to the ultimate achievement of cold shutdown. For those "CDA Possible" scenarios that lead to cold shutdown, no further phenomenological analysis is necessary. However, for those "CDA Possible" scenarios that are shown to lead to eventual core disruption, the phenomenological analysis continues, first by combining them with the "CDA Inevitable" protected accident scenarios, then by determining their timing to whole-core disruption via melt, and finally by assessing the final system/plant damage sustained as a result of their complete progression. Accident Initiation and ESS Response information necessary for meaningful delineation of protected accidents in CRBRP has been provided for

incorporation into and development of a new protected accident event tree in Accident Phenomenology. The previously developed protected accident phenomenology event tree, which only delineated timing to whole-core disruption for "CDA Inevitable" protected accidents, will be used to the extent possible in constructing this new protected accident event tree for the Accident Phenomenology area.

Because the definition of SHRS unavailability was modified as stated above, the SHRS fault tree developed for the CRBRP had to be revised also. This revision was accomplished during this period along with finalization of the Detection and SCRAM fault trees for the CRBRP.

Preparation of the Accident Initiation and ESS Response sections for the LMFBR Accident Delineation Study, Phase I Final Report began during this period. Although report preparation was temporarily halted to accomplish the modifications identified above, it has since continued with satisfactory progress and delineation has been improved.

Amendment No. 51 to the CRBRP Preliminary Safety Analysis Report (PSAR) was received. This amendment includes design and analysis information concerning the new CRBRP reference core design (bullseye heterogeneous configuration). Review of Amendment No. 51 was initiated and information about the CRBRP bullseye heterogeneous core and other associated system design changes will be incorporated into the draft version of the Phase I Final Report to the extent that time permits.

7.2   Accident Phenomenology (D. C. Williams, 4424)

Local Fault Propagation (LFP) accidents are being delineated in terms of a generic event tree organized along two lines of defense (LODs) against propagation up to whole core involvement. Termination at LOD-1 corresponds to detection and shut-down at a point where the damage can be coped with by relatively routine procedures, e.g., replacing the subassembly containing the fault using normal fuel handling proce-dures. This mode of termination is the intended mode and in CRBRP, it corresponds to detection of the fault by the Failed Fuel Monitoring (FFM) system and operator-initiated shutdown. LOD-2 corresponds to shutdown due to generation of signals that trip the Plant Protection System (PPS) sensors designed primarily to guard against whole core initiators. In general, this will involve a much greater degree of core damage than detection at LOD-1, but it still may be possible to prevent a full CDA.

The underlying rationale for this approach was discussed briefly in the pre-vious quarterly report[7-1] and will not be reviewed here. During this period, work centered upon applying the LOD-1 portion of the generic tree to a number of specific LFP initiators and assigning qualitative relative probability judgments to some of the key branch points. This format was used to summarize the review of LFP acci-dents given in the CRBRP PSAR to offer some critical comments on that review, and to consider the utility of some additional detection techniques for strengthening LOD-1. In summarizing the principle results, dividing local fault initiators into two classes is useful, as follows:

a. The initiator involves only a single pin, or at most a few pins; examples include stochastic endurance failure of clad and an over-powered pin.

b. The initiator involves a large number of pins, e.g., an entire sub-assembly. An overpower subassembly and the blockage of the inlet flow to a subassembly would be examples.

For the first type of initiator, the evidence reviewed in the CRBRP PSAR is reasonably convincing that LOD-1 offers a strong defense against propagation to a large-scale accident. In this type of fault, pins in the vicinity of the pin undergoing the first failure are themselves normal, and no mechanisms have been identified for inducing rapid propagation of failures among pins that are initially normal. Any propagation is expected to be slow, allowing ample time for detection, operator

response, and shutdown. Though the arguments offered in support of these conclusions are fairly convincing, some points were identified at which the analysis could be strengthened, in view of the low probability that must be demonstrated for large scale propagation if safety is to be judged acceptable.

In the second type of fault, a large number of pins are in an abnormal condition and perhaps much closer to their failure thresholds at the time the first failure occurs. In this case, rapid propagation among all the pins within the fault region is much more difficult to rule out. Furthermore, the sensors for LOD-1 in CRBRP (the FFM system) are sensitive to fuel failure effects only, and the fault is, therefore, unlikely to be detected before pin failure occurs. The PSAR, in fact, places considerable reliance on the extensive precautions taken to prevent this type of fault from occurring in the first place. No doubt these measures should keep the probability of such faults very low, but it is not clear that they can be shown to be so improbable as to be acceptable, given the assumption that such an initiator will inevitably result in a CDA. Hence, demonstrating that additional lines of defense (i.e., defense other than prevention) do lie between the occurrence of the initiator and the occurrence of a large-scale accident is desirable. Though this may prove possible to do, it was not always done in the PSAR; arguments were sometimes limited to why the initiator was extremely unlikely, without any consideration of what would happen if it did occur.

If the case against large-scale propagation is judged inadequate, one approach would be to strengthen LOD-1 by providing additional means of protection, perhaps tied into the PPS. For the second category of fault noted above, detection before fuel failure can be especially valuable. Detection methods based upon analysis of reactor noise (acoustic, thermal, and neutronic) has received considerable study; such techniques have shown considerable promise but they have not been brought to the point of proven effectiveness nor do they clearly provide the best protection against faults presenting the greatest potential threats. Monitoring of individual subassembly outlet temperatures would be useful protection for some initiators.

Delineation of the late stages (subassembly scale disruption and larger) is now underway and will not be treated in detail in the present study.

Delineation of protected accidents (i.e., shutdown succeeds but a CDA still may result due to inadequate decay heat removal) has also begun. A generic event tree is being developed for protected accidents.

In addition to the preceding activities on Phase I of the Accident Delineation Study, the work plan for Phase II is being revised substantially to reflect the planned closer integration of the Study with accident analysis code results. During the report period, significant time was also devoted to preparing for the ACRS meeting, November 18 through 30.

7.3   <u>Postaccident Phenomenology</u> (P. W. Conrad, 4424)

A reorganization of the Primary Envelope and Containment Response event trees into a large number of smaller and less complex trees has been completed. Each tree now applies to one of three regimes: In-Vessel PAHR, Reactor Cavity Response, and Upper Containment Response. A complete accident sequence can be traced by placing these three sections in series, except in cases where reactor vessel failure does not occur and the cavity response can be bypassed. In addition, the following improvements have been incorporated:

1. Although not previously considered, the unlikely possibility of energetic recriticality due to fuel slumping in the reactor vessel or in the reactor cavity after meltthrough, is now addressed without adding undue complexity to the corresponding event trees.

2. Primary sodium spills which do not lead to core disruption but have the potential of developing release pathways can now be treated directly in the reactor cavity and upper containment event trees.

3. All trees have been made as generic as feasible but have been applied to the specific CRBRP design as a demonstration example.

Preparations were made for presentations before the ACRS review meeting and the composition of the final Phase I report.

Reference for Section 7

7-1   <u>Advanced Reactor Safety Research Quarterly Report, July-September 1979,</u> SAND79-2158, NUREG/CR-1141 (Albuquerque, NM: Sandia National Laboratories, Advanced Reactor Research Department, April 1980).

8. TEST AND FACILITY TECHNOLOGY

8.1 ACRR Fuel Motion Detection System (J. G. Kelly, 4426; K. T. Stalker, 4426; D. A. McArthur, 4426; P. J. McDaniel, 4231)

8.1.1 Introduction

The fuel-motion-detection system for the ACRR has been developed to monitor the movement of fuel in simulated core disruptive accidents. Recent advances in data recording technology have been incorporated into this system so that the position of test fuel can be determined on millisecond timescales with millimeter spatial resolution by detecting gamma rays passing through a slot in the ACRR core and through a coded aperture. The coded image formed in a thin scintillator is amplified by an optical image intensifier and recorded by a high-speed framing camera. Because of the limitation imposed by the 3-m diameter reactor tank, the detection system is only about 1.5 m from core centerline and must be protected by a massive radiation shield.

This report covers three subjects. The first section will review the results and conclusions reached following the first full-scale test of the system, conducted in July 1979. The second section contains a detailed discussion of the studies that are being conducted and the changes that will be made in the system to improve its performance. These changes are dictated by experience gained in the full-scale proof test and by additional experiments and analyses which are continuing. The immediate objective is to ready the system for prompt burst energetics tests to be conducted in June 1980. Finally, the third section will update the analysis of the FM1 test.

8.1.2 Update on System Performance

In previous quarterlies the following observations about the system performance in the ACRR were made:

    a. In the slotted configuration, the ACRR core can be operated effectively during both steady-state and pulsed operation with only two transient rods.

b. The temperature rise in the lead collimators is not enough to cause damage in pulsed operation up to 250 MJ.

c. High-quality coded images of a 20% enriched pin were obtained on x-ray film. The background coming from the bulk shield and through the collimator comprises approximately 90% of the exposure on the film.

d. The signal observed with the active system scintillator was considerably poorer than that obtained with x-ray film. It constitutes approximately 1 to 2% of the total exposure when a 50% enriched pin is observed. This indicates that the scintillator is more sensitive to some backgrounds than is x-ray film.

e. Despite the low contrast in the scintillator, reconstructible coded images of fuel moving after disruption in ACRR were obtained that show both axial and radial motion.

f. The contrast in the coded image was greatly increased just after SCRAM. The backgrounds generated by neutrons are expected to die off much faster than would the delayed gamma rays emitted by the pin.

g. An additive background is induced in the image intensifier by the radiation, and additional shielding for this component is called for.

h. A back-illuminated x-ray film with a coded image obtained in the ACRR was recorded with good contrast by the active system during steady-state operation of the core.

i. Thin filters, in the collimator, for thermal neutron and soft gamma-ray attenuation have not provided very much improvement in signal-to-background ratio.

j. The neutron flux inside and outside the collimated beam is almost the same, indicating that the primary source of neutron flux at the detector may be the bulk shield. For a 95 MJ burst the detector sees about 3×10^{10} n/cm^2.

k. Calculations of detector response to gamma rays predict only small differences between scintillators and x-ray film (placed between Ta sheets). This contradicts the experimental results from the ACRR, indicating that direct neutron interactions in the scintillators may be responsible for the differences. This conclusion may yet be modified.

Two general conclusions can be drawn from studying the list above. First, more shielding is needed to protect the scintillator and the image intensifier. Second, the full potential of the system can be attained if a scintillator can be found which responds as x-ray film does. These conclusions came about because the x-ray film and active recording systems work well in the reactor environment.

8.1.3 Program for Improving the Coded Aperture Imaging System (CAIS)

The program for improving the CAIS has been broken down into five principal areas: (a) scintillator development, (b) radiation transport calculations, (c) modifications to the main shield, (d) scene beam studies, and (e) image reconstruction development. The first four areas are intimately interconnected because radiation-transport and scintillator response functions along with experiments will determine what shielding and beam collimator changes will lead to a better recorded signal-to-noise ratio.

8.1.3.1 <u>Scintillator Development</u> -- The calculated responses of scintillators and x-ray film to photons and to electrons (as reported last quarter) are not dramatically different. $CaWO_4$ and $BaSO_4$ tend to be about twice as sensitive to photons in the 100-keV range as the x-ray film. Therefore, if the background photons tend to be of lower energy, the performance of these scintillators might be poorer than the film. However, neutron-related background effects may be important also, and because the neutrons will in turn generate additional gamma rays, the response of the scintillator to the secondary radiations generated by the neutron reactions must also be examined.

8.1.3.1.1 <u>Neutron-Related Background Mechanisms in the Scintillator</u> -- Several possible neutron-related background mechanisms have been investigated using order-of-magnitude calculations: (a) neutron capture in the phosphor of the scintillator or in the Ta of a converter foil frequently used; (b) (n, p) scattering of energetic neutrons in the hydrogenous binder of the scintillator; and (c) inelastic scattering of high-energy neutrons in the phosphor of the scintillator or the Ta converter. In (a) and (c) the actual energy is deposited in the scintillator by gamma rays or internal-conversion electrons originating from excited nuclei. In mechanism (b) the recoil energy of the scattered proton is deposited in the binder and the phosphor, and presumably only that fraction deposited in the phosphor particles actually gives rise to the observed background. For typical phosphor particle sizes (diam $\approx 10\,\mu m$) and binder volume fractions ($\approx 50\%$), recoil protons with energies ≥ 20 keV will reach a phosphor particle.

8.1.3.1.1.1 <u>Photon and Electron Transport in the Scintillator and Film Pack</u> -- The transport of gamma rays and internal conversion electrons through typical scintillator and x-ray film pack geometries has been investigated with the Sandia coupled electron-photon Monte Carlo code TIGER.[8-1] using appropriate updates supplied

by J. A. Halblieb, Sr. of Sandia. This code has also been used to calculate the response of scintillators and x-ray film to the fission gamma ray spectrum (i.e., the "signal" spectrum which is to be imaged) after it has been filtered by the experiment package and by the various walls of the CAIS. Realistic dimensions and material compositions were used for these calculations.

Because the sensitive regions of the scintillator and x-ray film are thin (0.05 cm and 0.005 cm, respectively), most of the gamma radiation generated by neutron capture or neutron inelastic scattering might be expected to escape without depositing significant energy in the sensitive region. However, since the sensitive regions are so thin, the energy deposited by the signal photons is also very low. Therefore, the TIGER code was first used to calculate the energy deposition in various scintillator phosphors, resulting from photons of varying energies which originate from the signal beam or from various potential background sources. Figures 8.1-1, 8.1-2, and 8.1-3 show the energy deposited in $CaWO_4$, $BaSO_4$, and ZnS phosphors, per photon originating either in the signal beam, in the Ta converter, or in the phosphor itself, respectively. In these calculations, the signal photons are normally-incident, while the Ta and phosphor photons are emitted into 4π sterradians.

Figure 8.1-1 Energy Deposited in $CaWO_4$ $BaSO_4$, and ZnS Phosphors per Photon Originating in the Signal Beam (Detector structure: 0.063 in. Al/0.005 in. Ta/0.020 in. Scintillator)

Figure 8.1-2   Energy Deposited in CaWO$_4$, BaSO$_4$, and ZnS Phosphors
per Photon Originating in the Ta Converter (Detector
structure: 0.063 in. Al/0.005 in. Ta/0.020 in. scintillator)

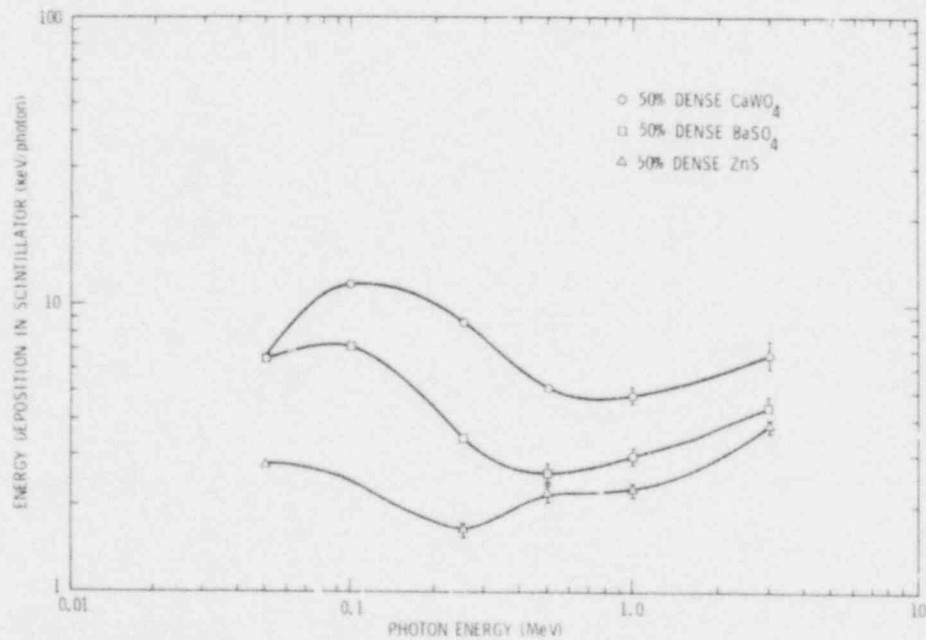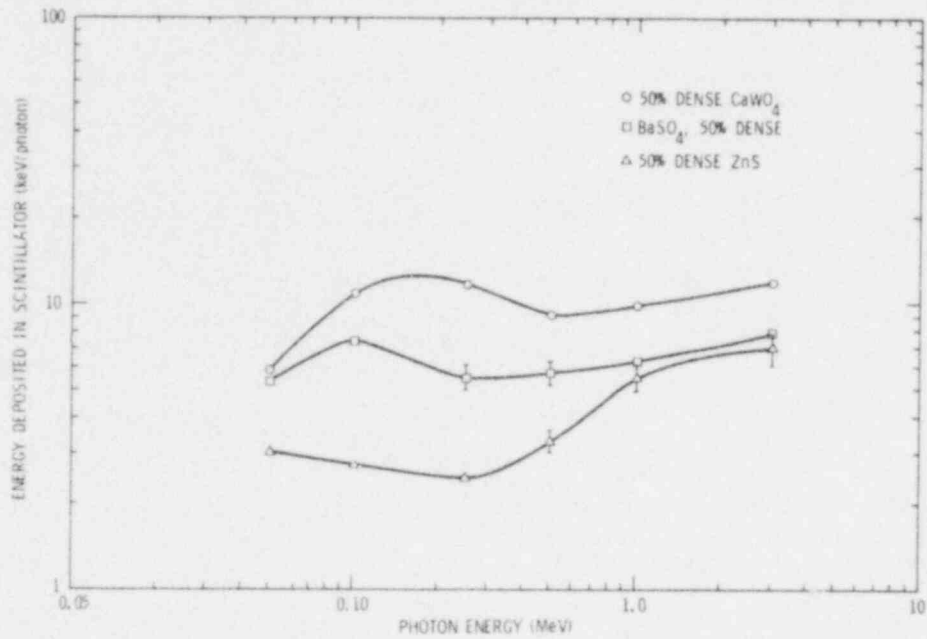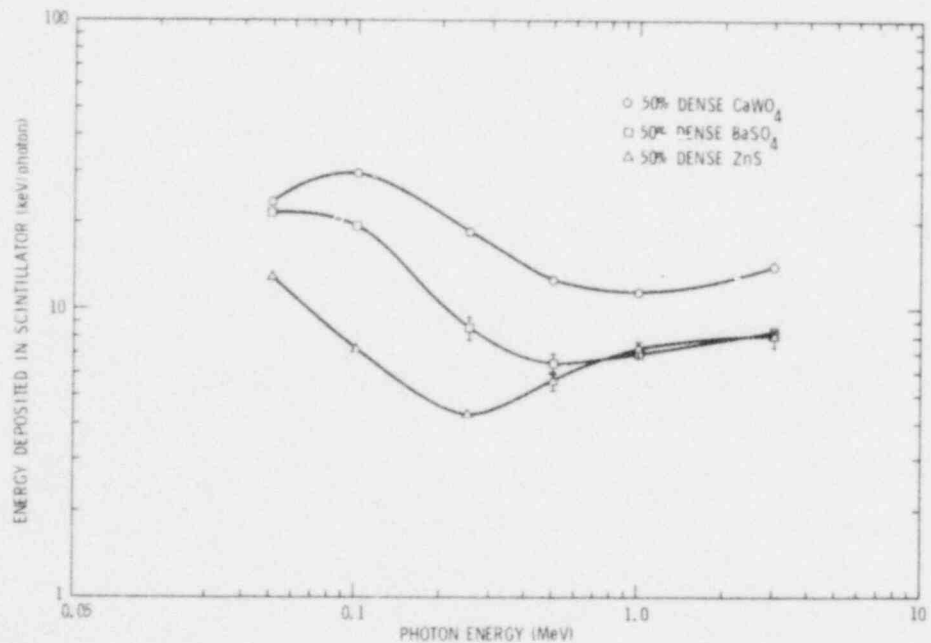Figure 8.1-3   Energy Deposited in CaWO$_4$, BaSO$_4$, and ZnS Phosphors
per Photon Originating in the Phosphor Itself (Detector
structure: 0.063 in. Al/0.005 in. Ta/0.020 in. scintillator)

Figures 8.1-1, 8.1-2, and 8.1-3 show differences in sensitivity among the individual phosphors, but phosphors which are more sensitive to the signal are typically also more sensitive to background photons. Low-energy photons deposit a much larger fraction of their energy than do high-energy photons (varying fo. example in Figure 8.1-3 in $CaWO_4$ from about 30% at 100 keV to less than 0.5% at 3 MeV). Thus, the low-energy portion of the capture-gamma spectrum, which is more difficult to measure and contributes little to the total de-excitation energy, is in fact most important in contributing to scintillator and x-ray film backgrounds. Finally, comparing Figure 8.1-1 with Figures 8.1-2 and 8.1-3 shows that at least twice as much energy is deposited per background photon than per signal photon. (Part of this may be accounted for v the recognition that energy deposited by photons generated in the scintillator will increase as thickness squared, but energy deposited by signal will only rise linearly with signal. These relationships occur because the source strength for the generation of photons in the scintillator is proportional to the thickness.) Therefore capture-gamma radiation may well be a significant source of background, but further calculations with measured capture-gamma ray spectra will be necessary to estimate the importance of this source.

For low-energy, forbidden gamma-ray transitions in high-Z nuclei, the nucleus may eject an atomic electron rather than er it a gamma ray for de-excitation.[8-2] These internal conversion electrons are acc apanied by characteristic x-rays which are emitted when the "hole" left by the ejected electron is filled. Both the conversion electrons and the characteristic x-rays are much more likely to deposit most of their energy in the thin scintillator structure, and are therefore likely to be very important components of the total background in spite of their small contributions to the total de-excitation energy of the nucleus.

The energy spectra of the capture gamma rays and the conversion electrons to be used in more detailed TIGER calculations are very important. In the low-energy region (≤ 1 MeV), detailed spectra for both capture gamma rays and internal conversion electrons have thus far been located only for Ta.[8-3] Although other capture-gamma ray spectra for $E \geq 0.2$ MeV are available for Ag, Ta, and W (the elements which contribute most to thermal neutron capture),[8-4] these spectra are probably unreliable for $E \leq 1.5$ MeV. Most of the tabulated gamma ray and conversion electron data[8-5] apply to the delayed decay of daughter nuclei resulting from neutron capture, and are thus not directly applicable to the prompt radiation which appears to be causing much of the scintillator background.

However, an estimate of the energy deposition caused by neutron capture can probably be obtained by using a combination of data from References 8-3 and 8-4. Therefore, the energy depositions in the sensitive layers of the scintillator and the x-ray film were calculated, including contributions from neutron capture in the Ta sheet, in the $CaWO_4$ scintillator, and in the Ag of the x-ray film emulsions. For these calculations the measured Ta, Ag, and W capture-gamma spectra of Reference 8-4 were used over the photon energy range $0.15 \leq E \leq 6$ MeV, but the Ta conversion-electron spectrum of Reference 8-3 was used not only for capture in Ta, but also in Ag and W, over the electron energy range $0.03 \leq E \leq 0.4$ MeV. The characteristic x-rays associated with the conversion electrons were neglected. A 0.05-cm-thick NDT/HI-PLUS scintillator was assumed ($CaWO_4$ with binder), and two 0.0025-cm-thick film emulsions were assumed on either side of the 0.015-cm-thick plastic film base. The results are shown in Table 8-I, expressed as keV deposited in the sensitive layer, per neutron captured in the radiation source layer. For comparison, the energy deposition produced by the fission gamma ray "signal" from a fuel pin viewed through the CAIS walls is also shown in Table 8-I (per gamma ray reaching the detector plane).

Table 8-I

Energy Deposition for Signal and Background Sources

Source	Radiation Type	Scintillator Deposition (keV/event)	X-ray Film Deposition (keV/event)
Signal	γ	5.2	0.69
Ta	γ	41	12.6
	e	0.7	1.4
W (Scintillator)	γ	51	--
	e	88	--
Ag (Emulsion)	γ	--	15
	e	--	116

Several conclusions can now be drawn: (a) the "background" gamma rays deposit energy much more efficiently in the sensitive layers than the "signal" gamma rays; (b) conversion electrons are quite important if they are emitted in the sensitive layer itself, but not so important if they originate in the Ta converter; (c) the TA converter

is a significant source of background because of the gamma rays it emits. (This has not yet been proven experimentally.)

The preceding energy deposition figures are probably underestimated, since the spectrum for Ta (n, γ) rays[8-4] is considerably smaller for low energies than the more recent Ta (n, γ) data[8-3] and since the conversion electron calculation neglects the K, L, and M x-rays associated with conversion electron emission, and the less intense but more energetic conversion electrons emitted for γ-ray transitions with $E \geq 0.4$ MeV. The conversion-electron energy deposition caused by capture in Ag may be too large since the strong Z-dependence of the conversion-electron coefficient was neglected.[8-2]

8.1.3.1.1.2 Signal-to-Background Resulting From Neutron Capture -- The signal-photon fluence from the fuel pin corresponding to a 95-MJ ACRR operation for a typical fuel pin enrichment is 3.67×10^9 photons/cm^2. The corresponding total background neutron fluence at the detector plane is 3×10^{10} n/cm^2, with about 50% of these neutrons below the ~0.5 eV Cd cutoff. Neglecting absorption for neutron energies above 0.5 eV, the neutron captures per cm^2, N_c, for the materials of interest for a 95 MJ ACRR operation are given in Table 8-II.

Table 8-II

Neutron Captures for a Typical ACRR Operation

Material	N_c (Captures/cm^2)
Ta	1.84×10^8
W(NDT/HI-PLUS)	6.95×10^7
Ag (Emulsion)	1.44×10^7

The preceding results permit an estimate of the signal and background components in the x-ray film and the NDT/HI-PLUS scintillator (in keV/cm^2):

Detector	B(Ta Capture)	B(Det. Capture)	B (Total)	Signal
Ta/(NDT/HI-PLUS)	7.69×10^9	9.66×10^9	1.74×10^{10}	1.92×10^{10}
Ta/(X-Ray Film)	2.58×10^9	1.89×10^5	4.46×10^9	2.53×10^9

These results imply a signal-to-background $S/B = 1.1$ for the scintillator, and $(S/B) \approx 0.57$ for the x-ray film pack. The calculated S/B for the x-ray film is about ten times higher than that observed. The implication is that capture gamma events in the detector structure are not the principal source of background exposure in the x-ray film. It may have some effect in the scintillator.

Other background sources which might be important are inelastic scattering of energetic neutrons, energetic recoil protons created in the binder of the scintillator, and a smooth gamma ray background caused by scattering and emission from the general field of view on either side of the fuel pin being imaged. Inelastic scattering of last neutrons in the W of the scintillator is estimated to produce a background which is only 1% of the background caused by thermal neutron capture, and should therefore be negligible. The gamma ray "scene" background, as determined by an analysis of x-ray film will be discussed later; however, this background component should not be responsible for the large difference in performance of the scintillator and the x-ray film, because both detectors respond similarly to gamma rays incident from the front (assuming Ta converter foils are used on the x-ray film). The background caused by recoil protons from the binder is very sensitive to the assumed neutron spectrum and has been estimated by assuming an E^{-1} dependence for the measured neutron flux above the ~ 0.5 eV Cd cutoff. The assumption that all the recoil proton energy is deposited in the phosphor particles yields recoil proton backgrounds in the scintillator and the x-ray film of 30% and 15% of the thermal neutron capture backgrounds, respectively. Adding this recoil-proton contribution causes a calculated S/B of 0.84 for the scintillator and 0.50 for the x-ray film, which does not greatly improve the agreement with experiment. In fact, as is discussed in Section 8.1.3.4.2 below, direct (n, p) scattering effects have not yet been experimentally identified.

The disagreement of these calculated S/Bs with experiment is still quite large. Although there are several ways in which the calculation of the detector-package background from neutron capture can be improved upon, the present result points out that the answer may still lie elsewhere as will be discussed in the conclusion of this section (8.1.3.1.1). That improvements can be made in the neutron capture calculation is indicated by the fact that the x-ray film is calculated to be worse than the scintillator, and the fact that the calculated S/Bs are generally too high. Two calculational refinements might improve both of these discrepancies, to a limited extent, if the data for individual elements were available. These refinements are (a) use of

more accurate capture-gamma ray spectra and (b) use of the actual prompt conversion-electron spectra and the associated x-rays for the elements W and Ag. For example, if the more detailed capture gamma-ray data of Reference 8-3 rather than the data from Reference 8-4 are used to calculate backgrounds in the energy region $0.04 < E < 0.99$ MeV, there is virtually no change in the total gamma ray energy emitted, but the calculated background contribution from this part of the spectrum increases by up to a factor of 3. Similarly, the use of actual conversion-electron data for Ag might decrease the calculated x-ray film background significantly, since there is a strong Z^3-dependence of the internal-conversion coefficient.[8-2] Finally, the calculated background in the scintillator should increase by more than 50% if the x-rays associated with the conversion electrons are included.[8-3]

There is a factor-of-two uncertainty in the magnitude of the measured thermal neutron flux, which results in an equal uncertainty in the calculated S/B. It is conceivable that recoil proton backgrounds could compete with thermal neutron capture backgrounds, if the suprathermal neutrons are concentrated at high energies. Better neutron diagnostic methods are being investigated, but data are not yet available to reduce this uncertainty.

8.1.3.1.1.3 Conclusions and Recommendations -- Although there are large uncertainties in the gamma-ray, neutron, conversion-electron and x-ray spectra involved in these calculations, the calculated backgrounds are large enough to justify a serious attempt to reduce them by changing the CAIS scintillator. In addition to the use of phosphors with low capture cross sections for thermal neutrons (such as ZnS or $Ba_xPb_{1-x}SO_4$), a non-hydrogenous binder (such as water glass) should be developed if possible, since the recoil-proton background mechanism cannot yet be ruled out and may in fact dominate the background, if thermal neutron capture is reduced. A vigorous attack on neutron-related backgrounds is also justified by the failure of previous background-reduction attempts which assumed that low-energy gamma rays or high-energy electrons were responsible for the observed background.

In choosing or developing new scintillators, very careful attention must be paid to the exact scintillator composition (to avoid the presence of even small amounts of Cd or Eu, for example). If a mockup geometry is used, careful simultaneous measurements of neutron and gamma backgrounds should be made so that extrapolation to the real imaging situation can be made. Finally, since small improvements in the observed

modulation may be significant in the development of new scintillators, very careful
and consistent film handling and development techniques should be used.

All of the above possibilities are being actively pursued, but even if the capture
neutron background is significantly reduced by the changes considered, it may not
lead to a large change in the S/B ratio because other backgrounds seem still to be
larger. Specifically, the signal from the fuel pin used in the S/B calculations above
was 3.67×10^9 photons/cm^2, (~ 1 rad). In contrast to this, the measured gamma-ray
dose at the detector plane is approximately 15 rads for a 95-MJ pulse (but out of the
beam the dose was about 5 rads). The capture gamma rays in the detector structure
alone cannot account for the measured gamma-ray background even if they do ulti-
mately account for the differences between scintillator and x-ray film response.

One final point must be made. There are two ways by which the performance
of the system may be raised to its design goals. First, even though the x-ray film
packages provide coded images with a S/B of only about 0.06 (as will be shown shortly)
excellent reconstructions can be obtained from them. Therefore, if a scintillator can
be found which performs as well as x-ray film, the objectives would be reached.
Second, if the S/B at the detector can be improved by a large factor with improved
shielding, collimator, and filter design, then coded images in the scintillator may
be obtained which have acceptable modulation even without a major improvement in the
scintillator. It has already been demonstrated that in a low background the CaWO$_4$
provides high contrast, high resolution images.

8.1.3.2 Radiation Transport Calculations -- The measurements made in the
vicinity of the imaging detector with neutron-sensitive thermoluminescent detectors
(TLDs) indicated that the neutron fluence was approximately the same both inside and
outside the beam. This is not surprising since the bulk shield was designed to mini-
mize the gamma ray fluence at the detector under the assumption that a detector would
be found that was not very sensitive to the neutrons. However, not all pathways toward
background minimization were initially pursued, and within the original plan for sys-
tem development, provision had been made for shield modifications after the first
full-scale tests provided information about which backgrounds were most important.
Even before the results of these tests are fully digested, however, calculations de-
signed to predict those results have been found useful for guiding the design of an im-
proved configuration.

A series of radiation transport calculations were initiated to provide a theoretical basis for possible refinements in the CAIS to improve its signal-to-background ratio in the ACRR environment. Because the transport problem is a complicated 3-dimensional, deep-penetration one, two parallel techniques are being used. The transport of neutrons and gamma rays down the collimator and throughout the aperture is being calculated with a multigroup integral transport code written for this specific problem. The transport through the bulk shield is being calculated with the 1-dimensional discrete ordinates code XSDRN. Both calculations are normalized to the radiation source generated in the imaged fuel pin as given by the XSDRN calculation.

The best calculations to date indicate a peak signal-to-background ratio (determined by energy deposited in the detector material) based only on the scene background (the background coming down the collimator) of approximately 0.12 to 1. When the background leakage through the bulk shield and the activation in the detector are added in, the calculated peak signal-to-background ratio drops to 0.08 to 1. This is surprisingly close to the 0.06 S/B measured in the x-ray films. Thus, it appears that if the bulk shield leakage could be eliminated, the relative signal strength could be improved by approximately 50%. The neutron flux leaking through the shield appears to be the main contributor to "non-scene" background. Thermal neutrons can readily diffuse through the bulk lead shield and collimator to activate the scintillator itself. Fast neutrons getting through the bulk shield are rapidly reduced to thermal neutrons in the water behind the shield and are subsequently captured. The gamma rays generated by these captures in the water produce a nearly isotropic flux of low energy gamma rays incident on all sides of the scintillator chamber.

The calculations suggest that some additional boral shielding should be installed on the outside of the lead collimator and bulk shield to absorb the thermal neutrons before they can diffuse through these components to the scintillator location and be captured in the lead. Also a small amount of lead shielding placed on the inside of the scintillator chamber should absorb most of the isotropic low-energy gamma background coming through the surrounding water. These two changes should produce an observable improvement in the system signal-to-background ratio.

Although the signal-to-background ratio calculated above seems quite close to the x-ray film results, the theoretical scene beam background does not contain some effects that may be important. There is no provision for finding the radiation that is

created or scattered in the collimator walls which arrives at the detector, and no provision is made for reactor radiations that scatter from the filters and containment materials within the collimator channels. There are aluminum walls between parts of the collimator system, a thermal neutron filter made of lithium hydride, and a 0.6-cm-thick steel wall between the fuel pin test canister and the reactor core. When the influence of these materials together with the lead attenuator behind the fuel pin are taken fully into account, the importance of the scene background is expected to increase.

The calculations also lend support to the conclusion in the previous section that neutron captures in the detector package do not account for the major part of the total background response. Rather, photons generated in the shield and within the collimator, possibly by the neutrons, are the major contributor. Some shift in thinking has occurred since the previous quarterly about the importance of neutron interactions directly in the detector package, but their influence will again become important if the gamma ray background is greatly reduced.

8.1.3.3 <u>Modifications to the Bulk Shield</u> -- As Figure 8.1-4 shows, the bulk shield was designed with four primary material components. These are water, steel, borated polyethylene, and lead. The water is interspersed in layers between parts of the shield where it also provides an ability to mechanically assemble the system while at the same time leaving no cracks in the neutron shield. The steel attenuates both core gamma rays and fast neutrons; the borated polyethylene thermalizes and captures neutrons, and the lead wall attenuates the core and secondary gamma rays. Room was intentionally left behind the lead wall for the instrumentation system (then incompletely defined) and for additional shielding should the latter be required. The ACRR tank is small, and problems with shielding were expected. This is one of the reasons a coded aperture system was chosen.

Figure 8.1-5 shows the configuration of the x-ray film or scintillator detector used for the full-scale tests (FM1). This is a view of the two collimators from the side. Although the borated polyethylene very effectively reduces the thermal neutron fluence, the detector was not well shielded from radiations which might be generated behind the lead, and even for thermal neutrons which are generated in front of the lead. A recent radiation transport calculation shows that the thin layer of water between the polyethylene tank and the lead will be a very large source of thermal neutrons.

There is no barrier to these thermals all the way through the lead in the shield wall or the collimators because the '· ·d has such a low thermal capture cross section (0.17 barn). Additional sourc of backgrounds may be from thermal neutrons inter- acting with the scintillator directly, or may be from capture gamma rays produced in the water behind the le. Even though the capture cross section for lead is very low, when a capture is made, a 7.4-MeV gamma ray is emitted. Because of the energy of this photon, the impurities in the lead and the mass of lead involved, the capture gamma rays from the lead may indeed be a major source of background. The other possibility in lead is that inelastic gamma rays produced by fast neutrons in the lead will produce some of the background. Only additional bulk shielding can reduce this latter contribution.
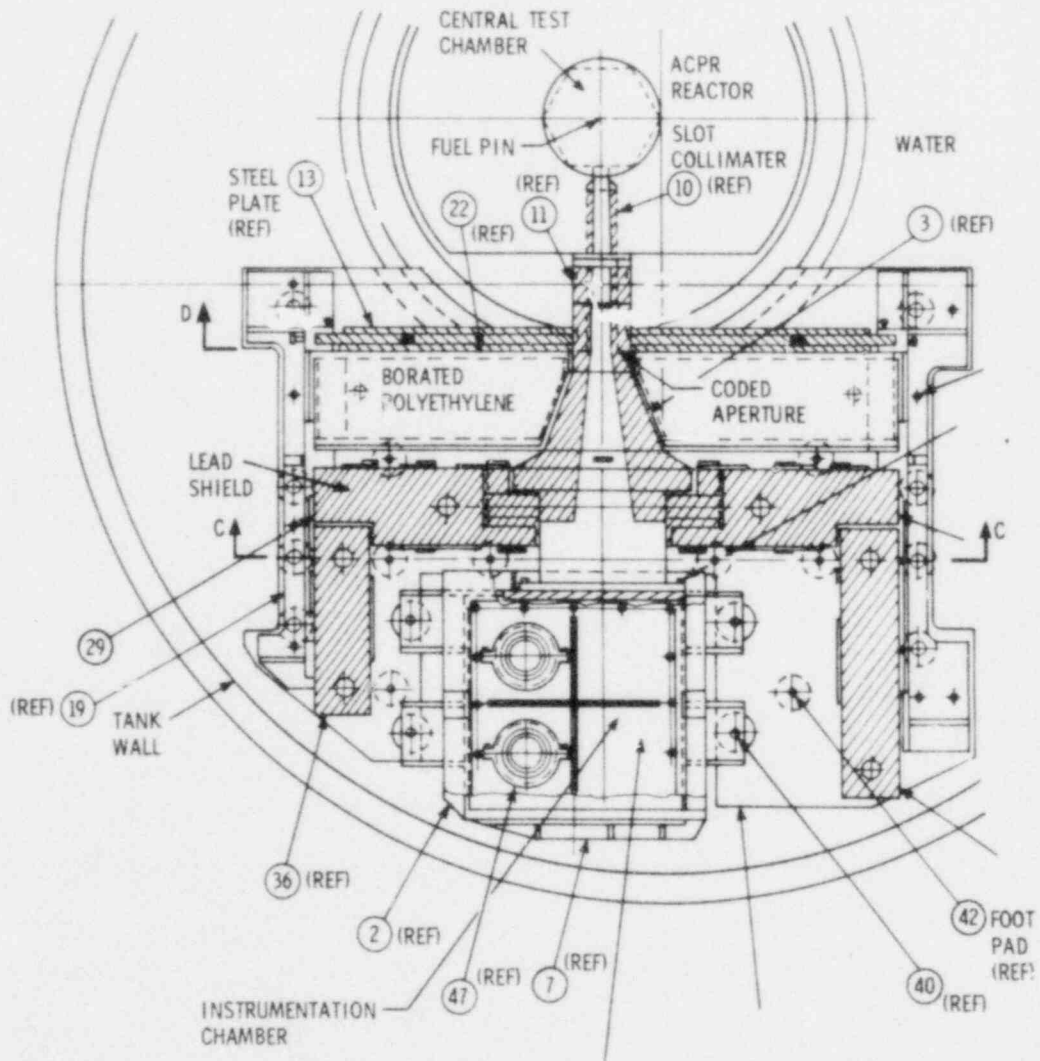

Figure 8.1-4   Horizontal Cross-Section Assembly Drawing of CAIS

IMAGE INTENSIFIER

SCINTILLATOR

MIRROR

SCINTILLATOR

IMAGE INTENSIFIER

CODED APERTURE

CODED APERTURE

LEAD
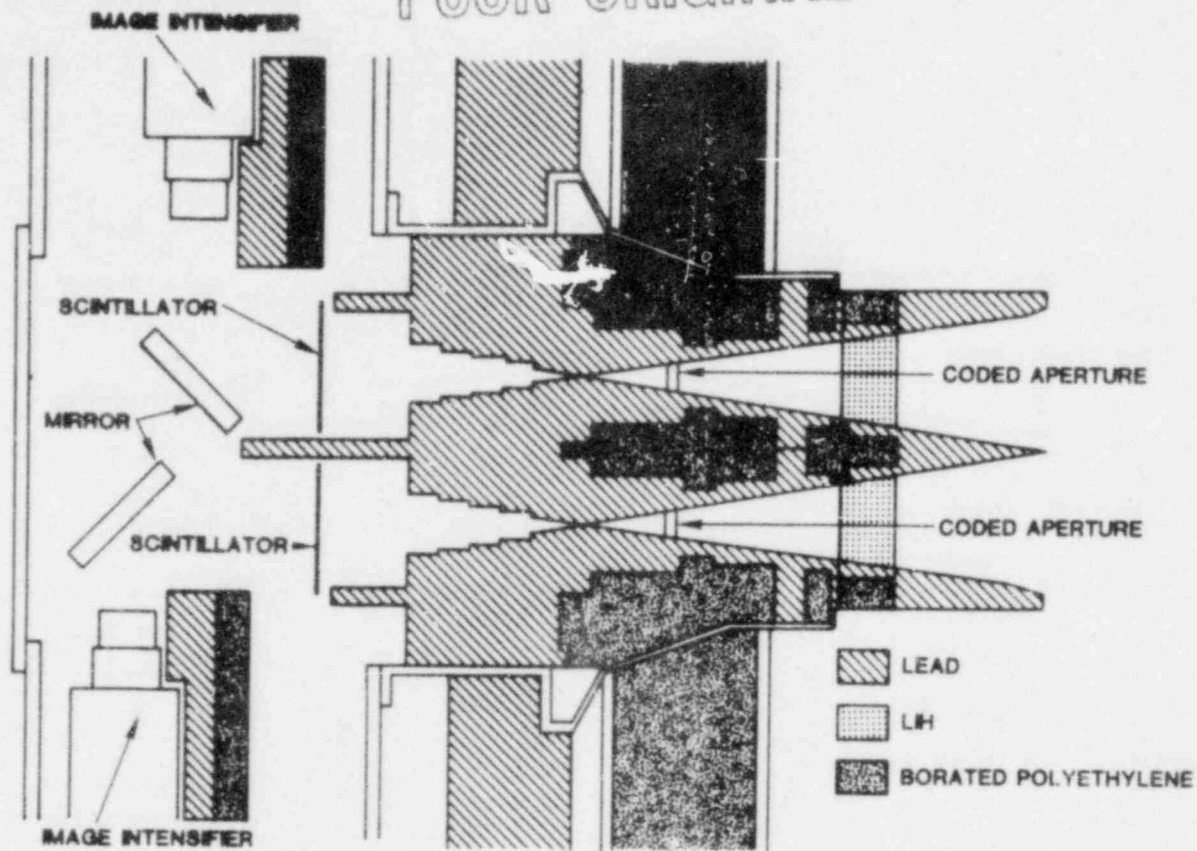
LIH

BORATED POLYETHYLENE

Figure 8.1-5   Detectors for Full-Scale Tests, and Collimators Viewed
From the Side

The bulk shield background problem is therefore being attacked in two ways: more massive shielding is being added around the scintillator and intensifier, and a thermal neutron barrier is being placed between the thermal neutron sources (such as water), and the final lead layers which face the scintillator. Boral and Cd sheets will stop the thermal neutrons, and the lead will attenuate the capture gamma rays generated by the thermal barriers. The new configuration is illustrated in Figures 8.1-6 and 8.1-7. At a later date, it may be helpful to reduce the amount of lead in the rear portion of the aperture chamber and replace it with borated polyethylene.

This additional shielding will add 1500 lb to the weight of the instrumentation chamber and will raise the weight of the instrumentation system to over 7000 lb. The strength of the lifting tabs at the top of the chamber has therefore been tripled. Much of the active recording-system hardware has also been modified. The turning

mirrors have been reduced in thickness by a factor of 5 and mounted in a much lighter support structure to reduce the scattering back toward the detector and toward the image intensifiers. The scintillator is mounted into the shielding. Behind the mirror a lead and boral shield will prevent thermal neutrons from returning to the chamber from the water behind.
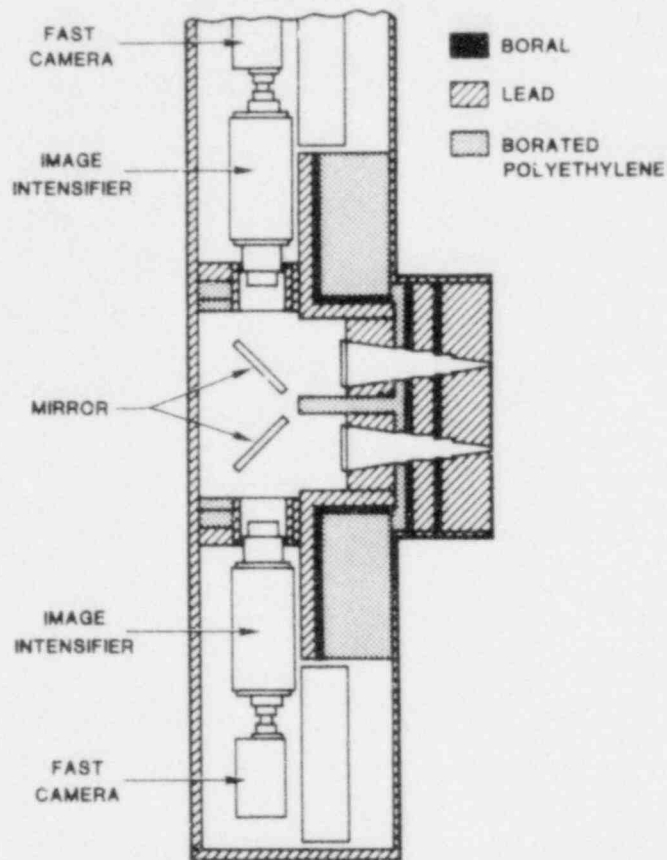

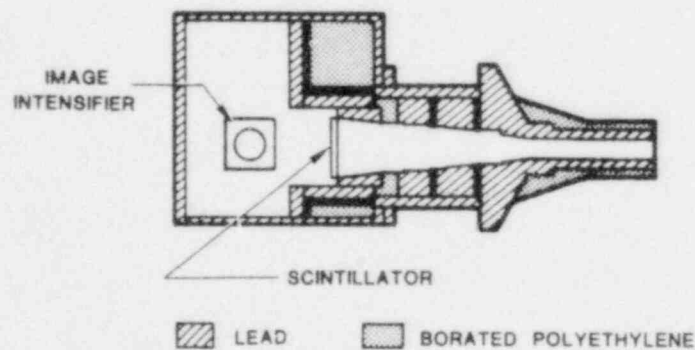Figure 8.1-6   Side View of New Chamber Shield

Figure 8.1-7   View of New Chamber From the Top

The smaller mirror supports can now be mounted at the same distance from the fuel pin without interference with each other so that both recording systems have the same geometry. Previously, the mirror on the lower channel was farther from the test pin, and the front of the lower image intensifier was very close and poorly shielded from the radiation beam. For full-scale tests involving the high speed motion picture cameras, this geometrical change has necessitated the use of a shorter image intensifier in the lower channel. Full-scale motion tests would then require the use of a two-stage or three-stage image intensifier tube. Since both the two- and three-stage tubes use the same focus coil, the decision would be made on the basis of the gain required. Initial tests will be performed using a two-stage tube because of its ready availability. Both the two- and three-stage tubes offer superior resolution and contrast compared to the four-stage tubes now in use. In the steady-state tests there is room for the four-stage tube to be used with the 35 mm camera. Both the two- and four-stage tubes may be used in the upcoming experiments on the ACRR to provide a direct comparison. The two-stage tube has considerably better resolution and image contrast than does the four-stage tube.

Tests of this new configuration are scheduled to be conducted in March 1980. At the same time measurements will also be made to explore what is called the reverse geometry. In this arrangement the scintillator would be placed behind the turning mirror on the rear door of the instrumentation chamber. In principle, this arrangement would permit another 30 cm of bulk shielding between the reactor and the detector and would make possible narrower collimation to reduce scene background. This change would not bring about a dramatic change in scene background, however, and backscattering of radiation from the rear wall would be more serious.

8.1.3.4 Scene Beam Studies --

8.1.3.4.1 Analysis of the Scene Beam Recorded on X-Ray Film -- The amplitude of the background exposure from radiation which comes through the collimators and aperture (the scene background) is roughly equal in magnitude to the bulk shield background in the experiment in which a 20% enriched pin was observed with x-ray film. A densitometer trace across the coded image is shown in Figure 8.1-8. The non-scene background here is assumed to be determined by the exposure level outside the beam and may therefore contain a component of radiation that comes through the collimator and is backscattered into the detector. The scene background

is the more difficult to handle because it is structured. Examination of the structure of this background, however, reveals a great deal about its origin. Of primary importance is the component responsible for the large shoulders in the density profile and the small hump beneath the first zone shadow of the fuel-pin signal. A dramatic drop occurs in the exposure just at the lateral location where the outer boundary of the coded aperture begins to cut off the view of the very front opening in the collimator system, and the shoulders in the aperture slant down to the level where complete cutoff takes place. The cutoff geometry is shown in Figure 8.1-9. In fact, most of the scene background can be accounted for by the radiation coming through the front collimator opening. The major background is, therefore, a convolution of that opening with the coded aperture. This result indicates that the largest component of the background is generated on the fuel pin side of that aperture and that much less is generated by the collimator walls, aluminum chamber walls, or the LiH window. There are five potential sources for this radiation: the steel experiment cavity liner, the Al test canister walls, the Be tube around the pin containment structure, the Pb wall behind the fuel pin, and penetration of reactor core radiation through the Pb wall.
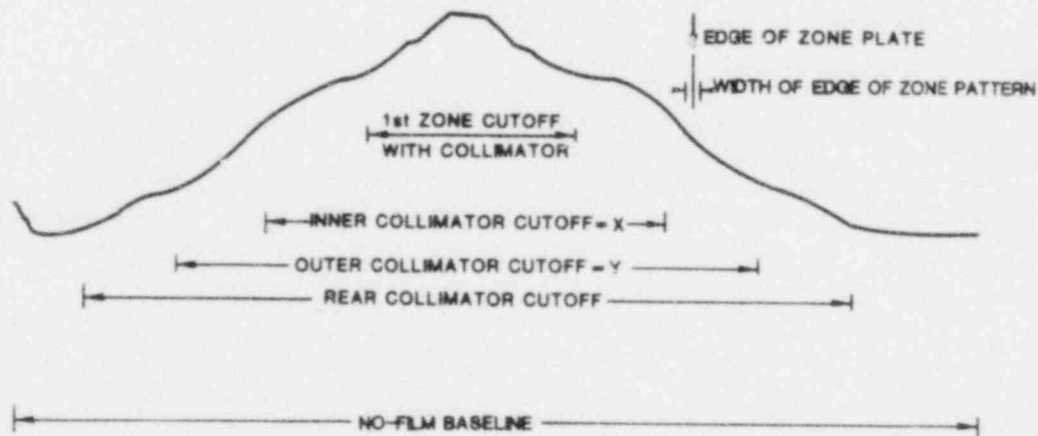
Figure 8.1-8   Densitometer Scan Across Fuel Pin Coded Image
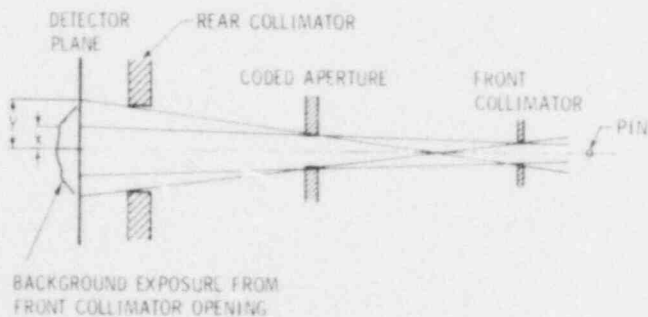(x and y from Figure 8.1-9 which follows)

Figure 8.1-9

Collimator Cutoff Geometry

Calculations are now being carried out to predict which of these sources are the most significant. The predictions will then be used in design modification studies. Because of the severe constraints imposed by geometry, structure, containment, reactivity, and thermal requirements, only limited options are available for reduction of the scene background. However, just before the full-scale proof test, investigators discovered that the attenuating lead block behind the pin contains 5% by weight of antimony. Lead alloyed with this element is stronger and more machinable. It also possesses a neutron capture cross section which is 33 times larger than that of unalloyed lead. If it turns out that the capture gamma rays are the major source of background emerging from the block, then the removal of the antimony may reduce this background by a factor of three. A new pure lead attenuator has been fabricated to explore this possibility. Once this background is reduced, the penetration component can be attenuated further by replacing the core fuel rod directly behind the pin with a lead-filled dummy rod. This dummy rod has already been tested and does improve the signal-to-background ratio. Some sacrifice of reactivity will result, but in partial compensation the flux tilt in the core will be reduced.

A thick Be liner which provides thermal inertia to the assembly surrounds the Inconel containment chamber which holds the test fuel pin. Beryllium has a very high atom density and a low attenuation coefficient for gamma rays. If the analysis shows that gamma rays scattering in this liner are a major source of background, reducing the liner's mass may be possible without compromising its function. The final two materials that can contribute to scene background are the Al canister surface and the 0.6-cm-thick steel wall at the inner core boundary. The aluminum should not be a major source and the steel cannot be removed at this time. On returning to the densitometer trace, Figure 8.1-8 shows that there are also two secondary shoulders of much lower amplitude. The location of these shoulders indicates that the LiH box may be a source of radiation. It is very close to the reactor and may scatter photons and energetic neutrons toward the detector. The location of this thermal neutron stop has therefore been shifted to a more protected position just in front of the coded aperture. Estimates of the potential for scattering by the LiH are being made.

8.1.3.4.2 <u>Studies of the Collimated Beam</u> -- Irrefutable proof that certain specific sources are the causes of unexpected low contrast in the fuel pin images has been extremely difficult to obtain. This is because the geometry of the system is so complicated and the number of potential radiation mechanisms is so large. Detailed radiation transport calculations are therefore very difficult to make, especially when the actual sources which produce the major fraction of energy deposition in the scintillator are yet to be identified. Additional testing has therefore continued in an effort to verify computer calculations and to identify the processes which are taking place in the system. Although useful for characterizing film properties, imaging schemes, etc, the ^{252}Cf source and the SPR-II (fast reactor) have much harder neutron spectra and do not reproduce the conditions encountered in the ACRR.

During the last several months, therefore, several experiments have been carried out in the ACRR in a manner designed to save some of the expense of using the full capability of the reactor. These tests have used only the unslotted core and the aperture chamber and have been conducted on a reactor "time available" basis. The configuration is illustrated in Figure 8.1-10. The instrumentation chamber could not be used during this period because of the shield modifications that are being made.
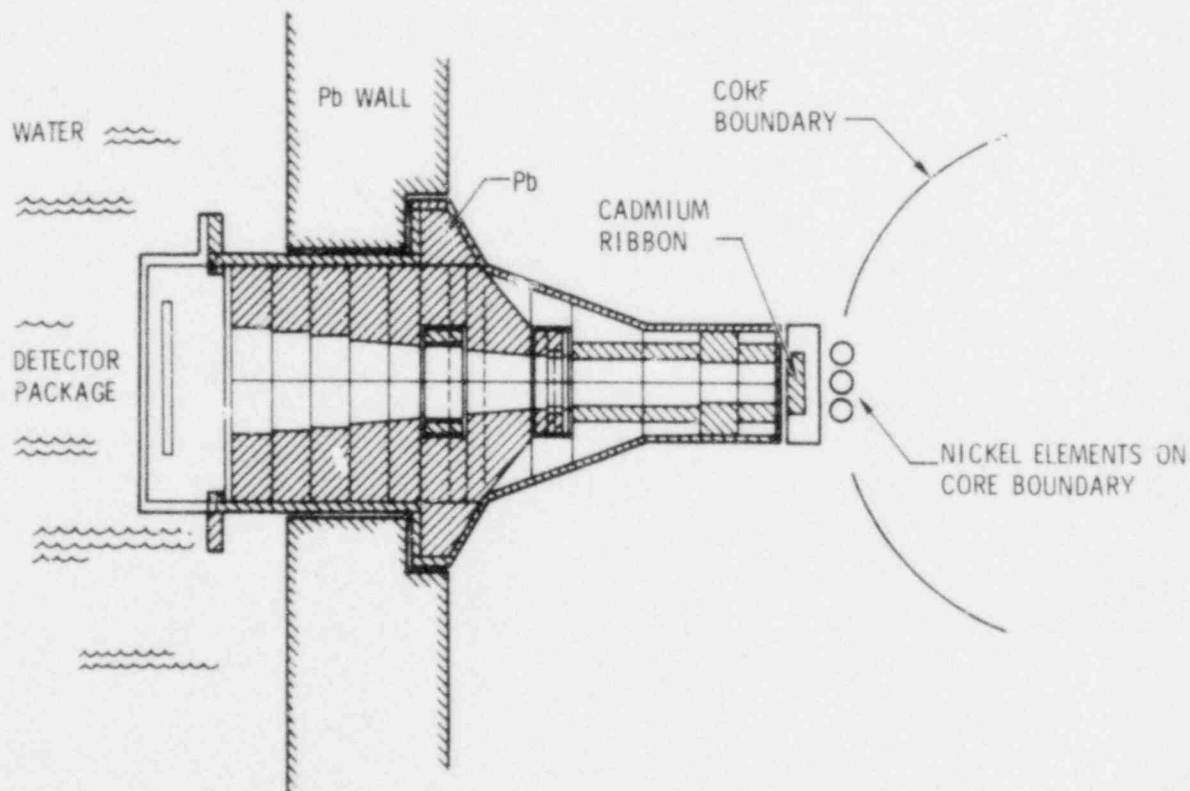

Figure 8.1-10   Apparatus for Collimated Beam Studies

The figure shows a cadmium ribbon mounted in a lead block in front of the chamber. This is a target assembly which was not present during the experiments to be described first. The radiation fluxes and structure in the beam matched quite well those observed during the slotted core tests. The conclusions should therefore have validity in the slotted core situation. During reactor runs in which 20 MJ were deposited in the core, the x-ray film showed that the exposure outside the beam was about 40% of that within the beam. The TLDs indicated the same ratio, about 12 rads measured in the beam and 5 to 6 rads outside the beam. Their neutron response implied 2 to 3 $\times$ 10^9 n/cm^2, almost independent of their placement inside or outside the beam, again in approximate agreement in the slotted core case.

8.1.3.4.3 Comparison of Detector Responses -- Several different scintillators were tested in this environment along with the x-ray film. Kodak Ektapan film was pressed against the rear surface of each scintillator. Most of the exposure in each case was caused by the light from the scintillator and therefore the density was proportional to the $\log_{10}$ of the true exposure just as in the active system. This logarithmic response must be unfolded for comparisons with the linear x-ray film. One of the coded apertures was placed 7 cm in front of the detector packs so that sharp coded images would impinge on the packages.

A number of observations can be made:

1. The x-ray film demonstrates considerably higher spatial resolution than any of the scintillators tested.

2. The exposure modulation (defined as $(E_1 - E_2)/E_1 + E_2/2)$ in energy units) induced by a 1.9-cm-thick tungsten bar at the side of the coded aperture is 0.75 for the x-ray film and 0.4 for the scintillators $CaWO_4$ and $BaSO_4(Pb)$. The implication is that the scintillator packages are more sensitive by about a factor of 2 to a background that is not coming through the aperture (the non-scene background).

3. The $CaWO_4$ screen has a higher spatial resolution than any of the screens tested despite its 0.05-cm thickness.

4. Two ZnS screens which contain cadmium activator (E-2, CD-2) were also tested. The film densities were quite high on both of them and their positions could be seen in the x-ray film mounted in a separate

package behind 0.3 cm of aluminum. The cadmium was therefore emitting capture gamma rays. The thermal neutron fluence at the detectors is high and materials with high capture cross sections are obviously unsuitable in this application.

8.1.3.4.4 Proton Recoil Effects -- As mentioned in Section 8.1.2, fast neutrons might deposit energy in the detector material by scattering protons from substrates or hydrogenous materials which bind the crystallites together in the scintillator screen. This potential contributor has been tested in three different locations by comparing the response of scintillators in pure powdered form (no hydrogen) with the same scintillator mixed in a binder. $CaWO_4$ powder was placed beside a $CaWO_4$ screen of the same thickness and against a sheet of the film. They were exposed beside the SPR-II, next to the core of the ACRR and at the detector location of Figure 8.1-10 in the ACRR. In all cases the average responses were virtually identical as measured by a densitometer. The proton recoil contributions appear to be negligible.

A potentially useful discovery about the pure $CaWO_4$ powder was that if it was compacted, the spatial resolution was better, the modulation was 60% higher, and the average granular fluctuations observed were smaller than in the standard screen. Large-size powder screens pressed down with optical flats may be worth developing.

8.1.3.4.5 Filter Studies -- Thermal neutrons may interact directly in the detector by capture and deposit energy when gamma rays emitted by the process generate electrons as discussed in Section 8.1.2. Both x-ray films and scintillation detectors have been surrounded by filters made of boron, lithium hydride, lithium metal, or cadmium, all with relatively minor improvement, although dosimeters do record a large drop in neutron fluence. Of course, since the boron and cadmium emit capture gamma rays, the potential advantage of their thermal shield would be masked by the additional gamma-ray background. The gamma fluence near the cadmium, for example, is usually higher by a factor of two.

However, a dramatic change occurred when two completely closed lead boxes were tested with and without a boron shield around them. In one case a small cask with 1.5-cm-thick lead walls was placed just outside the beam at the detector location in Figure 8.1-10. It contained TLD chips. Without the thermal shield the lead reduced the gamma-ray fluence by only a factor of two over that detected at the same

location but not enclosed in lead, but when a thin layer of boron-loaded flexible shield was wrapped around the cask, the gamma-ray dose dropped by a factor of 10. The 463 keV gamma rays emitted by the boron were being stopped by the lead and thermal neutrons did not reach either the lead or the detector. Since the lithium metal did not appear to help very much (in one simple test), much of the background exposure may really be due to the low-probability capture events in the lead which surrounds the detector region rather than direct interactions in the detector. This tentative conclusion has provided the justification for altering the shielding so that a thermal neutron barrier completely protects all lead surfaces that are themselves separated from the scintillator or image intensifier by less than 2.5 cm of lead.

Additional information has been obtained from the attempt to test modulation properties of scintillators by using the cadmium ribbon shown in Figure 8.1-10 as a source of gamma rays. Thermal neutrons near the edge of the core readily pass through the lead block and strike the ribbon. The capture gamma rays from the cadmium produce a fuel-pin shaped object for the coded aperture to observe. X-ray film at the detector plane did record a coded image with the same degree of modulation in the zones as was obtained with x-ray film in the imaging of the test pin through the slot. This modulation was 6%. The scintillator packages, however, seemed to record no observable modulation at all. Examination of the dosimetry revealed that the total neutron fluence was ten times higher than when the target block is removed and the space is filled with water. What was very much unexpected, however, was that the neutron fluence even outside the beam was also 10 times higher. This experiment needs to be repeated. If verified, either a tremendous stream of neutrons scatters down the collimator channel and then scatters in all directions near the detector, or the neutrons travel within the lead walls from the target area. To stop this streaming (if it is thermal) the collimator structure will contain thermal neutron barriers of boral and cadmium. Within the beam the LiH window will stop the thermals without producing capture gamma rays.

The influence of the boral-lead shield was again tested in this geometry with a lead box that was fabricated with 2.5-cm-thick walls and a cavity large enough to include a scintillator-film package. The difference in exposure both on x-ray film and in the scintillators, with and without boral around the box, was again impressive. Anticipation is growing that the increase in bulk shielding and the thermal neutron barrier will improve the signal-to-background ratio dramatically. Then it is expected

that the relative importance of direct neutron interactions in the detectors and contributions to the scene background in the test canister will be much more evident and tractable.

8.1.3.5 Improved Reconstruction Development -- In an attempt to better use existing noisy data and to determine how to better approach theoretical predictions with actual image reconstructions, a more extensive study of the reconstruction techniques has been undertaken. As part of the review, Prof. H. H. Barrett of the University of Arizona was consulted. From discussions with Prof. Barrett, three areas of investigation were identified for improving existing techniques.

First, the actual encoded point spread function or an analytical expression closely approximating it would be used in the reconstruction process. Currently, the aperture response for an ideal Fresnel zone plate as shown in Figure 8.1-11 is used in image reconstruction. Clearly, this response has a unit amplitude for the full width of the zone pattern. The measured aperture response, shown in Figure 8.1-12, has a decreased response in the outer zones. Use of the ideal response function instead of the measured response function tends to increase the noise at high frequency where the signal-to-noise ratio in the actual case is reduced. Use of the true aperture response function should help correct this shortcoming.

Second, a superior method of handling scene background will be developed. Presently, a similar pulse experiment with no fuel pin present is performed to obtain a scene background estimate, and this is used to subtract scene background in the actual (pin in) experimental case. One difficulty with this is that the scene background changes when the pin is present. This difficulty is most likely due to scattered radiation coming from the fuel pin and from changes in alignment between experiments. A second problem is that for the presently noisy data, subtraction of a noisy background image from an equally noisy "pin in" image increases the noise level by the square root of two. Two possible solutions to this problem have been suggested: first, because a major source of scene background appears to act effectively as a source which is the width of the slot collimator placed at that opening, an estimate of the source functions can be derived. This function can be fitted to the actual background in each case to yield a scene-dependent background for each frame which can then be subtracted away. Since an exact function is used, there is no increase in noise level due to subtracting two noisy quantities.
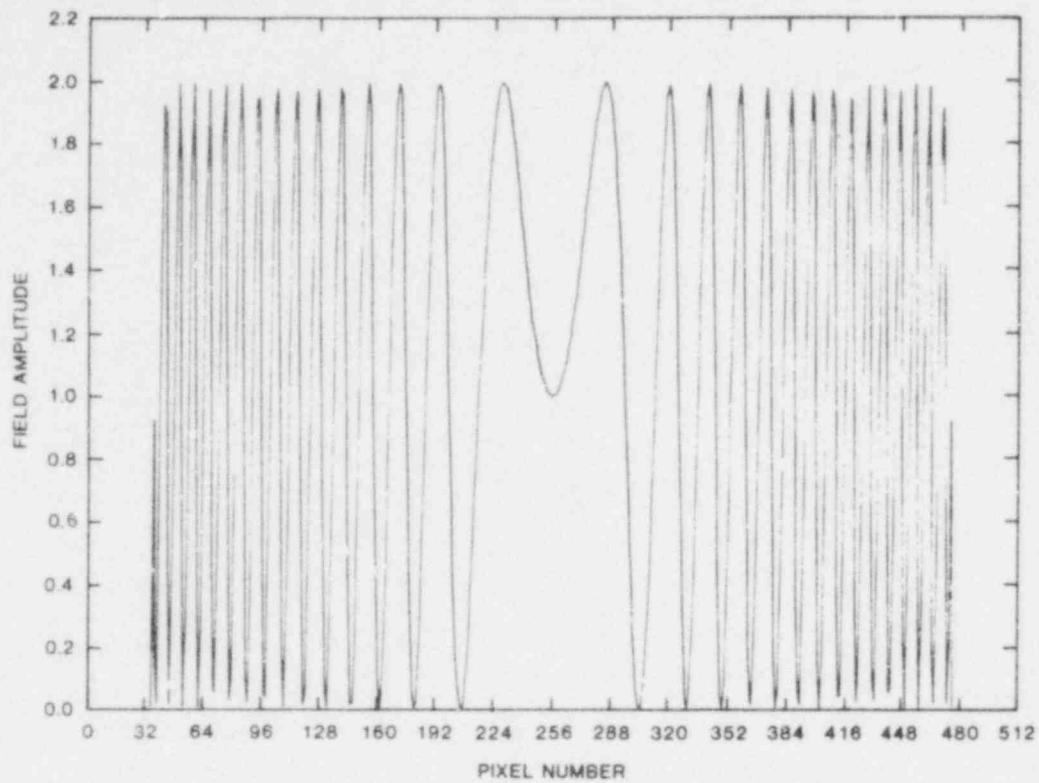
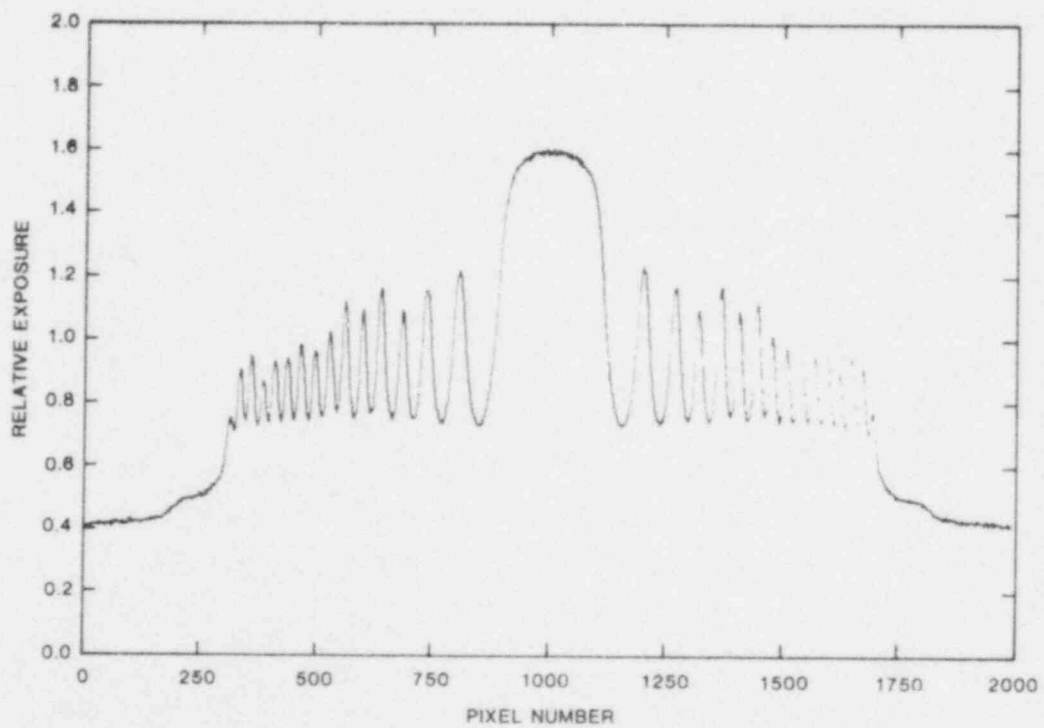Figure 8.1-11   Ideal Fresnel Zone Plate Response Function

Figure 8.1-12   Actual Aperture Response Function as Measured
at ^{252}Cf Source Using Coded Aperture From CAIS

197

A second technique to be studied will be the use of a variable width moving window average. In this case a moving-window average will be performed on the pseudohologram with the width of the window varying as a function of position to accommodate the varying zone widths in the encoded image. By keeping the window size on the order of two zone widths wide, the zone plate modulation can be averaged out, but the important broad background features will remain. Once the background has been derived in this manner it can then be subtracted from the total signal so that the signal modulation can be reconstructed.

The third area to be considered was reduction in the influence of film grain noise. For the situations in the FM1 test, film grain noise was the dominant source of noise in the image recording system. To help minimize the effect of this noise source, nonlinear filtering techniques such as median value filtering and noise cheating will be investigated along with linear techniques such as low pass spatial filtering at the time of reconstruction. These techniques, especially in conjunction with use of the proper response function for matched filtering, should produce a significant improvement in the quality of the images derived from the present low contrast coded images.

To facilitate the incorporation of these improvements into current reconstruction programs, a contract has been entered with Prof. Barrett so that a student can work on applying these new techniques to the data. Some work will also be carried on in parallel at Sandia, and the improved methods will be integrated into Sandia's production image-reconstruction code as they become available.

8.1.3.6 Summary -- The problem of low contrast in the coded images is being approached by every avenue available. More mass and thermal neutron shielding will protect the image intensifiers and the scintillator detectors; a thinner turning mirror will reduce beam scatter toward sensitive components; new intensifiers with fewer stages will improve resolution and contrast; special scintillators should be able to approximate x-ray film response; theoretical calculations will aid in identifying background sources for which reduction methods can be developed; improved beam stops, filter materials, and scene background attenuators are expected to raise the signal-to-background ratio; and finally, advancements in data analysis should contribute significantly to the ultimate capabilities of the system. At the present time, no single fix will permit major improvements to be made because there is no single dominant effect to be eliminated.

8.1.4 Fuel Motion Measurement

This quarter, work continued on data analysis of the fuel motion test FM1. Because of equipment problems with the COMTAC video output device, direct reconstruction of the data could not continue. However, a series of algorithms were developed to provide one-dimensional axial power profiles of each frame. From this information the axial movement of fuel within the test pin can be determined. Since the axial failure location and axial motion of fuel after failure have great impact on the accident sequence, this type of time-resolved measurement can prove very valuable in the analysis of test data.

Determining the axial motion of fuel undergoing disruption uses the same digital-scan data used for image reconstruction. However, to reconstruct the radial position information, each row of data is integrated rather than being subjected to a matched filtering operation. Since the CAIS acts as a pinhole camera in the axial direction and a coded aperture only in the radial direction, these radial averages provide a one-dimensional axial power profile of the pin under test. Performing this operation for each pseudohologram frame provides time-resolved axial power information.

The initial axial power profile for the lower channel is shown in Figure 8.1-13. This plot is the average of the power profiles of the first 10 frames of data obtained in the "pin-in" fuel motion test FM1. The slope of this plot also matches quite well the shape of the "pin-out" background test (as it should if no motion has occurred). Although this plot is for the lower recording channel only, it does cover the bottom 200 mm of the fuel pin including the core midplane region. In Figure 8.1-13, down-the-pin is to the left and up-the-pin is to the right. The steep sloped regions at both the left (bottom) and right (top) of the profile are caused by the collimators cutting off this field of view. The bump on the left is believed to be the flange at the bottom of the fuel pin. The space near the top of the field of view lying just below core midplane is the area of maximum fission density corresponding to maximum power in the core.

To accent the change in power profile from frame to frame, the axial power profile derived from each digitized frame was normalized to 1.0 by dividing each value by the maximum value. This normalized power profile was then divided by the similar normalized power profile for the initial fuel distribution shown in Figure 8.1-13.

The result can be seen for two frames of interest in Figure 8.1-14. Figure 8.1-14 shows the result for frames numbered 19 and 20 occurring approximately 260 and 280 ms after the peak of the pulse. This time frame precedes the onset of melting, according to calculations, and the plots show that there is very little deviation from 1.0 in the region between 0.0 mm and 180.0 mm along the pin. The deviation above and below this region is due primarily to the combination of steep slope and imperfect frame-to-frame registration during the process of digitizing the film. The variation of the plots in Figure 8.1-14 from the value of 1.0 (indicating a perfect match in slope) provide a feel for the uncertainty in the comparison techniques. The discussion immediately below refers to frame numbers illustrated in Figure 8.1-15. Because preliminary visual inspection of the pseudohologram film records indicated fuel motion commencing shortly after frame 50, the next series of frames to be digitized were frames 51 to 70, representing the time period from 0.9 s after the peak of the pulse to 1.3 s after the peak of the pulse. In this series of frames, axial fuel motion can be traced starting just below the core midplane in frame 52 where a sudden increase in power is noted about 20.0 mm above the bottom of the pin (160.0 mm above the bottom of the frame). This region of increased power with respect to the initial power distribution (values greater than 1.0 on graph) continues throughout the whole series. Also starting in frame 51, the power in the pin has decreased in the region below the core midplane (values less than 1.0 on graph) becoming quite noticeable by frame 56. Since only the bottom channel of data is available and all power profiles are normalized, investigators do not know whether there is an actual decrease in power in the lower half of the pin or whether fuel has moved out of the field of view into the upper part of the cavity. The latter explanation seems reasonable due to the presence of what seems to be a wave of fuel moving toward the bottom of the pin in frames 64 through 70 (see arrows). The movement of fuel in frames 51 to 70 seems probable in view of an EXPAND code calculation which has the clad melting at about 0.25 s after the pulse peak. Also the TAC code predicts molten fuel and fuel vapor to be present by 0.9 s (frame 51) after the peak of the pulse.

Figure 8.1-16 shows the axial power deviation for frame 101, 201, and 340 corresponding to approximately 1.9, 3.9, and 6.7 s after peak power. During this time, the pin began to slump and fuel started to run toward the bottom as indicated by increased power (values greater than 1.0) toward the bottom of the pin. Examination of frames 101 to 110, 151 to 160, and 201 to 210 still indicated fuel motion taking place which explains why frame 201 (time = 3.9 s) seems to have less fuel accumulated than

frame 101 (time = 1.9 s). Examination of frames 331 to 340 revealed a relatively large increase in power, probably due to increased fuel caused by slumping in the lower region of the cavity. Little motion was indicated in frames 331 to 340.
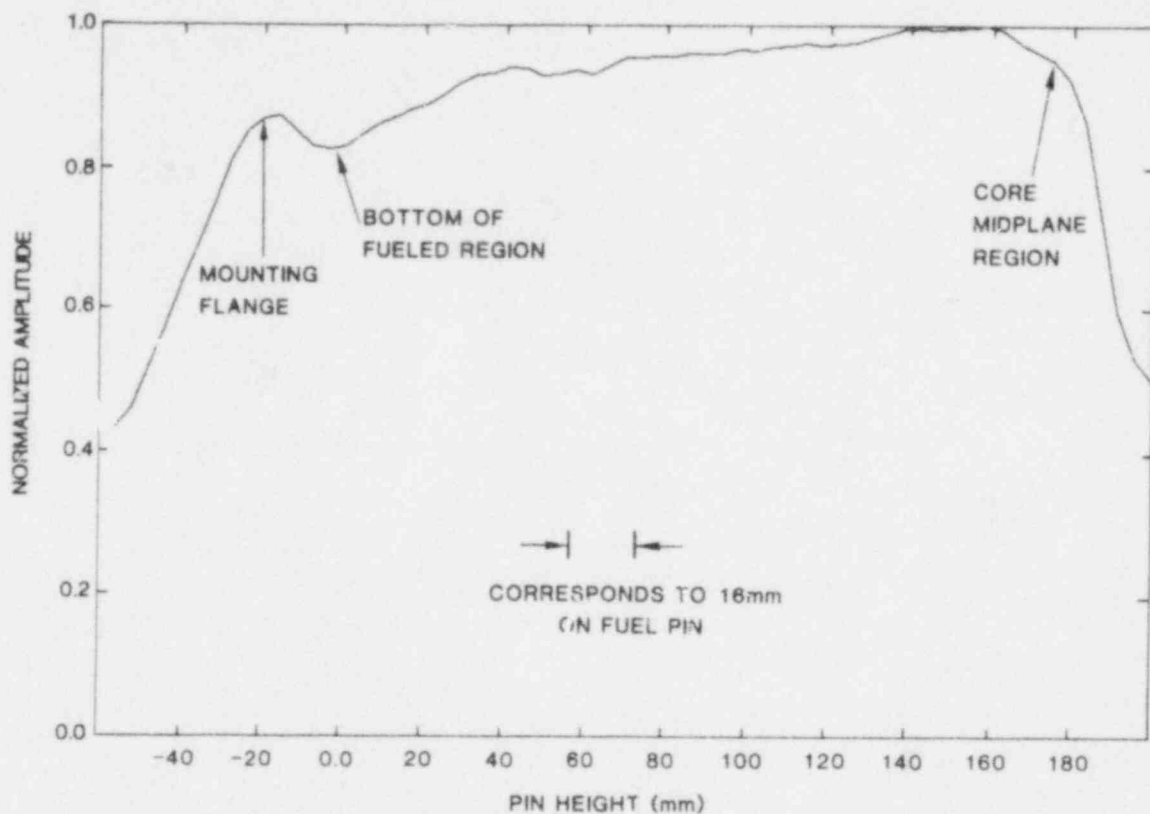

Figure 8.1-13 Initial Axial Power Profile for Lower Channel

To summarize, a technique for detecting axial fuel motion from scanned pseudohologram data has been developed. At present, this technique provides a quantitative indication of the relative increase or decrease in the fission gamma signal emitted by the fuel. Since no background has been subtracted from the digitized film records, part of the signal is due to core background which reduces the sensitivity of the method to small changes in fuel mass. Further, because only one channel of data was available and all data were normalized, the exact amount of fuel which moved could not be directly calculated. However, by comparing the amount of integrated reactor power per frame to the amount detected in the lower channel, an estimate of fuel mass may be derivable. Currently, attempts are being made to recover the integrated reactor power per frame from digitized power history tapes

for FM1. This information should be available for integration into the current data reduction algorithms in the near future so that a better estimate of fuel motion may be made.
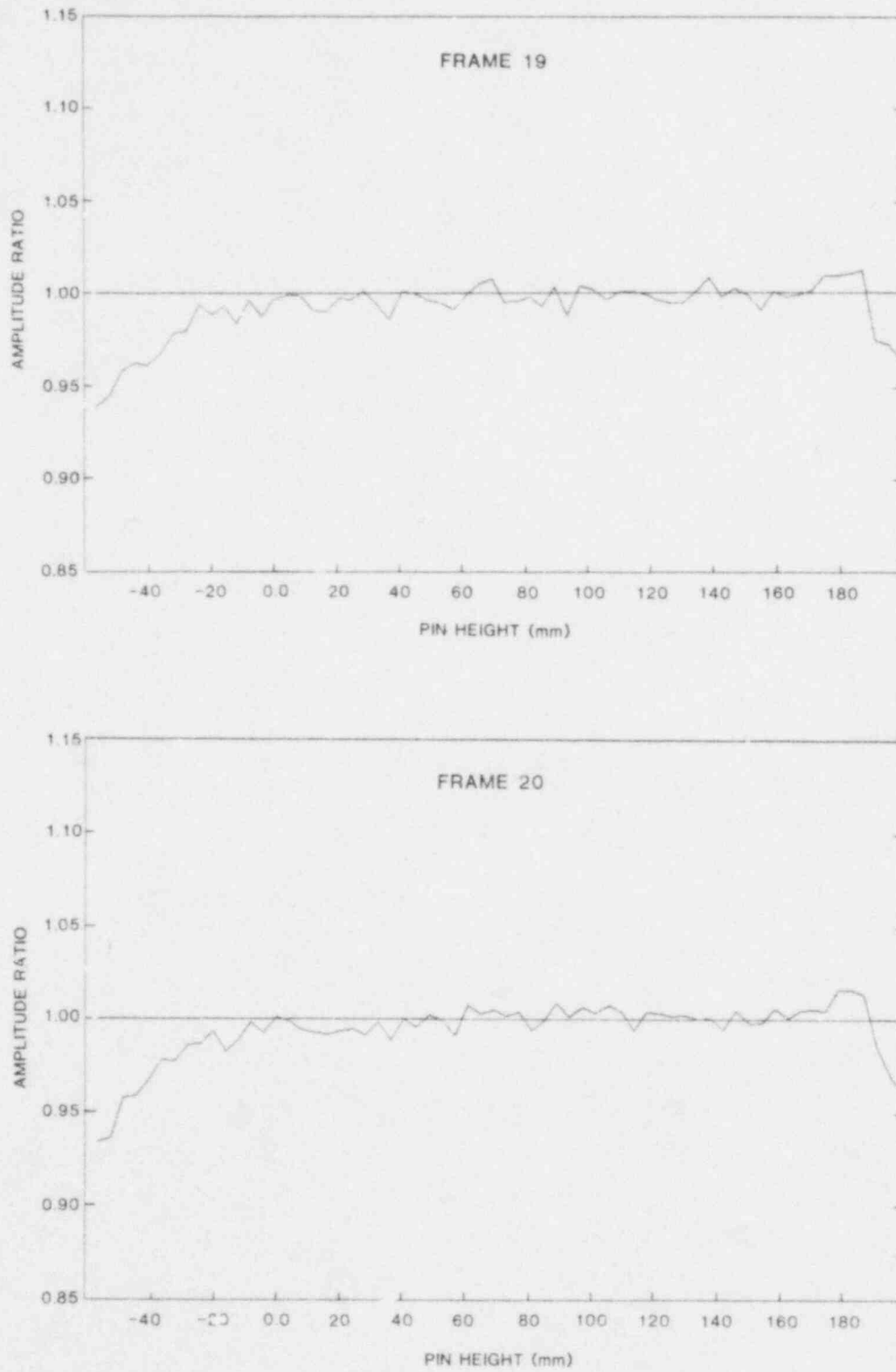

Figure 8.1-14   Power Profiles After a Normalizing Procedure
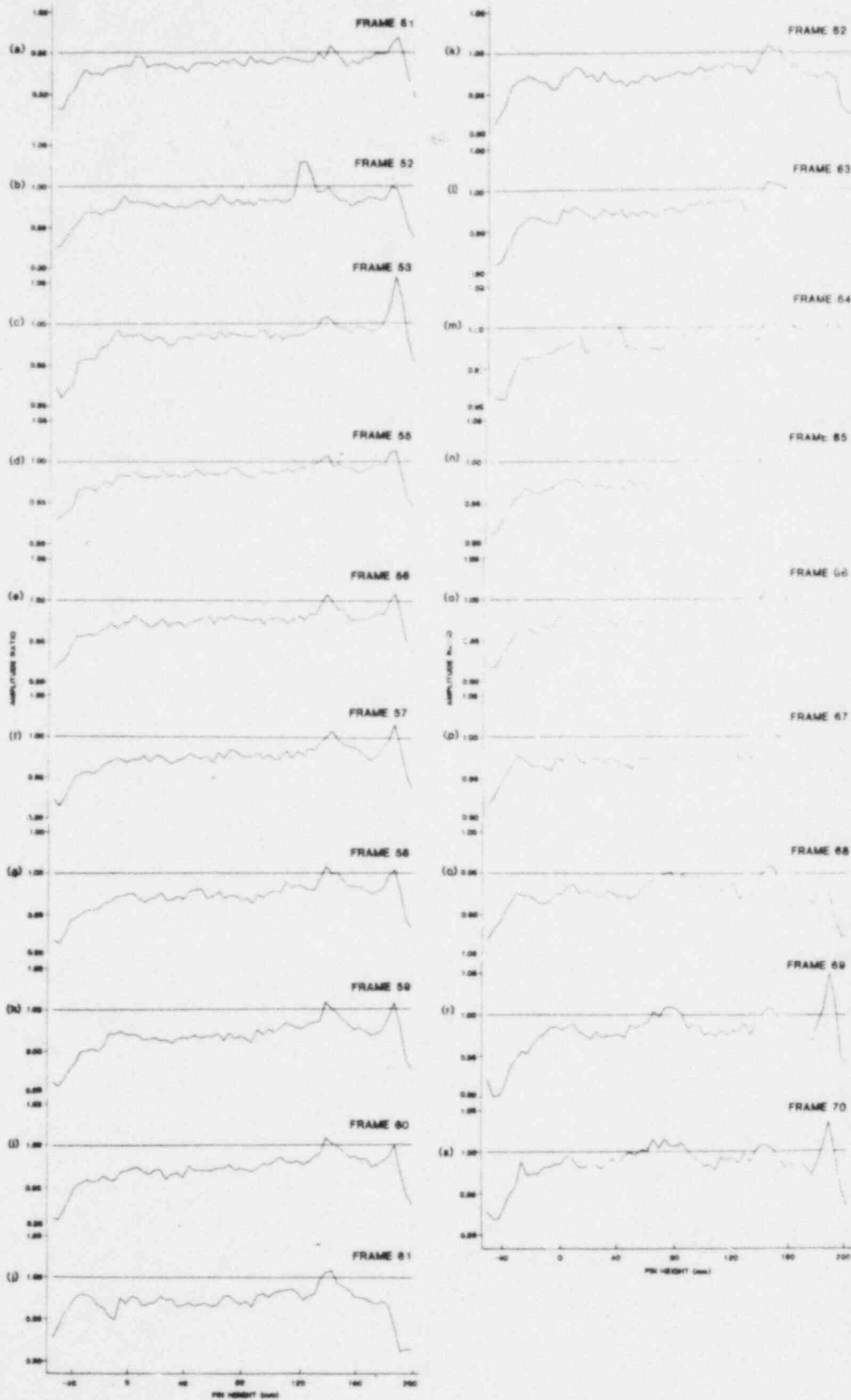
Figure 8.1-15   Time Resolved Axial Power History of Lower CAIS
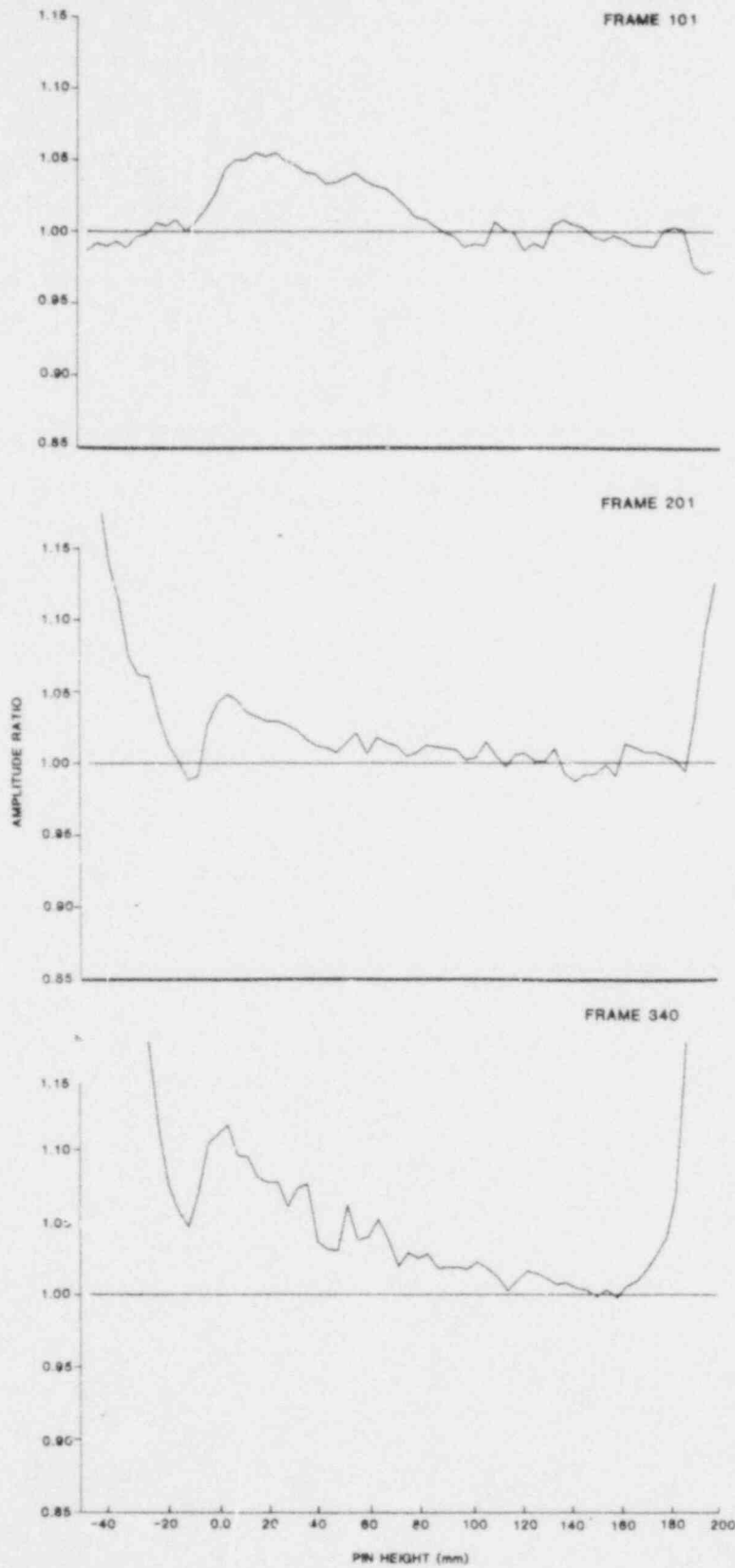Channel for Time, t = 0.9 to 1.3 s After the Peak of
the Pulse

203

Figure 8.1-16 Axial Power Deviation Corresponding to
Approximately 1.9, 3.9, and 6.7 s After
Peak Power

In addition to the axial fuel motion work, investigators attempted to identify alternate paths for the generation of two-dimensional image reconstructions. The extreme importance of this task was emphasized by the three-month down time for the COMTAL device. Further availability problems are anticipated for the COMTAL in the third or fourth quarter of Fy 1980 due to the planned exclusion of the SIGS graphics system from operation on the 6600/7600 computing system when its new operating system becomes available. Since COMTAL operation is dependent on SIGS, a down time of approximately six months to a year should be anticipated while new software is written. This realization has led to the consideration of alternative data paths.

Four candidate systems are currently being considered for potential use in obtaining outputs from the CAIS. First, software development has been started to allow output of reconstructed images on a VPI image analyzer. Second, tapes have been sent to the Sandia Laboratories, Livermore, CA which will investigate the feasibility of using the Stanford Technology Image Processing system for both output and image enhancement. Third, contact has been made with the appropriate Sandia applied mathematics personnel so that progress toward purchasing an image processing station might be monitored. Fourth, some preliminary program work has been done for outputting images using the DICOMED D48 plotter at Sandia's large computer facility. A fifth proposal which must be given some serious consideration due to the proposed volume of data to be produced is the purchase of an image processing/data output station for Sandia's Advanced Reactor Research Department. All of the above-mentioned alternatives will be investigated in the near future and the results of the study will be reported.

8.2 ACRR Status (T. R. Schmidt, 4451)

8.2.1 ACRR Technical Specification Modifications

A request to modify the Technical Specifications for the ACRR was submitted in September 1979 for the purpose of updating all the calculated performance values with measured values. The experimentally determined prompt-temperature coefficient of reactivity is more negative than the conservative values used in the reactor design and safety analysis. Hence, a change was requested in the reactivity worth of the transient rod bank from $3.20 to $4.25 to permit pulsing to the design temperature limits.

A maximum single pulse will use a reactivity insertion of $3.50 instead of the current $2.95. This will produce a peak power of 52 000 MW, up from 29 500 MW. The Technical Specification on pulse energy release was increased from 450 MJ to 500 MJ primarily because the operational core size (226 elements) is slightly larger than the calculated core (200 elements). There were essentially no changes in the safety limit (SL) and the limiting safety system settings (LSSS) on fuel temperature. Several other minor changes were requested. All the changes were approved by the DOE Albuquerque Operations Office in December 1979.

8.2.2 ACRR Control System Alterations

An additional control system has been designed to permit a programmed withdrawal of the transient rod bank. Also the transient rod drive motors have been replaced permitting rod drive speeds up to 23 cm/s as compared to the original maximum speed of 7.5 cm/s. Two systems for programming the rods were fabricated: (1) a hardwired system with eight program segments for speed, direction, and time; and (2) a system using a microprocessor with up to 64 program segments. The microprocessor-based system may be programmed on the front panel or by the ACRR minicomputer, an HP9845 system.

This programmed transient rod withdrawal mode coupled with the higher-worth transient rods, as discussed above, will provide new capabilities for producing required power histories for fuel dynamics and energetics experiments.

The use of the TRW programmers with the control system has been approved by the DOE Albuquerque Operations Office subject to a preoperational survey.

8.2.3 Modifications to the ACRR

During the end-of-year shutdown, storage holes for fuel experiments and the neutron radiography collimator were provided in the floor of the ACRR high bay. Three storage holes are 4.6 m deep and two are 9.7 m deep. These holes are aligned with the penthouse monorail so that full length experiments (like the debris bed experiments) may be remotely removed from the reactor, placed in a security-approved storage hole, and covered with a shield plug.

A new shield plug was also designed and fabricated for the central loading tube of the reactor. The new plug incorporates a central hole 10.2 cm in diameter and two off-axis holes 5.1 cm in diameter. This new shield-plug design permits a line-of-sight path for the fuel disruption experiments which currently use mirrors to transmit optical signals up the offset loading tube. Alignment of the transmitting mirrors is difficult and results in higher personnel radiation exposure, particularly in experiments with preirradiated samples.

References for Section 8

8-1   J. A. Halbleib, Sr, and W. H. Vandevender, Nucl Sci Eng, 57, 94 (1975).

8-2   R. D. Evans, The Atomic Nucleus (New York: McGraw-Hill Book Co) pp 218-225.

8-3   J. M. Vanden Cruyce, G. Vandenput, L. Jacobs, P. H. M. Van Assche, H. A. Baader, D. Breitig, H. R. Koch, J. K. Alksnis, J. J. Tembergs, M. K. Balodis, P. T. Prokofjev, W. Delang, P. Gottel, and H. Seyfarth, Phys Rev C, 20, pp 504-528 (August 1979).

8-4   L. V. Groshev, V. N. Lutsenko, A. M. Demidov, and V. I. Pelekhov, Atlas of γ-Ray Spectra From Radiative Capture of Thermal Neutrons, (New York: Pergamon Press) pp 117, 158, and 162.

8-5   C. Lederer and V. S. Shirley, Eds, Table of Isotopes, Seventh Edition (New York: John Wiley and Sons, Inc.).

US Nuclear Regulatory Commission
(380 copies for R7)
Division of Document Control
Distribution Services Branch
7920 Norfolk Avenue
Bethesda, MD 20014

US Nuclear Regulatory Commission (4)
Division of Reactor Safety Research
Office of Nuclear Regulatory Research
Washington, DC 20555
Attn: C. N. Kelber, Assistant Director
        Adv Reactor Safety Research
      R. T. Curtis, Chief
        Analytical Adv Reactor Safety
          Res., ARSR
      M. Silberberg, Chief
        Experimental Fast Reactor Safety
      R. W. Wright
        Experimental Fast Reactor Safety

US Department of Energy
Office of Nuclear Safety Coordination
Washington, DC 20545
Attn: R. W. Barber

US Department of Energy (2)
Albuquerque Operations Office
P. O. Box 5400
Albuquerque, NM 87185
Attn: J. R. Roeder, Director
        Operational Safety Division
      D. K. Nowlin, Director
        Special Programs Division
        For: C. B. Quinn
             D. Plymale

University of Michigan
Nuclear Engineering Department
Ann Arbor, MI 48104

Projekt Schneller Brueter (4)
Kernforschungszentrum Karlsruhe GMBH
Postfach 3640
D75 Karlsruhe
West Germany
Attn: Dr. Kessler (2)
      Dr. Heusener (2)

General Electric Corporation (7)
310 De Guigne Drive
Sunnyvale, CA 94086
Attn: J. O. Bradfute, Manager
        Dynamics and Safety
      R. A. Meyer, Manager
        Analytical Engineering
      S. M. Davies, Manager
        Conceptual Design Study
      J. W. McDonald, Manager
        Containment & Radiological Evalu.
      N. W. Brown, Manager
        Licensing and Systems Eng.
      M. I. Temme, Manager
        Safety Criteria & Assessments
      K. H. Chen, M/C S-54

W. E. Nyer
P. O. Box 1845
Idaho Falls, ID 83401

Joint Research Centre (2)
Ispra Establishment
21020 Ispra (Varese)
Italy
Attn: R. Klersy
      H. Holtbecker

Power Reactor & Nuclear Fuel (3)
  Development Corporation (PNC)
Fast Breeder Reactor Dev Project (FBR)
9-13, 1-Chome, Akasaka
Minato-Ku, Tokyo
Japan
Attn: Dr. Mochizuki
      Dr. Watanabe (2)

H. J. Teague (3)
UKAEA
Safety and Reliability Directorate
Wigshaw Lane
Culcheth
Warrington, WA3 4NE
England

R. G. Bellamy
Reactor Fuels Group
AERE Harwell
Oxfordshire, OX11 ORA
England

DISTRIBUTION (Cont):

R. G. Tryor, Head
Reactor Development Division
UKAEA - Atomic Energy Establishment
Winfrith, Dorchester
Dorset
England

1100 C. D. Broyles
　　　Attn: J. D. Kennedy, 1110
　　　　　　T. L. Pace, 1120
　　　　　　G. L. Ogle, 1125
1537 N. R. Keltner
1537 R. U. Acton
1537 T. Y. Chu
1550 F. W. Neilson
　　　Attn: O. J. Burchett, 1552
　　　　　　J. H. Gieske, 1552
2150 C. B. McCampbell
3434 B. N. Yates
4000 A. Narath
4231 J. H. Renken
4231 J. A. Halbleib
4231 J. E. Morel
4400 A. W. Snyder
4410 D. J. McCloskey
4420 J. V. Walker (5)
4421 R. L. Coats
4421 J. E. Gronager
4421 G. W. Mitchell
4422 R. H. Marion
4422 D. A. Powers
4422 J. B. Rivard
4422 J. E. Smaardyk
4422 D. W. Varela
4423 P. S. Pickard
4423 A. C. Marshall
4423 D. A. McArthur
4423 K. O. Reil
4424 M. J. Clauser
4424 E. R. Copus
4424 E. F. Haskin
4424 J. T. Hitchcock

4424 P. J. McDaniel
4424 J. P. Odom
4424 F. W. Sciacca
4424 M. E. Senglaub
4424 J. A. Sholtis
4424 D. C. Williams
4425 W. J. Camp
4425 E. Bergeron
4425 W. M. Breitung
4425 F. Briscoe
4425 R. J. Lipinski
4425 M. L. Schwarz
4425 A. Svo-Antilla
4425 M. F. Young
4426 C. L. Cano
4426 J. G. Kelly
4426 H. L. Scott
4426 K. T. Stalker
4426 W. H. Sullivan
4426 S. A. Wright
4441 M. L. Corradini
4442 W. A. Von Riesemann
4450 J. A. Reuscher
4451 T. R. Schmidt
4452 M. F. Aker
4723 D. O. Lee
5500 O. E. Jones
5530 W. Herrmann
5534 D. A. Benson
5800 R. S. Claassen
5820 R. E. Whan
5822 K. H. Eckelmeyer
5830 M. J. Davis
5835 C. H. Karnes
5846 E. K. Beauchamp
5846 R. A. Sallach
8266 E. A. Aas
3141 T. L. Werner (5)
3151 W. L. Garner (3)
　　　For DOE/TIC (Unlimited Release)
3154-3 R. P. Campbell (25)
　　　For NRC Distribution to NTIS